Donostia International Physics Center

eman ta zabal zazu
Universidad del País Vasco
Euskal Herriko Unibertsitatea

First-principles study of the electronic structure and dynamical electronic excitations of strong spin-orbit metal Pb: bulk, surface and nanosized films

Doctoral thesis submitted by

Xabier Zubizarreta Iriarte

for the degree of Doctor of Philosophy in Physics

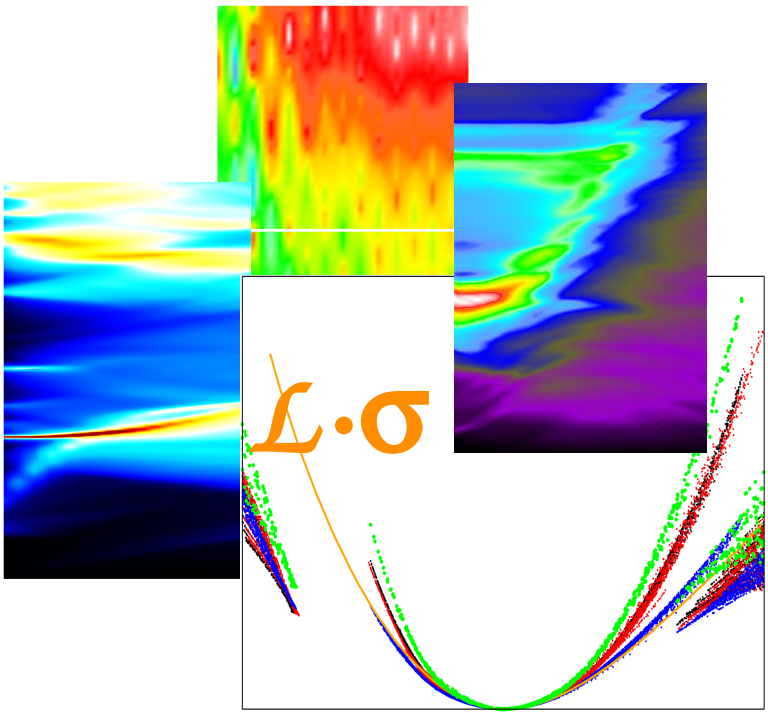

September 2012

Donostia International Physics Center

Universidad del País Vasco
Euskal Herriko Unibertsitatea

First-principles study of the electronic structure and dynamical electronic excitations of strong spin-orbit metal Pb: bulk, surface and nanosized films

Doctoral thesis submitted by

Xabier Zubizarreta Iriarte

for the degree of Doctor of Philosophy in Physics

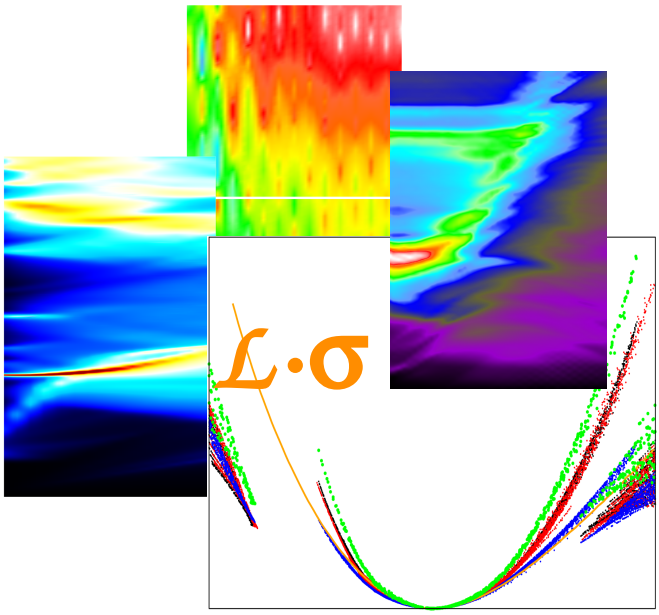

Supervisors:
Vyacheslav Silkin & Eugene Chulkov

September 2012

Gizonen lana jakintza dugu:
ezagutuz aldatzea,
naturarekin bat izan eta
harremanetan sartzea.

Xabier Lete

Acknowledgments

First, I want to thank Slava and Eugene for providing me the possibility to write this thesis. Specially, I thank Eugene for the confidence he put since the first stages of my PhD time and his support. I feel very thankful to Slava too, for all the *savoir faire* he has transmitted me, and for his huge patience when finding again and again brand new programming bugs. And also for the glass of good wine he is going to invite me to. To both of you, спасибо!

Of course, I am indebted to the Donostia International Physics Center (DIPC) as well as to the Univeristy of the Basque Country through the Department of Materials Physics for the financial support during these 6 years. Particularly, I want to thank Pedro Echenique the opportunity he gave me to start this journey. For the same reasons, Xabier, thanks a lot!

J'aimerais bien aussi remercier Nathalie d'avoir être si patiente et d'avoir devenue ma deuxième maman pendant cinq mois. Elle m'a donné plein des conseils qui me sont encore très utils. Merci beaucoup Nathalie, gros bisous!!

Also, I feel thankful to all the people in the DIPC's Computing Center, they did not only help me getting out from a lot a troubles, but also they have always been really kind people. So, Luz, Carmen, Belén, Diego and Txomin, muito obrigado! For similar reasons, I thank all they patience and support to the DIPC secretaries. Mil esker Patxiri ere laguntza guztiagatik.

I want to thank also Artur for his perseverance and ability to teach me the KKR method. I hope we will work together for a long time!! Udo, for all your patience, vielen dank. And thanks a lot also to all the people from the MPI, specially to Tamene, Alexander, Arkady, Mariana, David, María, Pawel, Hossein, Myriam, Ionela, Pedro and Lucila. I miss you!!

También me siento enormemente afortunado de haber compartido tantos buenos momentos y de haber recibido tantos consejos de mi querido Andrés (un abrazo a Luisa también). Qué suerte tiene mi medio tocayo. Qué decir de Axi, ese páharo, ese joven malo, sin cuya ayuda este manuscrito no se habría completado nunca. Mil esker denagatik Axi, espero det maiz elkar ikustea ta lan egitea ere! Graccie mile! Y Maia, muchas gracias por tu ayuda y fuerzas, ¡en bevre estaré allí!

A Íñigo le debo el haber podido acortar mucho el tiempo de cálculo, además de muchos consejos técnicos sobre programas, scripts y demás asuntos quasi-desconocidos para mí. Me siento agradecido de haber compartido muchos momentos con alguien que lo mismo te desvela los secretos de una película, que te descubre tascas de las que ya no quedan o comienza a las 3 de la madrugada una discusión sobre el principio de incertidumbre. Qué tío.

Compañeros de trabajo, pero también de cenas, juergas, catas de vino y demás escenas inolvidables, siempre estaré agradecido a Yon, Fernando, Gisela, Arturo, Marcus, Elton, Bruno, René, Alejandro, Rembri, Sampsa, Thomas, Alvise (a estos dos últimos por enseñarme Tolosa un domingo... y lunes), y a todos aquéllos que espero me perdonen su ausencia aquí. Muchas gracias también a Iñaki, la educación hecha perso... En serio, te echo de menos por aquí. Y también una mención especial para Giusssepe, un tío que siempre me sentiré agradecido de haber conocido, graccie mileee per tutto!!!!

Como "especial" es el nivel de juego desplegado por los artistas del balón del equipo CFM-DIPC, muchas gracias por todos los buenos ratos. En especial a Rubén por organizarlo y por ser como es. No se me olvida por supuesto mandar recuerdos a Sebas de parte de mis tobillos. Te diría que te van a echar de menos, pero...

No puedo dejar de mandar un fuerte abrazo a toda la tropa de italiano-colombianos: Marco, Juan Pablo, Leonardo, Amilcare, Guido, el gran capitán del Barco Pierluigi, Patrizia, ... Pero muy especialmente, a dos "parisinos" con los que espero seguir encontrándome en muchos lugares y demás bares: Feffe y Matteo, mil esker denagatik pareja! ¡Se os quiere!

Y como alguien me ha recordado que existe vida más allá del hespin-hórbit kaplin, cuadrilla, muchas gracias por tantos años de amistad, tantos momentos, tanto cariño, tantos abrazos. Luis, Asier (eta Elena), Sergio, el Nano (y Eva), Iker (eta Jone), Iván (et Anna), Dani (y Teresa), Maite (y Xabi), el Puma (y Carmen), Koldo, Peña; y cómo no, a Juli (y Marta) y a Patxi (eta Ainoah), muito obrigado!!! Eta Mil esker Soraya beti hor izategatik, muak!! Y gracias a Adriana también, sin ella algunos momentos hubieran sido mucho más duros.

No se me olvida agradecer al COFA (institución nodriza de la Escuela Polietílica) lo enormemente difícil que han hecho el que llegue este momento, qué grandes. Gracias a todos por la diversión, pero también por el cariño: Salsas, ZP, Edy, Ekain, Goibu, Iker, Mihel, Cresti, Borjita, Gari... ¡Un abraaaaaaaaaaaaazo! P.D.: Sobra decir que "esto es txupito".

Y un recuerdo muy especial a todos aquéllos con los que comencé este camino hace 12 años: David, Tocayo, Johnny... Muxus también a vosotros.

And last, but not least, mil esker aita ta ama guztiagatik, bihotz bihotzez. Eta Eli, Joan, Pani, Lurra, Kor, Sabai, Xibi eta besteei ere. Asko maite zaituztet.

Donosti, September 2012.

Contents

Chapter 1

Introduction

Aim of the thesis: relativistic effects on dynamical electronic excitations

The main aim of the work performed in this thesis has been the study of relativistic effects on the dynamics of electronic excitations in crystals. Relativistic effects are remarkable in elements presenting a big atomic number, whose core electrons are constraint to a tiny spatial region around the atomic nucleus. As a result, the kinetic energy of these core elecrons is large and they exhibit a velocity which represents an appreciable fraction of the speed of light. Consequently, a relativistic treatment is needed to study systems containing atomic species of big atomic number.

Throughout this thesis the relativistic effects have been incorporated via the spin-orbit coupling (SOC). SOC has been known to play an important role in the physics of semiconductors for decades [Win03]. However, in recent years SOC has been found to give rise to physical phenomena in metallic systems with previously unknown properties. It is the case of solids presenting Rashba splittings of electronic states [IR60, Win03, VEANMK$^+$12] and of the so-called topological insulators (TI) [ZHLK10], where SOC lifts the spin degeneracy of certain energy bands, the latter representing one of the hottest research fields in solid state physics nowadays. These two different physical systems are highly interesting materials not only for basic research, but also for the development of new technologies, mainly of spintronics [vFDS04].

Here, Pb has been chosen as subject of study, as it presents a big atomic number (Z = 82) together with a simple crystalline structure, namely the face-centered cubic (fcc) structure. Pb presents the second highest superconducting critical temperature among the elemental metals [YSBVC$^+$11], and relativistic effects have been shown to substantially affect the lattice vibrations (phonons) [JVTJ$^+$08] and their coupling to the electrons (electron-phonon coupling) [HBYSVC10] in bulk lead. Additionally, Pb(111) thin films have recently become the widest used playground in the study of the so-called quantum-size effects (QSE), giving rise to a broad experimental as well as theoretical bibliography (see, i.e., Ref. [JLZX07] for a review). Thus, it is of interest

to investigate the SOC effects on the dynamical electronic excitations of lead, both in the bulk and in nanosized films.

Chronological outline

The starting point of the work reported in this thesis consisted in the implementation of the SOC into the ground state computational code, based on density functional theory (DFT) [HK64, KJS65] and norm-conserving pseudopotentials (NCP) [EP89]. Once the band structure of bulk fcc lead was checked to be in fairly good agreement with experimental measurements and previous theoretical studies, the evaluation of the dynamical electronic excitations was undertaken. First, calculations of the inelastic electron-electron contribution to the decay rate of excited quasiparticles was performed. In principle, here the relativistic effects were included only through the SOC-corrected energy bands. Nevertheless, this *ad hoc* approximation was supposed to give a satisfactory description of the relativistic effects as the SOC-splitted bulk band structure of Pb is well reproduced in the first order perturbation theory.

Then, the study of the dielectric response of bulk Pb in the low-energy transfer range was performed, investigating the effects of several physical ingredients: SOC, exchange-correlation short-range effects, the inhomogeneity of the electron density... As expected, SOC effects on the low-energy transfer energy-loss function were found to be satisfactorily reproduced by only including the SOC-induced energy splittings while still using the scalar-relativistic wave functions, justifying the aforementioned *ad hoc* approximation in the evaluation of inelastic decay rates. Interestingly, acoustic plasmons (AP) were detected in our first-principles calculations, and a careful analysis allows us to suggest the most suitable momentum transfer range to experimentally detect the AP in bulk lead.

Once the investigation of the low-energy excitations in bulk Pb reached an advanced status, the study of the high-energy range of the dielectric response was undertaken. While the low-energy transfer results showed good agreement with previously published theoretical as well as experimental works, the energy of the main bulk plasmon was overestimated at any level of inclusion of the different physical ingredients in the calculations. At first sight, this was surprising, as lead is a simple metal whose bulk plasmon energy is well estimated by classical electrodynamics. As a possible reason for this problem the semicore $5d$ electrons were considered as the missing feature in our preliminary calculations. Then, the $5d$ electrons were explicitly incorporated in the computation of the dielectric response of bulk lead, and the discrepancy with the available experimental data was considerably reduced.

The second part of this thesis has been devoted to the study of the electronic structure and dielectric response of freestanding Pb(111) films, analyzing the SOC effects and possible appearance of QSE. Concerning the ground state of the films, SOC effects on the band structure of the slabs were found to be irrelevant except for the single monolayer (ML). The density of states (DOS) of the latter exhibits a transition

from a metallic to a semimetallic character upon SOC inclusion. Regarding the QSE, they were found in the thickness dependence of the DOS and work function of the films as a bilayer oscillation, with a beating pattern of 9 ML period superimposed, in good agreement with previous theoretical and experimental works.

Finally, the computational study of the dielectric response and plasma losses of 1 - 15 MLs thick Pb(111) films was initiated. The first retrieved results showed no sign of the split thin film modes stemming from the hybridization of the surface plasmons of both slab surfaces in the long wavelength limit. This finding is shown to be a consequence of the fully three-dimensional scheme applied to the supercell approach. Once the calculation scheme was modified in attempt to partially remove the artificial long-range Coulomb interaction resulting from the repeated slab geometry used, the split thin film modes were obtained.

QSE have been found in the single monolayer energy-loss spectra. The 2 MLs thick slab represents the crossover with the thickness range where no consequences of the quantization of the electron states were found. Interestingly, the low-energy plasmon mode of the films disappears upon SOC inclusion. This effect has been shown to arise from the incorporation of the two-component spinors into the evaluation of the dielectric response of the films. Work is still in progress to gain further insight into this SOC-induced disappearance of the low-energy symmetric mode.

Additional projects

The PhD candidate has been also involved in other research projects. Mainly, he has spent 7 months as a visitor in the Max Planck Insitute (MPI) of Halle (Germany) working under the supervision of Dr. Ernst.

The research project being carried out in collaboration with Dr. Ernst consists in the *ab initio* study of topological insulators out of stoichiometry. The employed theoretical method is the Korringa-Kohn-Rostoker (KKR) method formulated in terms of Green's functions [Ern07], which allows the treatment of off-stechiometry systems by the use of the coherent potential approximation, commonly known as CPA [Ern07].

The objective of the project is twofold. On the one hand, to study alloys of topological insulators, seeking to predict TI systems with improved characteristics for their application in devices. On the other hand, TIs are doped with magnetic impurities in order to get insight in the interplay between the characteristic features in the electronic structure of TIs and magnetism.

As we have been facing technical problems with the fully-relativistic version of the computational code used in this collaboration [Ern07], results are still incomplete and are not presented in this thesis.

Structure of the manuscript

The rest of the thesis is organized as follows.

The following three chapters present the theoretical frameworks applied in the present work. Chapter 2 is devoted to the theoretical methods used in the study of the electronic structure of both bulk Pb and Pb(111) films. The DFT-NCP are outlined and particular emphasis is made on the SOC inclusion. Chapter 3 deals with the linear-response theory and the explicit expressions derived from it as applied in this thesis to study the electronic excitations in crystalline Pb. Chapter 4 presents the concept of self-energy and describes the method used to compute it, known as *GW* approximation.

Then results on the electronic structure of bulk Pb as well as on its electronic collective and single-particle excitations are analyzed. Chapter 5 introduces the details of the calculated Pb bulk band structure calculations together with the SOC effects on it. Chapter 6 and 7 deal with the detailed study of the dielectric response and dynamics of electronic collective excitations in the low- and high-energy transfer ranges, respectively. In Chapter 8 we discuss the first-principles inelastic decay rates obtained in this thesis.

Chapter 9 is devoted to the study of the electronic structure of freestanding Pb(111) films, analyzing both QSE and SOC effects. Next, results of the calculation of the surface loss function of the films is presented and discussed in Chapter 10, highlighting again QSE as well as the role of SOC effects.

Last, in Chapter 11 the main contents of the thesis are outlined, together with a summary of the comparison of present results with available experimental data.

Unless otherwise stated, atomic units are used throughout this thesis, i.e., $e^2 = \hbar = m_e = 1$.

Chapter 2

Theoretical methods I: Electronic structure

2.1 Introduction

The microscopic description of solids is a formidable task, since the number of particles involved is $\sim 10^{23}$. Even taking advantage of periodicity of crystals, one still faces systems (unit cells) composed by $\sim$10 nuclei and $\sim$100 electrons. Therefore one would still be dealing with a $\sim 10^2 - 10^3$ coordinates dependent system [see Eq. (2.2)].

In this chapter we briefly review the different theoretical approaches used in our work to make the study of the electronic ground state properties of solids feasible. These approaches are among the most widespreadly applied theoretical frameworks in the chemistry and solid state physics communities. First the DFT is described pointing to its usefullness and limitations. Then the approach chosen for modeling the ion-electron interaction, namely the norm-conserving pseudopotential scheme, is shortly introduced.

Finally, we derive the SOC potential matrix element expression corresponding to the formalism used in the present thesis, and show its inclusion following two different schemes into the ground state computational code. Both the implementation of the spin-orbit interaction and its inclusion into the computational tools previously developed by his thesis supervisors were carried by the PhD candidate.

2.2 The many-particle problem

Ordinary matter is composed of electrons moving around and in between the massive nuclei, working as a glue and thus allowing the formation of molecules and solids. The ground state properties of such a system can be derived solving the (non-relativistic)

time-independent Schrödinger equation

$$\widehat{H}\Psi(\{\mathbf{r}\},\{\mathbf{R}\}) = E\Psi(\{\mathbf{r}\},\{\mathbf{R}\}), \tag{2.1}$$

being $\widehat{H}$ the Hamiltonian operator expressed as

$$\begin{aligned}\widehat{H} = &\sum_i \frac{1}{2m_e}\nabla_i^2 + \sum_j \frac{1}{2M_j}\nabla_j^2 \\ &+ \frac{1}{2}\sum_j^{N_{\text{nuc}}}\sum_{j'\neq j}^{N_{\text{nuc}}} \frac{Z_j Z_{j'}}{|\mathbf{R}_j - \mathbf{R}_{j'}|} + \frac{1}{2}\sum_i^{N_e}\sum_{i'\neq i}^{N_e}\frac{1}{|\mathbf{r}_i - \mathbf{r}_{i'}|} - \sum_j^{N_{\text{nuc}}}\sum_i^{N_e}\frac{Z_j}{|\mathbf{R}_j - \mathbf{r}_i|} \equiv \\ &\equiv \widehat{T}_e + \widehat{T}_N + \widehat{V}_{NN} + \widehat{V}_{ee} + \widehat{V}_{eN}, \end{aligned} \tag{2.2}$$

for a system with N_e electrons of mass m_e and N_{nuc} nuclei of atomic number (charge) Z_j and mass M_j. In Eq. (2.2) $\widehat{T}_e$ and $\widehat{T}_N$ stand for the kinetic energy operators of electrons and nuclei, respectively. The remaining three terms are Coulomb-like potentials between different nuclei $\widehat{V}_{NN}$, different electrons $\widehat{V}_{ee}$, and electrons and nuclei $\widehat{V}_{eN}$. $\{\mathbf{r}\}$ and $\{\mathbf{R}\}$ represent all the spatial and spin coordinates of all the particles, i.e., $\{\mathbf{r}\} \equiv (\mathbf{r}_1, \sigma_1, \mathbf{r}_2, \sigma_2, ..., \mathbf{r}_{N_e}, \sigma_{N_e})$.

In order to simplify the description of the many-particle system, we apply the well-known Born-Oppenheimer approximation [MM04], by which one decouples the nuclear and electronic degrees of freedom. The approximation is supported by the big difference of electron and nuclear masses, $M_j >> m_e$, $\forall Z_j$. Thus, in this approximation electrons see the nuclei motionless, and the nuclear coordinates $\{\mathbf{R}\}$ become parameters. As a consequence, the relevant equation is now given by

$$\widehat{H}_e\psi_i(\{\mathbf{r}\}) = E_i\psi_i(\{\mathbf{r}\}) \tag{2.3}$$

with the electronic Hamiltonian operator built for a fixed choice of the nuclear coordinates $\{\mathbf{R}\}$:

$$\widehat{H}_e = \widehat{T}_e + \widehat{V}_{ee} + \widehat{V}_{eN}(\{\mathbf{R}\}). \tag{2.4}$$

The eigenstates ψ_i of $\widehat{H}_e$ are now considered as the stationary states of the system once $\{\mathbf{R}\}$ are fixed.

In summary, the original many-particle problem has been reformulated as the study of a system of interacting electrons subject to a external potential due to the frozen nuclei. In several theoretical approaches the role of the nucleus is played by the ion composed of the tightly bound core electrons and the atomic nucleus itself (see Section 2.4).

2.3 Density Functional Theory

After applying the Born-Oppenheimer appoximation still the electronic problem is difficult to tackle, even numerically, as the remaining quantum-mechanical description of the system [see Eq. (2.3)] depends on the $3N_e$ degrees of freedom of all the valence electrons.

DFT [OJG89], the most widely used tool for determining the electronic structure of molecules and solids, greatly simplifies the problem. It reduces the study of a N_e interacting electron system to the resolution of a one-particle equation, moving in an *effective* external potential, different from $\widehat{V}_{eN}(\{\mathbf{R}\})$ of Eq. (2.4). As a result, the theoretical description of the many-particle system depending on $3N_e$ degrees of freedom is encoded in a formalism which depends only on 3, namely the spatial coordinates of the electron density.

Thomas [HT27] and Fermi [Fer28] were the firsts in proposing such a "change of variable" in the 1920s. However, it was in the 1960s when DFT was established as a powerful tool for electronic structure studies following the work of Hohenberg and Khon [HK64] and Kohn and Sham [KJS65]. We briefly review their work below.

2.3.1 Hohenberg-Kohn theorems

The Hohenberg-Kohn (HK) theorems [HK64] form the basis of the DFT. The original proof of the theorems was carried for the ground state of a non spin-polarized system subject to a static external potential. In this work we are not interested neither in spin-polarized nor in time-dependent systems. Generalization of the Hohenberg-Kohn theorems to those situations can be found elsewhere.

Suppose a system of interacting particles subject to an external potential $w(\mathbf{r})$ [see Eq. (2.4)] and presenting the ground state electron density $\rho_0(\mathbf{r}) = \rho_0(x, y, z)$. The first HK theorem states that if replacing $w(\mathbf{r})$ by a different $w'(\mathbf{r})$ the new ground state electron density $\rho'_0(\mathbf{r})$ is equal to $\rho_0(\mathbf{r})$, then $w(\mathbf{r})$ and $w'(\mathbf{r})$ can only differ by a constant shift. Hence, the ground state electron density determines the properties of the system.

The second HK theorem states that if we define the energy of a N electron system in an external potential $w(\mathbf{r})$ as a functional of the electron density as follows

$$E[\rho] = F[\rho] + \int w(\mathbf{r})\rho(\mathbf{r}), \tag{2.5}$$

then the minimum of $E[\rho]$ corresponds to the ground state of the system, that is, $\min\{\mathrm{E}[\rho]\} = \mathrm{E}[\rho_0] \equiv \mathrm{E}_0$. In our case, $\widehat{F}[\rho] = \widehat{T}_e[\rho] + \widehat{V}_{ee}[\rho]$, see Eq. (2.4).

The HK theorems have enormously simplified the problem of obtaining the ground state of our interacting electron system. Unfortunately, it is not possible to directly

evaluate the derivative of the energy functional with respect to the electron density. This is due to the lack of an analytical expression for $\widehat{T}_e[\rho]$, the kinetic energy *of an interacting electron system* as a functional of the density. Kohn and Sham overcame this obstacle with their formalism.

2.3.2 Kohn-Sham equations

The key of the Kohn-Sham approach [KJS65] is to replace the interacting electron system by a *fictitious* non-interacting one. Seeking this replacement, Eq. (2.5) is rewritten in the following form

$$E[\rho] = \int d\mathbf{r}\rho(\mathbf{r})w(\mathbf{r}) + \frac{1}{2}\int d\mathbf{r}\int d\mathbf{r'}\frac{\rho(\mathbf{r})\rho(\mathbf{r'})}{|\mathbf{r}-\mathbf{r'}|} + T[\rho] + E_{xc}[\rho], \tag{2.6}$$

where the second term is the Hartree energy, $T[\rho]$ is the kinetic energy *of a non-interacting electron system* and $E_{xc}[\rho]$ is a crucial term, the so-called exchange-correlation (xc) energy. It accounts for the many-body physics missing in the classical description of the Hartree energy and of the correlation effects absent now in the new non-interacting kinetic energy term.

With the HK theorems in mind, we minimize the energy functional of Eq. (2.6) and obtain the Kohn-Sham equations, which present the same form as a one-electron Schrödinger equation:

$$\left\{-\frac{1}{2}\nabla^2 + V_{\text{eff}}(\mathbf{r})\right\}\psi_i(\mathbf{r}) = \epsilon_i\psi_i(\mathbf{r}), \tag{2.7}$$

with the effective potential

$$V_{\text{eff}}[\mathbf{r},\rho(\mathbf{r})] = w(\mathbf{r}) + \int d\mathbf{r'}\frac{\rho(\mathbf{r'})}{|\mathbf{r}-\mathbf{r'}|} + \frac{\delta E_{xc}[\rho(\mathbf{r})]}{\delta\rho(\mathbf{r})}, \tag{2.8}$$

where the first term is the external potential, the one built by the ions in our case, the second term is the Hartree potential V_H and the third one is defined as the exchange-correlation potential V_{xc}.

Solving Eq. (2.7) we get the set of KS energies $\left\{\epsilon_i^{\text{KS}}\right\}$ and orbitals $\left\{\psi_i^{\text{KS}}\right\}$. Finally we compute the electron density as the sum of the contributions of each occupied KS orbital,

$$\rho(\mathbf{r}) = \sum_i^{occ} |\psi_i^{\text{KS}}(\mathbf{r})|, \tag{2.9}$$

where the occupation of the KS orbitals is known after obtaining the Fermi level through the condition

$$N_e = \int d\mathbf{r}\rho(\mathbf{r}). \tag{2.10}$$

Equations (2.7)-(2.10) are solved self-consistently.

2.3.3 Local Density Approximation

In principle, the KS formalism is exact. However, the expression for the exchange-correlation energy is unknown and V_{xc} has to be approximated. Throughout this thesis we have used the Local Density Approximation (LDA), the most widely applied one. It was already proposed in the original paper by Kohn and Sham [KJS65] as a good approximation for V_{xc} in systems presenting smoothly varying electron density, as it is the case of simple metals. Mathematically, this condition can be expressed as

$$\frac{|\nabla\rho(\mathbf{r})|}{\rho(\mathbf{r})k_F(\mathbf{r})} \ll 1, \tag{2.11}$$

where $k_F(\mathbf{r})$ is the Fermi momentum.

Nevertheless, LDA has prove itself to give acceptable results for a big variety of systems, with some well known limitations as it is the case of its bad description of absolut energy band gaps in semiconductors and insulators. In LDA, corrections to the exchange-correlation energy due to the inhomogeneities in the electron charge density around a position $\mathbf{r}$ are ignored. Considering this, it may at first seem surprising that LDA works satisfactorily not only for simple metals. This can be partially attributed to the fact that LDA gives the correct sum rule to the exchange-correlation hole [OJG89]. That is, using LDA there is a total electronic charge equal to one electron excluded from the neighbourhood of an electron positioned at $\mathbf{r}$. Indeed, it can also be shown that the exchange-correlation energy depends only weakly on the detailed shape of the exchange-correlation hole [GIL76].

Usually, the exchange-correlation energy term is written as

$$E_{xc} = \int \epsilon_{xc}[\rho(\mathbf{r})]\rho(\mathbf{r})d\mathbf{r}, \tag{2.12}$$

defining in this way ϵ_{xc} as the xc energy per electron. This quantity has been evaluated with a high precision for the homogeneous electron gas using Monte-Carlo simulations [MCJA80], and several parametrizations can be found in the literature. In the present work we use the one due to Perdew and Zunger [PPZ81], with the following expressions for ϵ_{xc} and V_{xc}

$$\epsilon_{xc} = \frac{0.458}{r_s} - \frac{\gamma}{1+\beta_1\sqrt{r_s}+\beta_2 r_s}, \tag{2.13}$$

$$V_{xc} = -\frac{0.611}{r_s} - \frac{\gamma(1+\frac{7}{6}\beta_1\sqrt{r_s}+\frac{4}{3}\beta_2 r_s)}{(1+\beta_1\sqrt{r_s}+\beta_2 r_s)^2}, \tag{2.14}$$

where the parameters $\gamma = 0.1423$, $\beta_1 = 1.0529$ and $\beta_2 = 0.3334$ are in atomic units. ϵ_{xc} and V_{xc} are functions of the density through r_s, the electron density parameter defined as

$$r_s = \left(\frac{3}{4\pi\rho(\mathbf{r})}\right)^{1/3}, \tag{2.15}$$

where $\rho(\mathbf{r})$ denotes the valence density of the solid at point $\mathbf{r}$.

For metallic surfaces [Lie97], LDA gives an exponential decay of the potential in the vacuum. This is an incorrect behaviour as the potential should present an image-like tail outside a metallic surface. To obtain the proper decay in vacuum a non-local exchange-correlation potential is needed (i.e., Ref. [DWWGMRJN98]). A different approach is the construction of a hybrid potential which coincides with the self-consistent LDA in the solid and close to the surface while enforcing it to present the correct image potential-like behaviour further in the vacuum [MSZG$^+$09]. Note that the incorrect exponential decay in the vacuum given by LDA is of no significance for occupied states, whereas it removes the whole Rydberg-like series of image states [MEBP78]. Hence, the LDA incorrect asymptotic behaviour in the vacuum needs to be corrected in any study of the physics of image potential states.

2.3.4 Validity and physical meaning of DFT-KS quantities

DFT has shown itself to be a priceless theoretical framework, making the electronic structure calculations of realistic systems feasible. However, care should be taken in using DFT results and KS quantities as exact or even valid. Below I review some points one should keep in mind in making use of DFT.

As stated above, the exchange-correlation functional has to be approximated. Thus, strictly speaking, any practical use of DFT gives unexact results. It is the record of satisfactory results which determines *a posteriori* the validity of any xc functional for a given kind of systems (metal, semiconductor, strongly correlated one, etc.).

Even though in practice there is no problem converging to the ground-state minimum of the energy density functional because of its convex nature [PPL85], *a priori* there is no reason for the self-consistent cycle of Eqs. (2.7)-(2.10) to converge. Actually, the naive scheme of using the output potentials (Hartree and xc) of one iteration as the input of the next one usually does not converge and a mixing of the output potentials of several previous iterations has to be used. In the present thesis the simplest mixing scheme is applied. The input potentials for the n-th iteration V_n^{in} have been chosen as $aV_{n-1}^{in} + bV_{n-1}^{out}$, with $a+b=1$ and $a \geqslant b$ for all bulk and films ground state calculations in the present work. As an example, for systems with d electrons around the Fermi level, i.e. noble metals, usually $a \gg b$ is needed to converge within the described simple mixing scheme.

Concerning KS quantities, only the electron density, total energy and highest occupied energy level [GV05] are physically meaningful. Even though the highest occupied energy level is correctly described by the solutions of the KS equation, in general the Fermi surface differs from the true one [Mea88]. As DFT is a ground state theory, in principle KS energies ϵ_i^{KS} and orbitals ψ_i^{KS} should not be used to perform studies of excitations, for example, in TDDFT or GW calculations [ORR02]. The ϵ_i^{KS} energies (occupied and unoccupied) are just Lagrange multipliers coming out the energy

functional minimization carried under the constraints of preserving the number of particles and the normalization of wave functions. Nevertheless, in Ref. [G̈96] the author states that, according to Görling-Levy perturbation theory [GL93], the difference of $\epsilon_i^{\mathrm{KS}} - \epsilon_j^{\mathrm{KS}}$ with $i \neq j$ has physical meaning as a transition energie at zeroth order in the electron-electron interaction.

KS orbitals have no physical interpretation as they are the eigenvectors of a fictitious non-interacting system. Still, a detailed study of the overlap between LDA and self-consistent *GW* (see Chapter 4) wave functions presented in Ref. [BVR06] showed LDA valence wave functions and ground state densities are in excellent agreement with the fully self-consistent *GW* ones, whereas in the case of conduction states LDA gives also a satisfactory description in metals. The authors proved that the good quality of LDA wave functions is a consequence of cancelation of errors in the self-consistent *GW* cycles [BVR06]. More generally, in Ref. [DPCECRS94] the KS orbitals were shown to represent a satisfactory approximation to the quasiparticle (see Chapters 3 and 4) wave functions. Again, it is *a posteriori* that the quality of KS-LDA orbitals is attested.

In conclusion, KS energies ϵ_i^{KS} and orbitals ψ_i^{KS} obtained using the LDA represent a good starting point for calculations of electronic excitations, specially in metals.

2.4 Norm-conserving pseudopotentials

In solving Eq. (2.7) with the potential given by Eq. (2.8) a choice for the external potential $w(\mathbf{r})$ has to be made. In the present study we use the so-called norm-conserving pseudopotentials (NCP). The following are the two main motivations for the development of the pseudopotential concept:

i) As it is well known, the core electrons are mainly insensitive to the chemical environment of the atom, chemistry being carried mostly by the valence electrons. Anyway, as shown in Chapter 7, in some cases there is no unambiguous definition of which are the core electrons.

ii) In modeling the atomic wave functions a huge number of basis functions (e.g., plane waves) is needed. This is due to the orthogonality between different orbitals of the same angular momentum, which results in a strongly oscillating nodal structure of the atomic wave functions mainly close to the nucleus.

Use of the pseudopotential approximation allows to freeze the core electrons and the substitution of true valence wave functions by smooth nodeless fictitious pseudoorbitals which far from the nucleus are identical to the true ones. Thus, pseudopotentials are *fictitious* potentials between the ion (formed by the nucleus and the core electrons) and the valence electrons which should fulfill the following demands:

i) Once introduced in a KS equation, pseudopotentials should give eigenvalues in agreement with the energy levels for the valence electrons of the true all-electron Schrödinger equation.

ii) Give smooth nodeless pseudo-wave functions indistinguishable from the all-electron orbitals beyond some cut-off radius r_c.

iii) Be soft. This is needed to ensure the smoothness of pseudo-wave functions.

iv) Be finite at $r \to 0$ (often pseudopotentials are also enforced to have a vanishing laplacian at $r \to 0$), in contrast to the $1/r$ divergence of the all-electron potential.

The pseudopotential approximation began as an extension of the Orthogonalized Plane Wave (OPW) method [CPK59]. Since then, the pseudopotential approach experienced several steps forward until in 1979 first-principles NCP were introduced by Hamann, Schlüter and Chiang [RHSC79]. NCP are built with two additional constraints:

v) Norm-conservation. This stands for the conservation of the square of the norm of any valence orbital integrated up to any $r > r_c$.

vi) Give pseudo-wave functions that present the same logarithmic derivative with respect to the energy as the true all-electron orbitals around the true energy eigenvalue of the orbital under consideration, again for $r > r_c$.

The latter two properties of NCP are related by the following equation [CTJH74],

$$-2\pi \left[(r\phi)^2 \frac{d}{dE} \frac{d}{dr} \ln\phi_i \right]_{R,\epsilon_i} = 4\pi \int_0^R \phi_i^2 r^2 dr, \tag{2.16}$$

where $R \geqslant r_c$ and ϵ_i is the eigenvalue energy associated with the orbital ϕ_i. The logarithmic derivative gives the scattering properties of the system [Mes99]. As a consequence NCP present the same scattering properties of the true all-electron orbitals around their energy eigenvalues. This ensures a crucial quality of NCP: transferability, that is, good performance of the atomic pseudopotential in different chemical environments.

There are several schemes to build NCP. In the present thesis the pseudopotentials used were generated following the Hamann-Schlüter-Chiang (HSC) recipe of Ref. [RHSC79], as implemented in the `atom` computational package [ATO], even though pseudopotentials generated by the scheme developed by Troullier and Martins (TM) [TLM91] were also tested (for further details on generation and testing of NCP, see Section 5.1). HSC pseudopotentials are semilocal, local functions of the distance to the nucleus r, while non-local in both the azimuthal and polar angles. Hence, there is a $\widehat{V}_l^{ion}(r)$ for each angular momentum l. For further details, in Ref. [BBRHS82] the authors give a detailed description of the generation of HSC-like NCP. Note also that as DFT is used to perform the atomic all-electron calculations from which the pseudopotentials are constructed, an election for the xc functional is also needed in working in the generation of the pseudopotentials, and LDA was chosen here.

2.5 Plane wave basis and Hamiltonian matrix elements

2.5.1 Plane wave basis

In order to write down the explicit expressions for the matrix elements of the different terms of the Hamiltonian in Eq. (2.7), a plane wave basis is used. Thus, wave functions are built as linear combinations of plane waves

$$\phi_{n,\mathbf{k}}(\mathbf{r}) = \frac{1}{\sqrt{\Omega}} \sum_{\mathbf{G}} c_{n,\mathbf{k}}(\mathbf{G}) e^{i(\mathbf{k}+\mathbf{G})\cdot\mathbf{r}}, \tag{2.17}$$

for an electron state with momentum $\mathbf{k}$ belonging to the first Brillouin zone (BZ). In Eq. (2.17) n labels the electronic states, whereas $\mathbf{G}$ are the reciprocal lattice vectors.

As plane waves represent a complete but infinite basis, in practice a truncation of the basis must be applied. This is done by fixing the maximum energy E_{cut} the plane waves of the basis can carry. Calculations must be checked to be converged with respect to this cut-off energy E_{cut}. The number of plane waves included in the truncated basis for a system (unit cell) of volume Ω and with a given E_{cut} is

$$N_{pw} \simeq \Omega(E_{cut})^{3/2}. \tag{2.18}$$

Therefore, the number of basis functions not only increases with E_{cut}, it also scales almost linearly with the volume of the unit cell. This is an important point, since in performing calculations of the ground state of freestanding films the usual supercell scheme is used in the present work. For such a supercell approach a thick region of vacuum is needed in between two subsequent films in order to avoid possible interactions of the different slabs. As a consequence, one of the dimensions of the unit cell in the slab calculations is ∼10 times bigger than in a three-dimensional (3D) solid making computations for films much heavier.

2.5.2 Matrix elements

By using NCP, the external potential in Eq. (2.7) is divided into two different contributions, one local $\widehat{V}^{loc}$ and one non-local $\widehat{V}^{nl}$ in the angular coordinates φ and θ. As NCP are used, both contributions are local in r. Then,

$$w(\mathbf{r}) = \sum_{l} \widehat{V}_l^{ion}(r)\mathrm{P_l} = \widehat{V}^{loc}(r) + \sum_{l} \widehat{V}_l^{nl}(r)\mathrm{P_l} \equiv \widehat{V}^{loc}(r) + \widehat{V}^{nl}(\mathbf{r}), \tag{2.19}$$

where $\mathrm{P_l}$ stands for the projector on the angular momentum channel l. Finally, the Hamiltonian reads

$$\widehat{H}(\mathbf{r}) = \widehat{T} + \widehat{V}^{loc}(r) + \widehat{V}^{nl}(\mathbf{r}) + \widehat{V}_H(\mathbf{r}) + \widehat{V}_{xc}(\mathbf{r}). \tag{2.20}$$

Using the plane wave basis one gets the following expressions for the matrix elements of each term in Eq. (2.20) between plane waves of momentum **k**+**G** and **k**+**G'** (explicitly in natural units):

$$T(\mathbf{G},\mathbf{G'}) = \frac{|\mathbf{G'}|^2}{2m}\delta(\mathbf{G}-\mathbf{G'}), \tag{2.21}$$

$$V_H(\mathbf{G}-\mathbf{G'}) = \frac{4\pi\rho(\mathbf{G}-\mathbf{G'})}{|\mathbf{G}-\mathbf{G'}|^2}, \tag{2.22}$$

$$V^{loc}(\mathbf{G},\mathbf{G'}) = 4\pi\frac{S(\mathbf{G}-\mathbf{G'})}{|\mathbf{G}-\mathbf{G'}|}\times \\ \times\left\{-\frac{Z}{|\mathbf{G}-\mathbf{G'}|}+\int_0^\infty\left[V^{loc}(r)+\frac{Z}{r}\right]r\ \ \sin(|\mathbf{G}-\mathbf{G'}|r)dr\right\}, \tag{2.23}$$

$$V^{NL}(\mathbf{G},\mathbf{G'}) = 4\pi S(\mathbf{G}-\mathbf{G'})\times \\ \times\sum_l(2l+1)P_l(\cos\gamma)\int r^2 j_l(K_G r)j_l(K_{G'}r)V_l^{NL}(r)dr, \tag{2.24}$$

and $V_{xc}(\mathbf{G},\mathbf{G'})$ is calculated numerically from Eq. (2.14).

In the Hartree potential matrix elements expression, $\rho(\mathbf{G})$ is the Fourier component of the electron density $\rho(\mathbf{r})$ corresponding to the reciprocal lattice vector $\mathbf{G}$. In Eq. (2.24) $P_l(x)$ are Legendre polynomials [AS64], $j_l(K_G r)$ are spherical Bessel functions [AS64], $K_G \equiv \mathbf{k}+\mathbf{G}$ and γ is the angle between vectors K_G and $K_{G'}$. $S(\mathbf{G'}-\mathbf{G})$ stands for the structure factor, which contains the information about the positions of the different atoms in the unit cell [see Eq. (B.5) in Appendix B].

2.5.3 Hamiltonian diagonalization and reconstruction of the valence electron density.

The Schrödinger equation with the Hamiltonian (2.20) is solved at a fixed **k** point of the irreducible BZ (IBZ) by direct diagonalization and $\rho_{n,\mathbf{k}}(\mathbf{G})$, the contribution of each energy band n to the Fourier components of the density at **k**, is obtained through

$$\rho_{n,\mathbf{k}}(\mathbf{G}) = \sum_{\mathbf{G'},\mathbf{G''}} c_{n,\mathbf{k}}(\mathbf{G'})c_{n,\mathbf{k}}(\mathbf{G''})\delta(\mathbf{G}-\mathbf{G'}-\mathbf{G''}). \tag{2.25}$$

This procedure is carried out for a mesh of **k** points spanning the IBZ, taking advantage of the symmetry operation of the point group of the particular system under study. Throughout the present work, regular Monkhorst-Park [JMDP76] grids are used both in bulk and film calculations. Then, the Fourier components of the electron density are retrieved summing the contribution of all occupied bands throughout the IBZ,

$$\rho(\mathbf{G}) = \sum_{n_{occ}}\int \rho_{n,\mathbf{k}}(\mathbf{G})d\mathbf{k} \simeq \frac{2\pi^3}{\Omega}\sum_{n_{occ},\mathbf{k}}\rho_{n,\mathbf{k}}(\mathbf{G}), \tag{2.26}$$

obtaining in this way the Fourier transform of the valence electron density, and then $\rho(\mathbf{r})$ in real space by Fourier transforming $\rho(\mathbf{G})$. If convergence has not been achieved, $V_H(\mathbf{G}-\mathbf{G'})$ and $V_{xc}(\mathbf{G},\mathbf{G'})$ are updated and the next iteration of the self-consistent loop starts.

The diagonalization of the Hamiltonian is the computationally most demanding step in the ground state calculations and the CPU time needed scales as N_{pw}^3. Note that as a consequence, the slab calculations where $N_{pw}^{slab} \sim 10 N_{pw}^{bulk}$ (see discussion at the end of Sec. 2.5.1) need roughly $\sim 10^3$ the CPU time of a bulk calculation if the same cut-off energy and similar number of $\mathbf{k}$ points is used in both cases.

2.6 Spin-orbit coupling

In large atomic number elements the core electrons are spatially constraint to a tiny region around the nucleus. As a consequence, their kinetic energy is extremely large and relativistic effects become important. Pure lead in different geometries is a subject under study here. Pb has a high atomic number $Z = 82$. Consequently, relativistic effects are relevant and should be taken into account in theoretical studies of any system which contains Pb, as it is the case here.

In this section the theoretical and technical details of the procedure followed to include relativistic effects in this thesis are described. The incorporation of the relativistic effects in the electronic structure is done by the spin-orbit coupling term in the Hamiltonian.

2.6.1 SOC pseudopotential and matrix element

SOC couples the spin and orbital angular momenta of the electrons. It appears as a relativistic correction to the non-relativistic Schrödinger equation. In the central field approximation, that is, for a spherical potential, it presents the following form,

$$\widehat{V}^{SOC} = \frac{1}{2Mc}\frac{1}{r}\frac{dV}{dr}\mathbf{L}\cdot\boldsymbol{\sigma}, \tag{2.27}$$

where $\mathbf{L}$ and $\boldsymbol{\sigma}$ are the angular momentum operators and Pauli matrices vectors, respectively. This SOC term is the relevant one here, as the pseudopotentials are unscreened from the interaction between the valence electrons, and their final expressions are spherically symmetric for each angular momentum channel l (see Section 2.4).

Working with NCP generated from a relativistic calculation, the pseudopotentials retrieved are dependent not on l but on the total angular momentum $l\pm1/2$ [BBRHS82, KMB82]. Then the total pseudopotential is written in the form

$$\widehat{V}^{ion}(\mathbf{r}) = \sum_l \left[\widehat{V}_l^{ion}(r) + \widehat{V}_l^{SOC}(r)\mathbf{L}\cdot\boldsymbol{\sigma}\right] \mathrm{P_l}, \tag{2.28}$$

where $\mathrm{P_l}$ stands for the projector on the angular momentum channel l, and

$$\widehat{V}_l^{ion} = \frac{1}{2l+1}\left[l\widehat{V}_{l-1/2}^{ion} + (l+1)\widehat{V}_{l+1/2}^{ion}\right], \tag{2.29}$$

is the average pseudopotential for the states with angular momentum $j = l \pm 1/2$ [see Eq. (2.19)], and

$$\widehat{V}_l^{SOC} = \frac{2}{2l+1}\left[\widehat{V}_{l+1/2}^{ion} - \widehat{V}_{l-1/2}^{ion}\right], \tag{2.30}$$

accounts for the SOC [BBRHS82,KMB82]. Following this procedure the scalar-relativistic effects are included in the Hamiltonian through $\widehat{V}_l^{ion}(r)$. In practice, when working with NCP Eq. (2.27) is replaced by the following expression

$$\widehat{V}^{SOC} = \sum_l V_l^{SOC}(r)\mathbf{L}\cdot\boldsymbol{\sigma}\mathrm{P_l}. \tag{2.31}$$

The matrix element of the SOC potential Eq. (2.31) are actually 2×2 matrices in the electrons 1/2 spin subspace through

$$\mathbf{L}\cdot\boldsymbol{\sigma} = \frac{1}{2}\begin{pmatrix}\hat{L}_z & \hat{L}_- \\ \hat{L}_+ & -\hat{L}_z\end{pmatrix}, \tag{2.32}$$

where $\hat{L}_\pm = \hat{L}_x \pm i\hat{L}_y$ are the usual angular momentum ladder operators. Then to include the SOC in the calculations, the matrix elements of the following operators are needed,

$$\widehat{V}_{\uparrow\uparrow}^{SOC} = \sum_l V_l^{SOC}(r)\hat{L}_z\mathrm{P_l}, \tag{2.33}$$

$$\widehat{V}_{\uparrow\downarrow}^{SOC} = \sum_l V_l^{SOC}(r)\hat{L}_-\mathrm{P_l}, \tag{2.34}$$

$$\widehat{V}_{\downarrow\uparrow}^{SOC} = \sum_l V_l^{SOC}(r)\hat{L}_+\mathrm{P_l}, \tag{2.35}$$

which present the following expressions in a plane wave basis,

$$\widehat{V}_{\uparrow\uparrow}^{SOC}(\mathbf{G},\mathbf{G'}) = S'(\mathbf{G},\mathbf{G'})\sum_{l,m} mY_{l,m}^*(\widehat{K}_{G'})Y_{l,m}(\widehat{K}_G)A_l(K_G,K_{G'}), \tag{2.36}$$

$$\widehat{V}_{\uparrow\downarrow}^{SOC}(\mathbf{G},\mathbf{G'}) = S'(\mathbf{G},\mathbf{G'})\sum_{l,m} C_-(l,m)Y_{l,m}^*(\widehat{K}_{G'})Y_{l,m-1}(\widehat{K}_G)A_l(K_G,K_{G'}), \tag{2.37}$$

$$\widehat{V}_{\downarrow\uparrow}^{SOC}(\mathbf{G},\mathbf{G'}) = S'(\mathbf{G},\mathbf{G'})\sum_{l,m} C_+(l,m)Y_{l,m}^*(\widehat{K}_{G'})Y_{l,m+1}(\widehat{K}_G)A_l(K_G,K_{G'}), \tag{2.38}$$

where $S'(\mathbf{G}-\mathbf{G'}) = 2\pi^2 S(\mathbf{G}-\mathbf{G'})$. $C_\pm(l,m) = \sqrt{l(l+1)-m(m\pm1)}$ are Clebsch-Gordan coefficients [JS94], $Y_{l,m}(\widehat{K}_G)$ are spherical harmonics of the azimuthal and polar angles in the reciprocal space defined by the vector $K_G \equiv \mathbf{k}+\mathbf{G}$, and

$$A_l(K_G,K_{G'}) = \int_0^\infty j_l(K_G r)j_l(K_{G'}r)V_l^{SO}(r)r^2dr. \tag{2.39}$$

See Appendix C for a detailed derivation of Eqs. (2.36)-(2.38).

Now the electron wave functions are spinors, in which each spin component presents a wave function built as a linear combination similar to Eq. (2.17). As a result, once the SOC is included in the calculations the electron states are represented in the form

$$\Psi_{n,\mathbf{k}}(\mathbf{r}) = \frac{1}{\sqrt{2\Omega}} \sum_{\sigma} \sum_{\mathbf{G}} c_{n,\mathbf{k},\sigma}(\mathbf{G}) e^{i(\mathbf{k}+\mathbf{G})\cdot\mathbf{r}} \chi_{\sigma} \equiv \sum_{\sigma} \psi_{n,\mathbf{k},\sigma}(\mathbf{r}) \chi_{\sigma} \tag{2.40}$$

with

$$\chi_{\uparrow} = \begin{pmatrix} 1 \\ 0 \end{pmatrix} \text{ and } \chi_{\downarrow} = \begin{pmatrix} 0 \\ 1 \end{pmatrix}. \tag{2.41}$$

In the present work all studied systems present inversion symmetry. For such systems the coefficients $c_{n,\mathbf{k}}(\mathbf{G})$ of the plane wave expansion of the scalar-relativistic electron states are real. However, once SOC is switched on the corresponding $c_{n,\mathbf{k},\sigma}(\mathbf{G})$ coefficients are complex. This has to be taken into account when implementing the SOC in a computational code, as the memory allocated for the wave functions is four times the one needed at the scalar-relativistic level for the same set of physical and computational parameters if the same precision is sought. The factor four is the result of needing twice as much coefficients [compare Eqs. (2.17) and (2.40)] and the double memory required for each of them once they become complex variables.

Also, the non-diagonal matrix elements of the SOC term Eqs. (2.37) and (2.38) are in general complex, turning the Hamiltonian a complex quantity. For centrosymmetric systems, for a given pair of reciprocal lattice vectors $\widehat{V}^{SOC}(\mathbf{G}, \mathbf{G'})$ is antihermitian in the spin subspace:

$$\widehat{V}^{SOC}_{\uparrow\downarrow} = -(\widehat{V}^{SOC}_{\downarrow\uparrow})^{*}, \tag{2.42}$$

offering the possibility of computational time and memory saving. The proof of Eq. (2.42) can be found in Appendix B.

2.7 Solving the Hamiltonian including the SOC

2.7.1 Diagonalization

As mentioned above, at the scalar-relativistic level the Hamiltonian is solved by direct diagonalization at each $\mathbf{k}$ point of a mesh spanning the IBZ. Including the SOC the matrix doubles its size as each scalar-relativistic matrix element becomes a 2×2 matrix of the form

$$H(\mathbf{G}, \mathbf{G'}) = \begin{pmatrix} H^{sca} + V^{SOC}_{\uparrow\uparrow} & V^{SOC}_{\uparrow\downarrow} \\ V^{SOC}_{\downarrow\uparrow} & H^{sca} - V^{SOC}_{\uparrow\uparrow} \end{pmatrix}, \tag{2.43}$$

where H^{sca} stands for the scalar-relativistic Hamiltonian Eq. (2.20). Immediatly the plane wave basis $\left\{\mathbf{G}_1, \mathbf{G}_2, ..., \mathbf{G}_{N_{pw}}\right\}$ transforms in the double sized basis which introduces the spinorial structure of the new electron states,

$$\left\{\mathbf{G}_{1,\uparrow}, \mathbf{G}_{1,\downarrow}, \mathbf{G}_{2,\uparrow}, \mathbf{G}_{2,\downarrow}, ..., \mathbf{G}_{N_{pw},\uparrow}, \mathbf{G}_{N_{pw},\downarrow}\right\}. \tag{2.44}$$

Note that due to the fact that the computational time required to diagonalize a matrix of size N is $\mathcal{O}(N^3)$, including SOC is a drawback as doubling the size of the Hamiltonian matrix increases the CPU time needed to carry its diagonalization by roughly a factor of 8. Indeed, as the Hamiltonian matrix becomes complex when SOC is switched on, reminding that the diagonalization of a complex Hermitian matrix costs 8 times the CPU time of a real matrix of the same size, one concludes that including SOC the calculation becomes roughly 64 times heavier. In practice, the diagonalization subroutine used in the implementation of the SOC [ABB+99] first reduces the Hermitian matrix to a real tridiagonal matrix, saving CPU time.

Diagonalizing the new $2N_{pw} \times 2N_{pw}$ Hamiltonian matrix the coefficients $\{c_{n,\mathbf{k},\sigma}\}$ of the expansion (2.40) are retrieved in the following order:

$$\left\{c_{1,\mathbf{k},\uparrow}, c_{1,\mathbf{k},\downarrow}, c_{2,\mathbf{k},\uparrow}, c_{2,\mathbf{k},\downarrow}, ...\right\}. \tag{2.45}$$

Next, the Fourier transform of the electron density in real space is constructed following a procedure analogous to the one described in Sec. 2.5.3.

This way of proceeding necessarily doubles also the number of energy bands. Actually, at the scalar-relativistic level with no spin-dependent terms in the Hamiltonian each energy level is doubly degenerated, corresponding to two electron states. Note there is no possibility of deducing this fact from the scalar-relativistic treatment (in which the spin does not figure at all) without explicitly including spin-dependent interactions.

Spin quantization axis

Switching on the SOC a spin quantization axis is fixed, which throughout this thesis is chosen as the z axis, both in bulk and films. Concerning the appearance of the quantization axis, two points should be underlined.

The symmetry is lowered in the passage from the point group of the scalar-relativistic system to the double point group [Lax01] after inclusion of the SOC. As a consequence the IBZ becomes larger, as only symmetry operations which leave the quantization axis unchanged are relevant in the double point group representation. In practice, this means that the IBZ and the Monkhorst-Pack grid used in spanning it must be doubled following

$$\begin{aligned}&\{(k_{x,1}, k_{y,1}, k_{z,1}), (k_{x,2}, k_{y,2}, k_{z,2}), ...)\} \Longrightarrow \\ &\Longrightarrow \{(k_{x,1}, k_{y,1}, k_{z,1}), (k_{x,1}, k_{y,1}, -k_{z,1}), (k_{x,2}, k_{y,2}, k_{z,2}), (k_{x,2}, k_{y,2}, -k_{z,2}), ...)\}.\end{aligned} \tag{2.46}$$

In using Eq. (2.31) one assumes that the electron spin represents a good quantum number. However, it is precisely the coupling between the atomic lattice and the spin of the electrons -the SOC- which rotates the spins out of the quantization axis. Then, in the self-consistent cycle this rotation should be evaluated after each iteration and SOC matrix elements updated taking it into account in a non-collinear calculation scheme. This makes calculations much longer as calculating the new SOC matrix elements involves the evaluation of the relative angles between different electron spins which present each its own rotation of the spin with respect to the global z quantization axis. In the present work those rotations are neglected, and calculations are performed following a collinear approach in which the electron spin still constitues a good quantum number. The electronic structure results shown in this thesis are in good agreement with other theoretical and experimental studies, implying that the local spin rotations with respect to the global spin quantization z axis are small and can be neglected in pure Pb systems.

2.7.2 Variational principle

For bulk Pb one additional method has been used to obtain its electronic structure incorporating the SOC. The approach consisted in applying once the variational principle after the scalar-relativistic problem was solved, including SOC as a perturbation. A short general description of this method and its application to the SOC inclusion can be found in Appendix C. Below the main expressions used in applying the variational principle to the inclusion of the SOC in the study of bulk lead are reviewed and briefly explained.

The following determinant must vanish in order to obtain the energy spectrum of the system once the SOC is included via the variational principle,

$$det|(\epsilon_{n,\mathbf{k},\sigma} - E_{n',\mathbf{k},\sigma'})\delta_{n,n'}\delta_{\sigma,\sigma'} - \langle\psi_{n',\mathbf{k},\sigma'}|\hat{V}^{SOC}|\psi_{n,\mathbf{k},\sigma}\rangle| = 0, \tag{2.47}$$

where δ stands for the Kronecker delta. $\hat{V}^{SOC}$ is given by Eq. (2.31), $E_{n,\mathbf{k},\sigma}$ are the values of the energy bands at $\mathbf{k}$ after switching on the SOC, while $\epsilon_{n,\mathbf{k},\sigma}$ and $\psi_{n,\mathbf{k},\sigma}$ are the scalar-relativistic energy and states which are doubled in the following manner (see the discussion at the end of Appendix C)

$$\epsilon_{n,\mathbf{k},\uparrow} = \epsilon_{n,\mathbf{k}\downarrow} = \epsilon_{n,\mathbf{k}}, \tag{2.48}$$

$$\psi_{n,\mathbf{k},\uparrow} = \psi_{n,\mathbf{k},\downarrow} = \phi_{n,\mathbf{k}}. \tag{2.49}$$

This procedure is satisfactory not only because it avoids doubling the size of the Hamiltonian matrix which results in a roughly 64 times longer computational load [indeed, note the small size of the determinant (2.47)]. It also gives insight into the way SOC mixes different states. This is due to the freedom in choosing which energy bands (labeled by n) enter Eq. (2.47), that is, in selecting which unperturbed (scalar-relativistic) energy levels are mixed by the perturbation (SOC) fixing the minimum and maximum band indexes n_{min} and n_{max} in Eq. (2.47).

Despite of the computational time saved by avoiding doubling the Hamiltonian matrix size, the sum over **G** and **G'** of the SOC matrix elements [see Eqs. (2.36)-(2.38)] which enters the calculation of the bracket $\langle\psi_{n',\mathbf{k},\sigma'}|\hat{V}^{SOC}|\psi_{n,\mathbf{k},\sigma}\rangle$ can make this procedure slow. For bulk lead both methods, full self-consistency and applying the variational principle, needed similar time to obtain the SOC-included electronic structure. For slabs, the present approach was too demanding from the point of view of the required memory, as the above cited sum over **G** and **G'** becomes enormous in computing $\langle\psi_{n',\mathbf{k},\sigma'}|\hat{V}^{SOC}|\psi_{n,\mathbf{k},\sigma}\rangle$. As a consequence, only for bulk Pb was the variational principle applied in the present thesis, whereas films were always solved self-consistently, also when SOC was included in the Hamiltonian.

Chapter 3

Theoretical methods II: Collective electronic excitations

3.1 Introduction: elementary excitations

In the previous Chapter we have described the procedure followed in the present work to obtain the ground state properties of a solid. The approach is based on a single-particle Hamiltonian. Now we are prepared to study the low-energy excitations of the system which arise from the charge degrees of freedom, leaving the ones related to the spin aside (see Section 3.3.4). Usually there is a concept introduced when the knowledge of the low-energy excitations of a many-particle is sought, namely the concept of *quasiparticles*.

Quasiparticles are *fictitious* particles representing elementary excitations which are built in such a way that low-energy excitations of a many-particle system, which are truly the result of many-body strong interactions between many particles, are reasonably described by weakly interacting quasiparticles. Quasiparticles are a good description of the low-energy excitations at low temperature, when the Boltzmann distribution makes high-energy excitation states highly improbable. A different way of characterizing the quasiparticles is to define them as the excitations arising from the *slow* degrees of freedom [GV05]. In principle the meaning of *slow* is ambiguous. For excited single electrons, *slow* means a frequency $\omega \sim E_F/\hbar$. Therefore quasiparticles are decoupled from higher frequency excitations as they are not able to follow them due to the different time scales [VCSK$^+$12].

In general, elementary excitations are usually divided into two different categories depending on whether they are fermions or bosons, and often the former are named quasiparticles while the latter are called collective excitations. In this sense, quasiparticles are single particles carrying a certain polarization of some degrees of freedom (charge, lattice, spin,...) of the system which are also known as *dressed particles*, whereas collective excitations are excited modes which truly involve many particles.

An example to see the different nature between quasiparticles and collective excitations is the difference between a polaron and a phonon. A polaron is an electron moving through a crystal carrying a certain lattice distortion in its way, while a phonon is a truly collective vibrational mode of a crystal lattice.

In the present Chapter we review the theoretical framework in which the study of the dynamical collective electronic excitations in Pb, both bulk and films, has been based. The main equations used in practice are also sketched.

First, linear-response theory (LRT) and its application to the density-density response function derivation is outlined, analyzing the main expressions and approximations used to obtain the dielectric function. Then the steps to derive the explicit expressions for bulk and surface energy-loss functions for periodic solids are shown. Next, the character of the different collective electronic excitations is briefly analyzed. And finally, we shortly review the physics of the electron energy loss spectroscopy experimental technique, which offers the possiblity of comparison with calculated dielectric energy-loss functions.

3.2 Linear-response theory

3.2.1 General remarks and Kramers-Kronig relations

Let us suppose that the ground state properties of a given many-electron system are known (note that as shown in Section 2.3.1, following the DFT the knowledge of the ground state electron density of the system is enough to that purpose), and an external perturbation (time-dependent in general) $U^{ext}(t)$ is switched on. Next, two main assumptions are made. On the one hand, a weak coupling is assumed between the system and the perturbation. On the other hand, we suppose that the ground state of the many-electron system is stable against the external perturbation we are interested in applying to it. If both conditions are fulfilled, LRT gives the relation between the *driving force* that the perturbation represents and the *response* of our many-electron system defining a crucial physical property of the system, namely the *generalized susceptibility*, also called *generalized response function*.

Let us recapitulate schematically the main assumptions and steps involved in the derivation of the generalized susceptibility as given by LRT (for further details, Ref. [GV05] is suggested). First, we assume that an observable $\hat{B}$ couples linearly to the perturbation $U^{ext}(t)$, so the coupling between them is weak (the first condition mentioned above). Then the system is supposed to be in thermal equilibrium before the perturbation is applied, and is supposed to be stable with respect to switching on $U^{ext}(t)$ (the second condition mentioned above). Particularly, the occupation numbers of each state (the probability for each state to be occupied) is assumed to remain unchanged once the system is perturbed.

Now, we seek to obtain the response of a second observable $\hat{A}$ of the system to the impulse represented by its coupling to the observable $\hat{B}$, the one weakly coupled to the perturbation $U^{ext}(t)$. It can be shown [GV05] that this response of $\hat{A}$ at time t is given by

$$\langle \hat{A}(t) \rangle = \int_0^\infty \chi_{AB}(t') U^{ext}(t - t') dt', \tag{3.1}$$

where the *retarded* susceptibility is defined as

$$\chi_{AB}(t) \equiv -\frac{i}{\hbar} \theta(t) \langle [\hat{A}(t), \hat{B}] \rangle_0, \tag{3.2}$$

where $\theta(t)$ is the Heaviside function [AS64], $[\hat{A}, \hat{B}]$ stands for the commutator of the two operators, $\langle ... \rangle_0$ denotes the average on equilibrium and $\hat{B}$ reflects the observable in the thermal equilibrium of the system before $U^{ext}(t)$ was switched on. In Eq. (3.2) $t > 0$ as the time at which the perturbation is turned on is chosen as $t_0 = 0$ without loss of generality. Thus, this generalized response function is appropietly called retarded, as it describes the response of observable $\hat{A}$ at time t to the action of the perturbation at a previous time $(t - t')$. Since it presents such a causal structure, it is also named the *causal* response function. Note that, supposing that $\hat{A}$ and $\hat{B}$ are hermitian operators and consequently their expectation values are real, one deduces from Eq. (3.1) that $\chi_{AB}(t)$ is also a *real* quantity.

Now, all three quantities appearing in Eq. (3.1) are Fourier transformed to the frequency domain (or equivalently, energy domain). This can be done if previously $U^{ext}(t)$ has been decomposed in its Fourier components, an allowed procedure for physically meaningful functions, which usually are well-behaved functions of time t. Then, in virtue of Eq. (3.1) $\langle \hat{A}(t) \rangle$ becomes also Fourier decomposed. Finally, the relationship between the Fourier components of the response $\langle \hat{A}(\omega) \rangle$ and the ones corresponding to the perturbation $U^{ext}(\omega)$ reads

$$\chi_{AB}(\omega) = \frac{\langle \hat{A}(\omega) \rangle}{U^{ext}(\omega)}, \tag{3.3}$$

where $\chi_{AB}(\omega)$ is the Fourier transform of the general susceptibility defined by Eq. (3.2).

Let us cite some general properties the general susceptibility obeys. As $\chi_{AB}(t)$ is real, $\chi_{AB}(\omega) = \chi^R_{AB}(\omega) + i\chi^I_{AB}(\omega)$ is *complex* because of the definition of Fourier transform, from which it also follows that (we drop the subscripts from here on),

$$\chi(-\omega) = \chi^*(\omega). \tag{3.4}$$

A crucial result in linear-response theory is the so-called Kramers-Kronig (KK) relations [LJSPMV05], which read

$$\chi^R(\omega) = \frac{2}{\pi} \mathrm{P} \int_0^\infty \frac{\omega' \chi^{\mathrm{I}}(\omega)}{\omega'^2 - \omega^2} \mathrm{d}\omega', \tag{3.5}$$

$$\chi^I(\omega) = \frac{2\omega}{\pi} \mathrm{P} \int_0^\infty \frac{\chi^{\mathrm{R}}(\omega)}{\omega'^2 - \omega^2} \mathrm{d}\omega', \tag{3.6}$$

where P stands for the Cauchy principal value. KK relations result from the principle of causality which allows the connection of the real and imaginary parts of a complex function through Hilbert transforms [LJSPMV05], together with Eq. (3.4) and the assumption that $\chi^R(\omega)$ and $\chi^I(\omega)$ are square-integrable functions. The latter is a reasonable supposition for any physical property. KK relations are Hilbert transforms, but rewritten so that the integration is extended only over the positive real axis of ω. Note the relevance of Eqs. (3.5)-(3.6), as the real and imaginary parts of the susceptibility are related to different phenomena, i.e. light absorption and light dispersion, which usually must be measured using different experimental techniques.

In the present thesis, we use (see below) the KK relations to obtain the real part of the susceptibility from its imaginary counterpart.

3.2.2 Density-density response function

The interest of the present work is in analyzing the electronic excitations in a metal. In order to perform such a study on *collective* electronic excitations, the above described LRT is applied to the case in which the observable $\hat{A}$ which follows the external perturbation and the observable $\hat{B}$ responding to the variations in $\hat{A}$ are both the density operator,

$$\hat{\rho}(\mathbf{r}) = \frac{1}{N} \sum_i \delta(\mathbf{r} - \mathbf{r}_i), \tag{3.7}$$

where $\mathbf{r}_i$ are the spatial coordinates of the electrons and N their total number. The perturbation $V^{ext}(\mathbf{r}, t)$ is taken as the potential generated by a probe charged particle or an applied electric field.

Then, applying the LRT to the operator (3.7), the following expression for the density-density response function is obtained [GV05],

$$\chi(\mathbf{r}, \mathbf{r'}, \omega) = \sum_n \frac{\langle \Psi_0 | \hat{\rho}(\mathbf{r}) | \Psi_n \rangle \langle \Psi_n | \hat{\rho}(\mathbf{r'}) | \Psi_0 \rangle}{\omega + (E_n - E_0) + i\eta}. \tag{3.8}$$

Here Ψ_n represents the many-electron wave function of the excited state of energy E_n of the perturbed system, whereas Ψ_0 stands for the ground state many-particle wave function of energy E_0. $\eta = 0^+$ is a positive infinitesimal. Now the question is how the many-electron wave functions can be represented. Time-dependent density functional theory (TDDFT) [RKUG84, KUGK85] gives an answer, making the assumption that the total electron density, given by the sum of the ground state density $\rho_0(\mathbf{r})$ of the isolated many-electron system and $\rho_{ind}(\mathbf{r}, t)$ the density induced by the external perturbation,

$$\rho(\mathbf{r}, t) = \rho_0(\mathbf{r}) + \rho_{ind}(\mathbf{r}, t), \tag{3.9}$$

can be reproduced by a *fictitious* system of non-interacting electrons in an effective single-particle potential [RKUG84, KUGK85]. Then, the susceptibility $\chi(\mathbf{r}, \mathbf{r'}, \omega)$ Eq. (3.8) can be replaced by the non-interacting KS susceptibility written in the following form,

$$\chi^0(\mathbf{r}, \mathbf{r'}, \omega) = \sum_{i,j} [\theta(E_F - \varepsilon_i) - \theta(E_F - \varepsilon_j)] \frac{\phi_i^*(\mathbf{r})\phi_i(\mathbf{r'})\phi_j(\mathbf{r})\phi_j^*(\mathbf{r'})}{\omega + (\varepsilon_i - \varepsilon_j) + i\eta}. \tag{3.10}$$

Here $\theta(x)$ is the Heaviside function representing in Eq. (3.10) the occupation numbers at T = 0 temperature, and again $\eta = 0^+$. Most importantly, ε_i and ϕ_i are KS eigenvalues and orbitals of the non-interacting system, obtained solving self-consistently the KS equations (2.7)-(2.10).

The density induced by the external perturbation $V^{ext}(\mathbf{r}, \omega)$ produces an induced potential $V^{ind}(\mathbf{r}, \omega)$ through new Hartree and *xc* potential terms

$$V^{ind}(\mathbf{r}, \omega) = \int d\mathbf{r'} \left[\frac{1}{|\mathbf{r} - \mathbf{r'}|} + K_{xc}(\mathbf{r}, \mathbf{r'}, \omega) \right] \rho_{ind}(\mathbf{r'}, \omega), \tag{3.11}$$

where $K_{xc}(\mathbf{r}, \mathbf{r'}, \omega)$, known as the *xc* kernel, represents the second functional derivative of the *xc* energy with respect to the density evaluated at the ground state electron density [see Eq. (2.8)],

$$K_{xc}(\mathbf{r}, \mathbf{r'}, \omega) = \left[\frac{\delta V_{xc}[\rho](\mathbf{r}; \omega)}{\delta \rho(\mathbf{r'}; \omega)} \right]_{\rho=\rho_0} = \left[\frac{\delta^2 E_{xc}[\rho]}{\delta \rho(\mathbf{r}; \omega) \delta \rho(\mathbf{r'}; \omega)} \right]_{\rho=\rho_0}. \tag{3.12}$$

Then the sum of the potentials $[V^{ext}(\mathbf{r}, \omega) + V^{ind}(\mathbf{r}, \omega)]$ induces a new $\rho_{ind}(\mathbf{r}, \omega)$,

$$\rho_{ind}(\mathbf{r}, \omega) = \int d\mathbf{r'} \chi^0(\mathbf{r}, \mathbf{r'}, \omega)[V^{ext}(\mathbf{r'}, \omega) + V^{ind}(\mathbf{r'}, \omega)]. \tag{3.13}$$

Comparing Eq. (3.13) with the relation given by ordinary time-dependent perturbation theory between the induced electron density and the external perturbative potential,

$$\rho_{ind}(\mathbf{r}, \omega) = \int d\mathbf{r'} \chi(\mathbf{r}, \mathbf{r'}, \omega) V^{ext}(\mathbf{r'}, \omega), \tag{3.14}$$

the following Dyson-like equation is deduced:

$$\chi(\mathbf{r}, \mathbf{r'}, \omega) = \chi^0(\mathbf{r}, \mathbf{r'}, \omega) + \int d\mathbf{r}_1 \int d\mathbf{r}_2 \chi^0(\mathbf{r}, \mathbf{r}_1, \omega) F(\mathbf{r}_1, \mathbf{r}_2, \omega) \chi(\mathbf{r}_2, \mathbf{r'}, \omega), \tag{3.15}$$

where

$$F(\mathbf{r}, \mathbf{r'}, \omega) = \frac{1}{|\mathbf{r} - \mathbf{r'}|} + K_{xc}(\mathbf{r}, \mathbf{r'}, \omega). \tag{3.16}$$

Solving Eq. (3.15) yields the *interacting* susceptibility $\chi(\mathbf{r}, \mathbf{r'}, \omega)$, also known as the density-density response function, which in principle is exact as derived above. However, as the exact form of the *xc* energy functional is unknown (see Section 2.3.3) the

xc kernel $K_{xc}(\mathbf{r}, \mathbf{r'}, \omega)$ must be approximated. In the present study we use two different approaches in modeling the xc kernel. One is the so-called random-phase approximation (RPA) which consists in simply neglecting the xc short-range effects in $\chi(\mathbf{r}, \mathbf{r'}, \omega)$, $K_{xc}^{RPA}(\mathbf{r}, \mathbf{r'}, \omega) = 0$. The second choice used for approximating $K_{xc}(\mathbf{r}, \mathbf{r'}, \omega)$ is known as the time-dependent local density approximation (TDLDA), an adiabatic extension of the LDA, also called adiabatic local-density appoximation (ALDA) [ZS80]. In the TDLDA one assumes that not only the ground state density (as in the LDA, see Section 2.3.3) but also the induced density shows a slow spatial variation. Therefore, in analogy with the LDA, the long-wavelength limit (therefore local) of the static (therefore frequency-independent) xc kernel of a homogeneous electron gas at the ground state local density is taken [MPMSVCME07],

$$K_{xc}^{TDLDA}(\mathbf{r}, \mathbf{r'}, \omega) = \left[\frac{\delta V_{xc}^{LDA}[\rho](\mathbf{r})}{\delta \rho(\mathbf{r'})} \right]_{\rho=\rho_0} \delta(\mathbf{r} - \mathbf{r'}). \tag{3.17}$$

As both RPA as well as TDLDA are *static* (frequency-independent), none of them seems to be appropiate to describe the excitation energies of a system at energies of the order of the characteristic one-particle transition energies (that is, of the order of E_F). However, TDLDA has been shown to give a satisfactory description of the screening in semiconductors [EB97, WSH$^+$06, WSH$^+$10] and metals [AQGE93, CWH$^+$11, Caz12]. This can be understood by considering that the relevant excitation energies for the xc potential are the ones corresponding to the multi-particle excitations, which usually lie much higher in energy than single-particle excitations. Consequently, TDLDA turns out to be reasonable to calculate the latter.

Note that finally one faces the problem of approximating the xc term twice when carrying a density response function study based in DFT. First, a xc functional enters the potential (2.8) in Eq. (2.7). Once the ground state properties are obtained, the choice of an additional approximation to $K_{xc}(\mathbf{r}, \mathbf{r'}, \omega)$ is unavoidable. In Sections 2.3.3 it was argued that LDA gives satisfactory results for the ground state of metals, while in Section 2.3.4 some ground for the usage of LDA energies and orbitals as an input to perform studies on excitations was given, specially in the case of metals. Hence, as stated in the previous Chapter, LDA has been chosen to obtain the ground state of Pb bulk and films and, consequently, the LDA energy bands and wave functions enter the calculation of collective electronic excitations [see Eq. (3.19) below].

3.3 Expressions for periodic solids

In the approach we use here, the starting point is the calculation of the Fourier transform of the non-interacting susceptibility $\chi^0(\mathbf{q}, \omega)$, sometimes named as KS suscepti-

bility, which for a 3D periodic solids reads

$$\chi^0_{\mathbf{G},\mathbf{G}'}(\mathbf{q},\omega) = \frac{2}{\Omega}\sum_{\mathbf{k}}^{\mathrm{BZ}}\sum_{n,n'} \frac{(f_{n,\mathbf{k}} - f_{n',\mathbf{k}+\mathbf{q}}) \left\langle \phi_{n,\mathbf{k}} | e^{-i(\mathbf{q}+\mathbf{G})\cdot\mathbf{r}} | \phi_{n',\mathbf{k}+\mathbf{q}} \right\rangle \left\langle \phi_{n',\mathbf{k}+\mathbf{q}} | e^{i(\mathbf{q}+\mathbf{G'})\cdot\mathbf{r}} | \phi_{n,\mathbf{k}} \right\rangle}{\varepsilon_{n,\mathbf{k}} - \varepsilon_{n',\mathbf{k}+\mathbf{q}} + (\omega + i\eta)}, \tag{3.18}$$

where Ω is the volume of the crystal, $\mathbf{q}$ is in the first BZ, $\mathbf{G}$ are reciprocal lattice vectors, $\eta = 0^+$, and $\varepsilon_{n,\mathbf{k}}$ and $\phi_{n,\mathbf{k}}$ are KS energy levels and orbitals. $f_{n,\mathbf{k}}$ are occupation numbers which in practice are modeled by error functions [AS64] representing a certain electronic temperature, this is a usual trick used in metals to avoid problems with the discretization of the Fermi surface due to the finite sampling of the BZ.

A crucial point is that not only the non-interacting susceptibility Eq. (3.18), but all the quantities involved in the calculation of the dielectric response are now matrices in the reciprocal lattice vectors (**G**,**G'**).

In practice we avoid the direct evaluation of Eq. (3.18). Instead we calculate the so-called spectral function [AG94, Ary01],

$$S^0_{\mathbf{G},\mathbf{G}'}(\mathbf{q},\omega) = \frac{2}{\Omega}\sum_{\mathbf{k}}^{BZ}\sum_{n}^{occ}\sum_{n'}^{unocc} \langle \phi_{n,\mathbf{k}} | e^{-i(\mathbf{q}+\mathbf{G})\cdot\mathbf{r}} | \phi_{n',\mathbf{k}+\mathbf{q}} \rangle \times \\ \times \langle \phi_{n',\mathbf{k}+\mathbf{q}} | e^{i(\mathbf{q}+\mathbf{G'})\cdot\mathbf{r}} | \phi_{n,\mathbf{k}} \rangle \delta(\varepsilon_{n,\mathbf{k}} - \varepsilon_{n',\mathbf{k}+\mathbf{q}} + \omega), \tag{3.19}$$

whose calculation saves computational time in comparison to the direct evaluation of $\chi^0_{\mathbf{G},\mathbf{G}'}(\mathbf{q},\omega)$, see Refs. [AG94, Ary01]. Note the factor 2 stems from the spin degeneracy. As we expand the wave functions in a plane wave basis [see Eq. (2.17) in Section 2.5.1], the expression for $S^0_{\mathbf{G},\mathbf{G}'}(\mathbf{q},\omega)$ is evaluated as

$$S^0_{\mathbf{G},\mathbf{G}'}(\mathbf{q},\omega) = \frac{2}{\Omega}\sum_{\mathbf{k}}^{BZ}\sum_{n}^{occ}\sum_{n'}^{unocc}\sum_{\mathbf{G''},\mathbf{G'''}} \left\{ c^*_{n,\mathbf{k}}(\mathbf{G''}) c_{n',\mathbf{k}+\mathbf{q}}(\mathbf{G''} - \mathbf{G}) \right\} \times \\ \times \left\{ c^*_{n',\mathbf{k}+\mathbf{q}}(\mathbf{G'''}) c_{n,\mathbf{k}}(\mathbf{G'''} - \mathbf{G'}) \right\} \delta(\varepsilon_{n,\mathbf{k}} - \varepsilon_{n',\mathbf{k}+\mathbf{q}} + \omega), \tag{3.20}$$

In practice, the Dirac delta $\delta(\varepsilon_{n\mathbf{k}} - \varepsilon_{n',\mathbf{k}+\mathbf{q}} + \omega)$ in Eqs. (3.19) and (3.20) is replaced by a modified Gaussian of finite width, see Appendix D for further details. From the knowledge of $S^0_{\mathbf{G},\mathbf{G}'}(\mathbf{q},\omega)$ the imaginary part of the non-interacting susceptibility is evaluated through the expression

$$S^0_{\mathbf{G},\mathbf{G}'}(\mathbf{q},\omega) = -\frac{1}{\pi} sgn(\omega) \mathrm{Im}[\chi^0_{\mathbf{G},\mathbf{G}'}(\mathbf{q},\omega)]. \tag{3.21}$$

where $sgn(\omega) = 1\,(-1)$ for $\omega > 0\,(\omega < 0)$. Then the real part of $\chi^0_{\mathbf{G},\mathbf{G}'}$, is obtained from its imaginary counterpart using the KK relations, more precisely Eq. (3.5).

As the Fourier transforms of the main quantities are used, now Eq. (3.15) becomes a matrix equation,

$$\chi_{\mathbf{G},\mathbf{G}'}(\mathbf{q},\omega) = \chi^0_{\mathbf{G},\mathbf{G}'}(\mathbf{q},\omega) + \sum_{\mathbf{G}''}\sum_{\mathbf{G}'''}\chi^0_{\mathbf{G},\mathbf{G}''}(\mathbf{q},\omega)\times \\ \times [v_{\mathbf{G}''}(\mathbf{q})\delta_{\mathbf{G}'',\mathbf{G}'''} + K^{xc}_{\mathbf{G}'',\mathbf{G}'''}(\mathbf{q})]\chi_{\mathbf{G}''',\mathbf{G}'}(\mathbf{q},\omega), \quad (3.22)$$

where $K^{xc}_{\mathbf{G},\mathbf{G}'}(\mathbf{q})$ stands for the Fourier components of the *xc* kernel, see Eqs. (3.15)-(3.16).

$\chi_{\mathbf{G},\mathbf{G}'}(\mathbf{q},\omega)$ is the most fundamental quantity retrieved, as it contains all the information on the response of a many-electron system to an external perturbation generated by a charged probe particle or applied electric field. Notice that the passage from the non-interacting susceptibility χ^0 to the interacting one χ, through Eq. (3.22) in its matrix form, reflects the screening of the non-interacting susceptibility built with transitions between independent particle energy levels [KS states and energies, see Eq. (3.19)], by the many-particle Hartree and *xc* interactions.

3.3.1 Three-dimensional crystals

Collective charge excitations in a 3D crystal are given by the peaks in the so-called *energy-loss function*, which corresponds to the imaginary part of the inverse longitudinal dielectric function of the solid, $\mathrm{Im}[\varepsilon^{-1}_{\mathbf{G},\mathbf{G}}(\mathbf{q},\omega)]$. The energy-loss function provides the information about the efficiency of an exchange of energy ω and momentum $\mathbf{q}+\mathbf{G}$ between the system and the perturbation.

More precisely, the energy-loss function inherits its name from the zero-temperature limit of the fluctuation-dissipation theorem for particles subjected to a Coulomb interaction [BCAW51],

$$S(\mathbf{q}+\mathbf{G},\omega) = -\frac{\Omega|\mathbf{q}+\mathbf{G}|^2}{2\pi}\mathrm{Im}[\varepsilon^{-1}_{\mathbf{G},\mathbf{G}}(\mathbf{q},\omega)], \quad (3.23)$$

where Ω is the volume of the perturbed system and $\mathbf{q}+\mathbf{G}$ is the reciprocal momentum carried by the perturbation [Kuz98]. Equation (3.23) states that the dynamical structure factor $S(\mathbf{q}+\mathbf{G},\omega)$ is proportional to the energy-loss function, since the dynamical structure factor describes the energy dissipated by the probe particle creating the perturbation the many-electron is responding to. More precisely, the inelastic scattering cross section of x-rays and electrons is proportional to $S(\mathbf{q}+\mathbf{G},\omega)$ within the first Born approximation. In experiments, the dynamical structure factor is directly probed in the inelastic x-ray and electron scattering measurements, see Section 3.5.

Note that the dielectric function $\varepsilon(\mathbf{q},\omega)$ is the response function (obeying the properties described in detail in Section 3.2.1) of the system to a charge probe particle, or equivantly to an electric field. Thus, the evaluation of $\varepsilon^{-1}_{\mathbf{G},\mathbf{G}'}(\mathbf{q},\omega)$ is seek to obtain the information on the collective electronic excitations of the many-electron system under

study that raise as a response to the perturbation. This goal is achieved using the following relation

$$\varepsilon^{-1}_{\mathbf{G},\mathbf{G}'}(\mathbf{q},\omega) = \delta_{\mathbf{G},\mathbf{G}'} + v_{\mathbf{G}}(\mathbf{q})\chi_{\mathbf{G},\mathbf{G}'}(\mathbf{q},\omega), \tag{3.24}$$

where $\chi_{\mathbf{G},\mathbf{G}'}(\mathbf{q},\omega)$ is given by Eq. (3.22).

3.3.2 Surfaces

The approach to the investigation of the surface collective electronic excitations differs from the one sketched in Section 3.3.1. First, we assume that the perturbation is due to a charge particle located far from the surface. This probe particle carries an energy ω and a two-dimensional (2D) momentum $\mathbf{q}_\parallel$ parallel to the surface of the solid. Then its cross section for the scattering by the electrons of the surface is proportional to the imaginary part of the quantity named *surface response function* $g(\mathbf{q}_\parallel,\omega)$ defined as [Lie97, NJPZ85],

$$g(\mathbf{q}_\parallel,\omega) = \int d\mathbf{r}\rho_{ind}(\mathbf{r},\omega)e^{q_\parallel z}, \tag{3.25}$$

where $\mathbf{r} \equiv (\mathbf{r}_\parallel, z)$. Thus, $\mathrm{Im}[g(\mathbf{q}_\parallel,\omega)]$ is defined as the *surface loss function*.

In the case of surfaces, the external perturbation is of the form

$$V^{ext}(\mathbf{r},\omega) = -\frac{2\pi}{q}\, e^{q_\parallel z}\, e^{i\mathbf{q}_\parallel \mathbf{r}_\parallel}\, e^{-i\omega t}, \tag{3.26}$$

and combining Eqs. (3.14), (3.22), (3.26) and (3.27) we finally obtain

$$g(\mathbf{q}_\parallel,\omega) = -\frac{2\pi}{q}\int dz \int dz' \chi_{\mathbf{G}=0,\mathbf{G}'=0}(z,z',\mathbf{q}_\parallel,\omega)e^{q_\parallel(z+z')}. \tag{3.27}$$

As we use the supercell approach, that is, a repeated slab geometry, the interacting susceptibility $\chi_{\mathbf{G},\mathbf{G}'}(\mathbf{q},\omega)$ is also evaluated following the 3D approach described above.

In order to save computational time, in most of the cases $\chi^0_{\mathbf{G},\mathbf{G}'}(\mathbf{q},\omega)$ has been calculated retaining only $\mathbf{G} = (0,0,G_z)$ reciprocal space vectors. Physically, this means that lateral crystal local field effects were neglected. This approach was already found to give indistinguishable results compared with the calculations carried out using the 3D **G'**s for metal surfaces [MSVCME04]. All important 3D effects are included in the evaluation of $\chi^0_{\mathbf{G},\mathbf{G}'}(\mathbf{q},\omega)$ through the use of the fully 3D Bloch functions and their respective one-electron energies.

Note that in contrast to the widely used jellium models [Lie97], here the surface response function depends not only in the value but also in the direction of the parallel momentum transfer $\mathbf{q}_\parallel$, allowing the study of possible anisotropy effects [MSMPVC$^+$08].

3.3.3 Local-field effects

3D and 2D Fourier transform density-density response functions are obtain solving a matrix equation. The procedure is common to both cases. We illustrate this in the case of a fully 3D periodic solid. Thus, the solutions of Eq. (3.22) are sought. In order to obtain them, we use the following expression:

$$\chi_{\mathbf{G},\mathbf{G'}}(\mathbf{q},\omega) = \sum_{\mathbf{G''}} A^{-1}_{\mathbf{G},\mathbf{G''}}(\mathbf{q},\omega) \cdot \chi^{0}_{\mathbf{G''},\mathbf{G'}}(\mathbf{q},\omega), \tag{3.28}$$

where the transition from the non-interacting to the fully interacting susceptibility is given by the matrix

$$A_{\mathbf{G},\mathbf{G'}}(\mathbf{q},\omega) = \delta_{\mathbf{G},\mathbf{G'}} - \chi^{0}_{\mathbf{G},\mathbf{G'}}(\mathbf{q},\omega) \cdot \frac{4\pi}{|\mathbf{q}+\mathbf{G'}|^2} - \sum_{\mathbf{G''}} \chi^{0}_{\mathbf{G},\mathbf{G''}}(\mathbf{q},\omega) \cdot K^{xc}_{\mathbf{G},\mathbf{G'}}(\mathbf{G''}-\mathbf{G'}). \tag{3.29}$$

Note that when making use of the RPA as the approximation for the xc kernel K^{xc} the last term in Eq. (3.29) is dropped.

Importantly, through the inversion of the $A_{\mathbf{G},\mathbf{G'}}(\mathbf{q},\omega)$, the matrix elements corresponding to different ($\mathbf{q}$+$\mathbf{G}$)'s are coupled. This mixing of the contributions stemming from different reciprocal lattice vectors represent the so-called crystalline local-field effects (LFE) [LA62, Wis63]. LFE are a consequence of the spatial variations in the electron density in real solids, that is, of the inhomogeneity of $\rho(\mathbf{r})$. Therefore excluding LFE can turn results of the dielectric response calculations wrong, even though their importance strongly depends of the class of material investigated. Nevertheless, as metallic bonding in a Fermi sea of electrons is often satisfactorily modeled by systems of interacting homogeneous electron gases, i.e. jellium models, the impact of LFE seems to be small. However, recent first-principles studies showed the full inclusion of LFE is needed for a correct quantitative description of the dielectric response of some metallic systems (see for example Refs. [NFAMS12, PEVCMEMS12]), specially at large momentum transfers.

Inclusion of LFE is important also from a macroscopic point of view. The macroscopic dieletric function of a periodic solid is defined as [ORR02]

$$\varepsilon_M(\mathbf{q},\omega) = \frac{1}{\varepsilon^{-1}_{\mathbf{G}=0,\mathbf{G'}=0}(\mathbf{q},\omega)}, \tag{3.30}$$

Thus, $\varepsilon_{\mathbf{G}=0,\mathbf{G'}=0}(\mathbf{q},\omega)$ is not the true macroscopic dielectric constant, once LFE are omitted. If LFE are neglected, the energy-loss function is simply given by

$$\mathrm{Im}[\varepsilon^{-1}_{\mathbf{G},\mathbf{G'}}(\mathbf{q},\omega)] = \frac{\mathrm{Im}\left[\varepsilon_{\mathbf{G},\mathbf{G'}}(\mathbf{q},\omega)\right]}{|\varepsilon_{\mathbf{G},\mathbf{G'}}(\mathbf{q},\omega)|^2} = \frac{\mathrm{Im}\left[\varepsilon_{\mathbf{G},\mathbf{G'}}(\mathbf{q},\omega)\right]}{\{\mathrm{Re}\left[\varepsilon_{\mathbf{G},\mathbf{G'}}(\mathbf{q},\omega)\right]\}^2 + \{\mathrm{Im}\left[\varepsilon_{\mathbf{G},\mathbf{G'}}(\mathbf{q},\omega)\right]\}^2}. \tag{3.31}$$

3.3.4 Spin-orbit coupling

In the case when the SOC is included in the ground state calculations, there are two aspects that must be revised in the evaluation of the susceptibilities, and more precisely in the calculation of the density-density response function as it is done in this thesis.

First, the transition from the non-interacting susceptibility χ^0 to the interacting one χ, i.e. Eq. (3.22), reflects the screening of the independent particle non-interacting susceptibility by the many-particle interactions. In the theoretical approach applied throughout the present work, the SOC is included in the Hamiltonian as a part of the non-local term in the external potential [see Eqs. (2.19,2.20)] using norm-conserving pseudopotentials. Consequently the density-density response function $\chi_{\mathbf{G},\mathbf{G}'}(\mathbf{q},\omega)$ is screened only by the Hartree and xc potentials here, also when SOC is included in the Hamiltonian.

Secondly, the calculation of the susceptibility can be carried out taking as a starting point a more general formulation [AB08], in which one formulates in a compact form the response of the charge and spin degrees of freedom to each other, thus generalizing the response-respone function. This formulation allows to treat systems with an existing spin-structure, as it is the case when SOC is switched on [AB08]. Nevertheless it is easy to see using the general formalism of Ref. [AB08] together with the expression of the non-interacting Green's function as function of the spectral function (see i.e. Ref. [ANVC09]) that the expressions we use in practice here remain unchanged. The only replacement we must carry is the substitution of the scalar wave functions by spinors in Eq. (3.20), which now reads

$$
\begin{aligned}
&S^0_{\mathbf{G},\mathbf{G}'}(\mathbf{q},\omega) = \\
&= \frac{1}{\Omega}\sum_{\mathbf{k}}^{BZ}\sum_{n}^{occ}\sum_{n'}^{unocc}\sum_{\mathbf{G}'',\mathbf{G}'''}\left[c^*_{n,\mathbf{k},\uparrow}(\mathbf{G}'')c_{n',\mathbf{k}+\mathbf{q},\uparrow}(\mathbf{G}''-\mathbf{G}) + c^*_{n,\mathbf{k},\downarrow}(\mathbf{G}'')c_{n',\mathbf{k}+\mathbf{q},\downarrow}(\mathbf{G}''-\mathbf{G})\right]\times \\
&\times\left[c^*_{n',\mathbf{k}+\mathbf{q},\uparrow}(\mathbf{G}''')c_{n,\mathbf{k},\uparrow}(\mathbf{G}'''-\mathbf{G}') + c^*_{n',\mathbf{k}+\mathbf{q},\downarrow}(\mathbf{G}''')c_{n,\mathbf{k},\downarrow}(\mathbf{G}'''-\mathbf{G}')\right]\delta(\varepsilon_{n,\mathbf{k}}-\varepsilon_{n',\mathbf{k}+\mathbf{q}}+\omega),
\end{aligned}
\tag{3.32}
$$

see Eq. (2.40) for the representation of the two-component spinors in the plane wave basis.

3.4 Collective electronic excitations

The response functions described in the present Chapter contain the information on the collective excitations of both bulk and surface electron densities of solids to a charged probe particle or external electric field. These modes are usually known as *plasmons* or *plasma modes* and represent the longitudinal oscillations of the electron density. Classically, in bulk these modes present energies corresponding to the zeros of

the longitudinal dielectric function,

$$\varepsilon(q,\omega) = 0. \tag{3.33}$$

Here we call this relation the *classical plasmon condition*.

3.4.1 Bulk

Concerning the plasmon mode of bulk systems, it is well known from classical electrodynamics [GPP00] that it exhibits an energy given by the simple expression (in atomic units) $\omega_p = \sqrt{3r_s^{-3}}$, where r_s is the average electron density parameter [see Eq. (2.15)]. For metallic densities, $\omega_p \simeq 3 - 20$ eV. A dispersion of the bulk plasmon can be deduced from a quantum-mechanical treatment, that is, analyzing the density-density response function $\chi_{\mathbf{G},\mathbf{G}'}(\mathbf{q},\omega)$. To obtain an analytical expression for $\omega_p = \omega_p(\mathbf{q})$ the limits $q \to 0$ and $\omega \gg qv_F$ (where v_F is the Fermi velocity) are applied to the Lindhard dielectric function (LDF). The LDF is the dielectric function of a homogeneous non-interacting electron gas, for the explicit expressions related to the LDF, see Appendix E. Then the dispersion of the main bulk charge oscillation is given to the lowest order in the momentum $q = |\mathbf{q}|$ by [GPP00, GV05]

$$\omega_p \simeq \omega_p \left[1 + \frac{3}{10}\frac{v_F^2 q^2}{\omega_p^2}\right], \tag{3.34}$$

which for a system of non-interacting electrons is a function of only the electron density through the expression $v_F = (9\pi/4)^{1/3} r_s^{-1}$. As the coefficient of the q^2 term in Eq. (3.34) is small for metallic densities, often ω_p is supposed to be dispersionless in metals. However, as it is shown in Chapter 7 in bulk lead the classical bulk plasmon disperses clearly as a function of the momentum $\mathbf{q}$.

3.4.2 Surfaces

Regarding surfaces (we suppose the surfaces and films are in contact with vacuum), the classical surface plasmon energy in the optical range $\mathbf{q} \to 0$ is given by [HR57]

$$\omega_s = \omega_p/\sqrt{2}. \tag{3.35}$$

There are several approaches to derive the surface plasmon dispersion as a function of the momentum $\omega_s = \omega_s(\mathbf{q})$, for a review see Ref. [MPMSVCME07]. In the classical electrodynamics approach leading to Eq. (3.35) the electron density is suppose to present a step-like discontinuity at the surface, passing from exhibiting a constant value inside the semiinfinite solid to vanishing outside. Note that the dispersion of the surface plasmon is a general consequence of the inhomogeneity of the electron density at the surface [Lie97].

The density induced in the direction perpendicular to the surface plane by the classical surface plasmon of energy ω_s presents the simple form of a monopole-like peak, whereas in the surface plane it propagates as a plane wave, with positive and negative induced density regions alternating.

3.4.3 Thin films

Thin films represent a special case in the study of collective electronic excitations. As the thickness of the film decreases, the surface plasmons of the surfaces can interact, breaking their energy degeneracy by hybridization. Based on classical electrodynamic arguments Ritchie first derived [HR57] the dispersion of the coupled thin film modes,

$$\omega_{\pm} = \frac{\omega_p}{\sqrt{2}}(1 \pm e^{-q_{\parallel}L})^{1/2}, \tag{3.36}$$

where L stands for the film thickness. The energy splitting between the modes depends on the film thickness L and the in-plane 2D momentum transfer $q_{\parallel}$, which is a scalar for a electron gas. The low-energy mode ω_- correponds to a symmetric induced charge profile in the direction perpendicular to the film plane, whereas the high-energy mode ω_+ corresponds to an asymmetric one. As L increases, the coupling between the two modes decreases. In the limit $L \gg 1/q_{\parallel}$ the two film modes are decoupled and the two classical surface plasmons of frequency $\omega_p/\sqrt{2}$ are retrieved. From Eq. (3.36) one deduces that for a given thickness L, the modes are decoupled and thus degenerate in energy for 2D momenta $q_{\parallel} \gtrsim 1/L$. Note that this classical model ignores the electronic structure of the films. However, the quantization of states in the direction perpendicular to the film plane affects the actual characteristic and dispersion of the film plasmon modes $\omega_{\pm}$ (see, i.e., Ref. [YG06]).

3.4.4 Acoustic modes

Finally, there is another kind of collective electronic excitation, the so-called acoustic plasmon (AP). In general, AP arises in a two-component electron gas, in which the slow component is incompletely screened by the fast one. At surfaces, the acoustic surface plasmon (ASP) [MSGLMP$^+$04, MPMSVCME07] has been recently experimentally detected [DPV$^+$07], while their existence was predicted years before [MPUNMS$^+$04]. ASP steem from a 3D (fast component) screening of 2D states (slow component), as it is the case of screening of surface Shockley states by bulk electrons in (111) surfaces of noble metals or in Be(0001) [MPUNMS$^+$04, DPV$^+$07, MPMSVCME07]. The Shockley states would support a purely 2D plasmon mode with dispersion $\omega_{2D} \propto \sqrt{q}$ in the absence of the 3D bulk crystal [GV05]. Nevertheless, in the presence of the three-dimensional bulk states, a novel collective electronic excitation appears which disperses linearly as a function of momentum, the surface acoustic plasmon mode.

Now the question raises whether acoustic-like plasmons can exist in the bulk of metals or there is no bulk analogous to ASP. Pines [Pin56,PN58] in the fifties predicted the existence of a very-low energy excitation, which should be present in systems with two energy bands crossing the Fermi level with different Fermi velocities, as it is the case of bulk Pb. This very-low energy mode presents an acoustic-like dispersion at small momenta, $\omega_{AP} = v \cdot q$, where v is the constant group velocity of the acoustic plasmon. Hence, ω_{AP} tends to zero as $q \to 0$. Exchange of acoustic plasmons have been suggested as a possible mechanism of electron pairing in superconductors (see, i.e., Ref [IR93] and references therein). Very recently detailed *ab initio* calculations of the dynamical dielectric response of several metallic bulk systems predicted the existence of bulk acoustic plasmons [MSBMEVC09, BVCMEMS08, MSPCMKVC09]. However, to the best of our knowledge this kind of acoustic excitations has not been shown to exist experimentally so far.

3.5 Electron energy-loss spectroscopy

Several experimental techniques probe the density-density response functions, i.e. x-ray inelastic scattering, optical absorption or ellipsometry. An additional technique which directly measures the dynamical structure factor, or equivalently, the energy-loss function is known as electron energy-loss spectroscopy (EELS).

In EELS experiments a beam of electrons carrying a momentum k_i and energy ω_i is scattered by the system under study. As a result of the scattering, the electrons transfer a momentum q and energy ω to the system. Note the EELS technique is conceptually the same as Raman scattering [Kuz98]. However, unlike the case of Raman scattering, the incident electrons in an EELS experiment can have a large range of wave vectors k_i so that the change in momentum for the electron in the solid can be comparable to Brillouin zone dimensions. The incident electrons typically have energies up to ~ 100 eV, with wave vectors up to $k_i \simeq 5\mathrm{A}^{-1}$.

Let us now derive the relation of the EELS measured scattered electrons and the above described energy-loss function $\mathrm{Im}[\varepsilon^{-1}_{\mathbf{G},\mathbf{G}}(\mathbf{q},\omega)]$. One defines the cross section $(d^2\sigma/d\Omega d\omega)$, where Ω is the solid angle, as the number of scattered electrons measured per unit of time, solid angle and energy for a given incident beam intensity. As it is mentioned in Section 3.3.1, within the first Born approximation $(d^2\sigma/d\Omega d\omega)$ is proportional to the dynamical structure factor $S(q,\omega)$,

$$\frac{d^2\sigma}{d\Omega d\omega} = f(q)S(q,\omega), \tag{3.37}$$

where function $f(q)$ reflects the elastic (energy-conserving) contribution to the cross section [Kuz98], which is assumed to show a $f(q) \propto q^{-4}$ dependence (Rutherford classical scattering).

On the other hand, the dynamical structure factor is linked to the energy-loss function by Eq. (3.23), where the prefactor $q^2/2\pi$ is the inverse of the Fourier transform of the Coulomb interaction. The resulting relationship between the measure cross section and the energy-loss function is given by

$$\frac{d^2\sigma}{d\Omega d\omega} \propto \frac{1}{|\mathbf{q}+\mathbf{G}|^2}\,\mathrm{Im}[\varepsilon^{-1}_{\mathbf{G},\mathbf{G}}(\mathbf{q},\omega)]. \tag{3.38}$$

Consequently, the energy-loss spectra calculated in this thesis can be directly compared with EELS experimental measurements.

Chapter 4

Theoretical methods III: Inelastic linewidth of excited quasiparticles

4.1 Introduction

In this thesis we study not only collective electronic excitations, but also those presenting a single-particle character. More precisely, we seek to study the decay of excited electrons and holes, analyzing their inelastic linewidth due to electron-hole pair creation (see below). In the present Chapter we review the formalism used to obtain information on the decay of quasiparticles through electron-hole pairs and plasmons, namely the so-called *GW* approximation (see i.e. Ref. [ORR02]). After that we analyze the main assumptions involved and its connection to the physical properties studied within the linear-response theory. Finally, the explicit *GW* expressions used in crystals are derived.

We call the excited electrons and holes *quasiparticles* as they represent a kind of dressed particle (see Section 3.1). Actually they are composed by an electron, a single-particle state represented here by a KS state in the formalism described in Chapter 2, and the so-called exchange-correlation hole they carry around. The *xc* hole stands for

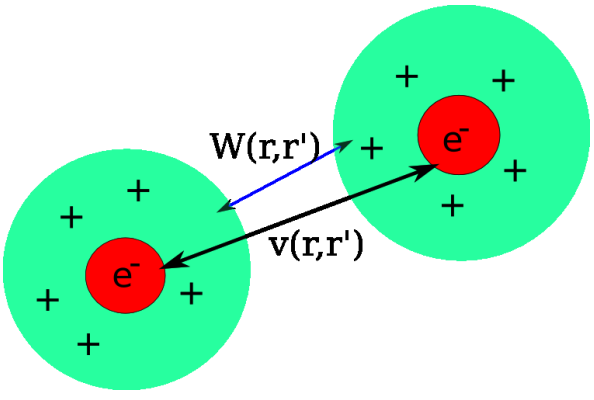

Figure 4.1: Cartoon showing the composition of the quasiparticles as the sum of an electron (red circles) and the *xc* hole. The thick line marks the strong Coulomb interaction $v(\mathbf{r}, \mathbf{r'})$ between electrons, which in the elementary excitations picture is replaced by the screened Coulomb interaction $W(\mathbf{r}, \mathbf{r'})$ between the quasiparticles, marked as a thin line in the plot.

the electron deficiency around an electron as a result of the repulsive interaction with the rest of the quasiparticles. As a consequence, a quasiparticle in the present study is the sum of an electron and the cloud of positively charged holes around it, which *screens* the electron. Each electron is screened by its own *xc* hole and the picture of weakly interacting quasiparticles sketched in Section 3.1 holds, see Fig. 4.1.

4.2 Quasiparticle lifetimes: self-energy and decay rate

It can be shown from many-body (Green's function) theory [FS06] that the quasiparticle energies E_i can be obtained from the one-particle quasiparticle equation

$$\hat{H}_0\Psi_i(\mathbf{r}) + \int \Sigma(\mathbf{r},\mathbf{r}';E_i)\Psi_i(\mathbf{r}')d\mathbf{r}' = E_i\Psi_i(\mathbf{r}) \tag{4.1}$$

$\hat{H}_0$ is a one-electron Hamiltonian of the form

$$\hat{H}_0(\mathbf{r}) = -\frac{1}{2}\nabla^2 + w(\mathbf{r}) + \int \frac{\rho(\mathbf{r}')}{|\mathbf{r}-\mathbf{r}'|}d\mathbf{r}', \tag{4.2}$$

where $w(\mathbf{r})$ is a mean-field external potential, as the one defined in the KS formalism, see Section 2.3.2. Eq. (4.1) is called a one-particle equation as it applies to one-particle-like states Ψ_i. One could include within the quasiparticle picture two-body elementary excitations [GV05], i.e., excitons, but in metals they are of negligible importance.

Even though Eq. (4.1) presents a similar structure to the KS Eqs. (2.7)-(2.8) or other mean-field equations, the quasiparticle equation exhibits important differences arising from the potential $\Sigma(\mathbf{r},\mathbf{r}';E_i)$, which is usually named the *self-energy* of the quasiparticles. From Eq. (4.1) one deduces that the self-energy is the responsible for including the many-body effects which represent the passage from a non-interacting particle picture (mean-field approaches) to the quasiparticle framework.

The energy dependence of the self-energy $\Sigma(\mathbf{r},\mathbf{r}';E_i)$ has important consequences as it makes the self-energy operator non-Hermitian. Thus, in general the quasiparticle energies E_i are complex and the associated quasiparticle wave functions Ψ_i are non-orthogonal.

As it was stated in Section 2.3.4, Kohn-Sham LDA energies ϵ_i and wave functions ψ_i represent good approximations of their quasiparticle counterparts, specially for metals. Then one is allowed to use first-order perturbation theory. From a comparison of the KS Eqs. (2.7)-(2.8) with the quasiparticle equation (4.1) it follows that the difference is the appearance of the self-energy term in Eq. (4.1) replacing the energy-independent *xc* in the KS equations. Thus we approximate the quasiparticle energies by

$$E_i \simeq \epsilon_i + \iint d\mathbf{r}d\mathbf{r}'\psi_i^*(\mathbf{r})\psi_i(\mathbf{r}')\left[\Sigma(\mathbf{r},\mathbf{r}';E_i) - V_{xc}(\mathbf{r}')\delta(\mathbf{r}-\mathbf{r}')\right]. \tag{4.3}$$

In order to solve this nonlinear equation the knowledge of the self-energy as a function of the quasiparticle energy is needed. However, its exact form is generally unknown. There are two different strategies to overcome this problem starting from some approximate *ansatz* for $\Sigma(\mathbf{r}, \mathbf{r'}; E)$ [GV05]. One consists in solving the Dyson equation $E_i = \epsilon_i + \mathrm{Re}[\Sigma(\mathbf{r}, \mathbf{r'}; E_i)]$, the second one (the one we apply here) is to take advantage again of the fact that $E_i \approx \epsilon_i$ and use the linear expansion

$$\Sigma(\mathbf{r}, \mathbf{r'}; E_i) \simeq \Sigma(\mathbf{r}, \mathbf{r'}; \epsilon_i) + (E_i - \epsilon_i) \left. \frac{\partial \Sigma(\mathbf{r}, \mathbf{r'}; \omega)}{\partial \omega} \right|_{\omega=\epsilon_i}, \tag{4.4}$$

which leads to the expression

$$E_i \simeq \epsilon_i + Z_i \iint d\mathbf{r} d\mathbf{r}' \psi_i^*(\mathbf{r}) \psi_i(\mathbf{r}') \left[\Sigma(\mathbf{r}, \mathbf{r}'; \epsilon_i) - V_{xc}(\mathbf{r}') \delta(\mathbf{r} - \mathbf{r}') \right], \tag{4.5}$$

where the so-called renormalization factor is expressed as

$$Z_i = \left(1 - \left\langle \psi_i \middle| \frac{\partial \Sigma(\epsilon_i)}{\partial \omega} \middle| \psi_i \right\rangle \right)^{-1}. \tag{4.6}$$

Finally, we suppose the renormalization factor is $Z_i = 1$ which is known as the *on-shell approximation* [MPPZK$^+$04], obtaining the following expression for the quasiparticle energies

$$E_i \simeq \epsilon_i + \iint d\mathbf{r} d\mathbf{r}' \psi_i^*(\mathbf{r}) \psi_i(\mathbf{r}') \left[\Sigma(\mathbf{r}, \mathbf{r}'; \epsilon_i) - V_{xc}(\mathbf{r}') \delta(\mathbf{r} - \mathbf{r}') \right]. \tag{4.7}$$

4.2.1 Spectral function

Also from many-body Green's function theory one can define a crucial quantity known as the *spectral function* [GV05] (not to be confused with the quantity S^0 defined in Section 3.3). The spectral function represents the probability of increasing or decreasing the many-particle system energy by an amount of ω by adding or removing a particle in the state Ψ_i. At zero temperature it has the following expression (dropping any spin-dependence),

$$A(\mathbf{k}, \omega) = -\frac{1}{\pi} \frac{\mathrm{Im}[\Sigma(\mathbf{k}, \omega)]}{\left\{ \omega - \epsilon_{\mathbf{k}} - \mathrm{Re}[\Sigma(\mathbf{k}, \omega)] \right\}^2 + \left\{ \mathrm{Im}[\Sigma(\mathbf{k}, \omega)] \right\}^2}, \tag{4.8}$$

where $\Sigma(\mathbf{k}, \omega)$ stands for the self-energy.

The spectral function exhibits the form of a Lorentzian centered in $\epsilon_{\mathbf{k}} - \mathrm{Re}[\Sigma(\mathbf{k}, \omega)]$ and of $\mathrm{Im}[\Sigma(\mathbf{k}, \omega)]$ half-width at half-maximum (HWHM). Let us now switch off the interactions adiabatically. For a non-interacting system $\Sigma(\mathbf{k}, \omega) = 0$. The spectral function Eq. (4.8) should smoothly become a Dirac delta, actually for a non-interacting system the spectral function is simply $A(\mathbf{k}, \omega) = \sum_{\mathbf{k}} \delta(\omega - \epsilon_{\mathbf{k}})$. This results from the fact that in the non-interacting limit the (KS) states ψ_i of energy ϵ_i are the true eigenstates of the system, and as such they present an infinite lifetime.

One deduces that the finite width of the interacting spectral function is related to the quasiparticle lifetime. The stronger the interactions between particles, the wider the peak in $A(\mathbf{k},\omega)$ and the shorter the lifetime of the quasiparticle. Even though this picture is valid in general, note that when the quasiparticle energy approaches the Fermi level, the width of the spectral function must vanish for a 3D ideal periodic solid no matter how strong the interaction is. This can be analytically derived for the homogeneous electron gas [GV05].

Thus, the imaginary part of the self-energy gives the lifetime of the quasiparticle. A practical way of realizing it comes again from taking the non-interacting limit of the many-particle system. In this limit, wave functions are well approximated by plane waves of well defined momentum k_i and energy $E_i = \mathrm{Re}[E_i] + i\mathrm{Im}[E_i]$, with $\mathrm{Im}[E_i]$ small (let us define small as $\mathrm{Im}[E_i] \ll \mathrm{Re}[E_i]$). Then the probability of finding that excited particle in position $\mathbf{r}$ decays in time as

$$|\Psi_i(\mathbf{r},t)|^2 \propto e^{-2\mathrm{Im}[E_i]t} \equiv e^{-t/\Gamma}, \tag{4.9}$$

where we have defined the *decay rate* Γ (also known as *damping rate*) as the inverse of the lifetime.

If the imaginary part of the quasiparticle energy is evaluated in the above mentioned on-shell approximation, from Eq. (4.7) follows that the decay rate of the excited state Ψ_i with energy ϵ_i can be calculated by the expression

$$\Gamma_i = -2\,\mathrm{Im}\left[\iint d\mathbf{r}\,d\mathbf{r}'\Psi_i^*(\mathbf{r})\Sigma(\mathbf{r},\mathbf{r}';\epsilon_i)\Psi_i(\mathbf{r}')\right]. \tag{4.10}$$

The spectral function $A(\mathbf{k},\omega)$ is directly measured in angle-resolved photoemission spectrocopy (ARPES) experiments. In ARPES an electron which was below the Fermi level is removed as the result of being photoexcited. By measuring the momentum and kinetic energy of the removed electrons for different energies and momenta $\mathbf{k}$ one can construct the spectral function for the occupied states, due to the fact that one is extracting an energy from the (photo-) excited system which corresponds precisely to the quasiparticle energy E_i. This way ARPES has access to detailed information about the band structure as well as many-body effects in the system. However, it is restricted to occupied quasiparticle states.

To study the unoccupied quasiparticle states the inverse procedure is needed. Consequently, an electron is added to the system with an energy $E_i > E_F$. This extra electron decays to the Fermi level emitting a photon which is detected and analyzed as a function of its energy. This technique is known as inverse photoemission spectroscopy (IPES).

Further developments in photoemission experimental techniques lead recently to the direct measurement in time of the population decay of quasiparticles [Kir08,SKRZ$^+$10] using the time-resolved two-photon photoemission (TR-2PPE) technique [SBW$^+$02].

4.2.2 Decay rate

As stated above, the linewidth of a quasiparticle represents the inverse of its *lifetime*, that is, the inverse of the time needed for the quasiparticle state to be depopulated. More precisely the lifetime of the state is determined by the Heisenberg energy-time uncertainty principle $\Delta E \Delta t \geqslant 1$, from where it follows $\tau^{-1} = \Gamma$. Usually the decay rate in metals is given in meV and the lifetime is measured in femtoseconds [1 femtosecond (fs) = 10^{-15} seconds]. The two quantities are related by

$$\tau \simeq \frac{658}{\Gamma} \text{ meV} \cdot \text{fs}. \tag{4.11}$$

As we have described, quasiparticles present a finite linewidth as a consequence of their interaction with other particles, that can be seen as scattering centers. Notice the latter can be electrons (γ_{e-e}) or any kind of elementary excitations [i.e., phonons (γ_{e-ph}), plasmons (γ_{e-pl}), magnons (γ_{e-mg}), polarons (γ_{e-po})]. Also, in real systems there are two more decay channels, namely the scattering by defects (γ_{e-def}) and the elastic scattering (γ_{1e}), if interfaces are present. The latter decay channel consists of energy-conserving resonant electron transfer mechanisms through an interface.

In general it is a good approximation to consider that the different decay channels contribute additively to the total decay rate [VCGBPG$^+$06],

$$\Gamma = \gamma_{e-e} + \gamma_{e-def} + \gamma_{1e} + \gamma_{e-ph} + \gamma_{e-pl} + ... \tag{4.12}$$

Now the question arises: which of the different scattering mechanisms are relevant in the quasiparticle decay for a given system? As Pb is the subject of study, we are interested in the decay channels of importance in metals. At low temperature quasiparticles in metals decay through three main scattering mechanisms [HBP$^+$09]: the inelastic electron-electron ($e - e$) scattering (properly, the quasiparticle-quasiparticle scattering), the electron-phonon coupling and the scattering by defects. Among them, the inelastic $e - e$ decay rate is usually the main contribution to the total decay rate or linewidth of quasiparticles in metals, specially for energies not close to the Fermi level.

Let us recall at this point (see Section 4.2) that in metals quasiparticles with energy $E_i > E_F$ can be viewed as electrons being promoted from an occupied state below the Fermi level to a higher energy unoccupied state, leaving a hole with energy lower than E_F. As a hole behaves like an electron with positive charge, the mutual interaction between the electron and the corresponding hole can form a bound state which represents a different kind of (two-body) excitation, the so-called exciton. However, the high density of free carriers in a metal results in an "instantaneous" screening of the excited electron and the excitonic effects become negligible in metals.

Note the quasiparticles are of paramount importance in many physical and chemical phenomena, as excitation mediated desorption and oxidation of molecules at surfaces, spin transport, energy transfer in photochemical reactions or catalytic reactions, to cite

some examples (see Ref. [VCGBPG+06] and references therein). And more specifically, the lifetime of the excitations determines the efficiency of any chemical reaction channel, therefore emerging as a key quantity.

4.3 The inelastic $e-e$ decay rate: GW approximation

Following the discussions of the previous Sections, in order to study the quasiparticle lifetime in Pb a procedure to calculate the self-energy stemming from electron-electron inelastic scattering processes is needed. Below we review the theoretical framework and practical expressions employed here in calculating the electron-eletron self-energy $\Sigma_{e-e}(\mathbf{k},\omega)$ and then γ_{e-e} using Eq. (4.10).

However, as a reference, let us first discuss the electron-electron inelastic lifetime of quasiparticles in a homogeneous electron gas for excitation energies close to the Fermi level and in the high density and low temperature limit, given by the Quinn-Ferrell (QF) formula [JQAF58]

$$\tau_{QF}(E) \simeq \frac{0.3997}{r_s^{5/2}(E-E_F)^2}, \tag{4.13}$$

where r_s is the average valence density parameter [see Eq. (2.15)]. For completeness, we outline the derivation of Eq. (4.13) in Appendix F. Thus $\Gamma_{QF}(E) \propto (E-E_F)^2$. A quadratic dependence of the decay rate on the quasiparticle energy is usually referred to as a 3D Fermi liquid behavior. In this quadratic dependence one factor $(E-E_F)$ arises from the phase space available to decay while the second one stems from the linear energy dependence of the number of electron-hole pair that can be excited when $E \to 0$ [GV05] (see Appendix E). It has been found that this model, although in principle only valid for the high density limit, does a good job in estimating the $e-e$ decay rates in metals with realistic densities. Then, an important issue to address when studying lifetimes of quasiparticles is to what extent the actual lifetimes behaviour deviates from the 3D Fermi liquid behavior, that is, from a simple quadratic dependence on the energy (see, i.e, [ANVCME07]). Note also that for a 2D homogeneous electron gas, the same approximations applied in deriving Eq. (4.13) lead to a different dependence which includes a logarithmic factor, $\Gamma^{2D}(E) \propto (E-E_F)^2 \ln|E-E_F|^{-1}$ [GV05].

4.3.1 Hedin's equations

In this thesis we use the Green's function theory to address the inelastic electron-electron contribution to the linewidth of quasiparticles. In a system of N interacting electrons, the probability amplitude of an additional electron to be propagated from $(\mathbf{r}',t')$ to $(\mathbf{r},t)$ for $t>t'$ is given by the one-electron Green's function

$$G(\mathbf{r},\mathbf{r}',t,t') = -i\langle N|\mathcal{T}[\hat{\psi}(\mathbf{r},t)\hat{\psi}^\dagger(\mathbf{r}',t')]|N\rangle, \tag{4.14}$$

where $\mathcal{T}$ is the time-ordering operator defined by

$$\mathcal{T}\left[\hat{A}(t_1)\hat{B}(t_2)\right] = \begin{cases} \hat{A}(t_1)\hat{B}(t_2) & \text{if} \quad t_1 > t_2 \\ \hat{B}(t_2)\hat{A}(t_1) & \text{if} \quad t_2 > t_1, \end{cases} \tag{4.15}$$

with $\hat{\psi}$ being the electron annihilation field operator in the Heisenberg picture and $|N\rangle$ is the many-body N-electron ground state [AG98]. The Green's function is the solution to an equation similar to the quasiparticle equation (4.1), namely

$$\hat{H}_0 G(\mathbf{r}, \mathbf{r'}) + \int \Sigma(\mathbf{r}, \mathbf{r''}; \omega) G(\mathbf{r''}, \mathbf{r'}; \omega) d\mathbf{r''} = G(\mathbf{r}, \mathbf{r'})\delta(\mathbf{r} - \mathbf{r'}). \tag{4.16}$$

Within many-body perturbation theory it is possible to obtain the self-energy as a series in the bare Coulomb interaction $v(\mathbf{r}, \mathbf{r'})$. However, due to the long range of this interaction such a perturbation series contains divergent contributions. In order to avoid these divergences, the infinite terms in the series build up the so-called *dynamical screened interaction* $W(\mathbf{r}, \mathbf{r'}; \omega)$ (see Fig. 4.1) and the self-energy is rewritten as a series in the frequency dependent $W(\mathbf{r}, \mathbf{r'}; \omega)$. This was first done by Hedin [Hed65] who reformulated the exact many-body mathematical problem codified in Eq. (4.16) as the following set of integro-differential equations, known precisely as Hedin's equations,

$$\begin{aligned} W(1,2) =& v(1,2) + \int v(1,3) P(3,4) W(4,2)\, d3d4, \\ \Sigma(1,2) =& i \iint G(1,3^+) W(1,4) \Lambda(3,2,4)\, d3d4, \\ G(1,2) =& G^0(1,2) + \iint G^0(1,3) \Sigma(3,4) G(4,2)\, d3d4, \\ \Lambda(1,2,3) =& \delta(1-2)\delta(1-3) - \iiint \frac{\delta\Sigma(1,2)}{\delta G(4,5)} G(4,6)\Lambda(6,7,3)G(7,5)\, d4d5d6d7, \\ P(1,2) =& -i \iint G(1,3)\Lambda(3,4,2)G(4,1^+)\, d3d4, \end{aligned} \tag{4.17}$$

which has to be solved self-consistently [Hed65, AG98]. In the notation above $(1) \equiv (\mathbf{r}, t)$ refers to the standard spatial and temporal compact notation and 1^+ refers to the $t \to t + i\eta$ substitution, where $\eta = 0^+$ is a positive infinitesimal. P stands for the time-ordered polarization operator and Λ is the so-called vertex function.

4.3.2 *GW* approximation

The functional derivative in the expression for the vertex function Λ prevents Hedin's equations to be solved in a straightforward manner and usually approximations are applied. The most widely used approximation consists in neglecting the second term in $\Lambda(1,2,3)$, thus writing the vertex function as

$$\Lambda^0(1,2,3) = \delta(1-2)\delta(2-3), \tag{4.18}$$

neglecting the commonly named vertex corrections. This is the so-called GW approximation [AG98, ORR02], resulting in the following set of equations

$$\Sigma(1,2) = iG(1,2)W(1,2), \tag{4.19a}$$

$$G(1,2) = G^0(1,2) + \iint G^0(1,3)\Sigma(3,4)G(4,2)\mathrm{d}3\mathrm{d}4, \tag{4.19b}$$

$$P(1,2) = -iG(1,2)G(2,1), \tag{4.19c}$$

$$W(1,2) = v(1,2) + \iint v(1,3)P(3,4)W(4,2)\mathrm{d}3\mathrm{d}4. \tag{4.19d}$$

These equations might be solved iteratively until self-consistency is obtained. Nevertheless, these calculations are still computationally hard, and usually different approximations or levels of self-consistency are employed within the general GW scheme.

Note that in the GW approximation the polarizability is related to the dielectric function ε through the expression $\varepsilon = 1 - Pv$, so that the screened interaction can be schematically written as

$$W = \varepsilon^{-1}v, \tag{4.20}$$

which is non-local in space and time.

More precisely, in this thesis we use two different approaches in evaluating the screened interaction, which result in two different GW schemes, which we call G^0W^0 and G^0W approximations. In both approaches G^0 stands for the non-interacting Green's function, thus the second term in Eq. (4.19b) has been neglected throughout the present work. G^0 can be expressed in terms of the one-electron states (here, KS states) as

$$G^0(\mathbf{r},\mathbf{r'};\omega) = \sum_i \frac{\psi_i(\mathbf{r})\psi_i^*(\mathbf{r'})}{\omega - \epsilon_i + i\eta\, sgn(\epsilon_i - E_F)}, \tag{4.21}$$

where in practice ψ_i and ϵ_i are KS wave functions and energies, $\eta = 0^+$ and $sgn(x) = 1\,(-1)$ for $x > 0\,(x < 0)$. Strictly, *all* states must be summed in Eq. (4.21). Obviously, in practice one seeks the convergence of G^0 with respect to the unoccupied states included in the sum.

The difference between the G^0W^0 and G^0W approximations then stems from the way the screened interaction is treated. With W^0 we denote the RPA form of the screened interaction, which is obtained using the RPA susceptibility in the calculation of the dielectric function entering Eq. (4.20), see Chapter 3. On the other hand, in the G^0W scheme the xc kernel is included in the calculation of the susceptibility, and consequently in the screened interaction W through ε.

The inelastic electron-electron scattering mechanism can be seen as the decay of the quasiparticle in energy by creating a electron-hole pair, that is, by promoting an electron from the Fermi sea to an unoccupied state. Obviously, energy conservation applies and the energy transfered to the system in the decay of the quasiparticle corresponds to the energy gained by the electron promoted above the Fermi level. In terms

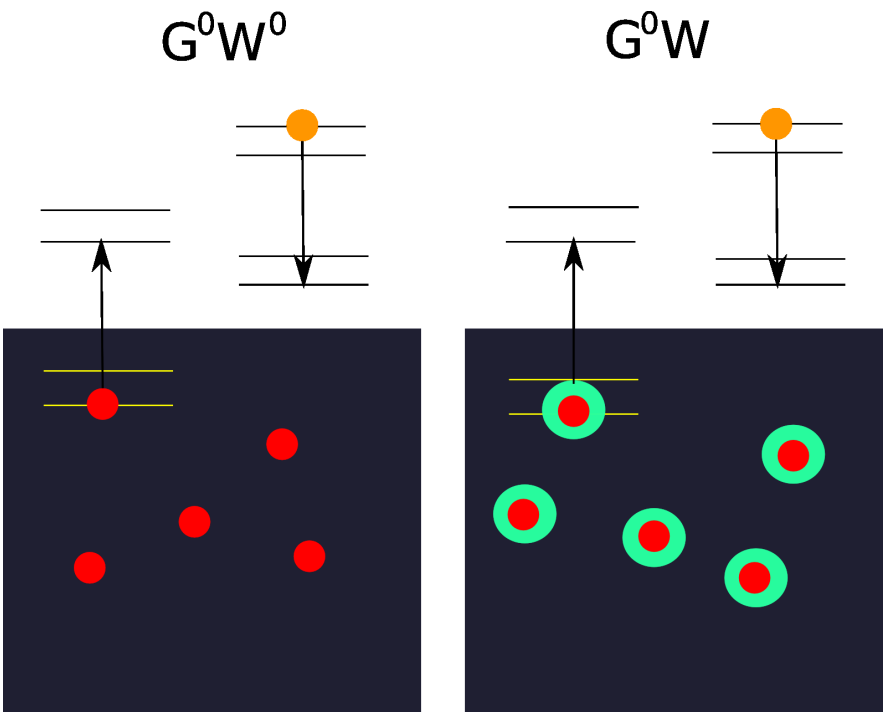

Figure 4.2: Sketch showing the mechanism of quasiparticle decay through inelastic electron-electron scattering. The two different approximations used in this thesis to evaluate the $e-e$ contribution to the linewidth are shown (see text). Orange and red circles represent the decaying quasiparticle and the electrons in the Fermi sea, respectively. The green circles signal the inclusion of the xc short range effects in the susceptibility from which the screened interaction $W(\mathbf{r}, \mathbf{r'}; \omega)$ is built (see text).

of this picture, in this thesis we neglect the xc hole of the quasiparticle resulting from adding an electron (hole) to (from) the system, as we make use of the non-interacting Green's function neglecting the second term in Eq. (4.19b). On the other hand, the xc short range effects in the dielectric function are taken into account when including the TDLDA xc kernel in the calculation of the susceptibility (G^0W scheme), and they are neglected in the G^0W^0 approximation, see Fig. 4.2.

4.3.3 Expressions for a periodic solid

In the present work we are interested in studying from first-principles the inelastic electron-electron contribution to the lifetime of excited electrons and holes in periodic solids. In order to obtain an expression for the $e-e$ contribution to the quasiparticle damping rate Eq. (4.10) following the approach outlined in Chapter 3, we combine Eqs. (4.10), (4.20) and (3.24). This leads to

$$\Gamma_{e-e}(i, \mathbf{k}) = \frac{1}{\pi^2} \sum_f \int_{\mathrm{BZ}} d\mathbf{q} \sum_{\mathbf{G},\mathbf{G'}} \mathrm{Im}[-\varepsilon^{-1}_{\mathbf{G},\mathbf{G'}}(\mathbf{q}, \omega)] \frac{\mathrm{B}^*_{i,f}(\mathbf{k}, \mathbf{q}, \mathbf{G}) \mathrm{B}_{i,f}(\mathbf{k}, \mathbf{q}, \mathbf{G'})}{|\mathbf{q} + \mathbf{G}|^2}, \qquad (4.22)$$

where i and j are energy band labels. This is the expression employed in this thesis for evaluating the inelastic $e-e$ linewidth of a quasiparticle of energy E_i and momentum k. The first sum is over all final states $\phi_{f,\mathbf{k}-\mathbf{q}}(\mathbf{r})$ with energies $\epsilon_{f,\mathbf{k}-\mathbf{q}}$ between $\epsilon_{i,\mathbf{k}}$ and the Fermi level E_F, $\omega = \epsilon_{i,\mathbf{k}} - \epsilon_{f,\mathbf{k}-\mathbf{q}}$, $\mathbf{G}$ and $\mathbf{G'}$ are reciprocal lattice vectors, and

$$B_{i,f}(\mathbf{k},\mathbf{q},\mathbf{G}) = \int d\mathbf{r}\phi^*_{i,\mathbf{k}}(\mathbf{r})e^{i(\mathbf{q}+\mathbf{G})\cdot\mathbf{r}}\phi_{f,\mathbf{k}-\mathbf{q}}(\mathbf{r}), \tag{4.23}$$

are coupling matrices. The KS wave functions $\phi_{i,\mathbf{k}}(\mathbf{r})$ are expanded in a plane wave basis as explained in previous Chapters [see Eq. (2.17)], and in practice $B_{i,f}(\mathbf{k},\mathbf{q},\mathbf{G})$ are calculated using the following expression,

$$B_{i,f}(\mathbf{k},\mathbf{q},\mathbf{G}) = \frac{1}{\Omega}\sum_{\mathbf{G'}} c_{i,\mathbf{k}}(\mathbf{G'})c_{f,\mathbf{k}-\mathbf{q}}(\mathbf{G'}-\mathbf{G}), \tag{4.24}$$

where Ω is the normalization volume.

4.3.4 Spin-orbit coupling

Recently, the Hedin's scheme has been generalized to include spin-dependent interactions [AB08]. However, this new generalized theoretical framework leaves unaffected our formalism also when SOC is included. This is due to the combination of two factors: we do not go beyond the GW approximation and we are interested in the decay of quasiparticles only through the creation of electron-hole pairs. The latter point means we are only including the density-density response in the calculation of the quasiparticle self-energy $\Sigma(\mathbf{r},\mathbf{r}';\omega)$, excluding the response of the electron density to changes in the spin degrees of freedom.

Consequently, when including the spin-orbit coupling in the ground state and susceptibility calculations, the only variation in evaluating $\Gamma_{e-e}(i,\mathbf{k})$ in the outlined scheme is the replacement of the scalar-relativistic wave functions $\phi_{i,\mathbf{k}}(\mathbf{r})$ by the two-component spinors $\Psi_{i,\mathbf{k}}(\mathbf{r})$ given by Eq. (2.40). Consequently, the coupling matrices when SOC is included present the form

$$B_{i,f}(\mathbf{k},\mathbf{q},\mathbf{G}) = \frac{1}{2\Omega}\sum_{\mathbf{G'}}\left[c^*_{n,\mathbf{k},\uparrow}(\mathbf{G'})c_{n',\mathbf{k}+\mathbf{q},\uparrow}(\mathbf{G'}-\mathbf{G}) + c^*_{n,\mathbf{k},\downarrow}(\mathbf{G'})c_{n',\mathbf{k}+\mathbf{q},\downarrow}(\mathbf{G'}-\mathbf{G})\right]. \tag{4.25}$$

Chapter 5

Bulk Pb electronic structure

5.1 Introduction: pseudopotentials

Before analyzing in detail the bulk Pb electronic structure and the SOC effects on it, let us outline the generation and testing of pseudopotentials as it has been applied to the present study. As it was stated in Chapter 2, in the present work the external potential in the Kohn-Sham equations is modeled by norm-conserving pseudopotentials.

In generating NCP, one has to fix the valence electronic configuration from which NCP are built, the cut-off radii r_c^l for each angular momentum channel l, the xc functional and the generation scheme. Whereas the LDA was always chosen as the xc functional (see Section 2.3.3) several combinations of valence electronic configurations and $\left\{r_c^l\right\}$ sets where examined for two different generation schemes. The two different flavours of NCP tested have been the HSC [RHSC79, BBRHS82] scheme and the one proposed by Troullier and Martins (TM) [TLM91].

The tests consist in comparing the true atomic valence energy eigenvalues for different electronic configurations with the ones retrieved using a pseudopotential generated for a fixed valence configuration. That is, transferability is checked, estimating the quality of the performance of the NCP in different chemical environments.

Pb (Z=82) presents an electronic structure in which usually the valence electronic configuration is chosen to be $[6_s^2\ 6_p^2]$. Concerning the starting electronic configuration, we found that the highest quality pesudopotentials for Pb (regardless of the generation scheme) correspond to the valence configuration

$$6s_{1/2}^{1.50}\ \ 6p_{1/2}^{0.42}\ \ 6p_{3/2}^{0.83}\ \ 6d_{3/2}^{0.10}\ \ 6d_{5/2}^{0.15}\ \ 5f_{5/2}^{0.11}\ \ 5f_{7/2}^{0.14}. \tag{5.1}$$

Note the presence of $6d$ and $5f$ orbitals, which play the role of polarizability orbitals aiming to improve the transferability. Also, notice that it is a positive ionic configuration with $+0.75e^-$ charge. This situtation is usual when generating NCP for metals, as

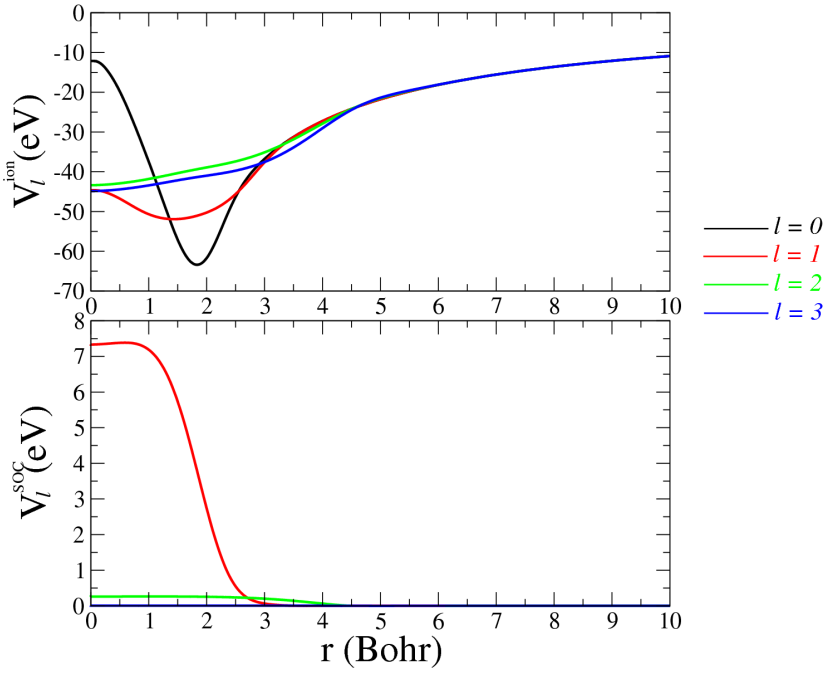

Figure 5.1: Ionic (top panel) and SOC (bottom panel) pseudopotentials used in this thesis.

the less strongly bounded electrons in the isolated atoms usually become delocalized in the solid, forming the Fermi sea. As a consequence, the valence electrons which remain localized are overbinded with respect to the neutral isolated atom. This effect is mimicked using positively charged valence configuration when building the NCP.

Regarding the two different flavours HSC and TM of the NCP generation, the TM scheme gives softer pseudopotentials than HSC, allowing cut-off radii which are usually slightly bigger than the position of the outermost maximum of the corresponding all-electron wave function. On the other hand, the procedure developed by HSC gives more accurate results than TM NCP, but at the price of deeper pseudopotentials. HSC cut-off radii are slightly smaller than the position of the outermost maximum of the corresponding all-electron wave function. Then one has to find a compromise between softness and quality of the NCP.

In this thesis we deal with simple systems and consequently softness of the NCP does not represent a concern. Thus, we chose a pseudopotential generated by applying the HSC scheme. The best transferability tests were obtained for the cut-off radii values $r_c^l = 1.60$, 2.00, 3.50 and 3.50 a.u. for s, p, d and f electrons, respectively. The maximum error of the pseudopotentials employed in this thesis for realistic transferability tests has been found to be $\Delta\epsilon \lesssim 200$ meV corresponding to promoting or removing a $6s$ electron, which are unlikely processes in bulk Pb. In the rest of the transferability tests, the errors were always below 100 meV.

As it is explained in Section 2.6.1, NCP are separated in two different contributions, mimicking the ionic (scalar-relativistic) $V_l^{ion}(r)$ and SOC $V_l^{SOC}(r)$ contributions to the atomic potential the valence electrons feel [see Eqs. (2.29)-(2.30)]. In Fig. 5.1 $V_l^{ion}(r)$ and $V_l^{SOC}(r)$ are plotted for each angular momentum channel l as a function of the

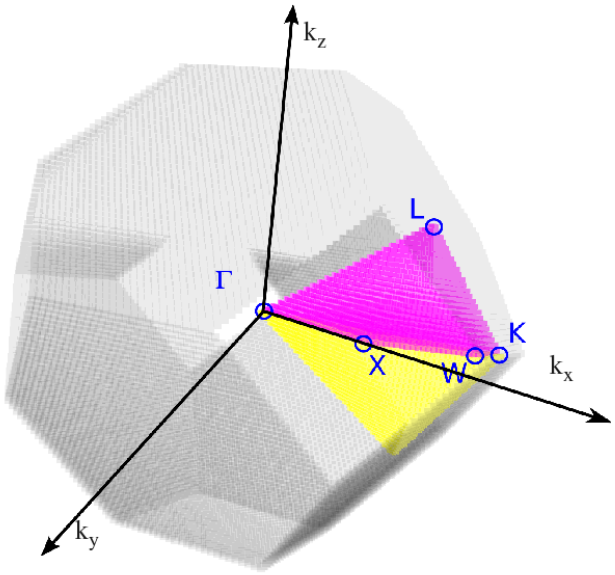

Figure 5.2: Plot of the first BZ for a face-centered-cubic crystal. The pink volume represents the irreducible BZ when SOC is excluded from the Hamiltonian. The yellow volume has to be added to the IBZ when SOC is turned on (see text). The symmetry points relevant to the work presented here are labeled. The arrows represent a cartesian coordinate system.

distance to the atomic nucleus r. For the SOC pseudopotentials, the $l = 1$ component is clearly the most important, whereas the $l = 3$ one vanishes. This is as expected because the $6p$ electrons are closer to the nucleus than the $6d$ and $6f$ ones, thus being more strongly affected by SOC. Hence, noticeable SOC effects are expected essentially on p-like states.

5.2 Electronic structure: SOC effects

Bulk Pb has a face-centered-cubic (fcc) crystal structure. In Fig. 5.2 the first Brillouin zone for an fcc structure is plotted. The pink volume corresponds to the irreducible BZ when working at the scalar-relativistic level. When SOC is switched on, the IBZ has to be doubled (see Section 2.7.1). Thus, in Fig. 5.2 the IBZ when SOC is included in the Hamiltonian consists in summing the pink and yellow volumes. Note the huge saving in computational load when taking advantage of the symmetries. More precisely, in the scalar-relativistic case the IBZ volume is only a 1/48 of the total BZ volume, while a 1/24 once SOC is taken into account.

The three reciprocal space directions in which the dielectric response has been studied in this thesis (see Chapters 6 and 7) correspond to the Γ−X, Γ−K and Γ−L BZ high-symmetry directions. In each of the mentioned directions, the momentum $\mathbf{q}$

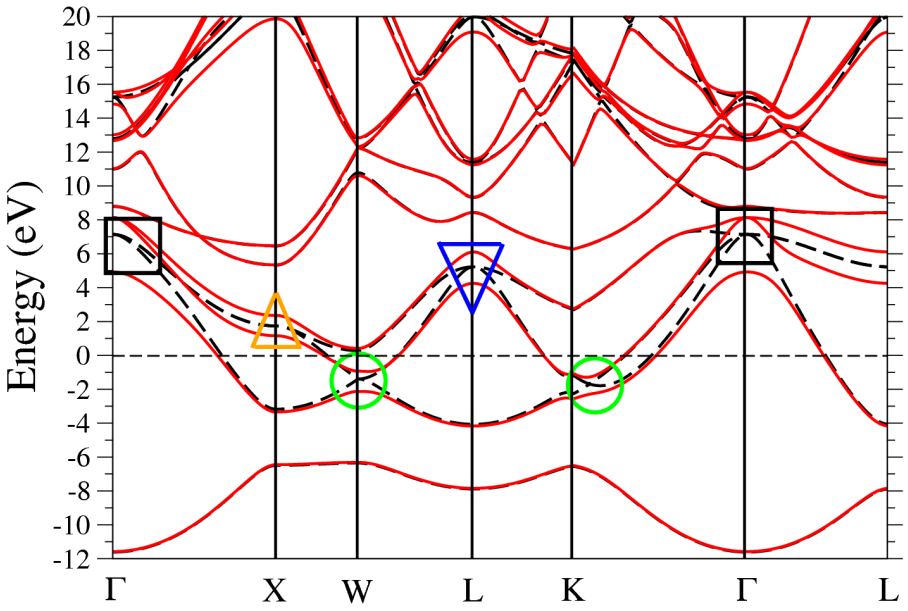

Figure 5.3: Calculated band structure of bulk lead, with (solid red lines) and without (dashed black lines) inclusion of the spin-orbit coupling. Symbols mark regions where the SOC-induced band splittings are reflected in the density of states shown in Fig. 5.4. The horizontal dashed line represents the Fermi level.

is of the form

$$\mathbf{q}_{\mathrm{X}} = \frac{2\pi}{a}\left(\frac{l}{\mathrm{M}}, 0, 0\right), \tag{5.2}$$

$$\mathbf{q}_{\mathrm{K}} = \frac{2\pi}{a}\left(\frac{l}{\mathrm{M}}, \frac{l}{\mathrm{M}}, 0\right), \tag{5.3}$$

$$\mathbf{q}_{\mathrm{L}} = \frac{2\pi}{a}\left(\frac{l}{\mathrm{M}}, \frac{l}{\mathrm{M}}, \frac{l}{\mathrm{M}}\right), \tag{5.4}$$

where a is the lattice parameter, l is any integer number and M corresponds to the M×M×M Monkhorst-Pack grid used (see below).

The convergence of the electron density has been performed using a 12×12×12 Monkhorst-Pack [JMDP76] grid for the scalar-relativistic calculations, while a 12×12×24 mesh replaced it once SOC was included. The band structure was converged with respect to the kinetic energy cut-off of the plane wave basis (see Section 2.5). It has been found that a kinetic energy cut-off of 190 eV, which corresponds to the inclusion of ∼180 plane waves in the expansion of the KS states [see Eq. (2.18)], gave satisfactory results with energy bands converged to within 20 meV.

Figure 5.3 presents the calculated band structure of bulk lead along the high-symmetry directions of the BZ obtained with the use of the experimental lattice parameter $a_c = 4.95$ Å. In the figure one set of data (solid red lines) corresponds to the calculation with the inclusion of the SOC in the KS Hamiltonian whereas dashed black lines represent the electronic structure obtained at the scalar-relativistic level. The Hamiltonian including the SOC was solved fully self-consistently. First, notice that as

the fcc lattice has inversion symmetry, due to the Kramers degeneracy [Tin71] each energy band is at least double degenerate in spin *no matter whether SOC is turned on or off*. The Kramers degeneracy is a consequence of the combination of time-reversal ($\epsilon_{n,\sigma,\mathbf{k}} = \epsilon_{n,-\sigma,-\mathbf{k}}$) and inversion symmetry ($\epsilon_{n,\sigma,\mathbf{k}} = \epsilon_{n,\sigma,-\mathbf{k}}$) , which necessarily leads to the spin-degeneration of all the energy bands: $\epsilon_{n,\sigma,\mathbf{k}} = \epsilon_{n,-\sigma,\mathbf{k}}$, $\forall(n,\sigma,\mathbf{k})$.

The calculated band structure is in good agreement with other theoretical results [JVTJ$^+$08] and with the experimental data [JP90] once SOC is taken into account. As can be seen in Fig. 5.3, the inclusion of SOC affects specially the three p energy bands (the only ones that cross the Fermi level), mainly around the high-symmetry points. In Table 5.I, a comparison of the energies of the p bands at the high-symmetry points with the inclusion and exclusion of SOC in the Hamiltonian is presented. However, notice following Fig. 5.3 that the Fermi surface remains nearly unchanged upon inclusion of the SOC.

On the other hand, remarkable SOC splittings appear also for d states at energies above 13 eV (see Fig. 5.3) around the high-symmetry point L and in the Γ-X direction. Taking into account the small intensity of the SOC pseudopotential for d electrons $V_{l=2}^{SOC}$ (see Fig. 5.1), the splittings of the d states reflect the importance of the mixing of scalar-relativistic states by the spin-orbit coupling. Nevertheless, these splittings occur at energies $\epsilon \gtrsim E_F + 20$ eV, therefore playing a marginal role in the results presented in the following Chapters of this thesis.

In general, one can see that SOC produces two main effects in the Pb band structure:

a) As SOC breaks the three-dimensional symmetry setting a preferential direction (see Section 2.7.1), its inclusion leads to a breaking of symmetry degeneracies at high-symmetry points and directions of the BZ. The most important ones in the case of bulk Pb are the SOC-split p electron bands along Γ-X and Γ-L symmetry directions and the energy splitting, $\Delta\epsilon^{SOC}$, at the high-symmetry points: $\Delta\epsilon^{SOC} = 3.21$ eV at Γ, 1.20 eV at X and W, and 1.85 eV at L. K is the only high-symmetry point where all three p-like states are nondegenerate even at the scalar-relativistic level (see Table 5.I).

b) SOC avoids band-crossings, as can be observed between p-like states marked by green circles in Fig. 5.3.

Table 5.I: Energies ϵ_i of p-like electronic states at some high-symmetry points in the Brillouin zone obtained at the scalar-relativistic (sc) and full relativistic (SOC) level. All energies are in eV with respect to the Fermi level.

	Γ		X		W		L		K	
	sc	SOC	sc	SOC	sc	SOC	sc	SOC	sc	SOC
ϵ_2	7.14	4.97	-3.18	-3.30	-1.40	-2.09	-4.07	-4.13	-2.25	-2.52
ϵ_3	7.14	8.18	1.73	1.20	-1.40	-0.89	5.23	4.30	-1.19	-1.04
ϵ_4	7.14	8.18	1.73	2.40	0.28	0.45	5.23	6.15	2.70	2.79

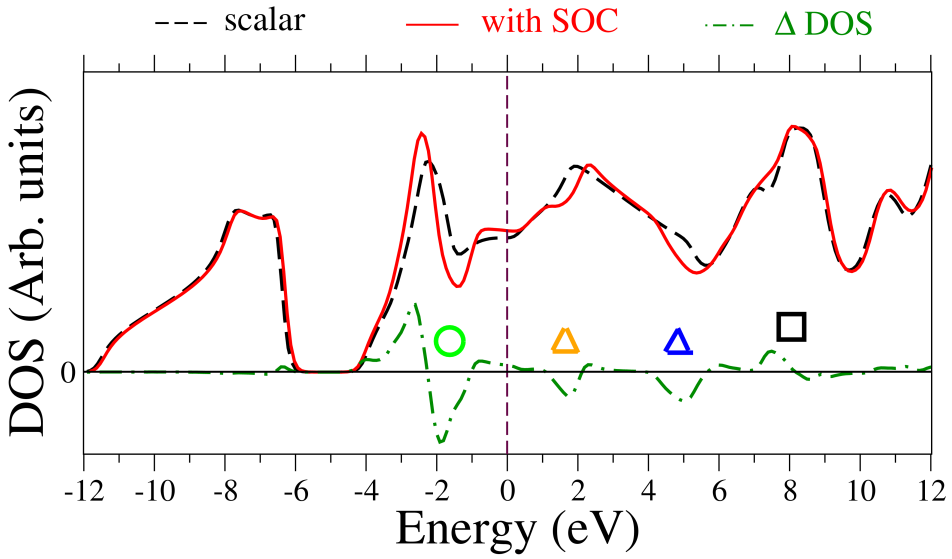

Figure 5.4: DOS obtained in the scalar-relativistic calculation (DOS_{sc}, dashed black line) and the calculation with inclusion of the SOC (DOS_{SOC}, solid red line). The main variations in the DOS upon the SOC inclusion reflected in the differential $\Delta DOS = DOS_{SOC} - DOS_{sc}$ (dashed-dotted green line) are related to different band structure splittings marked by the same symbols as in Fig. 5.3. DOS is in arbitrary units and energy is according to the Fermi level.

In Fig. 5.4 the total density of states (DOS) is plotted as a function of energy. The most important effect of the inclusion of SOC is the appearance of a valley at -1.4 eV and an amplitude increasing of the peak at -2.4 eV, whose position is also slightly shifted to higher binding energies. These variations reflect the disappearance of the band-crossing points. The additional effect of the SOC on the band structure mentioned above - breaking of band degeneracies - has no such important effects on the DOS, because it does not flatten significantly the band dispersion. Nevertheless, the SOC-induced splitting around X, L and Γ points affects remarkably the DOS at ∼1.6 eV, ∼5 eV and ∼8 eV, respectively, as can be seen in Fig. 5.4 (features in ΔDOS marked by symbols, see also Fig. 5.3).

5.2.1 Variational principle approach

Following the recipe outlined in Section 2.7.2 (and developed in detail in Appendix C), SOC was included also in the electronic structure of bulk Pb by means of the variational principle. In Fig. 5.5 we present the comparison of the electronic structure when SOC is taken into account both self-consistently (red lines) and through the variational approach (blue lines). As it is clearly seen, both methods give almost indistinguishable band structures.

This allows one to conclude that the electron density of bulk lead is nearly unaffected by the SOC. A similar conclusion was drawn in Ref. [GMV90] where the influence of SOC in the charge-density of bulk bismuth was found to be negligible in electronic

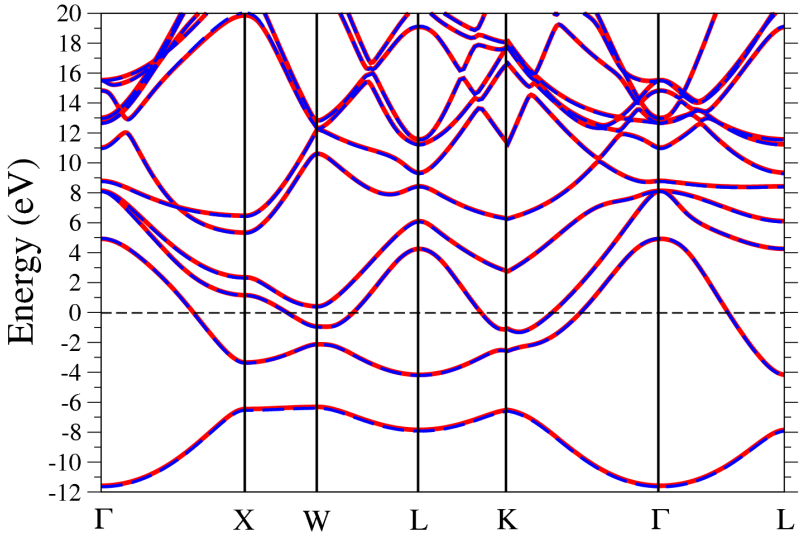

Figure 5.5: Calculated bulk Pb electronic structure including spin-orbit coupling. The red solid lines represent the energy bands obtained solving the SOC-included Hamiltonian self-consistently, whereas the blue dashed set of bands stands for the results obtained including the SOC by means of the variational principle. The horizontal dashed line represents the Fermi level.

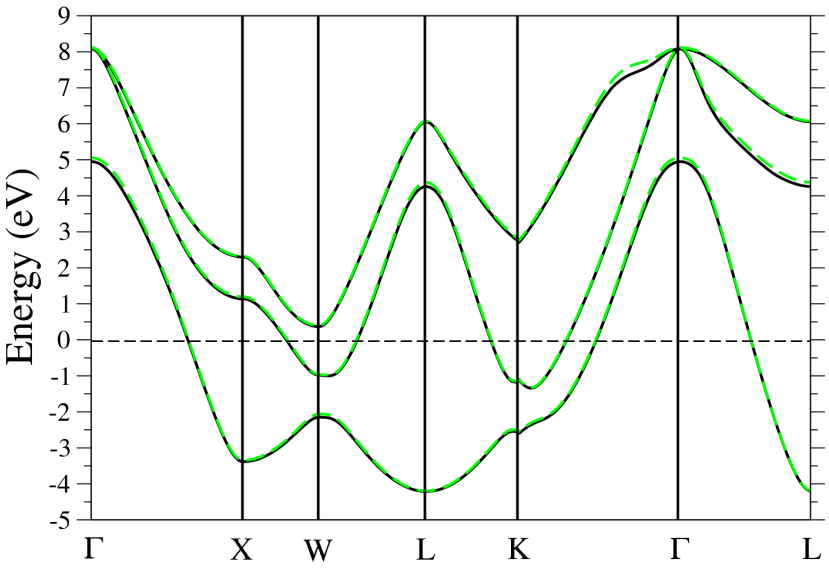

Figure 5.6: Comparison of the p-like bands in Pb bulk when including the SOC using the variational recipe with two different number of states mixed. Black solid (green dashed) lines stand for the energy spectrum obtained including up to 12 (4) bands, thus 24 (8) KS states, in Eq. (2.47). The horizontal dashed line represents the Fermi level.

structure calculations. More generally, the similarity between the band structures obtained using self-consistency and the variational principle as methods to include the SOC in the ground state calculations points to the fact that the contribution of each KS state to the electron density remains unaltered. Notice however that the density matrix [JS94] and more precisely the coupling matrices entering the expressions used in this thesis to calculate the dielectric response and quasiparticle lifetime [see Eqs. (3.19) and (4.22)-(4.23)] could still change significantly upon inclusion of SOC.

Let us now use the advantages offered by the variational principle to get further insight in the way SOC affects the electronic structure of bulk Pb. As it has been explained in Section 2.7.2 the variational approach gives here the possibility of choosing which scalar-relativistic states are "perturbed" by the SOC. In Fig. 5.6 a comparison of the p-like bands in bulk Pb when including the SOC using the variational recipe with two different number of states mixed is shown. Blue (green) lines stand for the band

structure obtained including up to 12 (4) bands, thus 24 (8) KS states, in Eq. (2.47). Clearly, the dispersion of the p states along the high-symmetry directions remains nearly the same when only the first 4 bands are introduced in the variational procedure. Nevertheless, small variations exist between the two different sets of bands plotted in Fig. 5.6, specially around the BZ center (Γ point), showing small but appreciable effects of SOC mixing between p and d states.

As a conclusion, the analysis carried out here applying the variational principle shows that the coupling matrices between different KS states are affected by the SOC, to first order, only for couplings between different p states. In addition, coupling matrices between a p state and other wave functions with a different orbital character could be also influenced by the switching of SOC, as the next correcting term in the "perturbation". Hence, the SOC effects on the calculated elementary excitations are expected to arise mainly from energy splittings (see Fig. 5.3), but also from the spinorial structure of the KS orbitals once the SOC is turned on.

Chapter 6

Low energy dielectric response of bulk Pb

6.1 Introduction

Lead represents a remarkable example of a system where SOC produces strong variations in the band structure (see Chapter 5). Moreover, SOC has a strong impact on the electron-phonon interaction in bulk Pb, increasing its strength as much as 44% [HBYSVC10]. Also, it was demonstrated that the SOC induces sizeable effects in the optical properties in the bulk of heavy elements [RLdB05, SMWRLdB09, GAD10] i.e. in the small momentum transfer limit. As a well known example of SOC effects on optical properties of metals, one can cite that the distinct colour of gold is due to a relativistic lowering of the $6s$ and raising of the $5d$ bands, which strongly affects the onset of absorption.

Even though the effect of the SOC on the electronic structure was investigated in the past very intensively, the inclusion of this interaction in the calculation of dielectric properties from first-principles was performed in counted cases. A detailed study of impact of the SOC on the excitation spectrum of Pb over a whole momentum-energy domain is still missing. Particularly in the low-energy region where the major effect is expected due to modifications in the band structure (see Chapter 5, specially Section 5.2.1). It is interesting to perform such study as the whole picture of a low-energy dynamics in elemental lead may be completed along together with phonon dynamics studied heavily up to now.

For many years the electron-density response of solids was studied using the free-electron gas (FEG) model, that is, the Lindhard dielectric function (see Appendix E) in which the valence electron density is parametrized by a single quantity: the average density parameter r_s [see Eq. (2.15)], which stands for the average inter-electron distance. The Lindhard dielectric function gave insight into basic properties of the momentum- and frequency-dependent dynamical dielectric response. However, band

structure effects that are missing in a FEG model can frequently produce strong impact on the dynamical dielectric response of solids. In particular, interband transitions (not presented in a FEG model) give rise, for instance, to a strong red shift of the Ag plasmon frequency [ACSDRME00] or to a negative momentum dispersion of the plasmon in Cs [AK94]. Additionally, interband peaks dominate the energy-loss in the optical range.

For 3D solids the FEG model predicts the existence of a r_s-dependent threshold for collective excitations, which gives for realistic metallic densities $\omega_p \simeq 3 - 20$ eV (see Appendix E). Hence, according to the FEG theory, plasmons can not participate directly in the low-energy dynamical processes near the Fermi surface. However, in the fifties it was predicted [Pin56, PN58] the existence of an acoustic-like very-low energy excitation, which should be present in systems with two energy bands crossing the Fermi level with different Fermi velocities, v_F, as it is the case of bulk Pb (see Section 3.4.4). Even though this kind of acoustic-like modes has not been demonstrated to exist in bulk metallic systems experimentally so far, recent detailed *ab initio* calculations of the dynamical dielectric response in variety of bulk metallic systems like MgB_2 [MSB-MEVC09,BVCMEMS08], Pd [MSPCMKVC09], and CaC_6 [PEVCMEMS12] predicted, after some initial controversy [PZMSVCME01, KEPTSGE02], the existence of a such kind of acoustic plasmons in metallic systems. In particular, in the case of Pd and CaC_6 this acoustic mode presents a 3D character while in a layered compound MgB_2 the corresponding mode exists only for the momentum transfers along the direction perpendicular to basal planes.

In the FEG model, the plasma frequency is determined as $\omega_p = \sqrt{3r_s^{-3}}$. For lead, using the value of $r_s^{\mathrm{Pb}} = 2.298$ determined on base of experimental data, one obtains $\omega_p^{\mathrm{Pb}} = 13.53$ eV. This value is in good agreement with the one obtained in electron energy-loss experiments (references are given in Ref. [MAWG73]). Thus, the energy transfer range $\omega \leqslant 8$ eV, which is of interest in the present Chapter, is well below the bulk plasmon energy in lead.

Recently the dielectric properties at small momentum transfers over a wide range energy transfer interval and optical properties of Pb were investigated in detail theoretically by *ab initio* calculations and experimentally by reflection electron energy-loss spectroscopy (REELS) [SMWRLdB09,GAD10] Therefore it would be useful to compare those data with the ones obtained by a different calculation method.

The aim of the present study is twofold. First, the complexity of the low-energy dielectric response of bulk Pb is demonstrated, together with the role played by the different physical ingredients. Second, the results on the modes characterized by an acoustic-like dispersion are presented and analyzed in detail. In particular we demonstrate the anisotropic character of such low-energy collective excitations in bulk lead.

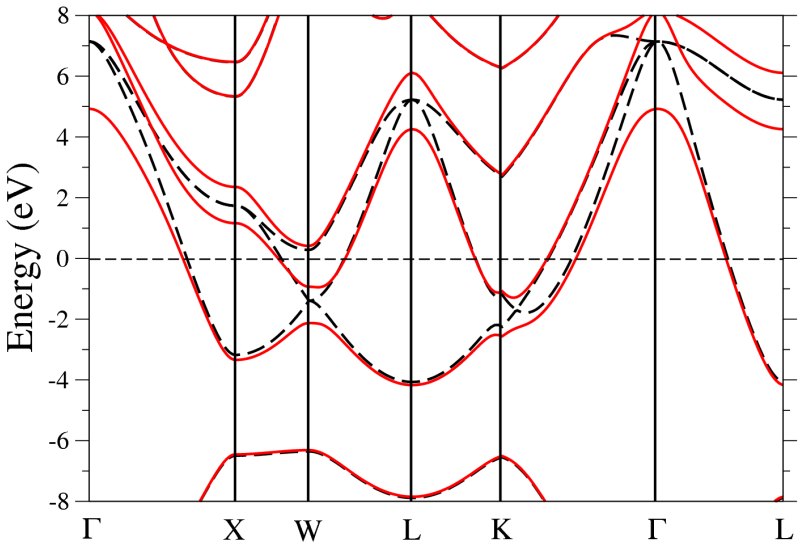

Figure 6.1: Relevant energy range of the band structure of bulk lead, calculated with (solid lines) and without (dashed lines) spin-orbit coupling term in the Hamiltonian. The horizontal dashed line represents the Fermi level set to zero.

6.2 Computational details

Two different sets of calculations were carried out in evaluating Eq. (3.20). First, $S^0_{\mathbf{G},\mathbf{G}'}(\mathbf{q},\omega)$ was calculated in the range $0 < \omega < 30$ eV with a step of $\Delta\omega = 0.005$ eV, the band indexes in Eq. (3.20) running up to $n = 25$. A Monkhorst-Pack 144×144×144 grid of $\mathbf{k}$ vectors was used in the BZ sampling which corresponds to inclusion of ≈ 32000 points in the irreducible part of the BZ (IBZ). The delta function was represented by a modified Gaussian (see Appendix D) of width of 0.05 eV. Second, Eq. (3.20) was evaluated in the $0 < \omega < 4$ eV range, with a step $\Delta\omega = 1$ meV and taking into account up to 12 energy bands. In this second set of calculations a fine 432×432×432 grid was used, with ≈ 850000 $\mathbf{k}$ points in the IBZ, and the width of the modified Gaussian replacing the delta function was set to 2 meV.

When performing the calculations with inclusion of the spinors through Eq. (3.32), in order to maintain the computational load reasonable, a 96×96×96 mesh was used. Also, a 144×144×144 mesh was used for the detailed calculations in the $0 < \omega < 4$ eV energy range. The results retrieved show fine enough structure, see Figs. 6.2-6.3.

Note that by calculating the dielectric response up to 30 eV the present results are well converged with respect to the finite energy range used in the numerical Hilbert transformation procedure.

For completeness in Fig. 6.1 a zoom over the relevant energy range for the results presented in this Chapter of the calculated band structure of bulk fcc lead along some high-symmetry directions of the first BZ is shown.

6.3 Optical range results

Comparison of the calculated energy-loss function with optical experimental data from Ref. [GMPM71] obtained at 140 K and room temperature is performed in Fig. 6.2. The calculated curves correspond to the smallest momentum transfer q=0.009 a.u. along the Γ-X direction, allowing comparison with optical measurements. As can be seen in the figure, the loss function calculated without spin-orbit splitting significantly deviates from both experimental curves. In particular, the first peak in the calculated curve is located at 1.5 eV, i.e. at a notably lower energy in comparison with experiment. Other broad peaks centered at energies of 2.35 eV and 3.4 eV, are also located at lower energies. Only full inclusion of the SOC effects in the band structure leads to a fairly good agreement in energy positions of all three features in this energy range with the experimental ones, specially with the measurements carried out at 140 K. Also our data with full inclusion of the SOC-induced splittings and two-component spinors are in good agreement with other *ab initio* calculation [GAD10].

The strong increase of intensity of the interband peak at ∼1.65 eV in the fully relativistic energy-loss function can be explained by the fact that, as seen in the upper panel of Fig. 6.2, the real part of the dielectric function reaches zero at fairly the same energy due to sharp increase in the corresponding imaginary part of the dielectric function at slightly higher energies. It seems in our calculation this effect is more pronounced than in the calculation of Glantsching and Ambrosch-Draxl [GAD10]. Nevertheless, the evaluated loss functions in both calculations are rather similar in this energy range. Only little difference can be observed at larger energies, where the loss function calculated in Ref. [GAD10] is slightly larger than the one evaluated here. This is explained by the larger imaginary part of the dielectric function on our calculation in the 1.7-2.7 eV energy region.

From the present analysis we can conclude that the experimental optical data reflect clear SOC effects. In order to get further insight in the way the spin-orbit interaction affects the energy-loss of bulk Pb in the optical range, in Fig. 6.3 we present the comparison of the results of the present study for the optical energy-loss function with experimental data obtained at T = 140 K (solid black line) and room temperature (dashed black curve), as published in Ref. [GMPM71]. Comparing the red and green curves the significance of including the two-component spinors in the calculation can be seen. By using the true two-component spinors states, the first dominating peak is slightly blueshifted and, most importantly, the intensity of the energy-loss spectrum for energies $\omega \gtrsim 2$ eV is considerably increased. Both changes visibly improve the agreement with the experimental data measured at T=140 K.

The effects of the inclusion of the spinors on the optics we have demonstrated here is in agreement with the analysis carried out in Section 5.2.1, where it was shown that SOC affects the overlap between different p states (the ones involved in the present energy transfer range), and consequently it should influence the interband transitions which dominate the optical properties ($q \to 0$).

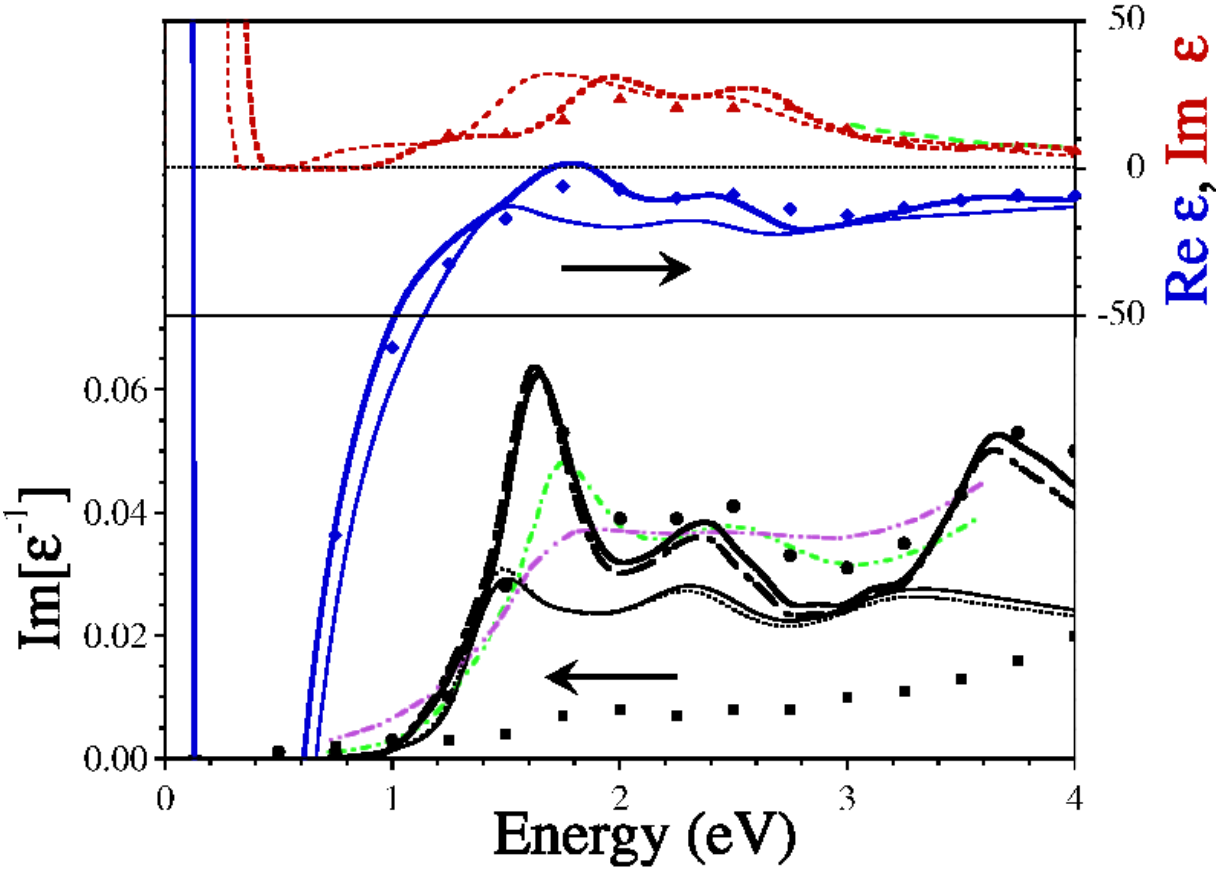

Figure 6.2: (Upper panel) Imaginary (dashed lines) and real (solid lines) parts of dielectric function obtained in the RPA calculations at q=0.014 a.u. along the Γ-X direction. In the lower panel corresponding energy-loss function evaluated with (solid lines) and without (dotted lines) inclusion of the LFEs is shown. Thick (thin) lines present results obtained with (without) inclusion of spin-orbit splitting. Experimental data for loss function from Ref. [GMPM71] measured at 140 K and room temperature are shown by thin green dashed-dotted and violet dashed-dashed-dotted-dotted lines, respectively. Thin long-dashed line in the upper panel shows the measured imaginary part of dielectric function [CLPR73]. Filled triangles, diamonds, and circles present corresponding data obtained in first-principles calculations of Glantschnig and Ambrosch-Draxl [SMWRLdB09,GAD10]. Filled squares show the energy-loss function obtained in the REELS experiment [SMWRLdB09].

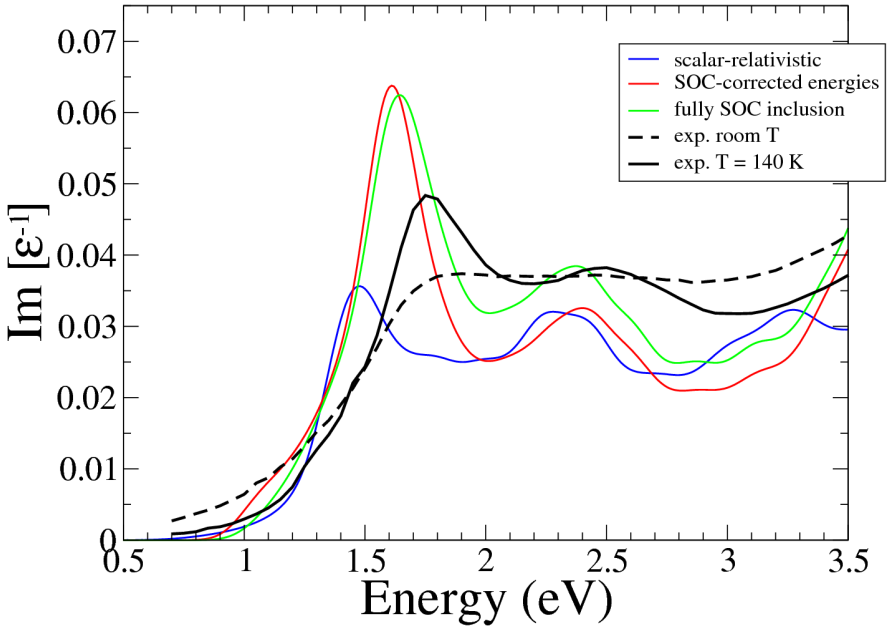

Figure 6.3: Comparison of the results of the present study for the optical energy-loss function with experimental data obtained at T = 140 K (solid black line) and room temperature (dashed black curve), as published in Ref. [GMPM71]. The blue line represents the results calculated at the scalar-relativistic level. The red line shows the energy-loss function obtained including the SOC-induced splittings in the band structure while using the scalar-relativistic wave functions. The green curve represents the results obtained with full SOC inclusion.

Note that in the experimental data of Ref. [GMPM71] the two first lowest energy peaks are barely visible in the room temperature loss spectra and significantly more pronounced in the measurements performed at T=140 K. This is in agreement with the fact that Pb presents a strong electron-phonon coupling, which modifies the one-electron energy levels with increasing temperature. Hence, one can expect that in measurements performed at even lower temperatures, the first interband peak might increase its intensity, decrease its width and downshift in energy, in such a way improving agreement with calculations.

On the other hand, comparison of the calculated data with the recently measured data obtained in reflection electron energy-loss spectroscopy (REELS) [SMWRLdB09] reveals only a broad weak peak around 2 eV in the experimental spectrum and presents significant underestimation in intensity of the whole spectrum. These might be a consequence that this REELS experiment setup might have insufficient resolution in this low-energy range, being apparently more suitable at higher energies [SMWRLdB09].

6.4 General results

In Figs. 6.4-6.6 the energy-loss function, $\mathrm{Im}[\varepsilon^{-1}(\mathbf{q},\omega)]$, calculated using the RPA approximation for the exchange-correlation kernel (see Section 3.2.2) and with full incor-

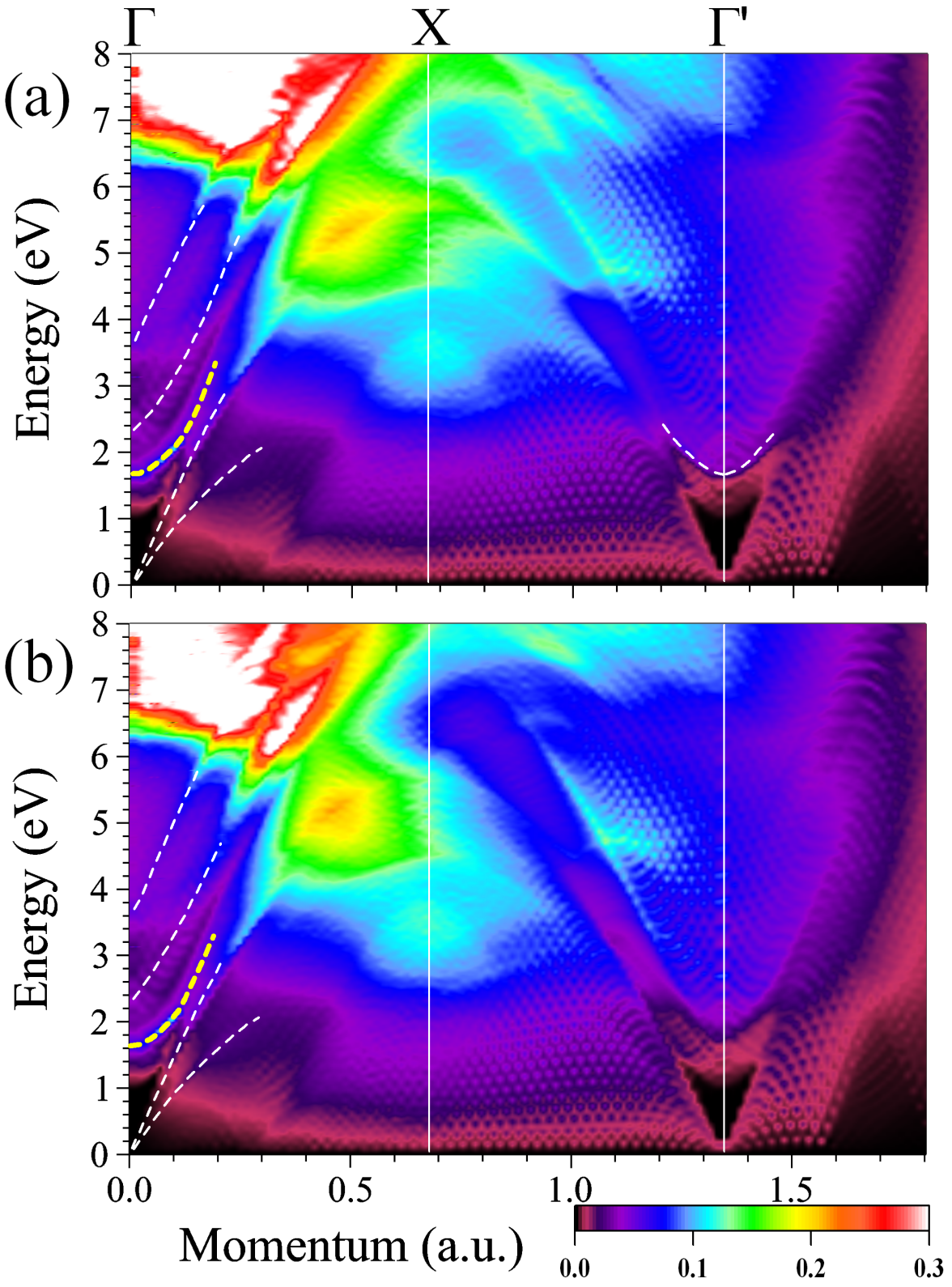

Figure 6.4: Calculated energy-loss function of bulk Pb versus energy ω and momentum transfer q along the Γ-X symmetry direction. Results are obtained with full inclusion of the SOC and the RPA kernel and (a) with and (b) without inclusion of the LFEs. Thick yellow dashed lines highlight dispersion of the plasmon modes. Thin white dashed lines show peaks corresponding to strongly damped modes. Vertical white lines mark positions of the X point and the Γ point in the subsequent BZ.

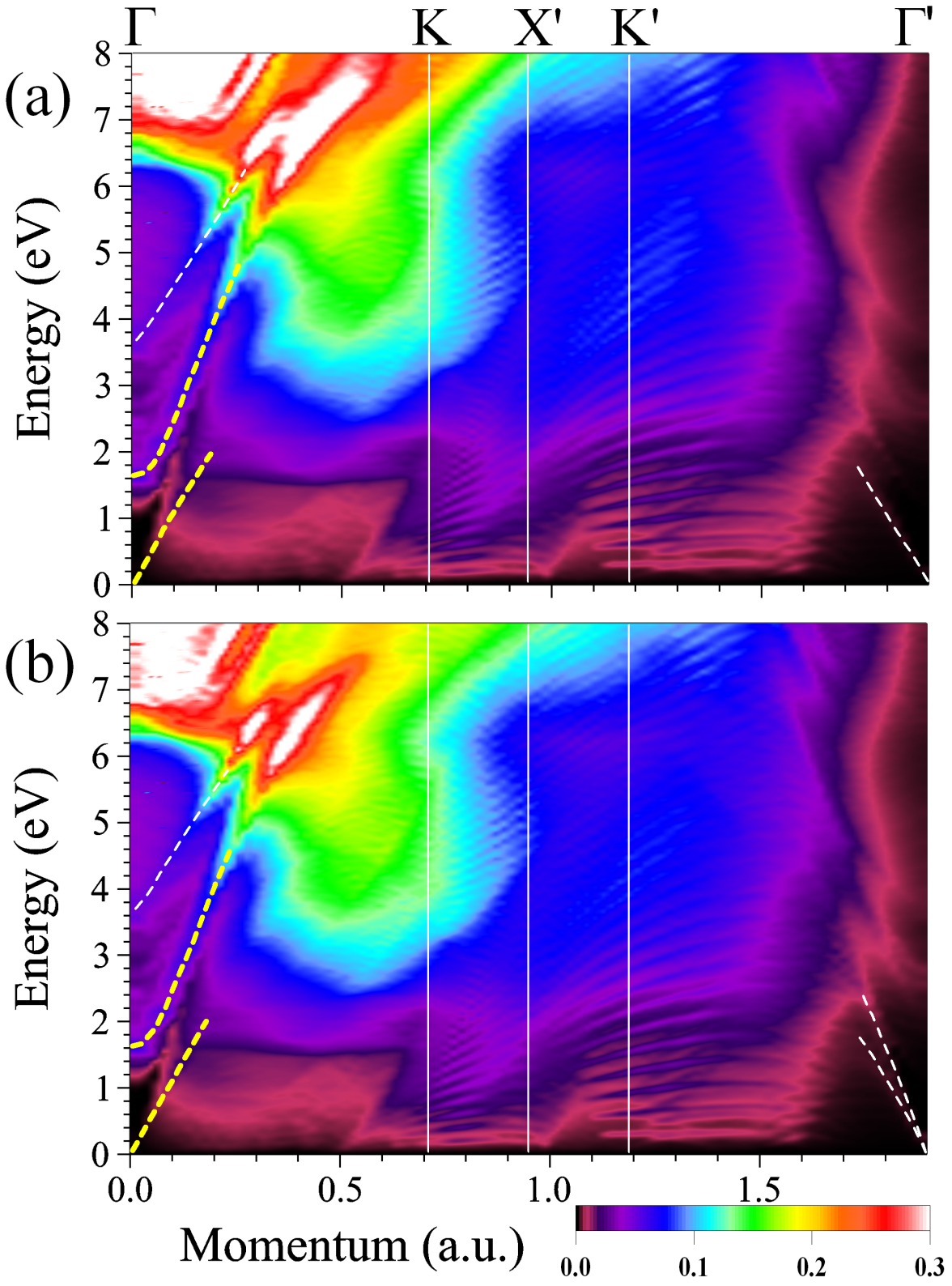

Figure 6.5: Calculated energy-loss function of bulk Pb versus energy ω and momentum transfer q along the Γ-K symmetry direction. Results are obtained with full inclusion of the SOC and the RPA kernel and (a) with and (b) without inclusion of the LFEs. Thick yellow dashed lines highlight dispersion of the plasmon modes. Thin white dashed lines show peaks corresponding to strongly damped modes. Vertical white lines mark positions of the K point and the X, K, and Γ points in the subsequent BZs.

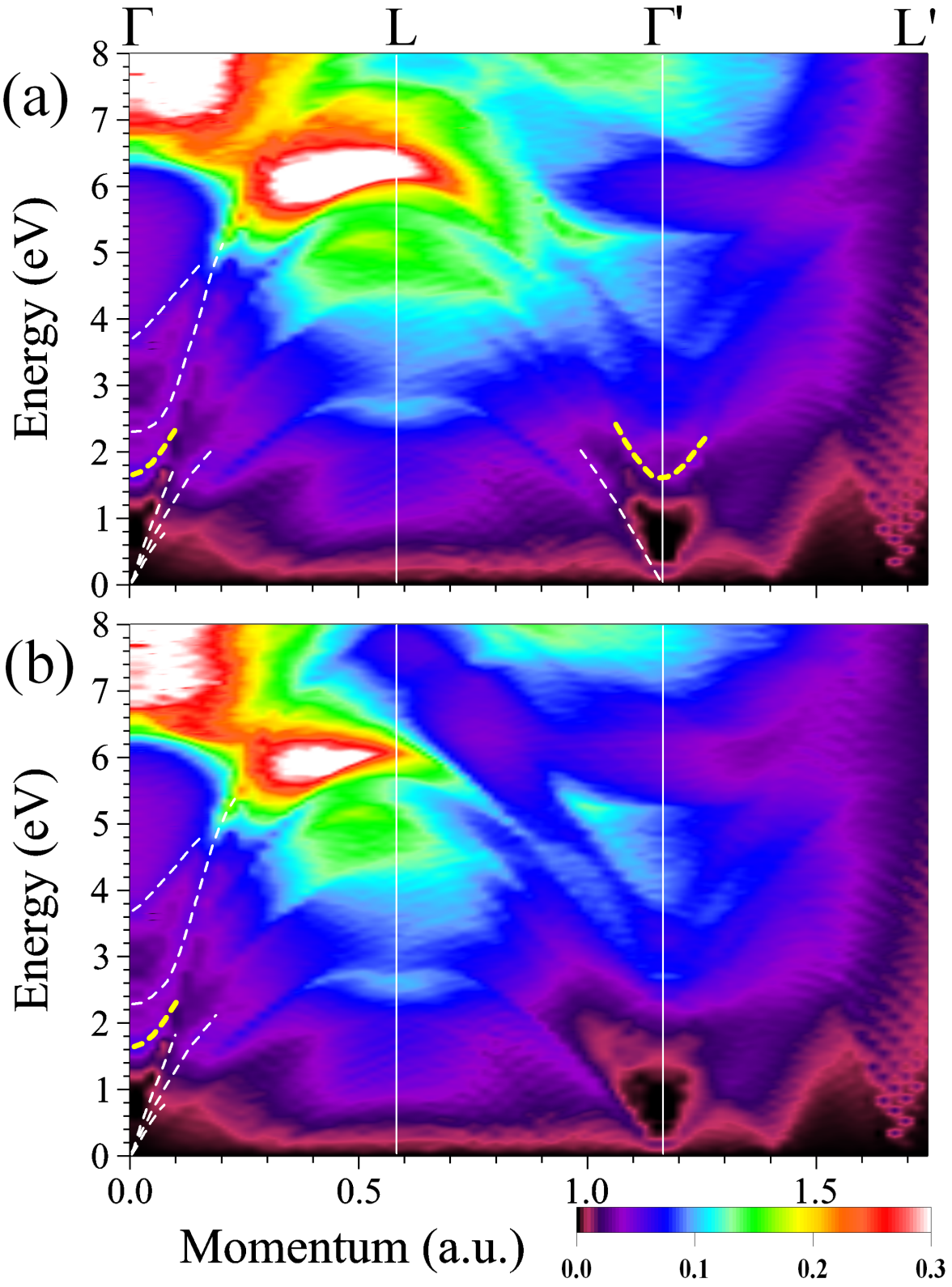

Figure 6.6: Calculated energy-loss function of bulk Pb versus energy ω and momentum transfer q along the Γ-L symmetry direction. Results are obtained with inclusion of the SOC and the RPA kernel and (a) with and (b) without inclusion of the LFEs. Thick yellow dashed lines highlight dispersion of the plasmon modes. Thin white dashed lines show peaks corresponding to strongly damped modes. Vertical white lines mark positions of the L point and the Γ and L points in the subsequent BZs.

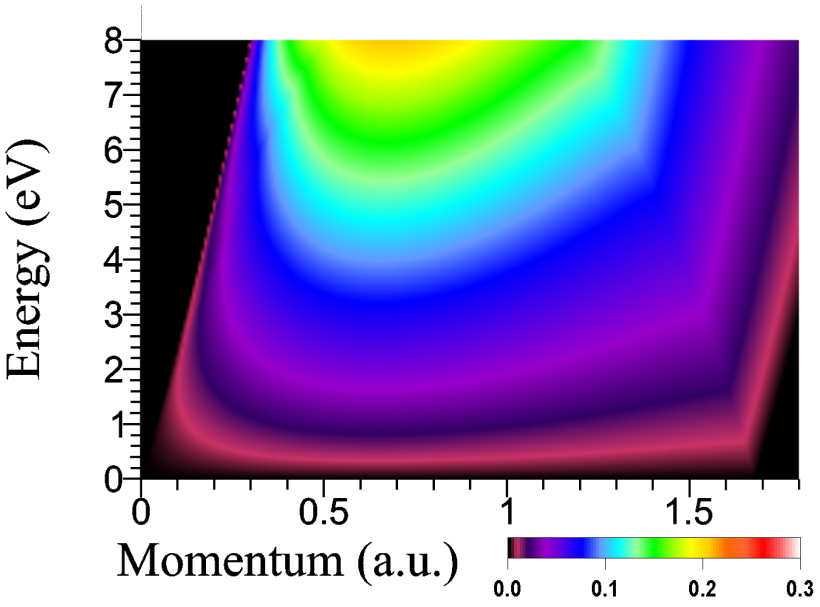

Figure 6.7: Energy-loss function derived from the Lindhard dielectric function (see Appendix E) for the valence electron density of Pb, $r_s^{\mathrm{Pb}} = 2.298$. Plot for approximately the same (ω, q) range and colour code as Figs. 6.4-6.6.

poration of the SOC, is presented as a function of energy transfer ω and the momentum transfer q along three main high-symmetry directions, both including and neglecting the LFEs (see Section 3.3.3). In these figures, at small q's one can observe several peaks in the energy range below the prominent broad peak structure presented at energies above ~ 6.5 eV (which coincides with the energy threshold for interband transitions from the occupied s and unoccupied d states to the p states around the Fermi level). This is in accordance with the DOS depicted in Fig. 5.4, with two prominent peaks raising at energies $|\epsilon - E_F| \gtrsim 6$ eV. Thus, at small q momentum transfer the structure of the DOS is reflected in the energy-loss function through interband transitions.

In Figs. 6.4-6.6 one can see how the peaks in the loss function strongly disperse upwards upon increase of momentum transfer values in all three directions. Thus the dominating 1.65 eV peak (marked by a thick yellow dashed line in Figs. 6.4-6.6) increases its energy up to ~ 7.5 eV at $q = 0.5$ a.u. along the Γ-K direction. The other weaker 2.35 eV (only with q along Γ-X) and 3.7 eV peaks (marked by thin white dashed lines in Figs. 6.4-6.6) disperse almost in a parallel fashion up to energies above 6 eV where they enter the manifold corresponding to s-p interband transitions and can be resolved as separate features up to $\omega = 8$ eV for q in the Γ-X and Γ-K directions. On the other hand, along the Γ-L direction the 1.65 eV possesses much less dispersion and quickly disappears at $\omega = 2.1$ eV. On the contrary, the upper-energy peaks disperse up to 5.5 eV where they merge each other and a much stronger peak continue dispersion up to energies above 6 eV. Starting from $q = 0.6$ a.u. the dispersion of this peak turns from positive to negative and it can be clearly resolved up to $q \sim 1$ a.u.

Note the highly anisotropic character of the dielectric response of bulk Pb, with the energy-loss function presenting a qualitatively different structure for the momentum transfer in the Γ-K high-symmetry direction in the $\omega \lesssim 3$ eV energy transfer range (see also Section 7.4). The anisotropy of $\mathrm{Im}[\varepsilon^{-1}]$ can be readily checked below in Fig. 6.10.

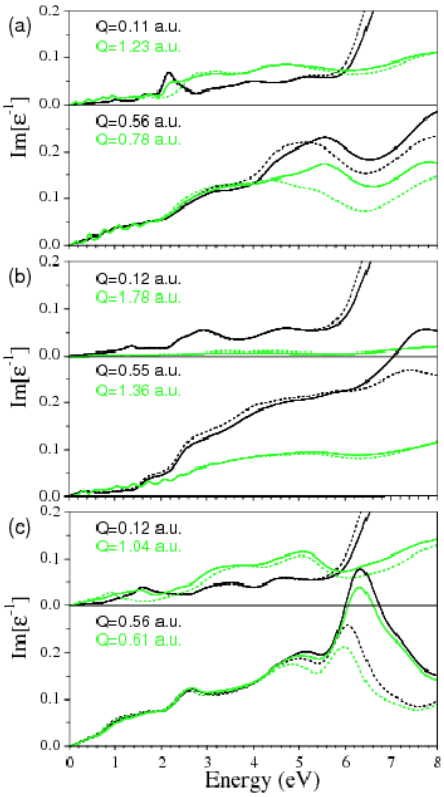

Figure 6.8: Calculated energy-loss function at some fixed momentum transfers q's as a function of energy. Calculations were performed with full inclusion of the SOC in the bandstructure and at the RPA level. Solid (dashed) lines are obtained with (without) inclusion of LFEs. The data at $\mathbf{q}$'s along Γ-X, Γ-K, and Γ-L symmetry directions are presented in (a), (b), and (c), respectively.

In order to further clarify the key role of the band structure in the density response of bulk lead, in Fig. 6.7 the energy-loss function of a FEG presenting the bulk lead valence electron density is plotted for approximately the same (ω, q) range and colour code as Figs. 6.4-6.6. As readily seen, the FEG model gives a completely wrong picture in which the interband transitions are missing (no optics). There is no dispersing feature in Fig. 6.7 and the complex and anisotropic character of the energy-loss function shown in Figs. 6.4-6.6 is entirely absent. Notice also the absence of any acoustic mode (see Section 6.6).

Below we present a systematic analysis of the effect of the main physical ingredients like LFEs and xc effects on the low-energy electronic collective excitations in bulk Pb.

6.4.1 Local-field effects

From comparison of the upper and lower panels in Figs. 6.4-6.6 one can deduce that the LFEs affect the calculated dielectric properties rather weakly. From Figs. 6.2 and 6.8 it is seen that this effect is barely visible at small momentum transfers. Along the Γ-X, Γ-K and Γ-L directions the main result of the LFEs in the formation of the excitation spectra in Pb is some distortion of the intensity of the aforementioned peaks at the finite momentum transfers. At energies above $\omega \sim 6$ eV the LFEs produce significant increases in the intensity of the dominant peaks.

Additionally the LFEs produce an upward shift in energy of all the features. However the effect is not very pronounced and in general do not exceed several tenths of eV. Thus in Fig. 6.8 one can see that the major upward shift about 0.3-0.4 eV occurs in the case of the $\sim$ 6 eV feature at intermediate momentum transfers along the Γ-L direction.

Another consequence of inclusion of the LFEs is the transmission of the 1.65 eV peak at small q's to momentum transfers close to $q = 2\pi/a = 1.35$ a.u. in the Γ-X direction. At momentum transfers close to this q one can see how the intensity of the loss function at $\omega \approx 1.65$ eV notably increases when the LFEs are included. At $q = 1.23$ a.u. the corresponding increasing in the loss function at $\omega \approx 2.25$ eV due to LFEs can be seen in Fig. 6.8(a). Also some increase in the loss function caused by the LFEs due to the $\omega = 1.65$ eV mode can be detected in the vicinity of $q = 1.16$ a.u. along the Γ-L direction. The example of this enhancement can be seen in Fig. 6.8(c), where a broad feature in the loss function appears at energies around 1.6 eV at $q = 1.04$ a.u. when the LFEs are taken into account.

However, in general, the impact of the LFEs on the loss spectra in Pb, being quite notable at certain energies, is not so strong as in other systems like in MgB_2 [MSB-MEVC09] and compressed lithium [ERPR$^+$10]. This signals about a less inhomogeneity in the valence charge density in Pb in comparison with these systems, as expected.

6.4.2 *xc* kernel

In Fig. 6.9, the calculated energy-loss function for several values of $\mathbf{q}$ belonging to the three different high-symmetry directions is plotted, where comparison between results obtained with the RPA and the TDLDA kernels is made. As can be seen in the figure, the main effect of the TDLDA with respect to the RPA is the increase of the intensity of the calculated $\mathrm{Im}\,[\varepsilon^{-1}(\mathbf{q},\omega)]$, but without qualitative changes in its shape. The most significant change is seen in Fig. 6.9(c) at energies between 6 and 7 eV in the Γ-L direction, where the dominant interband peak is downward shifted in energy by $\sim$0.1 eV upon inclusion of the *xc* effects at the TDLDA level.

6.5 SOC effects

Full inclusion of the SOC in the ground state affects the dielectric response of bulk Pb in an anisotropic way. In all three high-symmetry directions the SOC lowers the intensity of the broad feature located at energies above 6 eV at momentum transfer $q \lesssim 0.2$ a.u. As was previously discussed, inclusion of the SOC in the calculation of the energy-loss function has sizeable effects at small momentum transfers at energies of 1.65 eV, 2.35 eV, and 3.7 eV. The impact of the SOC on the excitation spectra can also be observed in Fig. 6.11. At $q = 0.11$ a.u. along the Γ-X the appearance of the

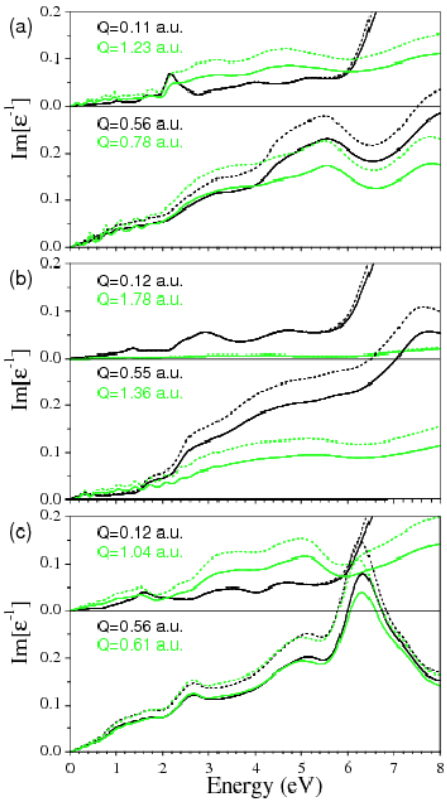

Figure 6.9: Solid lines represent the same as in Fig. 6.8, while the dashed lines show the energy-loss function evaluated at the corresponding **q**'s at the TDLDA level, also with full inclusion of SOC and LFE.

clear peak at 2.15 eV and two broad peaks at $\omega = 4.0$ eV and $\omega = 5.2$ eV caused by the SOC can be noticed. At larger q's the effect is smaller and consist mainly in the upward shift of the existing peaks. The same trend is observed in the Γ-K and Γ-L directions as well, although with less impact at intermediate and large momentum transfers. Additionally, In Fig. 6.11 one can detect that at small q's in the low-energy region the inclusion of the SOC leads to appearance of a pronounced peak. Thus at $q = 0.11$ a.u. along the Γ-X direction it is located at $\omega = 1$ eV, whereas at $q = 0.12$ a. u. the corresponding peak it is present at $\omega = 1.15$ eV and $\omega = 1.6$ eV along the Γ-K and Γ-L directions, respectively. The dispersion of these peaks is highlighted in Figs. 6.4-6.6 and discussed in the next section.

Another question is how important the inclusion of the two-component spinors is in the calculations of the dielectric properties of bulk lead. That is, which is the effect of using Eq. (3.20) instead of Eq. (3.32) once the energy spectrum has been evaluated with the SOC included. To clarify this point we plot in Fig. 6.10 the results obtained in the present thesis for the energy-loss function of bulk Pb up to 8 eV energy transfer and with the momentum transfer in three high-symmetry directions (all data calculated with LFE and TDLDA kernel inclusion). Three different levels of SOC inclusion are shown. Comparing the central and lower rows we conclude that the inclusion of the two-component spinors in the calculations leaves $\mathrm{Im}[\varepsilon^{-1}]$ qualitatively unchanged, with only small quantitative effects for the big-momentum transfer range in Γ-X and Γ-L.

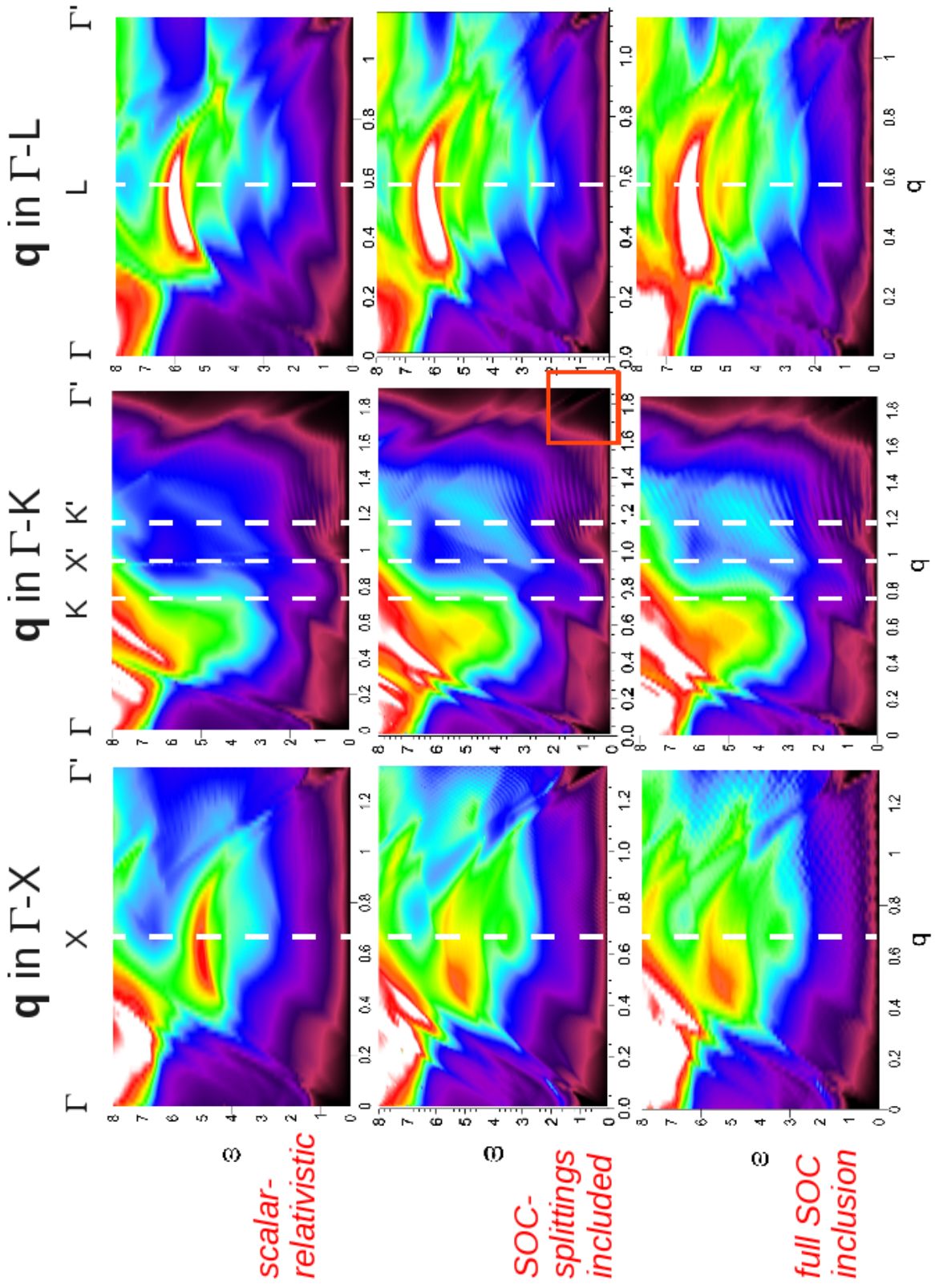

Figure 6.10: Comparison of the bulk Pb energy-loss function obtained up to 8 eV energy transfer and with the momentum transfer in three high-symmetry directions (all data calculated with LFE and TDLDA kernel inclusion). Three different levels of SOC inclusion are shown. Concerning the orange square in the central panel, see Section 6.6.

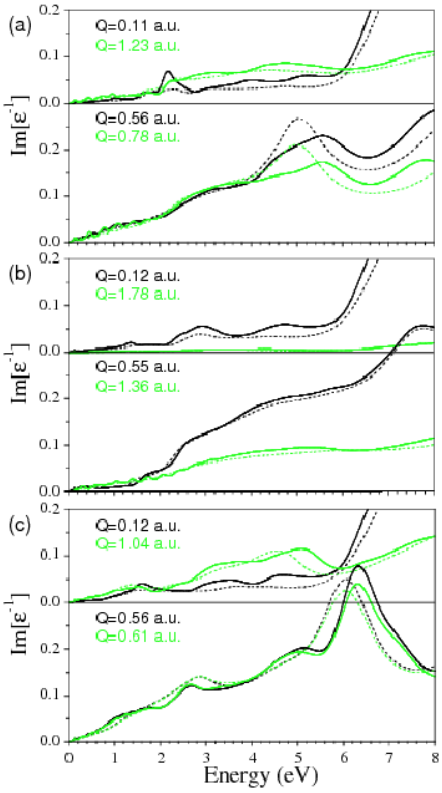

Figure 6.11: Solid lines represent the same as in Fig. 6.8, while the dashed lines show the energy-loss function evaluated at the corresponding **q**'s without inclusion of SOC, also at the RPA level and incorporating the LFE.

6.6 Acoustic-like excitations

In the "low momentum–low energy" region of Figs. 6.4-6.6 the calculated loss function presents several peaks dispersing almost linearly with momentum, i.e, with vanishing energy transfer at vanishing momentum transfer. Upon momentum transfer increase these peaks can be traced up to an energy of about 2 eV in Γ-K and Γ-L, and up to even higher energy in Γ-X. The number of such peaks depend on the direction, being two in the case of Γ-X, one in Γ-K, and three along Γ-L (in the scale of Figs. 6.4-6.6). To study in more detail the origin of these modes characterized by an acoustic-like dispersion, in Figs. 6.12-6.14 we report the calculated dielectric and energy-loss functions at small momentum transfers in all three directions. The red, blue, black and green curves correspond to the results obtained at the scalar-relativistic level, including the SOC-induced energy splittings, with full inclusion of the SOC and to the Lindhard dielectric function for $r_s^{\mathrm{Pb}} = 2.298$, respectively. All curves were obtained for $q \simeq 0.027$ and with inclusion of LFE and the TDLDA kernel, even though these two physical ingredients were found to affect negligibly the results in all cases.

In Fig. 6.12 one can observe three clear peaks in the loss function, whose shape and intensity depends on wheter SOC is included or excluded from the calcution. From the analysis of the real part of the dielectric function we conclude that neither of these peaks can be considered as a true plasmon mode as the real part of ε does not cross

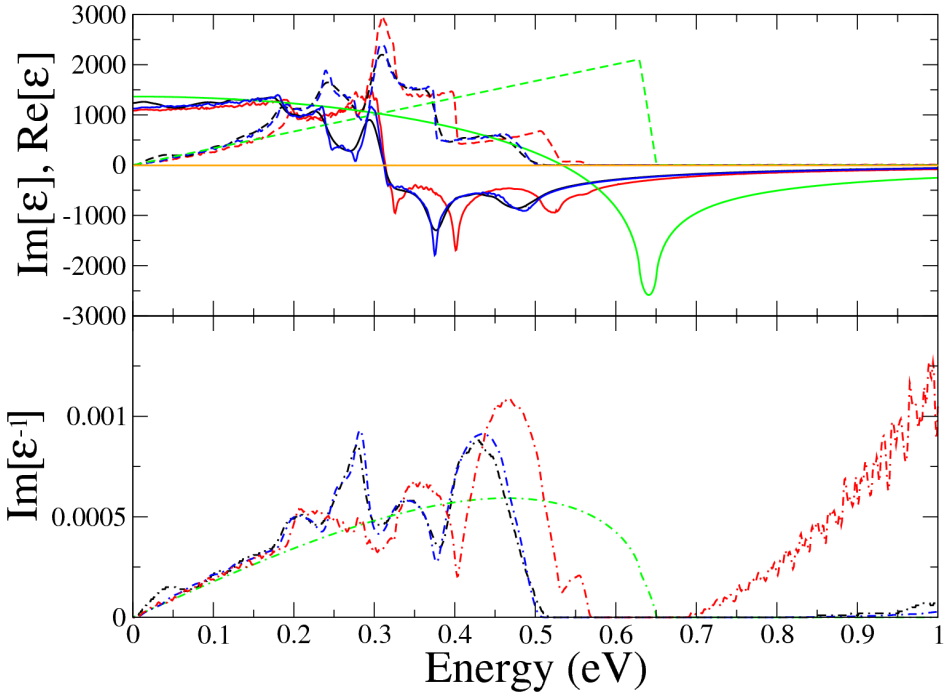

Figure 6.12: Calculated dielectric and energy-loss functions for $q \simeq 0.027$ a.u. in the Γ-X direction. Red, blue, black and green curves correspond to the results obtained at the scalar-relativistic level, including the SOC-induced energy splittings, with full inclusion of the SOC and to the Lindhard dielectric function for $r_s^{\mathrm{Pb}} = 2.298$, respectively. In the upper panel the solid (dashed) lines stand for the real (imaginary) part of ε.

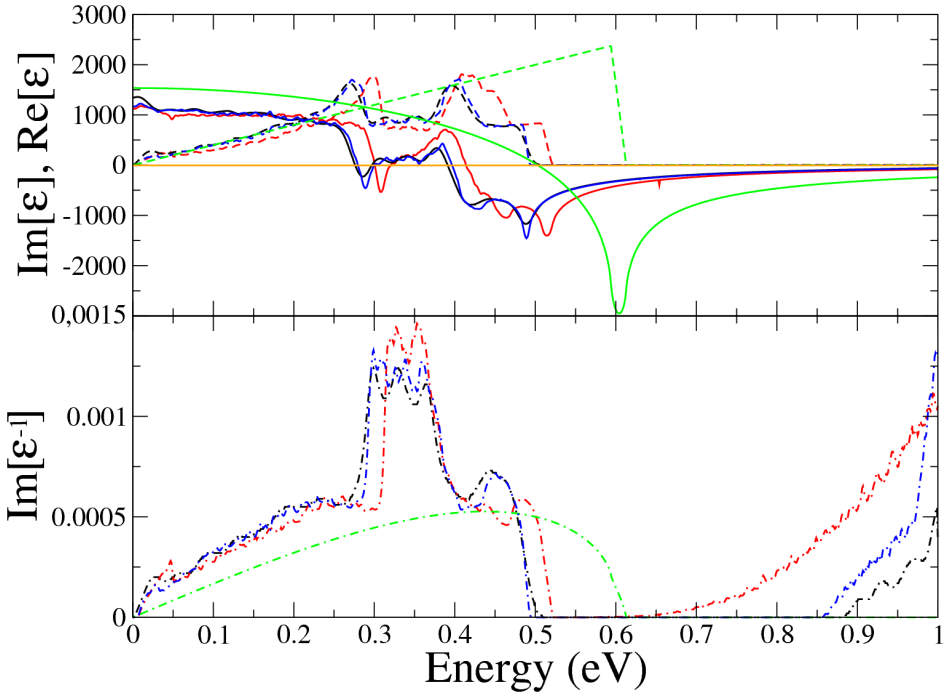

Figure 6.13: Same as Fig. 6.12 but for **q** in the Γ-K direction.

zero at the corresponding energies. The only zero-crossing in Re[ε] occurs at 0.32 eV close to the energy where Im[ε] has a maximum. As a result, at this energy the loss function presents a local minimum. Therefore this zero-crossing must be considered as a conventional Landau-overdamped mode which can not be realized [PN66]. At the same time inspection of Fig. 6.12 shows that the peaks present in the energy-loss function are located at energies where the Im[ε] possesses local minima. Hence, despite rather large values of the Re[ε] at corresponding energies these peaks can be considered as heavily damped acoustic plasmons. Compare with FEG model, where a zero-crossing of Re[ε] does not produce any peak in the loss function due to the peak in Im[ε].

The presence of peaks in the loss function is explained by the presence of a similar number of peaks in Im[ε]. These peaks are due to intraband excitations within the energy bands crossing the Fermi level. Although all these bands are of the same p-like character, their dispersion with different Fermi-velocity components in this symmetry direction is reflected in the presence of several peaks in Im[ε].

Concerning the Γ-K direction, the loss function presented in Fig. 6.13 shows a broad main peak which is centered at ∼0.35 eV when SOC is included in the calculations. Moreover, one can see that Re[ε] is rather small at that energy and even crosses zero at 0.30 eV with positive slope, when SOC is included in the calculations. This signals that this peak corresponds to a true plasmon mode, although severely damped due to decay into electron-hole pairs. The presence of this peak in Im[ε^{-1}] can be explained by the presence of two clear main peaks in Im[ε] at 0.26 eV and 0.40 eV, again when

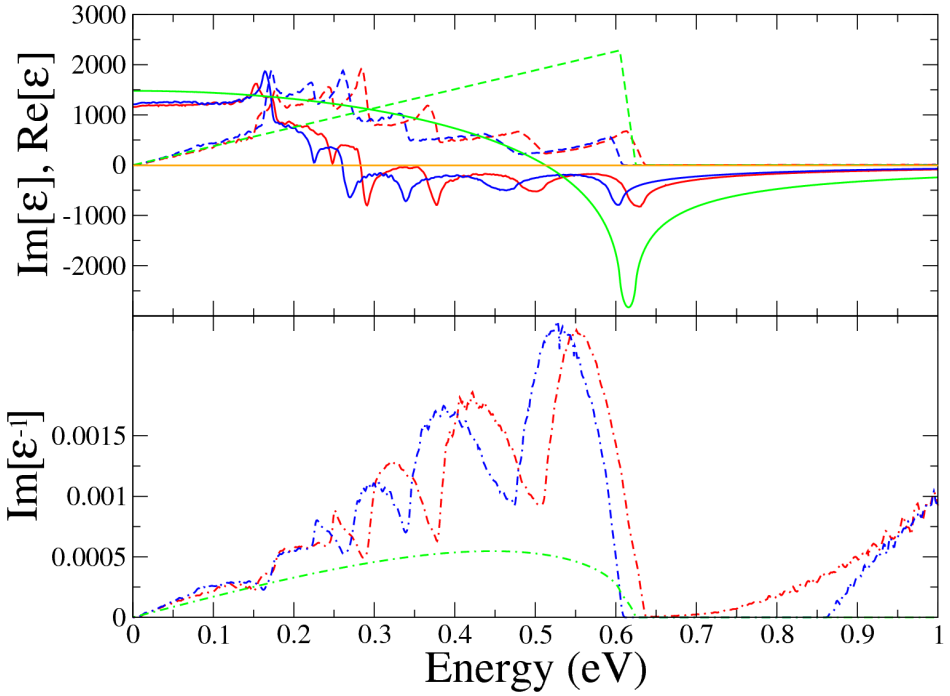

Figure 6.14: Same as Fig. 6.12 but for **q** in the Γ-K direction. Note the results obtained with full inclusion of SOC are missing (see text).

SOC is included in the calculations. This makes the real part of the dielectric function cross zero three times, the second one with positive slope leading to the appearance of the peak in the loss function. Again, as in the Γ-X direction, in the scalar-relativistic case all the peaks in Im[ε] and Im[ε^{-1}] are located at higher energies.

At momentum transfers along the Γ-L direction the number of peaks in the loss function is maximal. As an example, in Fig. 6.14 one can detect up to three peaks in Im[ε^{-1}] at energies of 0.30 eV, 0.39 eV, and 0.53 eV. Their dispersion is shown in Fig. 6.6. The presence of such large number of peaks in Im[ε^{-1}] can be again explained by a large number of peaks in Im[ε] seen in Fig. 6.14 (up to five). However, neither of this peak leads to an additional zero-crossing in Re[ε]. For this reason, al these peaks are can be considered as heavily damped plasmonic mode. Similar to what occurs in other symmetry directions the effect of inclusion of SOC is limited to the downward shift of these modes without qualitative changes. Note the results retrieved with full inclusion of SOC are missing in Fig. 6.14 as a consequence of the mismatch of the different momentum transfer meshes used at the different levels of SOC inclusion (see Section 6.2). However, based on the results obtained for Γ-X and Γ-K (compare blue and black lines in Figs.6.12 and 6.13) no change upon inclusion of the two-component spinors is expected.

In the calculation at the scalar-relativistic level we obtain that the upper border for the intraband e-h transitions is located at the higher energies than when SOC is included. This is explained by modifications in the energy bands around the Fermi

surface. The main effect of the inclusion of SOC is the flattening of the band dispersion accompanying the opening energy gaps seen in Fig. 6.1. Consequently, this causes modifications of intraband excitations reflected in the integrated form through Eq. (3.20) in Im[ε]. Regarding the shape of the acoustic-like dispersing modes, SOC only slighlty affects ε for $\mathbf{q}$ in Γ-X, where it gives rise to a new peak (which is located at $\omega \simeq 0.27$ eV in Fig. 6.12).

Notice from Figs. 6.12-6.13 that inclusion of the two-component spinors leaves the results unaffected with respesct to only correcting the band energies by the SOC splittings (in Fig. 6.14 the data obtained with full inclusion of SOC are missing because of unmatched $|\mathbf{q}|$ values of the different momentum transfer grids use, see Section 6.2). Note that the analysis of the SOC effects on the KS states carried in Section 5.2.1, where it was concluded that the contribution of a KS state to the electron density in bulk Pb remains the same upon SOC inclusion, pointed in the same direction.

6.6.1 Group velocities: comparison with v_F

Concerning the group velocities v_g of the acoustic modes, the values are dependent on the momentum transfer direction as readily seen from the slopes of the corresponding lines in Figs. 6.4-6.6, thus showing anisotropy as a result of band structure effects. More precisely, the group velocities present values of 0.33 and 0.41 a.u. in the Γ-X direction, 0.41 a.u. in Γ-K, and 0.40, 0.51 and 0.71 a.u. in Γ-L. The velocity atomic unit is 2.1877×10^6 m/s. All the reported velocities are lower than the Fermi velocity derived from the FEG model [WADM76] of $v_F^{FEG} = 0.84$ a.u. On the other hand, all the estimated v_g are higher than the experimental value of $v_F^{exp} = 0.23$ a.u. [BRS61] obtained in skin depth measurements.

Note the estimated group velocities of the acoustic modes can not be simply assigned to the Fermi velocities of the bands crossing the Fermi surface on a fixed reciprocal space point in the calculated band structure. As an example, comparison of the above reported values of v_g with the Fermi velocities of the bands in the high-symmetry directions (see Fig. 6.1) of 0.60 a.u. (Γ-X), 0.47 and 0.54 a.u. (Γ-K) and 0.84 a.u. (Γ-L) shows clear deviations between the calculated v_F and v_g values. In all cases $v_F > v_g$. This is as expected, since collective electronic excitations can not be built faster than the velocity of the individual electrons. Thus, in each $\mathbf{q}$ direction, the maximum v_F can be seen as the upper bound for the group velocities of the acoustic modes.

Notice that the modified Gaussian used to model the Dirac delta which ensures energy conservation in Eq. 3.19 (see Appendix D) affects negligibly the group velocities reported here, as the acoustic modes preserve their character up to energies ~ 2 eV.

As a conclusion, let us emphasize the relevance of the acoustic modes present in the results of our calculations. In Figs. 6.4-6.6 comparing our first-principles energy-loss function with the one derived from the Lindhard dielectric function, it is readily seen that the accurate inclusion of the band structure provides to the FEG structureless

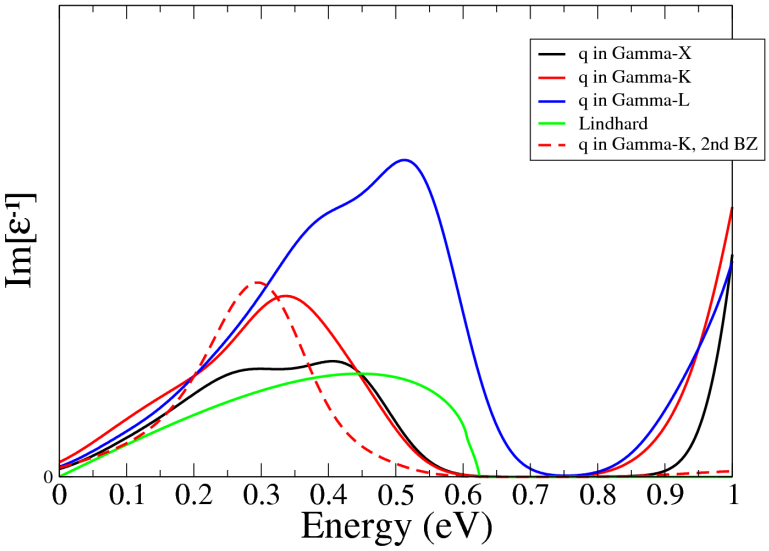

Figure 6.15: Comparison of the energy-loss function for the acoustic dispersing peaks for a momentum transfer of $q = |\mathbf{q}| \simeq 0.027$ a.u. in all three high-symmetry directions, together with the loss function derived from the Lindhard dielectric function (see Appendix E) at the same q. First-principles results are broadened with a broadening parameter of 75 meV (see text).

intraband peak a complex shape. Some of the raising acoustic modes can be clearly identified even after a 75 meV broadening is applied (see Fig. 6.15). Thus, we predict that this modes exhibit a well defined dispersion relation, which is crucial as it shows the collective nature of the acoustic plasmons. The fact that these features exhibit a well defined energy for a given momentum transfer means they represent well defined coherent oscillations of the electron density in bulk lead, even at $\omega \to 0$.

6.6.2 Possibility of detection in EELS experiments

In order to evaluate the possibility of experimental detection of the aforementioned acoustic modes, in Fig. 6.15 a comparison of the energy-loss function for the acoustic dispersing peaks for a momentum transfer of $q = |\mathbf{q}| \simeq 0.027$ a.u. in all three high-symmetry directions, together with the loss function derived from the Lindhard dielectric function (see Appendix E) at the same q. Also the acoustic-like plasmon mode is shown for $\mathbf{q}$ in the second BZ in the Γ-K direction as a dashed red curve, corresponding to the peak marked by the orange square in the central panel of Fig. 6.10. A Gaussian broadening has been applied to the first-principles results. The broadening parameter was fixed as 75 meV corresponding to the experimentally measured linewidth of quantum-well states in Pb(111) thin films [HBP+09] at T = 5 K. The intensity of the acoustic mode peak is maximal in the Γ-L direction. However, from Fig. 6.15 we conclude that the most suitable acoustic plasmon for experimental detection corresponds to the peak dispersing in the second BZ in the Γ-K direction. It presents the smaller linewidth once the broadening is applied, and more importantly it is located in a (q, ω) range in which the energy-loss function presents vanishing values except for the acoustic mode itself, getting isolated this way (see Figs. 6.10 and 6.15). Note also that the presence of the factor q^{-2} in Eq. (3.38) makes weak features in the low-momentum transfer range more difficult to be resolved in EELS experiments.

However, an additional possibility of detecting an acoustic plasmon in bulk Pb is suggested based on the general results obtained for the momentum transfer along the Γ-X direction. As seen from Fig. 6.4, the fastest dispersing acoustic mode reaches an energy of ∼5 eV at $q \simeq 0.45$ a.u., gradually increasing its intensity. Thus, once the peak at ∼5 eV and $q \simeq 0.45$ a.u. would be detected, one could think of tracing back its dispersion towards vanishing energy and momentum transfer values.

6.7 Summary

We have presented first-principles calculations of the low-energy ($\omega \leqslant 8$ eV) electronic collective excitations in bulk Pb and studied in detail the effect of the main physical ingredients involved, as well as the existence and character of acoustic-like modes. Good agreement with available optical experimental data [GMPM71] is interpreted as an evidence of remarkable SOC effects, also in agreement with other theoretical works [SMWRLdB09, GAD10].

In general, strong anisotropic effects are found, results showing a distinct topology of $\mathrm{Im}[\varepsilon^{-1}_{\mathbf{G},\mathbf{G}}(\mathbf{q},\omega)]$ for $\mathbf{q} \in$ Γ-K. LFE and SOC have sizeable effects on the dielectric screening of bulk Pb, showing an anisotropic behavior. For $\mathbf{q}$ vectors in the second BZ, LFE on the energy-loss function are remarkable. Inclusion of exchange-correlation effects through the TDLDA kernel increases the intensity of the energy-loss function in the studied range, however without affecting its shape in a significant way.

Very-low energy modes with acoustic-like dispersions are found in all three studied high-symmetry directions and are shown to be a consequence of band structure effects. The character of these acoustic modes depends on the direction of $\mathbf{q}$. The possibility of experimental check of the existence of these acoustic modes by electron energy-loss measurements seems feasible as these modes keep their character up to $\omega \simeq 2$ eV. As a result of a detailed analysis, the acoustic plasmon along Γ-K in the second BZ is suggested as the most suitable for its experimental detection.

Chapter 7

High energy dielectric response of bulk Pb

7.1 Introduction: something is missing

In the present Chapter we report on the calculations of bulk Pb dielectric and energy-loss functions obtained up to energy transfer values of 30 eV.

As seen in Fig. 7.1, a value higher the experimental one of the bulk plasmon energy for small momentum transfer is found at all levels of inclusion of the SOC. The disagreement with the experimental data is independent of the xc kernel used and of incorporation of LFE. As shown in Fig. 7.1, the values of $\omega_p(q \to 0)$ obtained is roughly ~ 1.5 (~ 2.5) eV higher than the EELS data of Ref. [JP60] (green thick line) when SOC is excluded from (included in) the calculations. This seems surprising as Pb is a simple elemental metal, whose experimental bulk plasmon frequency is well reproduced

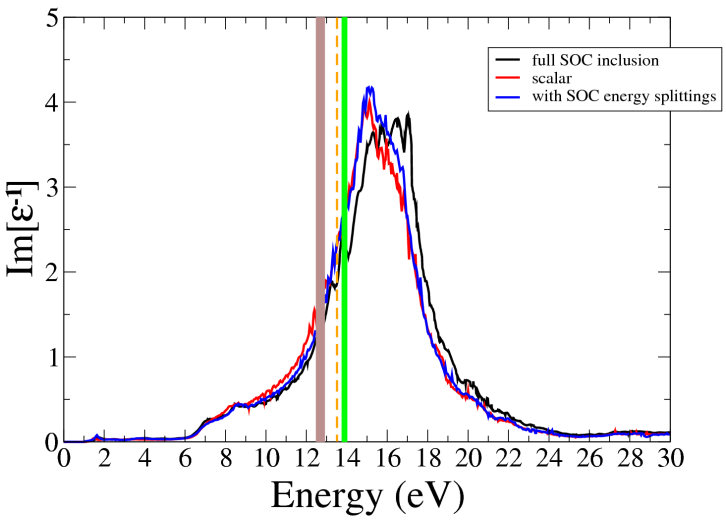

Figure 7.1: Energy-loss function for $q \to 0$ calculated without inclusion of the semicore electrons at the scalar-relativistic level (red curve), including the SOC-induced energy splittings (blue curve) and with full inclusion of SOC (black curve). The vertical dashed line represents the FEG plasmon energy of $\omega_p^{\mathrm{Pb}} \simeq 13.5$ eV, while green and brown thick lines mark the EELS and optical experimental data from Ref. [JP60] and Ref. [MAWG73], respectively.

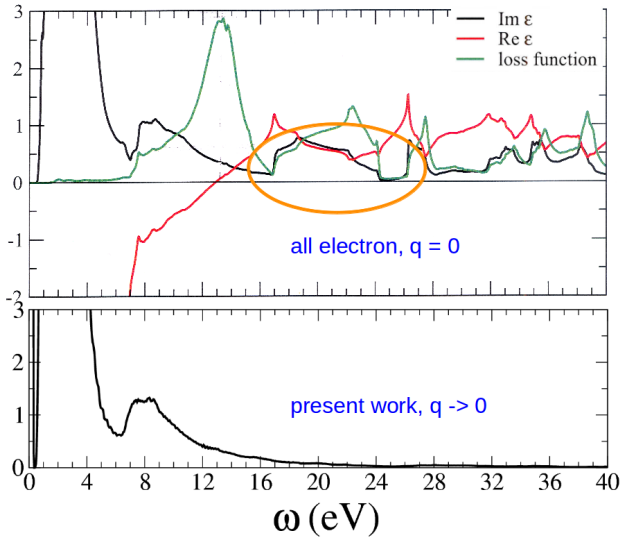

Figure 7.2: Upper panel: optical ($q = 0$) dielectric and energy-loss functions calculated by an all-electron method at the scalar-relativistic level. The orange ellipse marks the important transitions missing in the results shown in the lower panel. Lower panel: the present results for the energy-loss function with $q \to 0$ with the $5d$ electrons in the core, also at the scalar-relativistic level. All-electron calculation courtesy of Prof. Krasovskii.

by simply applying the expression $\omega_p = \sqrt{3r_s^{-3}}$ derived from classical electrodynamics (see Section 3.4.1), which gives a value of $\omega_p^{\mathrm{Pb}} \simeq 13.5$ eV (dashed orange line in Fig. 7.1).

Following the comparison of our results for $q \to 0$ with all electron optical ($q = 0$) calculations as shown in Fig. 7.2, the semicore $5d$ electrons (which have been included in the core so far in this thesis) seem to be a necessary physical ingredient to be taken into account when performing calculations of the main bulk Pb plasmon. Actually, in reflectance measurements reported in Ref. [MAWG73], the authors found two peaks in Im$[\varepsilon]$ at 18.7 and 21.5 eV, assigning them to transitions from the $5d_{5/2}$ and $5d_{3/2}$ semicore levels to the Fermi surface.

Hence, we need to explicitly include the $5d$ electrons in the calculations through their incorporation in the valence configuration. Its inclusion in the pseudopotentials and the band structure is shown in the following Section.

7.2 Semicore electrons of Pb

As stated in Section 2.4, the difference between core and valence electrons is blurred for several elements of the periodic table, and the number of the valence orbitals must be increased in some cases, depending not only on the atomic species but also on the precise physical property under consideration. As examples of elements whose semicore electrons play an important role in their physical properties, let us cite the semicore $3d$ electrons of gallium which usually need to be treated using the so-called non-linear core correction [GLFLC82], and the $3s$ and $3p$ electrons of titanium whose inclusion in the valence electrons leads to a different theoretical crystal structure [ETJA12].

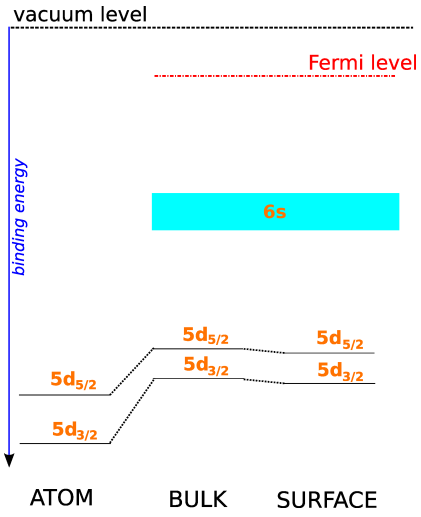

Figure 7.3: Cartoon showing schematically the binding energy of the semicore $5d$ electrons of lead in the atom, bulk and surface. The blue rectangle represents the $6s$ band in solid Pb, with a finite bandwidth. For simplicity the bulk and surface Fermi levels are considered equal.

In Fig. 7.3 we show schematically the binding energy of the semicore $5d$ electrons of atomic, bulk and surface lead. Note the big SOC splitting between the $5d_{5/2}$ and $5d_{3/2}$ levels. The upward shift of the binding energy of the $5d$ electrons when solid phases are formed opens the possibility to find effects arising from the semicore $5d$ states in the density-density response of lead on its different solid forms.

Thus, $5d$ electrons have been included in the valence configuration to perform the dielectric response calculations of bulk Pb as reported in the present Chapter. The first step in incorporating the semicore electrons in the calculations is to build new NCP with the $5d$ electrons present in the valence configuration. To that purpose we use the new valence configuration

$$5d_{3/2}^{3.33} \quad 5d_{5/2}^{6.66} \quad 6s_{1/2}^{1.50} \quad 6p_{1/2}^{0.42} \quad 6p_{3/2}^{0.83} \quad 5f_{5/2}^{0.21} \quad 5f_{7/2}^{0.29} \tag{7.1}$$

which again is $+0.76e^-$ positively charged (see Section 5.1). In Fig. 7.4 the new ionic and SOC NCP are shown (solid lines), together with the ones generated with the $5d$ electrons in the core (dashed lines). As expected, the $l = 2$ ionic pseudopotential becomes now deeper, while the ones corresponding to other angular momentum channels are also stronger than those in the previous case. The latter change is a consequence of the orthogonality of the wave functions for different l. Nevertheless, only the cut-off radius for $l = 2$ must be changed, and the new set of cut-off radii (see Sections 2.4 and 5.1) is $r_c^l = 1.60$, 2.00, 1.00 and 3.50 a.u. for s, p, d and f electrons, respectively. Note that in Fig. 7.4 the new SOC pseudopotentials for p and f electrons are indistinguishable from the ones retrieved when the $5d$ electrons were in the core, whereas $V_{l=2}^{SOC}(r)$ is clearly enhanced. This is as expected, as the more localized the electrons are, the stronger the effect of the spin-orbit interaction is.

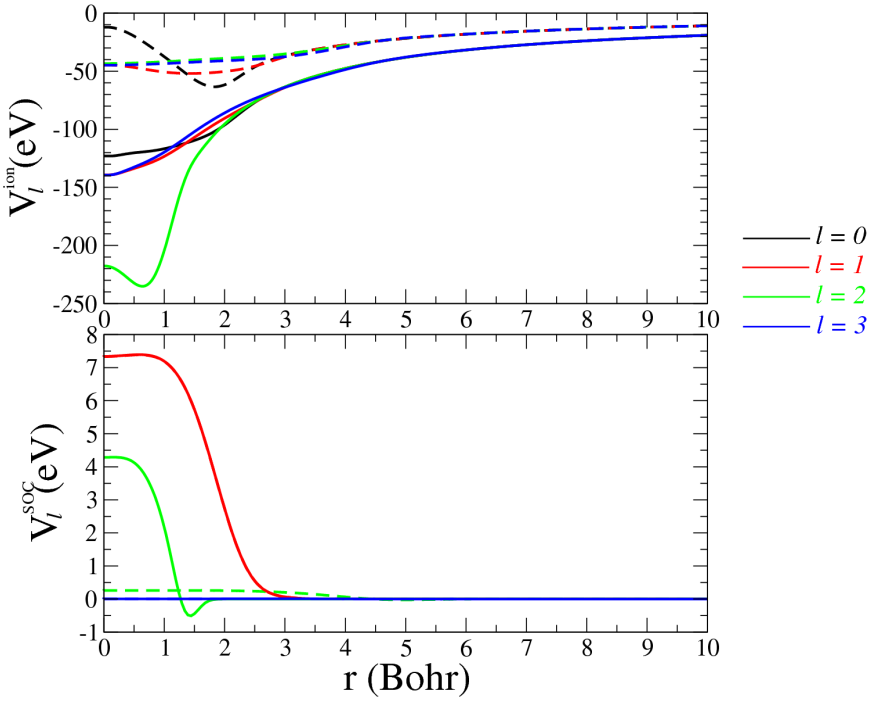

Figure 7.4: Ionic (upper panel) and SOC (lower panel) pseudopotentials used when the 5*d* electrons are included in (solid lines) and excluded (dashed lines) from the valence configuration.

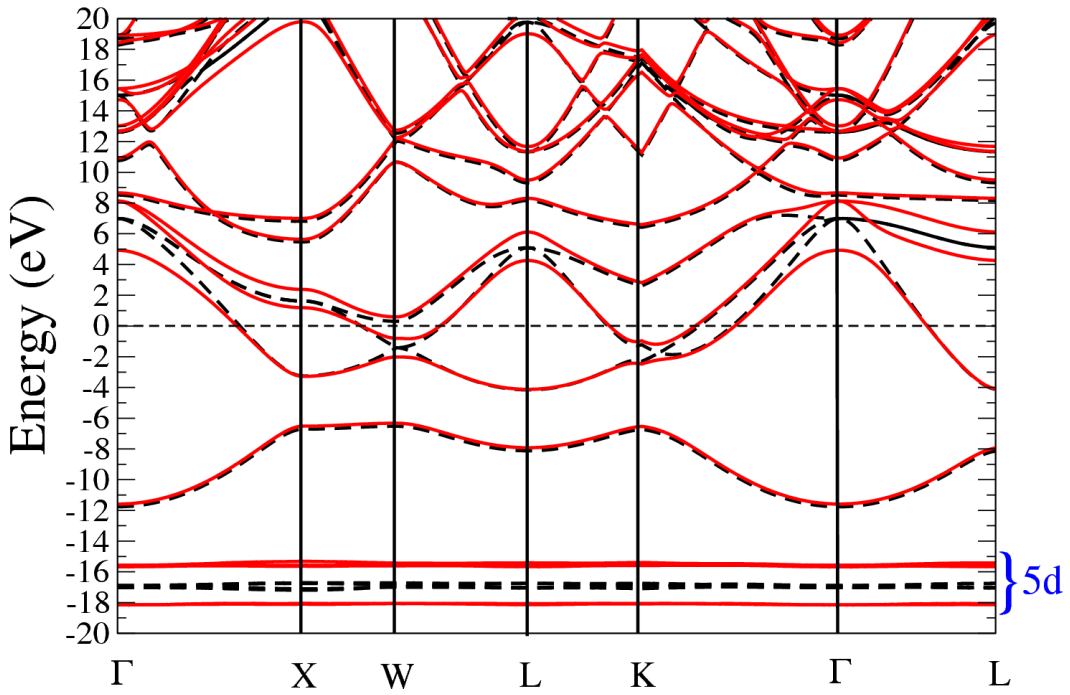

Figure 7.5: Calculated band structure of bulk lead, calculated with (red solid lines) and without (black dashed lines) the SOC term in the Hamiltonian with inclusion of the 5*d* semicore electrons, which are located at energies $\epsilon - E_F <$ -15 eV. The horizontal dashed line represents the Fermi level set to zero.

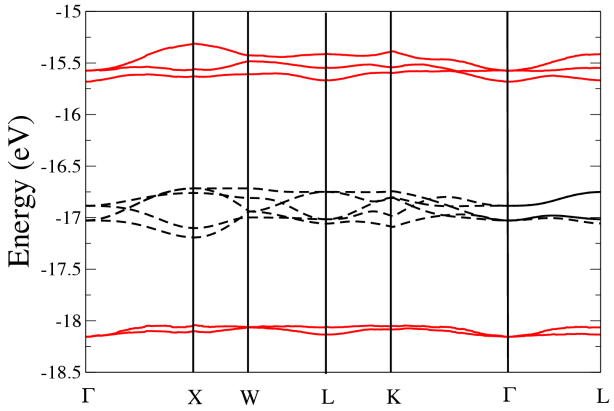

Figure 7.6: Zoom of Fig. 7.5 over the energy range of the 5*d* bands.

The calculations of the electronic structure including the 5*d* electrons were carried using a kinetic energy cut-off of 544 eV, which corresponds to the inclusion of ∼880 plane waves in the expansion of the KS states [see Eq. (2.18)] and satisfactory convergence of the energy bands was found. In Fig. 7.5 the bulk Pb band structure calculated with the semicore 5*d* electrons included is shown. First, notice that all the rest of the bands remain unchanged with respect to the electronic structure obtained with the 5*d* electrons in the core, both excluding and including the SOC (compare Figs. 5.3 and 7.4). Second, the semicore electrons appear as dispersionless bands, clearly showing their highly localized character. Note however that, as shown in Fig. 7.6, zooming in the appropiate energy range reveals some dispersing structure in the 5*d* bands.

The energies of the 5*d* bands obtained are located (with respect to the Fermi level) at ∼ -17 eV at the scalar-relativistic level, while when SOC is included they are splitted into the $5d_{5/2}$ and $5d_{3/2}$ levels with energies ∼ -15.6 and ∼ -18.1 eV. The electronic structure of bulk Pb shown in Fig. 7.5 is in fairly good agreement with a recent theoretical study [JVTJ$^+$08] in which the NCP-DFT theoretical framework was also used. In particular, the semicore states in Ref. [JVTJ$^+$08] present the same energies as the reported ones in the present work.

Recently, the photoionization spectra of atomic and solid lead was measured [IPAA12] and the $5d_{5/2}$ and $5d_{3/2}$ levels were found in the latter at energies (with respecto to E_F) of -17.93 and -20.58 eV, respectively. This is in clear disagreement with the present results as shown in Fig. 7.5 by ∼ 2.4 eV. In order to check the calculated binding energies of the semicore electrons, we performed the calculation of the band structure using a completely different method, namely the KKR Green's function method as implemented in the HUTSEPOT code [Ern07]. The energies of the 5*d* bands obtained are (with respect to the Fermi level) at ∼ -17.4 eV at the scalar-relativistic level, while of ∼ -16.3 and ∼ -19.2 eV for the $5d_{5/2}$ and $5d_{3/2}$ levels respectively when SOC was included. The results on the semicore energy levels obtained with the two different theoretical approaches are in disagreement both with each other and with respect to the photoionization data [IPAA12].

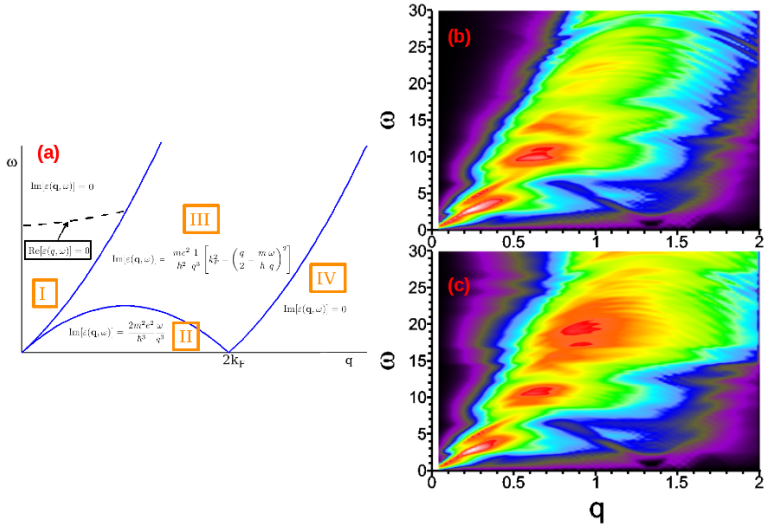

Figure 7.7: Imaginary part of the non-interacting susceptibility, $\mathrm{Im}[\chi^0(\mathbf{q},\omega)]$. Panel (a) shows the different domains of the e-h continuum in a FEG (see Appendix E). Panels (b) and (c) show $\mathrm{Im}[\chi^0(\mathbf{q},\omega)]$ for momentum transfers along the $\Gamma-$X direction with full inclusion of SOC, excluding [(b)] and including [(c)] the semicore $5d$ electrons. ω in eV and q in a.u.

The reasons for the aforementioned disagreements are still unclear. The experimental measurements were carried on a polycristalline sample and no structure characterization was performed. However, the data obtained are in good agreement with previous experimental works (see Table I in Ref. [IPAA12]). On the other hand, once the $5d$ electrons are included in the dielectric response calculations, we retrieve results in fairly good agreement with the all-electron optical scalar-relativistic calculations shown in the upper panel of Fig. 7.2 (see below).

7.3 Computational parameters

When $5d$ electrons are included in the calculations of the dielectric and energy-loss functions at the scalar-relativistic level [see Eq. (3.19)], a Monkhorst-Pack 144×144×144 grid of $\mathbf{k}$ vectors was used as the BZ sampling. The broadening of the modified Gaussian modeling the energy conservation Dirac delta (see Appendix D) is fixed as 50 meV, while the energy transfer mesh step is $\Delta\omega = 40$ meV.

For full SOC inclusion, a coarser 48×48×48 mesh was employed in evaluating Eq. (3.32). The broadening of the modified Gaussian ensuring the energy conservation is fixed as 150 meV, while the energy transfer mesh step is $\Delta\omega = 20$ meV.

In both cases up to 40 plane waves were employed in the expansion of the the susceptibility and dielectric function matrices.

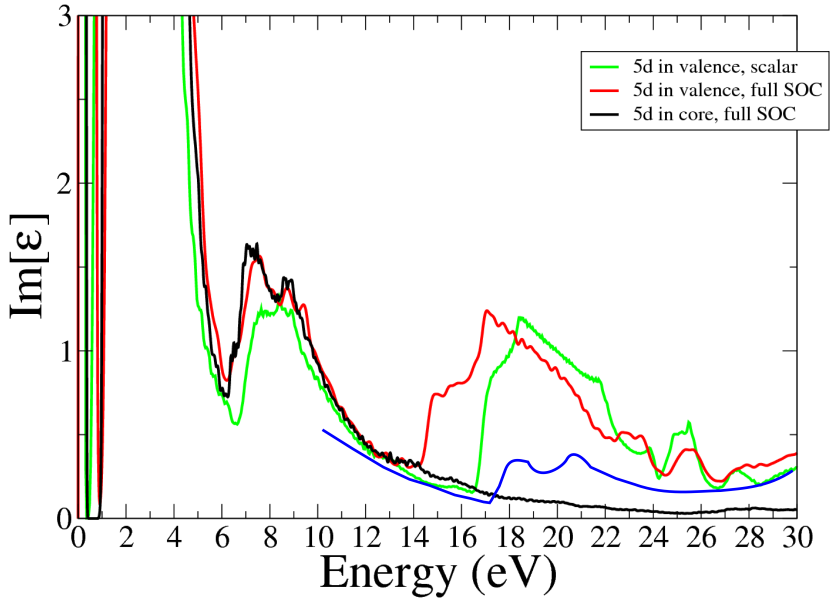

Figure 7.8: Calculated imaginary part of the dielectric function for $q \to 0$. Red (black) curve represents the results with full SOC inclusion and the $5d$ electrons incorporated in (excluded from) the valence electons. The green curve stands for Im[ε] obtained at the scalar-relativistic level and taking the semicore electrons into account. The TDLDA kernel and LFE were included in all three calculations. The blue curve stands for the Im[ε] retrieved from reflectance measurements as reported in Ref. [MAWG73].

7.4 Semicore effects on the dielectric response

In Fig. 7.7 we compare the obtained imaginary part of the non-interacting susceptibility evaluated excluding [panel (b)] and including [panel (c)] the $5d$ semicore electrons in the valence configuration. Also, in panel (a) the different domains of the e-h continuum in a FEG (see Appendix E) are depicted. As readily seen, Im[$\chi^0(\mathbf{q},\omega)$] when the $5d$ electrons are excluded from the valence ones shows a free-electron like behaviour and the different domains sketched in panel (a) can be easily recognized. However, once the semicore $5d$ electrons are included in the valence configuration, Im[$\chi^0(\mathbf{q},\omega)$] is distorted for energy tranfers $\omega \gtrsim 15$ eV, as seen in Fig. 7.7(c). Thus, upon inclusion of the $5d$ electrons in the valence configuration, not only a lowering of the main bulk plasmon energy ω_p is expected (see Section 7.1), but also a non-free-electron like behaviour of its dispersion induced by the transitions from the semicore to unoccupied states. Nevertheless, as shown below, this deviation from a FEG-like response is less significant when the calculations are carried at the scalar-relativistic level.

In order to check whether the inclusion of the semicore electrons in the calculations leads to an agreement with the all-electron optical calculations shown in Fig. 7.2, in Fig. 7.8 the imaginary part on the dielectric function is plotted. Red (black) curve represents the results with full SOC inclusion and the $5d$ electrons incorporated in (excluded from) the valence electrons, while the green curve stands for Im[ε] obtained at the scalar-relativistic level and taking the semicore electrons into account. The

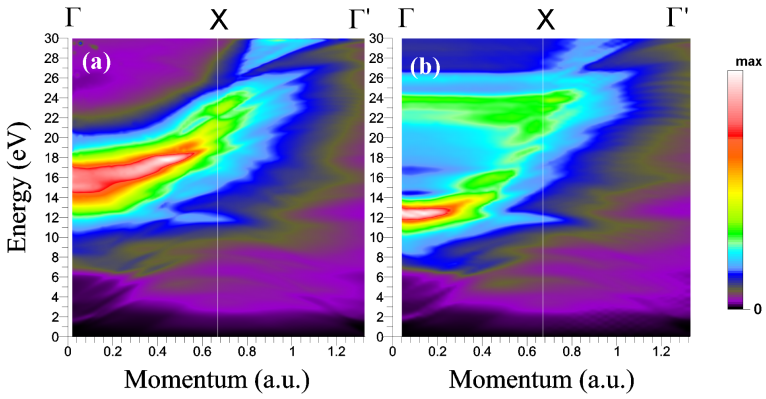

Figure 7.9: Energy-loss function evaluated (a) without and (b) with inclusion of the semicore $5d$ states. Calculations were performed taking into account SOC, LFE and the TDLDA xc kernel.

TDLDA kernel and LFE were included in all three calculations. Comparing the green curve in Fig. 7.8 with the black one in the upper panel of Fig. 7.2, a fairly good agreement is found.

Moreover, in Fig. 7.8 the imaginary part of the dielectric function as deduced from reflectance measurements [MAWG73] is also shown as a blue curve. The position of the broad peak between ∼17 and ∼24 eV in the experimental Im[ε] is in disagreement with the present results when SOC is included, while presenting good agreement with both the scalar-relativistic results (the present result for $q \to 0$, and the all-electron one for $q = 0$ as shown in the upper panel of Fig. 7.2).

Before analyzing in detail the general results on the high energy dielectric response of bulk Pb, as an example of the lowering of the bulk plasmon energy by the inclusion of the semicore electrons, we show in Fig. 7.9 the energy-loss function calculated without (a) and with (b) inclusion of the semicore $5d$ states. Calculations were performed taking into account SOC, LFE and the TDLDA xc kernel and with the momentum transfer along the Γ−X direction. Incorporation of the semicore $5d$ electrons in the calculations lowers the bulk Pb plasmon energy in the long wavelength limit by roughly 3 eV (see also Fig. 7.10). Notice it also shortens significantly the momentum transfer range in which the plasmon is well defined. These remarkable effects of the semicore inclusion on the bulk Pb dielectric response calculations are found independently of the level of description of xc effects (RPA or TDLDA) and inclusion of LFE. Also, note that the lowering of the long wavelength limit of the bulk plasmon energy $\omega(q \to 0)$ is slightly affected by exclusion of the SOC, as shown in Fig. 7.10.

As we show below, the interplay between the transitions involving the $5d$ electrons and the SOC effects shapes the dielectric response of bulk Pb at energies $\omega \gtrsim 8$ eV, strongly affecting the energy-loss function at high energy transfer values.

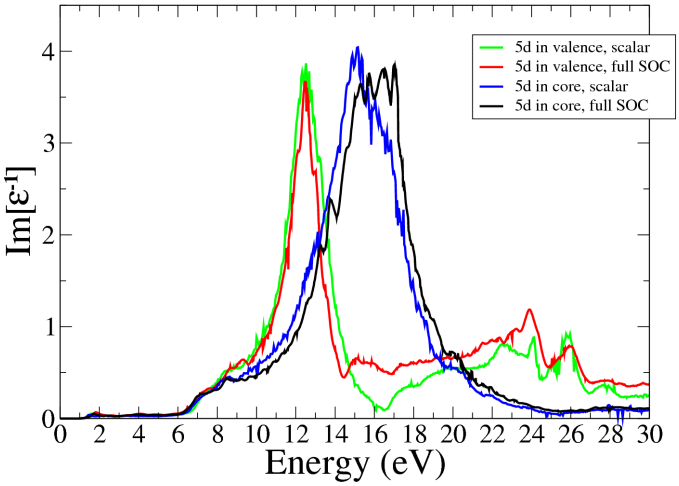

Figure 7.10: Energy-loss function at $q \to 0$ calculated with SOC and semicore inclusion (red curve), with semicore inclusion at the scalar-relativistic level (green curve), with SOC and no semicore incorporated (black curve) and at the scalar-relativistic level without including the semicore electrons (blue curve). All calculations were carried including LFE and the TDLDA xc kernel.

7.5 General results: LFE and SOC effects

In Fig. 7.11 the general results are shown for the $\mathrm{Im}[\varepsilon^{-1}_{\mathbf{G}=0,\mathbf{G'}=0}(\mathbf{q},\omega)]$ surfaces obtained with the $5d$ semicore electrons included in the valence configuration, at the momentum transfer along the three reciprocal space high-symmetry directions studied. The right column stands for the results obtained with full SOC and LFE inclusion, while SOC (LFE) was excluded from the calculations corresponding to the left (middle) column.

As was demonstrated in Fig. 7.9, the incorporation of the semicore electrons in the calculations of the dielectric response of bulk Pb leads to a completely different picture of the energy-loss function. Instead of finding a broad bulk plasmon peak presenting a full-width at half-maximum (FWHM) of roughly 4 eV and exhibiting a manifest upwards dispersion, now it only slightly disperses while its linewidth is decreased to $\sim$ 1.5 eV (see Fig. 7.10). This strong effect of including the $5d$ electrons is found independent of the direction of the momentum transfer and of inclusion of the SOC, LFE or the TDLDA xc kernel. The latter plays a negligible role in the dielectric response results obtained here and xc effects are not analyzed. Thus, all the results reported in the present Chapter were obtained using the TDLDA xc kernel.

However, the spin-orbit interaction and the local-field effects still affect remarkably the energy-loss function when the semicore is explicitly taken into account. First, the presence of the large SOC-induced energy splitting of the $5d_{5/2}$ and $5d_{3/2}$ states should sizeably influence the calculated dielectric response. Second, because LFE are a consequence of the inhomogeneity of the electron density (see Section 3.3.3), when highly localized states as the Pb semicore $5d$ states are present in the calculations LFE are expected to give raise to substantial changes, specially in the energy transfer range corresponding to transitions stemming from the localized electronic states.

In fact, as seen in Fig. 7.11, both SOC and LFE considerably affect the calculated $\mathrm{Im}[\varepsilon^{-1}_{\mathbf{G}=0,\mathbf{G'}=0}(\mathbf{q},\omega)]$ of bulk Pb once the $5d$ electrons are included in the valence configuration. Thus, ignoring the LFE (compare the left and middle columns in Fig. 7.11)

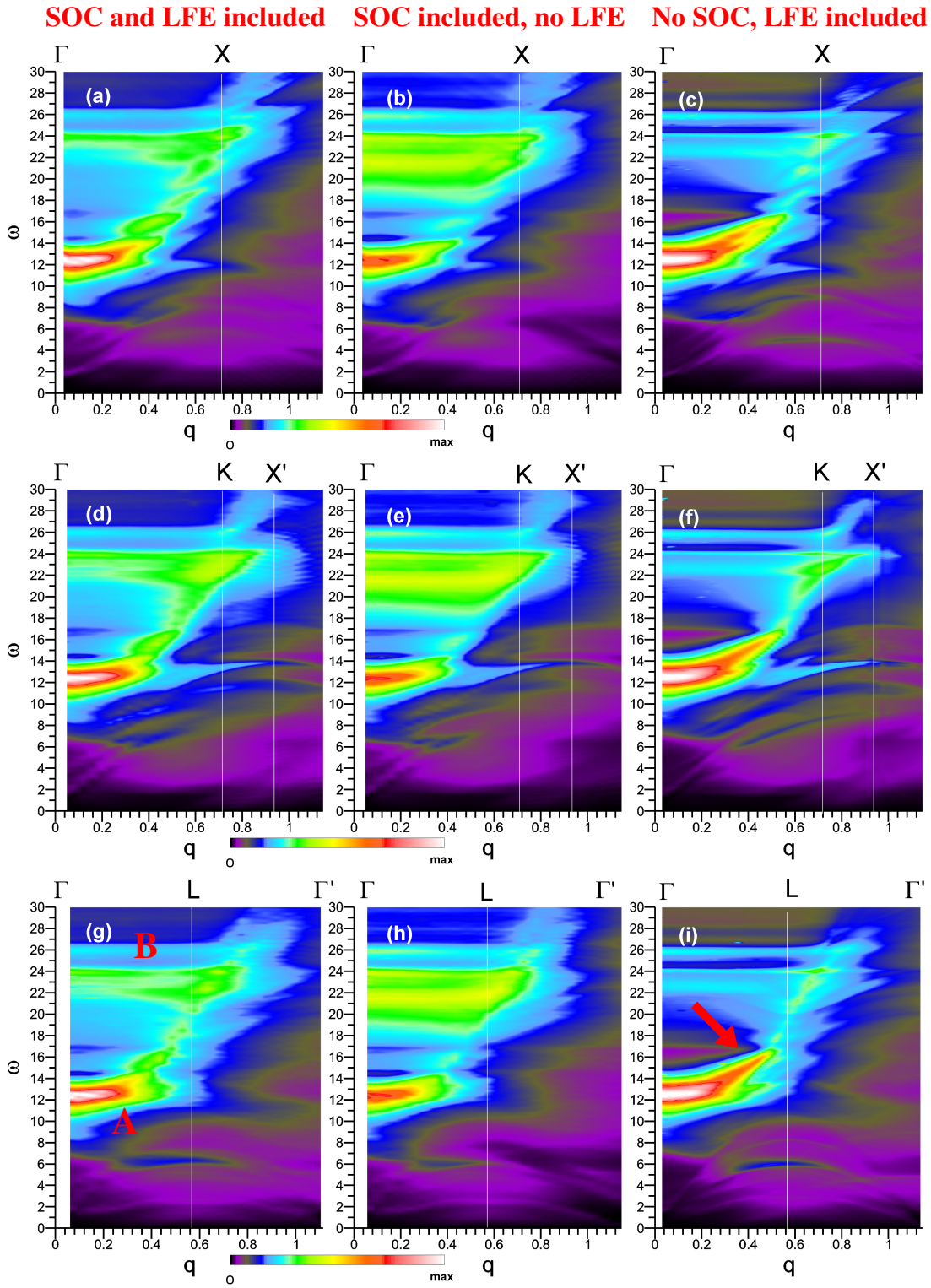

Figure 7.11: Energy-loss function obtained once the semicore electrons are included in the valence configuration. The upper, middle and bottom rows correspond to the results with $\mathbf{q}$ along Γ−X, Γ−K and Γ−L, respectively. High-symmetry points are marked by thin white lines and labeled. The right column stands for the $\mathrm{Im}[\varepsilon^{-1}_{\mathbf{G}=0,\mathbf{G}'=0}(\mathbf{q},\omega)]$ retrieved with full SOC and LFE inclusion, whereas SOC (LFE) was excluded from the calculations corresponding to the left (middle) column. See the text for the meaning of the symbols in panels (g) and (i). ω in eV and q in a.u.

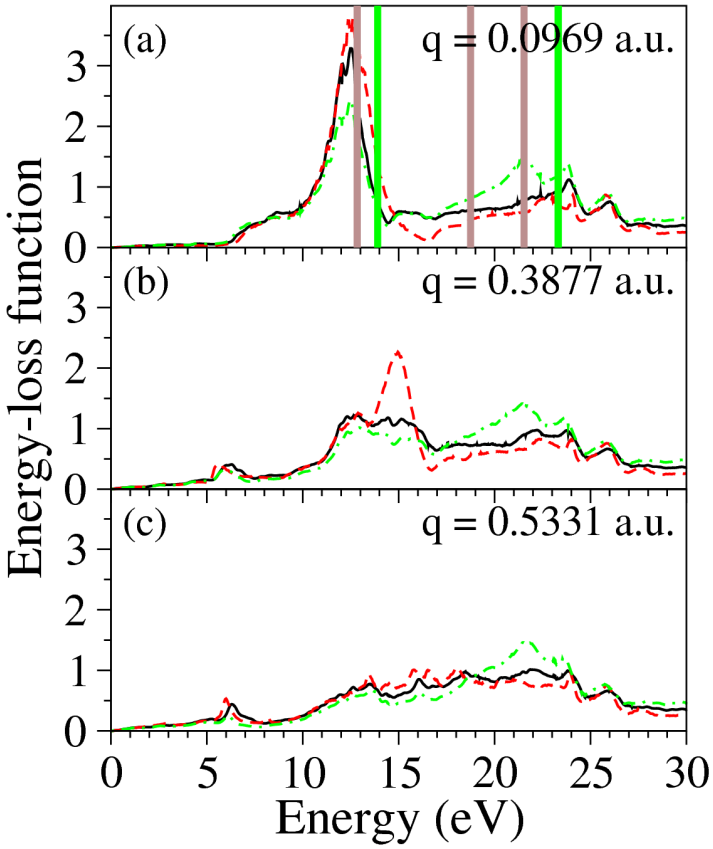

Figure 7.12: Energy-loss function at three different values of **q** along Γ−L. Black solid, red dashed and green dashed-dotted curves stand for the results obtained with full SOC and LFE inclusion, excluding SOC, and ignoring LFE, respectively. The vertical shaded green intervals in (a) represent the experimental electron energy-loss data of Ref. [JP60], while the brown ones stand for the reflectance measurements results as reported in Ref. [MAWG73].

results in a spectral weight transfer from the bulk plasmon at $\omega \simeq 12-13$ eV [labeled by the letter A in panel (g) of Fig. 7.11] to the broad peak formed by transitions from the $5d$ electrons to the lowest unoccupied states [labeled by the letter B in panel (g) of Fig. 7.11] occupying an energy transfer range of ~ 5 eV ($19 \lesssim \omega \lesssim 24$ eV). Thus exclusion of the LFE decreases the bulk plasmon intensity. Also, ignoring LFE weakens the strongly upwards dispersing feature [signaled by the red arrow in panel (i) of Fig. 7.11] which connects the final stages of the bulk plasmon dispersion at $q \simeq 0.4$ a.u. with the high-energy peak involving transitions from the $5d$ semicore states. This connection actually follows the border of the intraband e-h continuum (see also Fig. 7.13 below) represented by the left parabola in panel (a) of Fig. 7.7. The mentioned LFE effects are readily seen by comparing the black solid and green dashed-dotted lines in panel (a) of Fig. 7.12.

On the other hand, comparing the right and left columns of Fig. 7.11, it is found that full SOC inclusion in the evaluation of the energy-loss function leads to an increased intensity of high-energy peak related to the semicore presence (compare also the green and red curves in Fig. 7.10). More importantly, SOC shortens the momentum transfer range in which the bulk plasmon is well-defined, smearing its intensity in the $0.35 \lesssim q \lesssim 0.5$ a.u. range. This strong SOC effect is clearly observed in the cut of $\mathrm{Im}[\varepsilon^{-1}_{\mathbf{G}=0,\mathbf{G'}=0}(\mathbf{q},\omega)]$ plotted in Fig. 7.12 (b) where the bulk plasmon peak is still well-

defined in the scalar-relativistic results. Also, inclusion of the SOC leads to a smaller bulk plasmon linewidth by 0.5 eV, as seen in Fig. 7.10.

7.5.1 Comparison with experimental results

In Fig. 7.12 (a) the vertical thick green lines mark the peak positions in experimental electron energy-loss data of Ref. [JP60], while the brown ones stand for the reflectance measurements results as reported in Ref. [MAWG73]. The explicit semicore inclusion in the calculations gives a value of $\omega_p(q \to 0) = 12.3$ eV, close to the reflectance peak reported at 12.7±0.2 eV [MAWG73]. On the other hand, comparison with the EELS value of 13.9±0.2 eV is unsatisfactory.

The situation at higher energy transfer values is different. As seen in Fig. 7.12 (a), two peaks at 18.7 and 21.5 eV where found in the reflectance measurements [MAWG73], while a broad peak was detected in Ref. [JP60] centered at 23.3 eV. Close inspection of the black curve in Fig. 7.12 (a) reveals a small peak at 23.9 eV (and a second one at 26 eV) which is in good agreement with the broad feature in the reported EELS measurements, while no peaks corresponding to the measured ones in Ref. [MAWG73] at 18.7 and 21.5 eV are found in our calculations.

The disceprancy between the two different experimental techniques prevents from getting a clear conclusion. However, the reflectance experiments probe the optical ($q = 0$) dielectric function. On the contrary, EELS experiments carried out 50 years ago probably presented a finite unknown range of momentum transfer of the probe electrons, resulting in peaks averaged over a appreciable momentum transfer range.

As a conclusion, new EELS experiments probing the energy-loss function of bulk Pb at high energy transfers are highly desirable, as they could shed light on the precise role played by the localized polarizable $5d$ electrons, as well as on the SOC effects.

7.5.2 Anisotropy

In order to analyze possible anisotropy effects arising from the real atomic structure, in Fig. 7.13 the bulk Pb imaginary part of the non-interacting susceptibility [(a)-(c)] and the corresponding energy-loss function [(d)-(f)] are shown up to 30 eV energy transfer values, with $\mathbf{q}$ along Γ−X [(a) and (d)], Γ−K [(b) and (e)] and Γ−L [(c) and (f)]. Calculations were performed with full inclusion of the $5d$, SOC, LFE and the TDLDA xc kernel.

Analyzing the energy-loss function and its dependence on the direction of $\mathbf{q}$ in light of the corresponding non-interacting susceptibility helps clarifying several aspects. First note the appearance in $\mathrm{Im}[\chi^0(\mathbf{q},\omega)]$ of the two thresholds for transitions from the strongly SOC-splitted $5d_{5/2}$ and $5d_{3/2}$ states to the Fermi surface, as marked by arrows in panels (a)-(c) of Fig. 7.13.

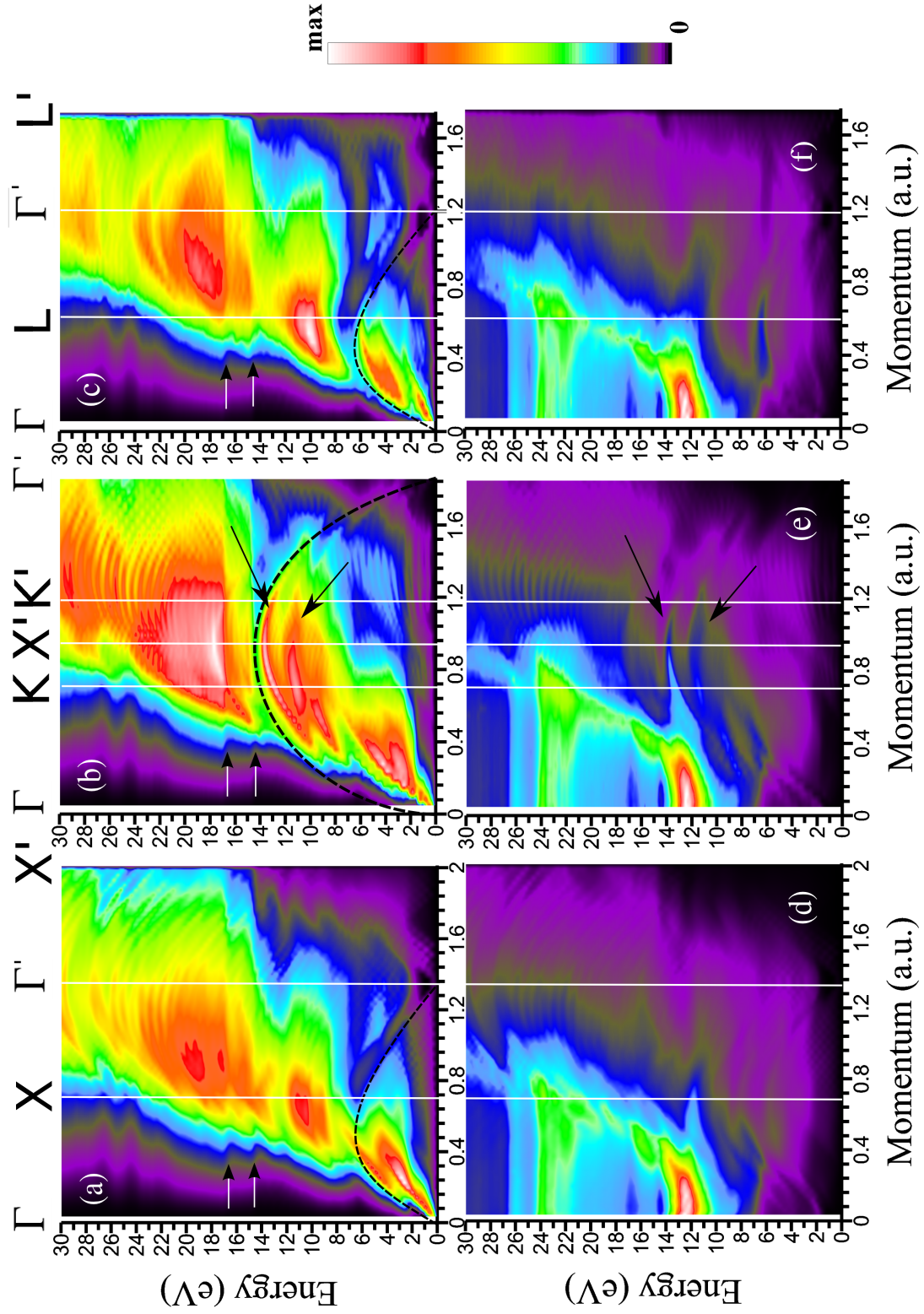

Figure 7.13: Comparison of the imaginary part of the non-interacting susceptibility of bulk Pb [(a)-(c)] and the corresponding energy-loss function [(d)-(f)] shown up to 30 eV energy transfer values, with **q** along Γ−X [(a) and (d)], Γ−K [(b) and (e)] and Γ−L [(c) and (f)]. Calculations were carried with full inclusion of the 5*d* electrons, and of SOC, LFE and the TDLDA *xc* kernel in the energy-loss evaluation. White short arrows point to the onset of the transitions from the semicore electrons to the Fermi surface. See the text for the meaning of the black dashed curves and long black arrows.

Moreover, from Fig. 7.13 it is clear that anisotropy effects are present in the energy-loss function of bulk Pb at finite momentum transfer. Comparison with the corresponding non-interacting susceptibility sheds light on this issue, showing that anisotropy effects originate from the distinct shapes of the e-h continuum. In the $\mathrm{Im}[\chi^0(\mathbf{q},\omega)]$ results shown in Fig. 7.13, black dashed lines highlight the border betwen different $(\mathbf{q},\omega)$ regions on the non-interacting susceptibility in analogy with the clearly defined domains on its FEG counterpart [see Fig. 7.7 (a) and Appendix E]. One can appreciate a different topology of the e-h continuum in $\Gamma-\mathrm{K}$. Focusing on the black dashed lines on (a)-(c), one concludes that the different character of $\mathrm{Im}[\chi^0(\mathbf{q},\omega)]$ in $\Gamma-\mathrm{K}$ stems from the distinct size of the e-h continuum region delimited by the black dashed line, which is proportional to the reciprocal space distance between the center of two subsequent BZs. Note that for $\mathbf{q}$ vectors along $\Gamma-\mathrm{K}$, the region delimited by the black dashed line is enlarged up to values of ω corresponding to the lower threshold for transitions from the semicore states. This anisotropic character of $\mathrm{Im}[\chi^0(\mathbf{q},\omega)]$ was already detected in the low-energy results reported in Chapter 6.

Thus, the manner in which the main bulk plasmon decays into electron-hole pairs when entering the region of the e-h continuum in which intraband transitions are allowed is dependent on the direction of the momentum transfer $\mathbf{q}$. As a result, only for $\mathbf{q}$ along $\Gamma-\mathrm{K}$ well-defined peaks are present beyond the first BZ limit in the energy transfer range $10 \lesssim \omega \lesssim 14$ eV. These features directly reflect the existence of analogous peaks showing exactly the same dispersion in the imaginary part of the non-interacting susceptibility [see Fig. 7.13 (b)]. Thus, in spite of presenting an energy close to the one corresponding to the main bulk plasmon, both peaks present a strong single-particle-like character.

7.6 Summary

Semicore electrons are found to play a crucial role in the high-energy dielectric properties of bulk Pb, strongly affecting the dynamics of the main bulk plasmon by redshifting its energy at $q \to 0$ by ~ 3 eV and producing the appearance of a broad peak at higher energies. The latter reflects the plasma losses due to transitions between the strongly SOC-splitted $5d_{5/2}$ and $5d_{3/2}$ states to the Fermi surface.

Once the $5d$ electrons are explicitly incorporated to the dielectric response calculations, the energy-loss function is shaped by the interplay between LFE and SOC effects. Inclusion of the SOC shortens the momentum transfer range in which the bulk plasmon is well-defined, while enhancing the high-energy broad peak. On the other hand, a spectral weight transfer from the high-energy broad feature to the main bulk plasmon due to LFE has been found.

Anisotropy effects are understood in terms of the different shapes of the electron-hole continuum depending on the momentum transfer direction, showing that the dif-

ferent sizes of the reciprocal space paths between subsequent BZ centers are the origin of the anisotropy effects found in the dielectric response of bulk Pb.

Comparison with reflectance measurements [MAWG73] shows good agreement with the calculated bulk plasmon energy ω_p once the semicore has been incorporated in the evaluation of the energy-loss function, while no agreement has been found with the ω_p obtained in electron energy-loss measurements as reported in Ref. [JP60]. However, on the latter experimental work a broad feature centered at 23.3 eV was found, which is in fairly good agreement with our results.

Finally, one could think on using a model dielectric function ε_d to include the semicore effect without its explicit incorporation in the calculations, in the usually known as $s-d$ polarization model [Lie97]. This is based on the picture of the response of free-like valence electrons embedded in a polarizable medium originated on the presence of the semicore d electrons. However, the choice of ε_d is ambiguous and its use has been discarded in this thesis.

Chapter 8

Inelastic electron-electron damping rate of excited quasiparticles in bulk Pb

8.1 Introduction: summary of recent advances

In metals electron-electron inelastic scattering processes give rise to the main contribution to the damping rate of excited electrons (and holes) with energies $\gtrsim$0.5 eV above (below) the Fermi level. As for the dielectric response studies, for a long time the basic knowledge for such kind of processes was based on FEG models [JQAF58, Noz62, ANVC06] or convolution of density of states [RPAMG85, ZAME99, PZVC09]. Recently, when the calculations from first-principles became to be computationally feasible, this field has experienced profound modifications. Thus the first-principles calculations [CMPR$^+$99, SKBE99, KSE00, LHPAD04, VCGBPG$^+$06, ANPZVC07, DMSPMS$^+$11] have shown that the inelastic lifetime of excited electrons indeed is a result of balance between localization, screening and band structure details, even in metals whose electronic structure is frequently considered as being a free-electron-like one [CMSMP$^+$00, ANYSMS$^+$08].

In previous theoretical works a non-free-electron like behavior of damping rates in Be [CMSMP$^+$00, MSVCME03], the role of the screening of the d-electrons in inelastic lifetimes on Cu [CMSMP$^+$00, KSE00], transient exciton [ESK00, Sch03] and full inclusion of xc effects [GGMPME04] as well as renormalization effects on quasiparticle lifetimes in noble and transition paramagnetic [PZAVC$^+$01, RBSKE02, Sch07] and ferromagnetic metals [PZVCME04] and compounds [ANVC09, ANVC10] were studied by means of the GW approximation (see Chapter 4). Using the T-matrix theory [LFDW71, DM90] the consequences of spin-flip processes on damping rates in magnetic materials were found to be significant for the spin-minority states [PZVCME04, PZVCME05, BSPD$^+$10]. In Ref. [PZAVCME02] good agreement was found between

the inelastic lifetimes for excited electrons and holes in several metals evaluated within the *GW* approximation and the semiempirical scattering-theory approach. Role of inclusion of the accurate quasiparticle band structure of Cu and Ag in the quasiparticle lifetimes was also investigated [MDSRO02, YMR$^+$10].

At the same time, in heavy elements an additional ingredient, namely the SOC starts to be important in the description of the electronic structure. Well-known examples are the corresponding modifications in the band structures of Bi and Pb. However, to the best of our knowledge, up to now the effect of the SOC on quasiparticle lifetimes in real materials taking into account its band structure evaluated from first principles has not been investigated. In this thesis, for the first time, inelastic lifetimes of excited electrons and holes are studied in bulk lead by means of first-principle calculations, analyzing in detail the band structure as well as SOC effects.

Recently thin films of Pb grown on different substrates have obtained great deal of attention. The questions regarding growth, transport, magnetic, and superconducting properties of these systems have been considered. For instance, the confinement effects on the superconducting transition temperature [GZB$^+$04, EQCKS06, QKNS09, BHP$^+$09, ZCL$^+$10] and quasiparticle decay rates [HBP$^+$09, SKRZ$^+$10] were studied. Recent lifetime measurements by two-photon spectroscopy [SKRZ$^+$10] for few monolayers thick Pb films deposited on a silicon substrate point out to the conservation of the bulk-like behavior of decay processes in Pb even in the very thin slabs. Quasiparticle inelastic lifetime in bulk Pb was investigated with a 2PPE photoemission in Ref. [MRD$^+$10]. In this material the absence of a momentum dependent anisotropy in the derived lifetime of the excited electrons with energies in the 2.6-3.2 eV range was observed. At the same time in a single monolayer of Pb on Cu(111), the strong dependence of lifetime on the momentum was found [MRD$^+$10]. Ultrafast electron dynamics in unoccupied quantum well states (QWSs) in ultrathin Pb films on Si(111) has been investigated by femtosecond-time-resolved 2PPE [MRD$^+$10, SKB08]. Lifetime broadening of QWSs has been measured by scanning tunneling spectroscopy in Pb films on Ag(111) [BB10] and Cu(111) [MLBSLL$^+$10]. Therefore detailed first principles investigation of the inelastic decay rates of quasiparticles in bulk lead can serve as a reference for existing and future experiments.

8.2 Computational details

The inelastic electron-electron damping rates were calculated through Eq. (4.22) using a Monkhorst-Pack 24×24×24 grid of $\mathbf{q}$ wave vectors, for a total amount of 1504 $\mathbf{q}$ in the IBZ. The evaluation of Eq. (3.19) was carried out using a finer 144×144×144 $\mathbf{k}$ sampling with $\approx$ 32000 vectors in the IBZ. Also, 25 energy bands were included in calculating χ^o, spaning energies up to 38 eV above the Fermi level. The broadening parameter of the modified Gaussian (see Appendix D) replacing the energy conservation Dirac delta was set to 10 meV. In the expansion of the dielectric matrices 40 plane

waves have been considered. The sums over reciprocal vectors $\mathbf{G}$ and $\mathbf{G}'$ in Eq. (4.22) have been extended over 40 vectors.

The main convergence parameter in the calculation of the damping rates is the size of the inverse dielectric matrices used in the evaluation of Eq. (4.22). The truncation of $\mathrm{Im}[-\varepsilon^{-1}_{\mathbf{G},\mathbf{G}'}(\mathbf{q},\omega)]$ has been found to affect the value of τ_i^{-1} differently for each $\mathbf{k}$. In practice, the convergence of the damping rates with the size of the inverse dielectric matrices is found to be monotonic, allowing an empirical estimation of the error in the reported τ_i^{-1} of $\approx 5\%$ in the most pathological cases.

Comparing the central and lower lines of Fig. 6.10 we see that the inclusion of spinors leaves the energy-loss function for $0 < \omega < 8$ eV almost unchanged with respect to the results of the calculations including the SOC effects only through the corrected energy bands. Therefore we do not expect that the replacement of the spinor wave function by a scalar one should significantly modify the evaluated SOC damping rates. Thus Eq. (4.25) is not used here and only the energy bands are SOC-corrected when including the spin-orbit interaction in the calculations of the inelastic electron-electron decay rate.

8.3 Results

In Fig. 8.1 the calculated distribution of the damping rates $\Gamma_{n\mathbf{k}} = \tau^{-1}_{n\mathbf{k}}$ of hot electrons and holes for all the values of band index n and wave vectors $\mathbf{k}$ - with $\mathbf{k}$ belonging to the IBZ - used in the calculations, both using the scalar-relativistic energy spectrum (black dots) and the one including the SOC in the band structure (red dots), are presented. In addition, the results obtained using the Lindhard dielectric function (see Appendix E) together with the *ab initio* scalar-relativistic wave functions and one-particle energies are shown (blue dots). The orange line is the result for a FEG model, i.e. when the band structure is described by a band with parabolic dispersion, the wave functions are represented by plane-waves, and the Lindhard dielectric function is used for the screening. In the inset of Fig. 8.1, the green curve represents the Quinn-Ferrel result [JQAF58] for the damping rate for very low energy quasiparticles as given by Eq. (4.13). In the following we shall refer to these five kinds of lifetime calculations as SC, SO, LDF-SC, FEG, and QF ones, respectively.

There are three main features in the distribution of the damping rates in Fig. 8.1. First, for -8 eV $< \epsilon <$ -6 eV the damping rates corresponding to the s-like holes are presented. On the opposite side of the studied energy range, the values of $\Gamma_{n\mathbf{k}}$ for excited electrons in the d-like bands appear for energies in the 5.5 eV $< \epsilon <$ 8 eV interval. However the main feature of Fig. 8.1 is the parabolic-like distribution of the damping rates for the p-like holes and electrons in bands crossing the Fermi level. The linewidth data for the p states is separated from that for the s-like holes by the energy gap of ≈ 2.5 eV presented in the Pb band structure, see Fig. 5.3.

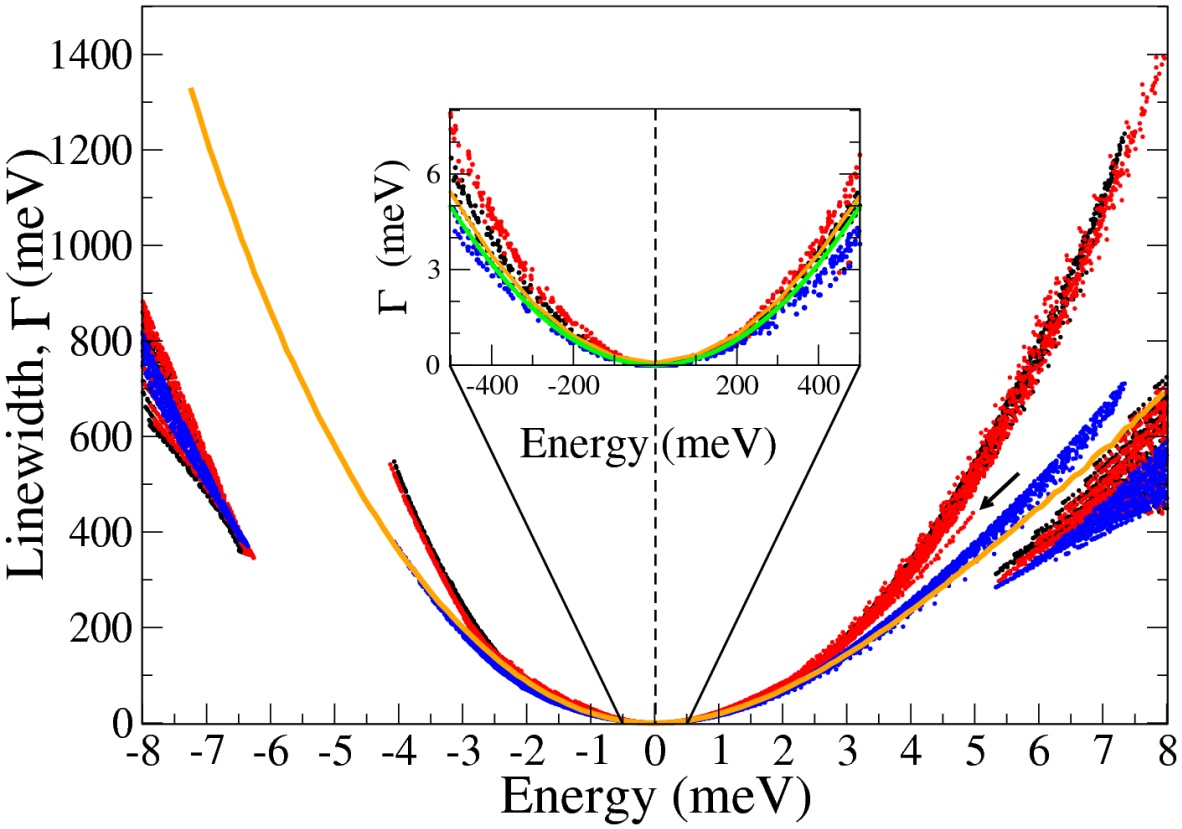

Figure 8.1: Calculated damping rate for excited quasiparticles (electrons and holes) in all the bands and **k** points set over the irreducible part of the Brillouin zone. Red dots represent the values calculated including the spin-orbit coupling in the band structure, the black dots represent the purely scalar-relativistic (SC) results and the blue dots are the results obtained using the Lindhard dielectric function together with the scalar-relativistic wave functions (LDF-SC). The orange line shows the linewidth obtained from a free electron gas model with the Pb valence charge density parameter $r_s^{\mathrm{Pb}} = 2.298$ a.u. The green curve in the inset represents results for linewidth calculated according to the Quinn-Ferrel expression of Eq. (4.13) also for r_s^{Pb}. The black arrow points to the linewidth results for the lowest p band near the BZ center calculated with the inclusion of the SOC (see the text).

It is interesting to compare the observed difference in the calculated damping rates for p and d electrons with the same energies. As can be seen in Fig. 8.1, at the same energy in the 5.5 eV $< \epsilon <$ 8 eV interval quasiparticles in the d bands present a damping rate roughly two times smaller in comparison with that for the p bands. This is a consequence of the different coupling matrices [see Eq. (4.23)] for p and d states thereby signalling about strong localization effects in the inelastic electron-electron contribution to the lifetimes in bulk Pb.

For quasiparticles in the p-like states, the role of final states in its decay [see Eq. (4.22)] can be seen in Fig. 8.1 from comparison of the distribution of the LDF-SC results (blue dots) with the FEG line. As in both these cases the Lindhard dielectric function was employed, the difference arises only in the wave functions entering the coupling matrix expression, Eq. (4.23). The blue dots show the result of the calcula-

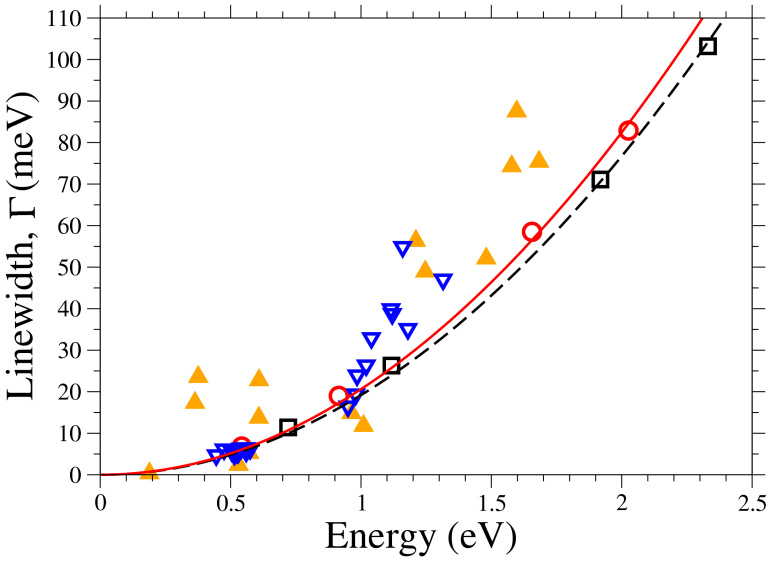

Figure 8.2: Calculated *ab initio* damping rates for excited electrons in states near the Fermi level with wave vectors along the Γ−L direction without (squares, black line) and with (circles, red line) inclusion of the SOC. Lines are fits by a quadratic function, $\Gamma = \alpha \times \epsilon^2$. Filled triangles and empty inverted triangles show experimental values extracted from Pb thin film measurements of Ref. [HBP+09] and Ref. [SKRZ+10], respectively.

tions using the self-consistent Kohn-Sham scalar-relativistic wave functions, whereas the orange line was obtained when wave functions are represented by plane waves. For the p electrons and holes in the energy range -4 eV$\leqslant \epsilon \leqslant$ 5 eV, both sets of data look very similar. Nevertheless, a more careful analysis (presented below) shows some differences which are reflected in the calculated inelastic lifetimes (see Table 8.II below).

The strongest SOC effect in lifetime is observed for p states in vicinity of the BZ center. In Fig. 8.1, the arrow points to the Γ(n=2,**k**) results for the second band from the bottom and **k** vectors close to the Γ point calculated with the inclusion of the SO splitting in the band structure. As an example, in Table 8.I the linewidth values for the lowest p band states at some **k**'s along the Γ−X direction are presented. Note that the same trend holds for **k**'s along the other symmetry directions as well. These data demonstrate how the giant SOC-induced splitting of the p bands around the Γ point reduces the linewidth of the excited states in this band by as much as $\approx 60\%$ which is mainly explained by the reduction of lower energy states available for the excited electron to decay. Hence, SOC remarkably affects the inelastic decay rates of p-like excited electrons around the BZ center through the reduction of the avalaible phase space for decay processes.

Table 8.I: Linewidth of the lowest p states at **k**'s in vicinity of the Γ point along the Γ−X direction, calculated at the scalar-relativistic level (Γ^{sc}) and including the SOC splitting (Γ^{so}) in the band structure. All values are in meV. The **k** vectors are labeled with the κ index, corresponding to $\mathbf{k} = \frac{2\pi}{24a_c}(\kappa, 0, 0)$.

κ	0	1	2	3	4	5	6
Γ^{sc}	1135	1100	1010	895	776	663	559
Γ^{so}	440	430	410	381	345	307	268

8.3.1 Link with damping rates of quantum-well states

Very recently lifetime measurements have been performed for the thin Pb films with (111) orientation grown on silicon substrates [HBP$^+$09, SKRZ$^+$10]. Such orientation corresponds to the quantization of bulk electronic states along the Γ−L symmetry direction [MWYC02, HBP$^+$09]. Figure 8.2 presents the calculated damping rates for the excited electrons in p states along this high-symmetry direction of the bulk. In contrast with the situation for the electronic states around the Γ point one can see that the SOC produces small effect on the inelastic lifetime for these states. Note also that the lifetime data for states along the Γ−L direction in Fig. 8.2, both at the SC and SO levels, are well fitted by a quadratic function over a rather extended energy range.

Note the good agreement of the parabolae fitted to the bulk results in Γ−L with the experimental data for electron energies below 0.7 eV. The agreeement is worsen for higher energies. As in both experiments lead films were deposited on a silicon substrate, the underestimation of the theoretical parabolae can be assigned to the additional decay channels opened above the silicon band gap edge located 0.8 eV [SKRZ$^+$10].

Then, from Fig. 8.2 one can deduce that the calculated results are in reasonably good agreement with the experimental data for thin films [HBP$^+$09, SKRZ$^+$10]. This signals that low energy quasiparticles dynamics in such systems can be well represented by that in bulk Pb. This can be understood in terms of the screening length, which in the Thomas-Fermi theory [GV05] presents the form

$$\lambda_{TF} = \frac{1}{2}\sqrt{\pi(4/9\pi)^{1/3} r_s}, \tag{8.1}$$

where r_s is the average valence electron density. For Pb, $r_s^{\rm Pb} = 2.298$ and hence $\lambda_{TF}^{\rm Pb} = 0.97$ a.u., which is smaller than the effective electronic thickness of a single Pb monolayer (ML), $d = 5.41$ a.u. Thus, even for a single Pb ML, the screening of an excited quasiparticle is bulk-like allowing satisfactory estimation of its $e-e$ inelastic lifetime from bulk results [SKRZ$^+$10].

8.3.2 Dependence on the quasiparticle energy

Although the damping rate $\Gamma_{n\mathbf{k}}$ of a quasiparticle in a state $(n, \mathbf{k})$ depends on its band index n and on its wave vector $\mathbf{k}$, one can define $\Gamma(\epsilon)$ as an average of $\Gamma_{n\mathbf{k}}$ over states with all wave vectors and bands lying at the same narrow energy window in the BZ. In Fig. 8.3 the results for $\Gamma(\epsilon)$ are presented for quasiparticles in the p-like bands. Notice the good agreement with the experimental data of Ref. [MRD$^+$10] as shown in Fig. 8.3. If one takes into account that the electron-phonon contribution to the decay rate is absent in our computational study, the agreement is satisfactory.

In Fig. 8.3 a different energy dependence of the averaged damping rate for holes is observed for energies below and above $\epsilon \approx$ -2.5 eV. At energies ϵ above -2.5 eV, the

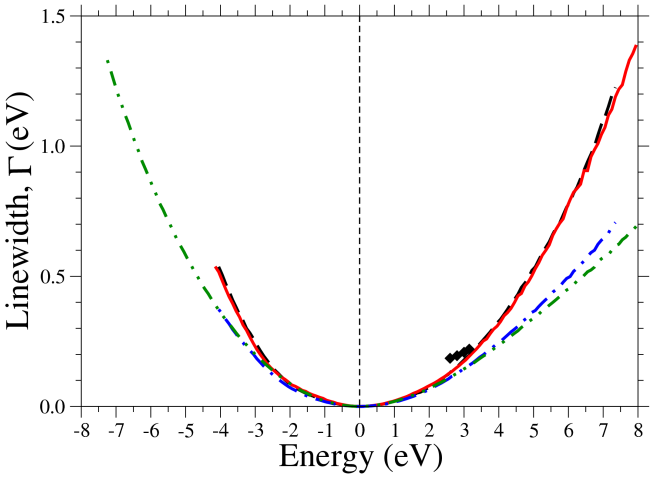

Figure 8.3: Energy dependence of the averaged damping rates, $\Gamma(\epsilon)$, of quasiparticles in the p-like bands obtained in the scalar-relativistic calculation (black dashed line), the one including the SOC (red solid line) and the calculation which includes the *ab initio* eigenstates and the Lindhard dielectric function (blue dashed-dotted line). The green dashed-dotted-dotted line shows the same as the orange solid line in Fig. 8.1. Black diamonds show the averaged lifetimes in bulk Pb measured with TR-2PPE [MRD$^+$10].

Table 8.II: Fitting coefficients of the $\Gamma(\epsilon)$ data using a third-order polynomial [see Eq. (8.2)] for holes in the energy interval above -2.5 eV and p electrons. Meaning of abbreviations "SC", "SO", "LDF-SC", and "FEG" is explained in the text (see page 85). a_2 in eV^{-1} and a_3 in eV^{-2}.

	holes				electrons			
	SC	SO	LDF-SC	FEG	SC	SO	LDF-SC	FEG
a_1	−0.0030	0.0000	−0.0020	0.0000	0.0007	−0.0020	0.0002	0.0060
a_2	0.0195	0.0313	0.0150	0.0216	0.0175	0.0190	0.0180	0.0161
a_3	0.0000	0.0050	−0.0009	−0.0002	0.0007	0.0004	−0.0007	−0.0008

averaged linewidth presents a quasi-quadratic dependence on quasiparticle energy. For more detailed analysis of this dependence, we fitted the $\Gamma(\epsilon)$ data for -2.5 eV $\leqslant \epsilon \leqslant 0$ by a third-order polynomial:

$$\Gamma_{\text{fit}}(\epsilon) = a_1 \times \epsilon + a_2 \times \epsilon^2 + a_3 \times \epsilon^3. \tag{8.2}$$

The coefficients a_i obtained from this fitting are presented in Table 8.II for all four kinds of linewidth calculations. Note the highest value of the curvature in the SO case which is a direct consequence of the avoiding of band-crossings effect produced by inclusion of the SOC in the Hamiltonian (see Fig. 5.3). In the -4.2 eV $\leqslant \epsilon \leqslant$ -2.5 eV energy range the coefficients $a_1 \approx a_2 \gg a_3$ for the SC, SO, LDF-SC levels of calculation present a strong contribution of a linear term in contrast with the FEG results which are well described by a quadratic function for any energy. Hence the quasi-linear behavior of the averaged damping rates in all the calculations performed with the use of the *ab initio* eigenstates reflects the non-free-electron like behavior of holes in the lowest p band at energies below -2.5 eV.

In the case of electrons, all curves in Fig. 8.3 present an apparent quadratic dependence on the quasiparticle energy. Nevertheless, in this case we performed also the fitting procedure with the use of Eq. (8.2). Table 8.II presents the obtained corresponding coefficients a_i as well. At first sight, all four studied curves show the expected quadratic energy dependence with the FEG results presenting the greatest deviation.

Table 8.III: Effective charge density parameters obtained from Eq. (8.3) on base of four sets of data as explained in the text. δr_s stands for the deviation from a conventional value for Pb $r_s^{\rm Pb} = 2.298$ a.u.

	SC	SO	LDF-SC	FEG
$r_s^{\rm eff}$	2.37	2.49	2.18	2.33
$\delta r_s^{\rm eff}(\%)$	+3.0	+8.3	-5.2	+1.3

At the same time, from the data of Table 8.II it is clear that the SO curve has the strongest curvature (biggest quadratic coefficient).

An interesting point comes from the comparison of the two $\Gamma(\epsilon)$ curves calculated using the Lindhard dielectric screening (LDF-SC and FEG cases), with the two curves calculated using the *ab initio* screening (SC and SO cases). The former ones deviate considerably from the two latter for energies above $\sim$ 3 eV. This fact can not be explained by difference in the curvature (i.e., a_2 coefficients) which is similar for all four curves (see Table 8.II) and originates from different signs of the a_3 coefficients (the sign of which being related to the screening). As a result, though $a_2 \gg a_3$, for sufficiently high electron energies ($\epsilon \geqslant \sim 3$ eV) the cubic term in the dependence of $\Gamma(\epsilon)$ on the energy can start to play a significant role.

From the results for $\Gamma(\epsilon)$ an effective charge density parameter $r_s^{\rm eff}$ can be derived with the use of the Quinn-Ferrel expression Eq. (4.13). Fitting again the averaged linewidth curves with Eq. (8.2), new a_i coefficients are calculated. Because of the approximations that lead to Eq. (4.13) (see Appendix F), τ_{QF}^{-1} is only valid for very low energy quasiparticles. Thus, the new fitting is carried in the energy range -1 eV $\leqslant \epsilon \leqslant 1$ eV, averaging the effect of possible different curvatures for electrons and holes. Finally, the $r_s^{\rm eff}$ parameters are found using the following expression:

$$r_s^{\rm eff} = (399.7 \times a_2)^{2/5}. \tag{8.3}$$

In Table 8.III the calculated values of $r_s^{\rm eff}$ and their deviation from the conventional $r_s^{\rm Pb} = 2.298$ a.u., derived from average valence density in Pb, are presented. One can see that in this energy interval the lifetimes derived in the FEG model can closely be described by the QF expression. The effect of inclusion of the *ab initio* band structure at the LDF-SC level consists in notable reduction of the $r_s^{\rm eff}$, whereas incorporation of the screening evaluated at the *ab initio* level works in opposite direction increasing $r_s^{\rm eff}$. Also higher value of $r_s^{\rm eff}$ in the SO case in comparison with the SC one signals about weaker effective screening in the former case at such low energies. In Table 8.IV we present the calculated values for averaged inelastic lifetimes for excited electrons and holes in Pb at $|\epsilon - E_F| = 0.5$, 1.0, 2.0 and 3.0 eV obtained in all the calculations. For excited electrons, the QF, FEG, and SC calculations give similar results. Noting that the calculated lifetimes using the self-consistent eigenstates and the Lindhard screening differ from that three ones, we can conclude that, even if lead is a free-electron-like metal, lifetime of quasiparticles in bulk Pb is the result of a balance between screening

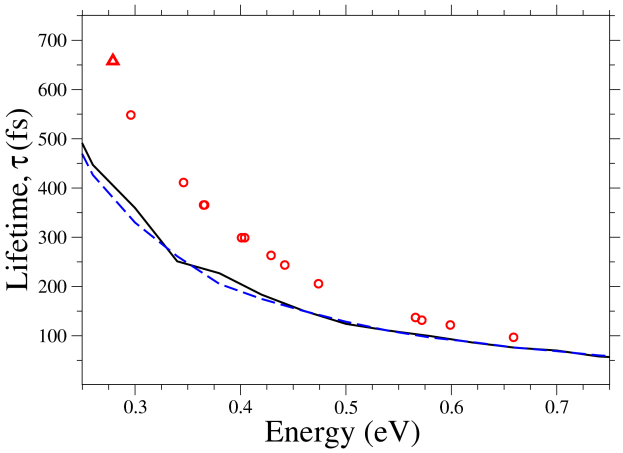

Figure 8.4: Averaged inelastic lifetimes of electrons (black solid line) and the lifetimes calculated for states at **k**'s in the vicinity of the W point (red circles) evaluated in the scalar-relativistic calculation. The triangle highlights τ at the W point. Dashed line: FEG results.

and localization. Interestingly, the lifetimes in this energy interval calculated including the SOC splittings in the band structure are the lowest ones for each quasiparticle energy, both for electrons and holes. This is in agreement with the aforementioned analysis of the effective screening, see Table 8.III.

As seen in Fig. 5.3, at the W point only one unoccupied p band approaches but does not cross E_F, presenting a local minimum. This proximity to the Fermi level together with the absence of available unoccupied states for decay with small momentum transfers leads to notably longer inelastic lifetimes for the states around the W point. This is a strong band structure effect. In Fig. 8.4 we compare the averaged inelastic lifetimes, τ^{av}, of electrons with very low energies (solid line) with the values calculated for states close to W (shown by symbols) obtained in the scalar-relativistic calculation (note that for this analysis the SOC has negligible effect). For comparison, the FEG results are shown by dashed line. As can be seen, upon approaching the W point (reducing energy) τ increases faster in comparison with the averaged inelastic lifetime at those energies, being by $\approx 50\%$ higher than τ^{av} at the same energy in other parts of the BZ. Hence, around the W point, τ behaves in a non-free-electron-like manner.

Table 8.IV: Lifetime of excited electrons (holes) at four different values of $|\epsilon - E_F|$. All values are in fs.

$\lvert\epsilon - E_F\rvert$	SC	SO	LDF-SC	FEG	QF
0.5 eV	130(114)	114(87)	162(145)	128(130)	133
1.0 eV	34(29)	31(23)	41(36)	34(31)	33
2.0 eV	9(8)	8(7)	10(9)	9(7)	8
3.0 eV	4(3)	4(3)	4(3)	5(3)	4

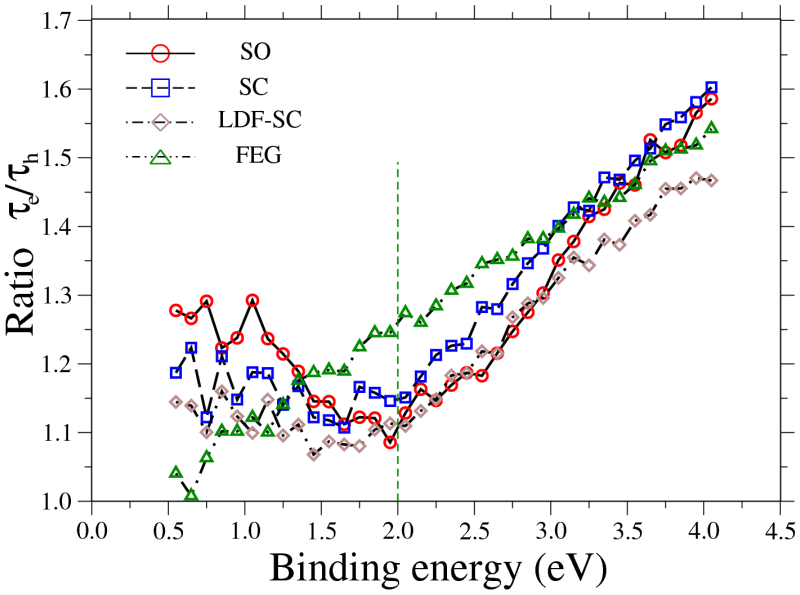

Figure 8.5: Ratio $\tau_e(\epsilon)/\tau_h(\epsilon)$ as a function of the quasiparticle energy $|\epsilon - E_F|$ for four levels of calculations. The dash line separates two energy regions with different physical behavior (see text). Lines are guides to the eye.

8.3.3 Ratio of the lifetime of electrons and holes

In Fig. 8.5, the ratio of lifetimes for electrons, τ_e, and holes, τ_h, at the same absolute value of the quasiparticle energy are shown for four different calculations. The curves show two energy ranges with different behavior. At energies $|\epsilon - E_F| \geqslant 2$ eV all the four curves present a quasi-linear behavior. However, for quasiparticle energies below 2 eV, only the FEG curve remains quasi-linear. The other three calculations present quite different dependence of the τ_e/τ_h ratio at those energies. The quasi-linear behavior of τ_e/τ_h is found in the homogeneous electron gas calculations (see as an example Fig. 2 of Ref. [MEMPVCR00]). Hence in bulk Pb the band structure effects are remarkable on the electron-electron inelastic scattering processes for quasiparticles with energies $|\epsilon - E_F| < 2$ eV. As the LDF-SC curve deduced from the lifetime results obtained with the use the Lindhard screening and the *ab initio* eigenstates presents also the band structure effects, these effects are the consequence of using the true eigenstates in the evaluation of the coupling matrices [see Eq. (4.23)], and not of the *ab initio* screening used. Note also that $\tau_e > \tau_h, \forall|\epsilon|$, for all four levels of calculations.

8.3.4 *xc* effects: preliminary results

So far we have reported G^0W^0 calculations (see Section 4.3.2) analyzing the band structure, localization and SOC effects. However, based on the results reported in Section 6.4.2, *xc* could affect remarkably the damping rates of excited quasiparticles. It has been shown that the main effect of including the *xc* short range effects on the low-energy transfer dielectric response of bulk Pb is the enhancement of the energy-loss function without changing its shape with respect to its RPA counterpart (see Section

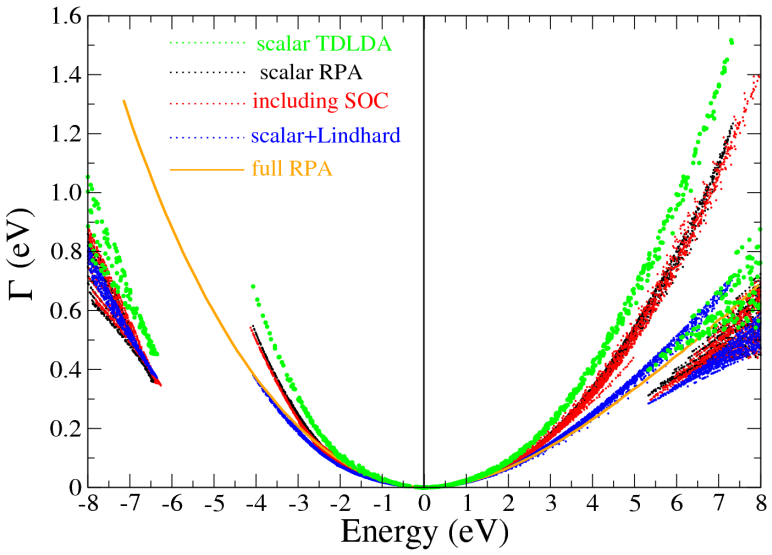

Figure 8.6: Distribution of calculated damping rates. Data are the same as in Fig. 8.1, except the green dots which stand for the G^0W results obtained using the scalar-relativistic ground state (see text).

6.4.2). This has been found not only when SOC is included, but also at the scalar-relativistic level of calculations.

Thus, we have carried G^0W calculations (see Section 4.3.2) to evaluate the impact of the xc effects on the inelastic lifetime of excited electrons and holes through the inclusion of the xc kernel in the evaluation of the screened potential $W(\mathbf{r}, \mathbf{r'}, \omega)$. For the evaluation of the screened potential as well as of the decay rates through Eq. (4.22) a 24×24×24 Monkhorst-Pack grid with 240 $\mathbf{k}$ points in the IBZ was used. These are preliminary results, reported here only at the scalar-relativistic level.

In Fig. 8.6 the distribution of the damping rates is plotted again, this time with the additional G^0W results shown as green dots. As readily seen from the figure, the G^0W inelastic decay rates are the highest for all the energies and orbital characters of the decaying electron or hole. This is in agreement with the aforementioned enhacement of the energy-loss function, and hence, of the screened potential at low energy transfers.

Also, in Fig. 8.7 the averaged calculated damping rates as a function of the quasiparticle energy for states of p character is shown. The plot is a copy of Fig. 8.3 with the addition of the G^0W scalar-relativistic results shown by a thick orange line. Comparing the newly obtained results with the experimental TR-2PPE data of Ref. [MRD$^+$10], the TDLDA kernel incorporated at the G^0W level of calculations seems to give a satisfactory description of the quasiparticle $e-e$ inelastic decay rates in bulk Pb. However, note that the experiments reported in Ref. [MRD$^+$10] were carried at a temperature of 150 K. Thus, electron-phonon could remarkably contribute to the measured inelastic damping rates [HBP$^+$09]. We conclude that the present scalar-relativistic TDLDA-G^0W results seem to overestimate the electron-electron inelastic decay rates in bulk Pb.

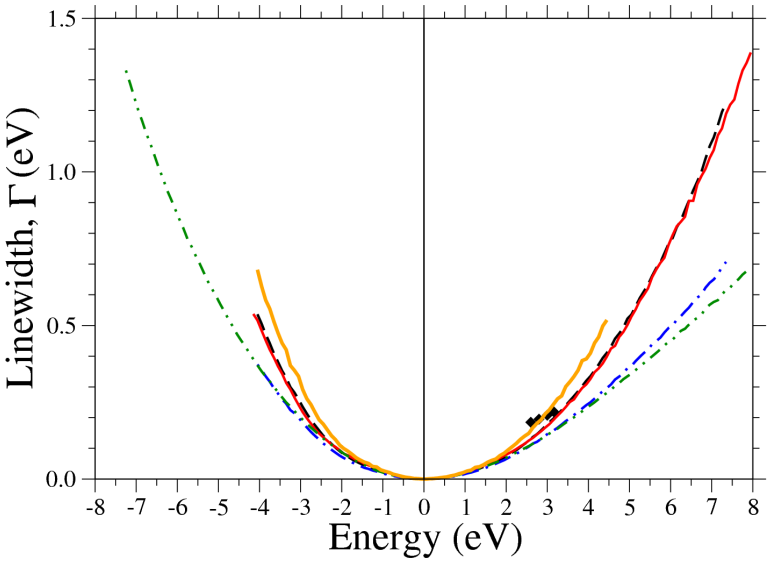

Figure 8.7: Energy dependence of the averaged calculated damping rates. Data are the same as in Fig. 8.3, except the thick orange line which stands for the G^0W results obtained using the scalar-relativistic ground state (see text). Black diamonds show the averaged lifetimes in bulk Pb measured with TR-2PPE [MRD+10].

The inclusion of the SOC in the G^0W level of calculations could improve the agreement with the experimental data. This work is in progress, as we need to make use of Eq. (4.25), and some modifications are necessary in the computational tools.

8.3.5 SOC effects on lifetime

Modifications in the Pb band structure upon inclusion of the SOC increase the lifetime of electrons in the d bands and reduce that for holes in the s ones, as demonstrated in Fig. 8.1. In all the cases the variation of τ upon inclusion of the SOC does not exceed 10% in comparison with values obtained in the scalar-relativistic calculations. In Fig. 8.8 the ratio $\tau(\epsilon^{\mathrm{SC}})/\tau_(\epsilon^{\mathrm{SO}})$ as a function of energy is plotted for the p holes and electrons. For holes with $\epsilon \leqslant -2$ eV and electrons with 2.5 eV $\leqslant \epsilon \leqslant$ 5.5 eV inclusion of the SOC splittings increases the quasiparticle lifetimes, in both cases less than 10%. On the other hand, for holes with binding energies less than 2 eV, SOC-induced splittings reduce lifetimes as much as by 30%. For electrons with $\epsilon \leqslant 2.5$ eV, as can be seen in Fig. 8.8, SOC lowers τ by $\approx 10\%$. One can expect that this tendency will continue for electronic states around the Fermi surface.

8.4 Summary

Strong localization effects are found on the inelastic electron-electron contribution to the decay rate of excited electrons with energies 5.5 eV $\leqslant \epsilon \leqslant$ 8 eV, where $\Gamma_{n\mathbf{k}}$ for d states is roughly 2 times the one for p states.

The states in the lowest valence p energy band at the center of the BZ reduce their damping rates by roughly 60% upon inclusion of the SOC in comparison with the pure

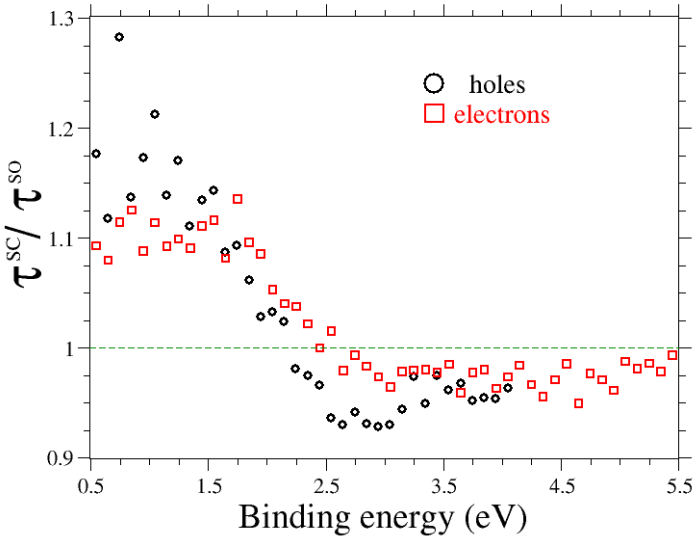

Figure 8.8: Ratio $\tau^{SC}(\epsilon)/\tau^{SO}(\epsilon)$ as a function of the quasiparticle energy $|\epsilon - E_F|$ for p-like states, both for holes (circles) and electrons (squares).

scalar-relativistic calculation. For the p electrons the damping rates $\Gamma(\epsilon)$ averaged over the BZ present a quadratic dependence on energy ϵ, whereas for p holes the quasi-linear dependence of $\Gamma(\epsilon)$ for energies ϵ below -2.5 eV reflects a non-free-electron-like nature of the electronic states at the bottom of the lowest p band. The calculated lifetime ratio $\tau_e(\epsilon)/\tau_h(\epsilon)$ reveals that band structure effects are important in electron-electron inelastic scattering processes for quasiparticles with binding energies less than 2 eV.

Present lifetime calculations for bulk Pb are in good agreement with inelastic damping rates of quantum well states of metallic thin films measured recently, presenting thereby evidence that quasiparticle dynamics can be considered as being bulk-like even in very thin Pb films.

Finally, one can think of new experiments that could test the effect of the physical ingredients studied in the present work. As an example, studies of field emission resonances (FERs) on Pb(111) [CYLLBS$^+$09, ZZGBVC11a] could shed light on SOC effects analyzed in the present work. Band structure effects may be tested too by experimental studies on Pb films grown in different crystallographic directions, even though, to our knowledge, nowadays only Pb(111) films can be grown epitaxially with thicknesses greater than 2 MLs [HDHUK$^+$10].

Chapter 9

Pb(111) films: ground state

9.1 Introduction: quantum-size effects

In thin metallic films, the confinement in the direction perpendicular to the film plane gives rise to the quantization of the electronic wave functions. As a result of the appearance of these so-called quantum-well states (QWS) [Chi00], the properties of the metallic slabs might strongly depend on the exact thickness of the film. This dependence is a purely quantum phenomena known as quantum-size effect (QSE), which often appears as an oscillatory dependence of a variety of physical properties on the film thickness. In particular, QSE also affect the dielectric response of films and overlayers (see, i.e., Ref. [PC12]).

Thin lead films exhibit important quantum-size oscillations in the layer-by-layer growth [JHKPTZ89], first observed by He-atom scattering and attributed to interference with the quantum-well states. The latter modulate the electron density of states at the Fermi level, causing oscillations with varying thickness in the superconducting critical temperature and the upper critical field [MORTHW06, YSBVC$^+$11], interlayer distances [JWHWYZ06], island height distributions [OLVdPM02], zone-center phonon frequencies [YPJ08, BRZ$^+$09], electronic transport [JHB96], photoemission properties [SKWHD$^+$07], work functions [KQY$^+$10] and quasiparticle lifetimes [HBP$^+$09, SKRZ$^+$10].

Also, recently superconductivity was discovered in a single lead monolayer on silicon [ZCL$^+$10]. Thus, lead films have become an important model system for exploring electronic and structural properties of metals on the nanoscale [JLZX07].

In the present Chapter we analyze the ground state properties of Pb(111) films, with thicknesses ranging from 1 to 15 MLs. SOC effects are found to be remarkable only for the single Pb(111) monolayer, which is understood in terms of the bulk band structure. QSE are found on the DOS, QWS effective masses and the work function of the films, in agreement with previous theoretical works.

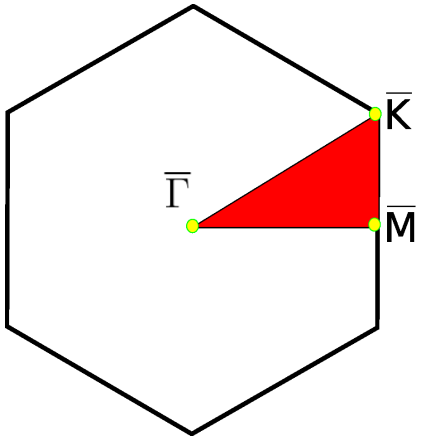

Figure 9.1: Surface Brillouin zone for a fcc crystal in the (111) direction. The red area represents the ISBZ. The high-symmetry points are labeled.

9.2 Band structure of Pb(111) freestanding films

9.2.1 Supercell approach and surface Brillouin zone

In this thesis the supercell approach is used in dealing with slabs. Thus, Pb(111) films are represented by freestanding slabs infinite in the xy plane and periodically repeated in the z direction, separated by a vacuum region whose thickness is fixed in all cases as 10 interlayer distances of the lead atoms of the film in the z -(111)- direction, which gives a vacuum region thickness of $d = 28.6$ $\mathring{A}$. Films were not relaxed, representing ideal cuts of the face-centered cubic bulk Pb in the (111) direction with the bulk experimental lattice parameter of 4.95 $\mathring{A}$. Thus, the in-plane lattice parameter is $a = 3.50$ $\mathring{A}$ and the interlayer distance is $c = 2.86$ $\mathring{A}$. However, in the case of 4 - 6 MLs thick films were also converged for atomic positions corresponding to the films relaxed in the z direction, their band structure showing negligible variations with respect to their unrelaxed counterparts. The main effect of the relaxation was a slight change of the energies of the QWS in $\overline{\Gamma}$, by at most a few tenths of eV, as a consequence of the modification of the film thickness by the structural relaxation.

Well-converged results have been found with a kinetic energy cut-off of ∼220 eV, including from ∼ 2200 (1 ML) to ∼ 5300 (15 MLs) plane-waves in the expansion of the Bloch states [see Eq. (3.19)]. A Monkhorst-Pack 12×12×1 grid of $\mathbf{k}$ vectors was used in the convergence of the electron density.

As the supercell size in the z direction is roughly 10 times larger than in the plane of the films, throughout this thesis we make use of the surface Brillouin zone (SBZ), in which $k_z = 0$. In Fig. 9.1 the SBZ is shown, in which the irreducible SBZ (ISBZ) has been highlighted together with the high-symmetry points. For the 1 - 4 MLs thick films, the Hamiltonian was also solved including the SOC term fully self consistently. Note that as the SBZ is used, the $\mathbf{k}$ vectors lie always in the $k_z = 0$ plane and the ISBZ once SOC is included is the same than at the scalar-relativistic level (represented by the red area in Fig. 9.1).

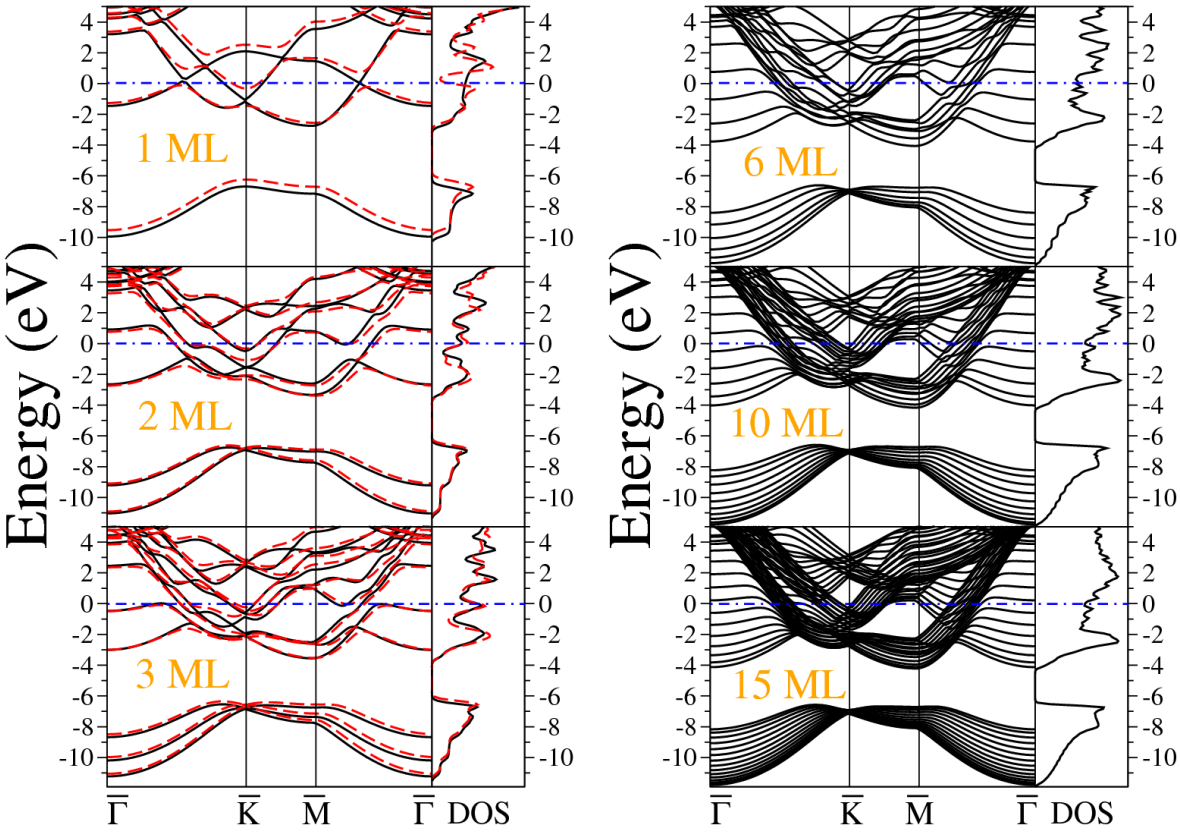

Figure 9.2: Calculated band structure and density of states of Pb(111) freestanding films 1 - 3, 6, 10 and 15 MLs thick, without (solid black lines) and with (dashed red lines) inclusion of the SOC in the Hamiltonian. The horizontal dashed-dotted blue lines represent the Fermi level of each film. DOS in arbitrary units.

The two reciprocal space directions in which the surface dielectric response has been studied in this thesis (see Chapter 10) correspond to the $\overline{\Gamma}-\overline{\mathrm{K}}$ and $\overline{\Gamma}-\overline{\mathrm{M}}$ SBZ high-symmetry directions (see Fig. 9.1). In each of the mentioned directions, the momentum $\mathbf{q}$ is of the form

$$\mathbf{q}_{\overline{\mathrm{K}}} = \frac{2\pi}{a}\left(\frac{2l}{\mathrm{M}}, 0, 0\right), \tag{9.1}$$

$$\mathbf{q}_{\overline{\mathrm{M}}} = \frac{2\pi}{a}\left(\frac{l}{\mathrm{M}}, \frac{1}{\sqrt{3}}\frac{l}{\mathrm{M}}, 0\right), \tag{9.2}$$

where a is the in-plane lattice parameter, l is any integer number and M corresponds to the M×M×1 Monkhorst-Pack grid used.

9.2.2 Band structure

As an example, in Fig. 9.2 the calculated electronic band structure of Pb(111) freestanding films of several thicknesses is shown. For a N MLs thick film, each electron

state energy level is unfolded in N subbands. The subbands below -6 eV are of s character. They are separated by a gap from the 3N subbands of p character which form the Fermi surfaces of the slabs. As can be seen from Fig. 9.2, the width of the gap is already fixed as $\sim$2 eV for the 3 MLs thick film.

Around the SBZ center ($\overline{\Gamma}$ point) the energy bands present a parabolic free-electron-like dispersion. The p bands around $\overline{\Gamma}$ have a p_z character, while acquiring an increasing $p_{x,y}$ component as they loss their parabolic-like dispersion moving away from $\overline{\Gamma}$. The p_z states at $\overline{\Gamma}$ represent the QWS of the Pb(111) films. The present work found that the inverse of the energy separation of the QWS around E_F is linearly proportional to the film thickness, in good agreement with a previous study [MWYC02].

SOC effects

As a centrosymmetric supercell was used in the calculations, due to the Kramers degeneracy (see Section 5.2) the electron energy bands are doubly degenerated also when SOC is included in the Hamiltonian (see Fig. 9.2). In contrast with its remarkable effect on the bulk electronic band structure, SOC has little impact on the energy bands of the Pb(111) films. In Fig. 9.2 the band structure and DOS for the 1 - 3 MLs thick films is shown with (dashed red lines) and without (solid black lines) SOC included in the Hamiltonian. As readily seen, SOC effects are remarkable only for the single monolayer case, which becomes semimetallic when SOC is switched on, as a result of the avoiding of the band-crossings present for the scalar-relativistic system around the Fermi level. Also, the s band is shifted upwards by $\sim$ 0.4 eV for the 1 ML upon switching on the SOC.

As the slab thickness is increased, also the filling of the phase space by the unfolding of the subbands increases. Because of the fast filling of the phase space, SOC effects on the ground state of Pb(111) films become small for slabs as thin as 3 MLs (see Fig. 9.2), as avoiding of the band-crossings is the only SOC effect noted on the electronic structure of the films. As a result only for the somewhat artificial semimetallic single Pb(111) monolayer SOC effects are remarkable. Also, inclusion of SOC leaves the effective masses of the QWS and the Fermi contours unchanged, except for the single monolayer. Notice that SOC affects the states with a remarkable $p_{x,y}$ character, while the p_z QWS around $\overline{\Gamma}$ remain unchanged upon inclusion of the spin-orbit interaction.

The small significance of the SOC effects on the electronic structure of Pb(111) films is in agreement with the fact that the QWS arise from the quantization of bulk electronic states along the $\Gamma-$L symmetry direction [MWYC02, HBP$^+$09], direction in which (as was shown in Fig. 5.3) SOC has negligible effect on the p band crossing E_F for energies $\epsilon - E_F < 3.5$ eV. Actually, it has been found that in Pb(111) films SOC effects on the energy bands are negligible for $\epsilon - E_F \gtrsim 5$ eV. This finding seems surprising at first sight as the bulk Pb parental energy band in $\Gamma-$L present strong SOC-induced energy lowering when approaching the BZ center, at energies $\epsilon - E_F \gtrsim 3.5$ eV (see Fig. 5.3). However, at those energies the electrons in the Pb(111) films are

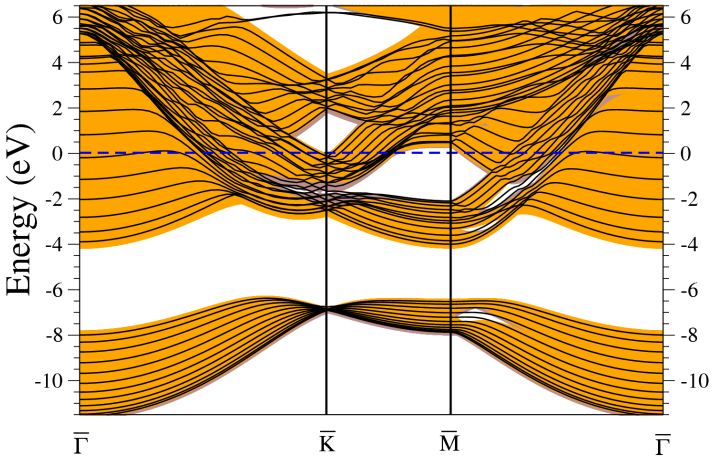

Figure 9.3: Pb(111) surface electronic structure. The orange (brown) area represents the bulk band structure projected on the (111) surface without (with) the SOC included. Black lines are the bands corresponding to the electronic structure of a 12 MLs thick film, obtained at the scalar-relativistic level. The dashed blue horizontal line marks the Fermi level.

close to the vacuum level (see Section 9.3.3) and start to acquire and image state-like character [ZZMS$^+$12]. As a consequence, electrons in the Pb(111) films with energies $\epsilon - E_F \gtrsim 4.2$ eV are unbounded, their wave functions being located in the vacuum and thus resting unaffected by the SOC potential.

9.2.3 Electronic structure of the Pb(111) surface

In Fig. 9.3 the calculated electronic structure of a 12 MLs thick film at the scalar-relativistic level is shown together with the bulk band structure projected on the (111) surface without (orange area) and with (brown area) the SOC included in the Hamiltonian. The surface states, that is, the bands of the 12 MLs thick slab which are non-degenerated in energy with the continuum of the bulk electronic structure projection, were found to be converged with respect to the film thickness for the 12 MLs case shown in Fig. 9.3. As seen in the figure, surface states are present along the $\overline{\Gamma} - \overline{\mathrm{M}}$ high-symmetry direction at energies of -7 eV, -3.3 eV and an additional strongly dispersing surface state band is also seen between roughly 1 and 2 eV binding energies.

On the other hand, around the $\overline{\mathrm{K}}$ and at energies from ~ -1.3 to ~ -2.2 eV, bands appear degenerated with the bulk continuum only when SOC is incoporated. Also, an unocuppied surface state at energies ~ 6 eV above E_F is found around $\overline{\mathrm{K}}$ in a sizeable region of the BZ, presenting a negative effective mass (see Fig. 9.3). However, this unoccupied state is unbounded as it is energetically located above the vacuum level (concerning the work function of Pb(111) surface and films, see Section 9.3.3 below).

To the best of our knowledge, no surface states of lead have been experimentally detected so far.

9.3 Quantum-size effects on Pb(111) films

QSE reflected in the bilayer oscillations detected in several physical properties of Pb(111) films as a function of the thickness (see Section 9.1) are a consequence of the stability of electronic standing waves formed in the direction perpendicular to the slab plane. In Pb(111) films, the magnitude of the interlayer spacing c is close to $3\lambda_F/4$ [JLZX07], where λ_F is the Fermi wavelength. Thus, in a layer-by-layer growth, films presenting an even number of MLs (or odd number of MLs depending on the details and definition of the wetting layer/interface with the substrate [BAYCT00, YBBZW$^+$00, JWHWYZ06]) should be highly stable [AOZ07], forming the so-called magic heights which have been detected in several experimental works (for a review, see Ref. [JLZX07]). However, the ratio λ_F/c is not exactly of 4/3 and a beating pattern is formed of period 9 ML.

The results of the calculations for the films ground state show bilayer oscillations with the slab thickness on the density of states at the Fermi level and on the work function (see Section 9.3.3), with a beating pattern of period 9 ML superimposed. This is in agreement with previous experimental and theoretical studies (see, i.e., Refs. [KQY$^+$10] and [MWYC02]).

9.3.1 QSE on the DOS of Pb(111) films

In Fig. 9.4 the DOS in the -4 eV $< \epsilon <$ 4 eV energy range is plotted as a function of the film thickness. Good agreement is found with previous theoretical works, see Ref. [MWYC02]. Note the branches of QWS can be labeled by a quantum number n (see, i.e., Ref. [ZZMS$^+$09]). The beating pattern of period 9 ML superimposed on the bilayer oscillations of ground state properties is expected from an inspection of Fig. 9.4. In particular, the period of 9 MLs of the beating pattern is observed in Fig. 9.4 as QWS with $\epsilon \sim E_F$ appear for the 4 and 13 MLs thick films.

9.3.2 Effective masses of the QWS

It is of interest to analyze if QSE appear on the values of the effective masses of the QWS, that is, the p_z states at $\overline{\Gamma}$. In order to clarify this question, the dispersion of the QWS bands around $\overline{\Gamma}$ have been fitted to a parabola up to $\mathbf{q} = (0.12, 0, 0)$ a.u. Note that the results are independent of inclusion of SOC, as explained in Section 9.2.2. The results are plotted in Fig. 9.5 for the energy range of $-4.2 \lesssim \epsilon \lesssim 4.2$ eV.

First, note that the values of m^* show a distinct quantitative behaviour in two different energy ranges, below and above $\epsilon = 0.7$ eV. Nevertheless, in both ranges the values of the effective masses tend to a thick film limit of m^* as a function of the QWS energy. This is seen in Fig. 9.5 by noting that the results for the QWS corresponding to the thickest studied slabs are marked by diamonds. For $\epsilon < 0.7$ eV m^* exhibit small

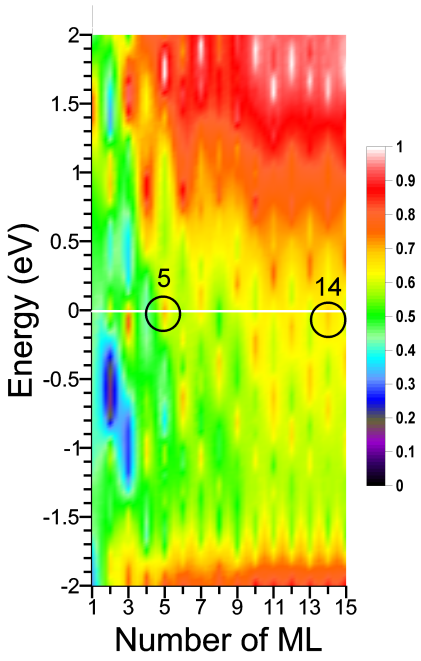

Figure 9.4: Normalized DOS of the films in the $-4\,\text{eV} < \epsilon < 4\,\text{eV}$ energy range as a function of the film thickness. The white horizontal line represents the Fermi level. The energy of the QWSs at $\sim E_F$ are marked and labeled with the number of MLs of the corresponding film.

scattering, however, as shown in the left inset of Fig. 9.5 still the QWS corresponding to the thinnest slabs show no convergence of their effective masses with respect to the limit represented by the values of m^* marked by diamonds. Thus, not only the energies of the QWS, but also their effective masses show QSE.

Notice that there is a QWS at $\epsilon \sim 0.7$ eV for each film presenting an even number of MLs (see right inset in Fig. 9.5). This is in agreement with previous theoretical works [ZZGBVC11b,MWYC02], scanning tunneling spectroscopy (STS) measurements on Pb/Cu(111) [CYLLBS$^+$09] and 2PPE experiments in Pb/Si(111) [SKRZ$^+$10]. In the latter the series of QWS were clearly resolved as their energy lies in the silicon absolut band gap.

Actually, two additional series of QWS at different thickness exhibiting roughly constant energies are found, which are marked in the left inset of Fig. 9.5 by ellipses. The series marked by a blue (orange) ellipse for QWS energies $\sim$ -2.6 eV (-1.6 eV) corresponds to states of Pb(111) films with a $2+4n$ ($1+3n$) number of MLs, where n is an integer. This is in qualitative agreement with the results reported in Ref. [MWYC02]. The appearance of the constant-energy series is a clear QSE. Again, as for the series at $\epsilon \sim 0.7$ eV, the effective masses of these states tend to converge for the thickest slabs. Note that the scattering of the $m^* = m^*(\epsilon)$ increases after each of the constant-energy QWS series.

Clearly enough, the constant-energy series reflect the particle-in-a-box character of the quantum-well states. For a particle in an infinite potential well, the allowed energies are of the form

$$\epsilon_n = \frac{\pi^2 n^2}{2m^* d^2}, \tag{9.3}$$

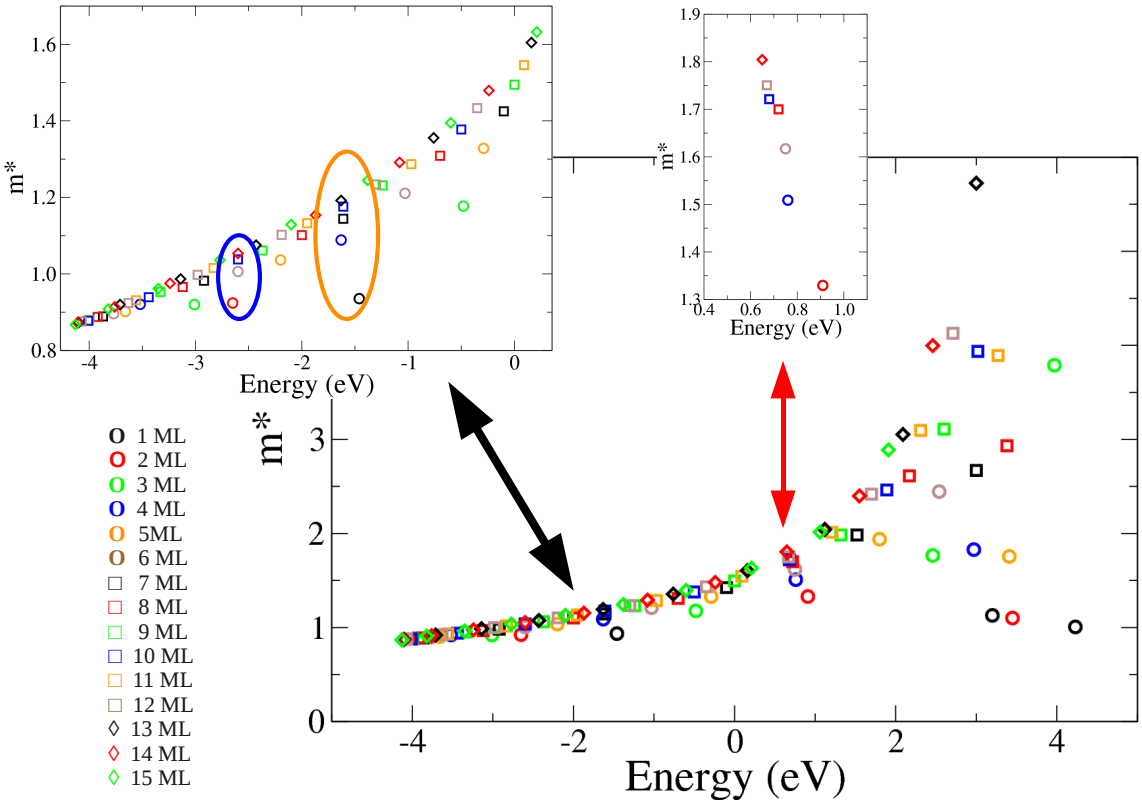

Figure 9.5: Effective masses of QWS in Pb(111) films of 1 - 15 MLs thick, obtained from scalar-relativistic band structure calculations. See the text for an explanation of the insets. Effective masses in units of the free electron mass.

where n is an integer and d stands for the width of the well. Thus, for a constant n/d ratio, a series of QWS presenting the same energy are found. Notice that the small scattering of the energies for a given n/d series is due precisely to the actual effective masses which are a consequence of the band structure effects together with the deviation of the actual potential from an infinite potential well. Also, in Ref. [SMOHD11] it was shown that the QWS effective masses are highly sensitive to variations of the in-plane lattice constant.

9.3.3 Work function of the Pb(111) films

It has been shown both theoretically [MWYC02] and experimentally [KQY+10] that the work function of Pb(111) thin films exhibits bilayer oscillation on its thickness dependence. In Fig. 9.6 we report the values of the work functions of Pb(111) thin films as obtained in this thesis. Black squares (red circles) correspond to the work functions of slabs converged using a 10×10×1 (12×12×1) Monkhorst-Pack grid. Note that for the coarser k point mesh the values of the work function are higher than for

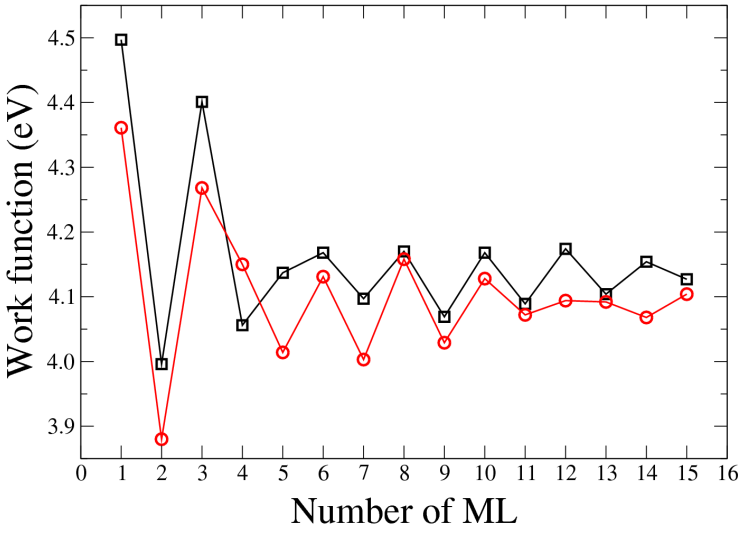

Figure 9.6: Thickness dependence of the work function of Pb(111) films. Black squares (red circles) correspond to the work functions of slabs converged using a 10×10×1 (12×12×1) Monkhorst-Pack grid.

the finner mesh at every thickness except for the 4ML case, which is related to the appearance of the aforementioned beating pattern.

Interestingly, using the 10×10×1 grid the beating pattern of 9 ML period is missing, while it appears for the finner 12×12×1 SBZ sampling mesh calculations, where two crossovers are found at 4 and 13 MLs (see Fig. 9.6).

The present results reported in Fig. 9.6 are in perfect agreement with the data obtained in the theoretical study of Ref. [MWYC02]. This is in spite of the different *xc* functional used, as the generalized-gradient approximation (GGA) [PPBE96] was used in Ref. [MWYC02], and of the fact that the films were structuraly relaxed in Ref. [MWYC02]. Thus, the agreement points to the insignificant relaxation effects in the electronic structure of Pb(111) films (see Section 9.2.1).

9.4 Summary

In the present first-principles study of the ground state electronic properties of free-standing Pb(111) thin films SOC effects were found remarkable only for the single monolayer case, which can be understood in terms of the bulk band structure in the $\Gamma-$L high-symmetry direction.

QSE have been observed in the QWS effective masses, DOS and work function of the films. The two latter show a bilayer oscillatory dependence on the slab thickness, with a beating pattern of period 9 ML superimposed. This is in failry good agreement with previous theoretical and experimental results, reflecting the quality of the calculations reported in the present Chapter and their convergence with respect to the different computational parameters.

Chapter 10

Dielectric response of Pb(111) films

10.1 Introduction: plasmons of thin metallic films

Even if Pb(111) thin films represent one of the most widely used playgrounds in the study on QSE (see Section 9.1), to the best of our knowledge, there are few experimental studies on the surface response of Pb thin slabs [JSZ02, JSZ04, PKFJ06], and no theoretical works. Thus, the aim of the present work is to perform a computational systematic study of the surface energy-loss function of Pb(111) films with different thicknesses, starting from a single monolayer case, up to a 15 MLs thick slab.

An approximate description of thin film plasmons is given by the solution of the Maxwell equations applied to a slab geometry [HR57]. It leads to the coupling between the classical surface plasmons of the two different surfaces of the film. The resulting coupled modes of the film disperse as [HR57, YG06, MPMSVCME07]

$$\omega_{\pm} = \frac{\omega_p}{\sqrt{2}}(1 \pm e^{-qL})^{1/2}, \tag{10.1}$$

where ω_p is the bulk plasmon frequency, which is given by $\omega_p = \sqrt{3r_s^{-3}}$ with r_s the average valence electron density parameter (see Fig. 10.1). The energy splitting between the modes depends on the film thickness L and the value of the in-plane momentum transfer q. The low-energy mode ω_- correponds to a symmetric induced charge profile in the direction perpendicular to the film plane, whereas the high-energy mode ω_+ corresponds to an antisymmetric one [YG06]. As L increases, the coupling between the two modes decreases. In the limit $L \gg 1/q$ the two film modes are decoupled and the two classical surface plasmons of frequency $\omega_p/\sqrt{2}$ are retrieved. This model description ignores the electronic structure of the film. This is a serious drawback since the ground state electronic structure has been shown to strongly affect the surface response to external perturbations. More detailed classical models showed the dependence of the surface plasmon dispersion on the microscopic details of the surface electronic density profile [JB70, SLS82].

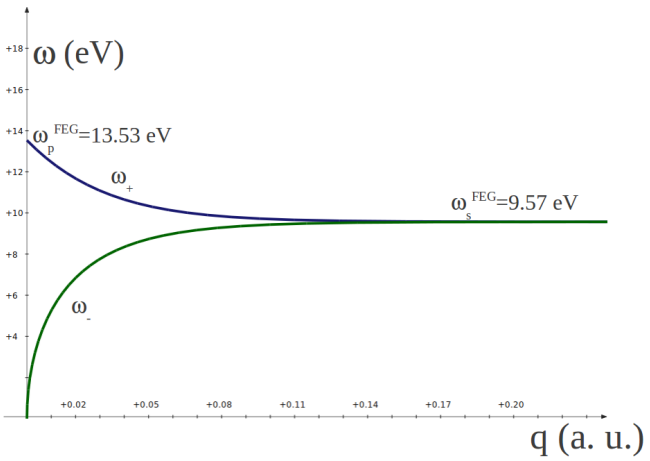

Figure 10.1: Classical plasmon modes in a thin film, Eq. (10.1). The curves are evaluated for the parameters corresponding to a 7 MLs thick Pb(111) film.

On a more quantitative level, the jellium model [DLK70] has been used to study the quantum-mechanical electrodynamical response of metal slabs [GE83, FD92, LSFD94], gaining basic insight into the nature of electronic excitations of metallic films. As an example, Yuan and Gao have shown [YG06], using the jellium model with the electron density corresponding to Ag, the disappearance of the antisymmetric mode ω_+ for $q \to 0$ when the film thickness is comparable to the Fermi wavelength. Instead, a few discrete interband peaks were found [YG06].

A more precise description of the electron band structure in the direction perpendicular to the film plane [VCMSME97, VCMSME99], allowing to describe the surface states which are missing in a jellium model, was recently used to study new collective electronic excitations at metal surfaces [MSMPVCME05, PDV+10, EKMSUN+10] and thin metal films [MSND+11]. However, the recipe of the improved one-dimensional potential [VCMSME97, VCMSME99] can not give a satisfactory description of the electronic structure of Pb(111) films. Thus, in the present work a first-principles approach is used to study the dielectric response of Pb(111) films. Indeed, using an *ab initio* calculation scheme possible anisotropy effects can be studied, which are missing in jellium models or in using the potentials of Refs. [VCMSME97] and [VCMSME99], as they assume in-plane free-electron-like behavior.

10.2 Computational parameters and choice of the xc kernel

The calculation of $\chi^0_{\mathbf{G},\mathbf{G}'}(\mathbf{q}_\parallel, \omega)$ was carried out using a Monkhorst-Pack 96×96×1 (192×192×1) grid (see Section 9.2.1) of $\mathbf{k}$ vectors as the hexagonal SBZ sampling with 817 (3169) $\mathbf{k}$ vectors in the ISBZ for the 1, 2, and 6-15 MLs (3-5 MLs) thick films. Up to 500 bands were included in the evaluation of $\chi^0_{\mathbf{G},\mathbf{G}'}(\mathbf{q}_\parallel, \omega)$ for the thickest studied slabs.

The width of the modified Gaussian replacing the energy-conservation Dirac delta (see Appendix D) in the calculation of $\chi^0_{\mathbf{G},\mathbf{G}'}(\mathbf{q}_\parallel,\omega)$ through Eqs. (3.19)-(3.21) was set to 0.15 eV, a value which has produced smooth resulting curves while not smearing out any feature on the surface loss function of the films. Well converged results are found including 750 plane waves in the expansion of the wave functions in the calculation of $\chi^0_{\mathbf{G},\mathbf{G}'}(\mathbf{q}_\parallel,\omega)$ and expanding the size of the polarizability matrices up to 60 $\mathbf{G}$ vectors.

Throughout the work reported in the present Chapter we use the RPA in which the *xc* kernel is set to zero (see Section 3.2.2), i.e., the dynamical short-range exchange-correlation effects are ignored. The previous studies of collective excitations at the surfaces [Nag10, NHHH01, TWPL$^+$91, MSVCME04] and in the bulk [AK94, EKS99] of many metallic systems suggest that *xc* effects should have little impact on the study of the surface dielectric response of Pb films. Actually, *xc* effects are known to remarkably affect the dielectric response of solids presenting a low valence average density ($r_s > 4$) [Lie97], while slightly influencing it in high valence density systems. Pb is a high-density metal ($r_s^{\mathrm{Pb}} = 2.298$), and thus *xc* effects should not be substantial. In fact, studies on the surface loss function of aliminium [TWPL$^+$91], which presents an average valence electron density similar to Pb, showed appreciable but small *xc* effects on the dispersion of the surface plasmon.

10.3 Results obtained using Eqs. (3.28)-(3.29)

In Fig. 10.2 the general results obtained using the recipe described in Section 3.3.2 together with the expressions (3.28)-(3.29) for the interacting susceptibility are presented. Based on the model of thin film plasmons Eq. (10.1), one expects the film modes to be splitted in the range of momentum transfer studied. However, comparing the results shown in Fig. 10.2 with the classical model of Eq. (10.1) remarkable dissimilarities are revealed. No feature analogous to the classical antisymmetric mode ω_+ is found starting from the single monolayer case. On the other hand, the symmetric mode seems to be present. However, a detailed analysis of $\mathrm{Im}[g(\mathbf{q}_\parallel,\omega)]$ of the single monolayer shows that the peak in its surface loss function at $\omega \simeq 4.5$ eV at $q \to 0$ does not correspond to the symmetric mode ω_- predicted by Eq. (10.1).

In order to get further insight on this issue, the dispersion of the low-energy peak seen in Fig. 10.2 for the single monolayer results has been fitted to $\omega_-(q)$ as given by Eq. (10.1), ignoring the first q values. The fitting parameters are then the surface plasmon energy $\omega_p/\sqrt{2}$ and the film thickness L. In Fig. 10.3 the results on the dispersion of the low-energy mode are shown together with the fitting. The fitting helps to clarify that the mode presents two different behaviors. For $q \geqslant 0.1$ a.u. it follows a classical-like dispersion. However, for $q < 0.1$ a.u. the dispersion clearly deviates from the classical description of $\omega_-(q)$. Thus, from Fig. 10.3 a finite value of ~ 4.5 - 5 eV is deduced for the low-energy mode at $q \to 0$.

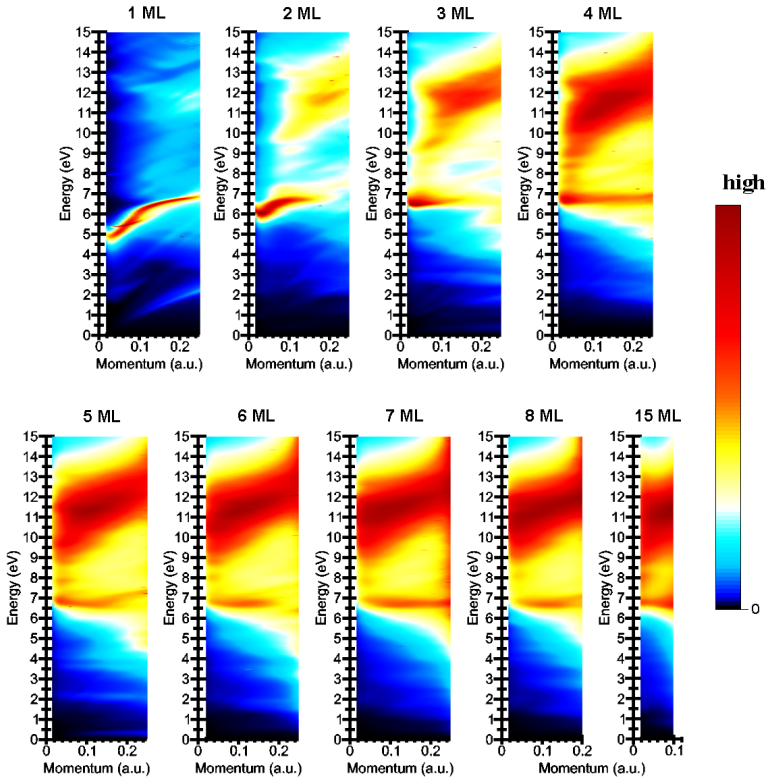

Figure 10.2: Surface loss function surfaces $\mathrm{Im}[g(\mathbf{q}_{\parallel},\omega)]$ for 1 - 8 and 15 MLs thick Pb(111) films calculated at the scalar-relativistic level, obtained using Eqs. (3.28)-(3.29) for the evaluation of $\chi_{\mathbf{G},\mathbf{G}'}(\mathbf{q}_{\parallel},\omega)$. The momentum transfer vector $\mathbf{q}_{\parallel}$ is along $\overline{\Gamma}-\overline{\mathrm{M}}$. The colour bar applies to all plots, with its maximum normalized individually for each case.

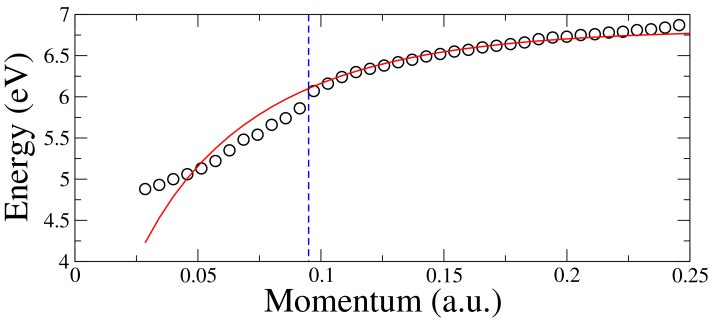

Figure 10.3: Dispersion of the low-energy peak for the single Pb(111) results as shown in Fig. 10.2. The circles represent the results of the calculations, while the solid line is the result of fitting the data for $q \gtrsim 0.1$ a.u. to the low-energy solution of Eq. (10.1).

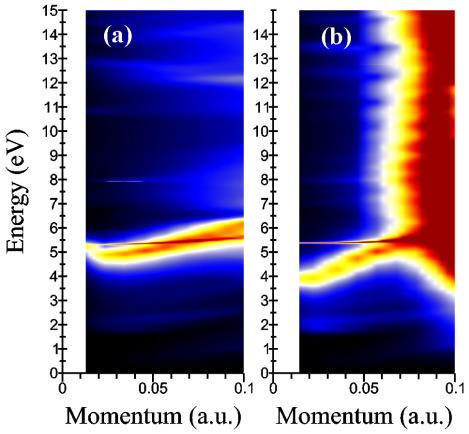

Figure 10.4: 1 ML surface loss function obtained using Eqs. (3.28)-(3.29)), and with 54.1 and 108.2 a.u. of vacuum thickness in the supercell in panel (a) and (b), respectively.

To explain the origin of this finite value of the low-energy peak for the single monolayer case, the calculations were repeated doubling the amount of vacuum in the supercell up to 108.2 a.u. (20 interlayer distances). In Fig. 10.4 the comparison of the $\mathrm{Im}[g(\mathbf{q}_{\parallel},\omega)]$ of 1 ML evaluated for both vacuum thicknesses is shown. As readily seen, the low-energy peak at $q \to 0$ is redshifted to a value of ~ 3.5 - 4 eV, but still it exhibits a finite energy. This points to a defficiency of the computational scheme used so far when applied to supercell calculations.

The defficiency stems from the evaluation of Eqs. (3.28)-(3.29) resulting from the Dyson-like equation Eq. (3.15), in which both integrations are extended over the whole space. This makes the perturbation in the long wavelength limit see the infinite series of slabs in the spatial z direction. As a consequence, the perturbation at $q \to 0$ feels an average electron density, which can be parametrized by an effective density parameter r_s^{eff} by distributing the number of valence electrons over the whole supercell volume. Then, introducing r_s^{eff} in the expression $\omega_p = \sqrt{3r_s^{-3}}$ the energy of the artificial supercell-bulk plasmon is obtained. Note that the supercell containing a vacuum region of 10 (20) interlayer presents a volume 10 (20) times larger than the bulk Pb unit cell. Then, as $\omega_p \propto \Omega^{-1/2}$, where Ω is the unit cell or supercell volume, the finite values of the low-energy peaks at $q \to 0$ in Fig. 10.4 can be assigned to the aforementioned artificial supercell-bulk plasmon.

The incorrect picture drawn by Eqs. (3.28)-(3.29) in the long wavelength limit when dealing with supercell calculations was recently noted by Yuan and Gao in Ref. [YG09]. The authors showed that the three-dimensional periodicity must be removed in the evaluation of the interacting susceptibility in order to avoid interaction between neighboring slabs through the long range Coulomb interaction.

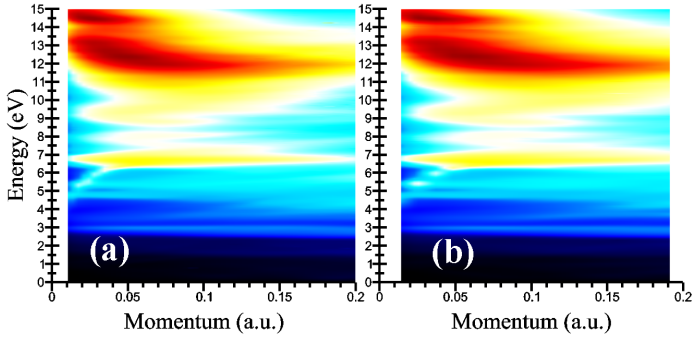

Figure 10.5: Calculated surface loss function for the 3MLs thick Pb(111) film, with $\mathbf{q}_{\parallel}$ along two different high-symmetry directions, $\overline{\Gamma}-\overline{\mathrm{M}}$ (a) and $\overline{\Gamma}-\overline{\mathrm{K}}$ (b).

10.4 General results: corrected evaluation of $\chi_{\mathbf{G},\mathbf{G}'}(\mathbf{q}_{\parallel},\omega)$ for the supercell scheme

As shown in the previous Section, the calculation of $\chi_{\mathbf{G},\mathbf{G}'}(\mathbf{q}_{\parallel},\omega)$ as given by Eqs. (3.28)-(3.29) has to be corrected when dealing with supercell calculations. The way this problem is tackle in the present work is to still make use of formally the same Eqs. (3.28)-(3.29), but constraining both integrations in Eq. (3.15) to a finite z range, which here is fixed as the supercell size in the z direction. In practice, we keep using Eqs. (3.28)-(3.29), but now the non-interacting susceptibility matrix $\chi^{0}_{\mathbf{G},\mathbf{G}'}(\mathbf{q}_{\parallel},\omega)$ is replaced in Eqs. (3.28)-(3.29) by the following modified form:

$$\chi^{m}_{\mathbf{G},\mathbf{G}'}(\mathbf{q}_{\parallel},\omega)=\sum_{\mathbf{G}''}\chi^{0}_{\mathbf{G},\mathbf{G}''}(\mathbf{q}_{\parallel},\omega)\cdot\delta_{\mathbf{G}'',\mathbf{G}'}\times$$
$$\times\left[\delta_{G''_z,G'_z}-\frac{(|\mathbf{q}_{\parallel}+\mathbf{G}''|^2-G''_zG'_z)\cos\left[\frac{(G''_z+G'_z)T}{2}\right](1-e^{-|\mathbf{q}_{\parallel}+\mathbf{G}''_{\parallel}|T})}{|\mathbf{q}_{\parallel}+\mathbf{G}''_{\parallel}|T(|\mathbf{q}_{\parallel}+\mathbf{G}''_{\parallel}|^2+G''^2_z)}\right], \quad (10.2)$$

where $2T$ is the size of the integration domain (the supercell size in the z direction in our case). G_z stands for the z-component of the reciprocal space vector $\mathbf{G}$. Let us remind that, as explained in Section 3.3.2, we actually work with the basis of reciprocal vectors of the form $\mathbf{G}=(0,0,G_z)$.

Before analyzing the general results retrieved with this corrected scheme, in Fig. 10.5 the calculated surface loss function for the 3MLs thick Pb(111) film, with $\mathbf{q}_{\parallel}$ along two different high-symmetry directions, namely $\overline{\Gamma}-\overline{\mathrm{M}}$ [panel (a)] and $\overline{\Gamma}-\overline{\mathrm{K}}$ [panel (b)] is shown. It is clear that $\mathrm{Im}[g(\mathbf{q}_{\parallel},\omega)]$ exhibits a highly isotropic character. In all the carried tests the same isotropic behaviour of the surface loss function was found independently of the film thickness. Thus, from here on only results for $\mathbf{q}_{\parallel}$ along $\overline{\Gamma}-\overline{\mathrm{M}}$ are shown in this thesis, as the used grid in this high-symmetry direction is finer than the one along $\overline{\Gamma}-\overline{\mathrm{K}}$ (see Section 9.2.1).

The general results obtained using the corrected scheme are shown in Fig. 10.6. First, note the different general picture in comparison with the uncorrected results presented in Fig. 10.2. Now the thin film modes analogous to the $\omega_{\pm}$ plasmons of

Eq. (10.1) are found. In order to get further insight, the dispersion of $\omega_{\pm} = \omega_{\pm}(q)$ is represented by green lines. For each freestanding slab, $\omega_{\pm}(q)$ are plotted for an effective thickness corresponding to a number of interlayer distances equal to the MLs forming the slab, as the jellium edge in the first-principles calculations was fixed at half an interlayer distance away from the outermost atomic layers.

10.4.1 Thin film modes

The results of the present work as plotted in Fig. 10.6 show several modes of different character. First, the low-energy symmetric mode is detected for the thinnest slabs at small momentum transfer values, closely following the dispersion described by the low-energy ω_{-} mode of Eq. (10.1) for all thicknesses as represented in Fig. 10.6 by the bottom green line in each panel. However, notice that it disappears upon entering the almost dispersionless peak present around $\omega \simeq 7$ eV for all thicknesses.

Also, the high-energy plasmon mode analogous to the classical thin film ω_{+} mode is found for thicknesses greater than 2MLs. Note however that it is placed at too high energies in comparison with the predictions of Eq. (10.1). Unfortunately, calculations including the $5d$ semicore electrons (see Section 7.2) are too computationally demanding in the supercell scheme used here. Thus, it has not been checked whether the too high energy of the antisymmetric mode found in this thesis is due to the absence of the semicore states in the evaluation of the surface response function. Note that the inclusion of the polarizable $5d$ semicore electrons through the use of a model dielectric function ε_d [Lie97] is ambiguous and its use has been discarded in this thesis (see Section 7.6).

As mentioned in Section 10.1, in Ref. [YG06] using jellium calculations it was shown that the antisymmetric mode disappears for film thicknesses comparable or smaller than the metal Fermi wavelength when $q \to 0$. Instead, peaks corresponding to discrete interband transitions show up. For Pb, using the value $r_s^{\mathrm{Pb}} = 2.298$, one finds $\lambda_F^{\mathrm{Pb}} = 7.52$ a.u. which is roughly 1.4 times the interlayer distance in Pb(111) films. Thus, the 1 and 2 MLs thick Pb(111) films present electronic effective thicknesses equal to 0.7 and 1.4 times λ_F^{Pb}, respectively. As seen in Fig. 10.6, our results are in agreement with the work of Ref. [YG06] as far as the disappereance of the high-energy mode for thin films is concerned. In the surface loss function of the single monolayer shown in Fig. 10.6, a manifold of interband peaks is present for energy transfers $\omega \gtrsim 11$ eV [see also the black solid curve in Fig. 10.8 (a)], where the high-energy mode should be present (see the upper green line in the first panel of Fig. 10.6). This is a manifestation of strong QSE in the surface-loss function of the single Pb(111) monolayer. The 2 ML $\mathrm{Im}[g(\mathbf{q}_{\parallel}, \omega)]$ results (see Fig. 10.6) correspond to the transition between the two different thickness regimes, at $L \simeq 1.4\lambda_F^{\mathrm{Pb}}$.

An important conclusion of the present work is the large difference in spectral weight between the low- and high-energy modes of the film, in sharp contrast with the

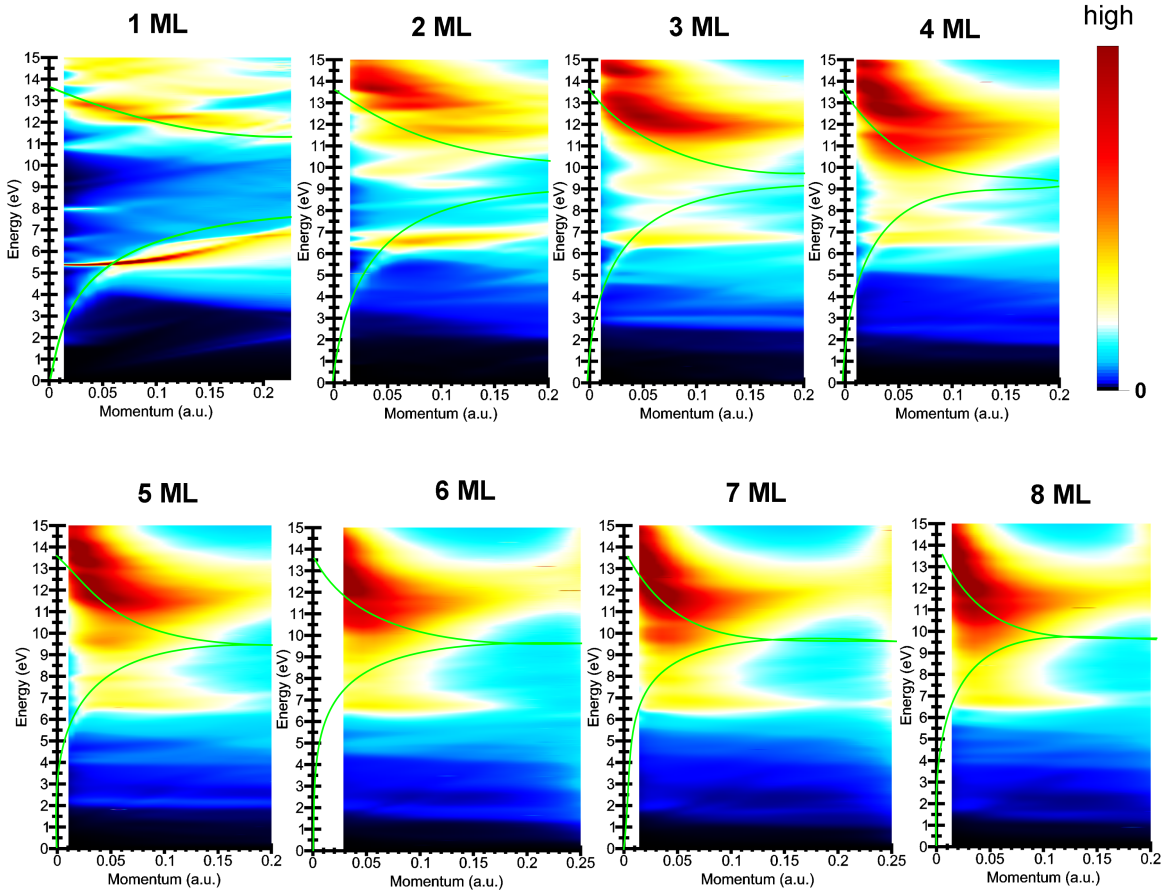

Figure 10.6: Surface loss function surfaces $\mathrm{Im}[g(\mathbf{q}_{\parallel},\omega)]$ for 1 - 8 MLs thick Pb(111) films obtained with the corrected scheme at the scalar-relativistic level. The momentum transfer $\mathbf{q}_{\parallel}$ is along $\overline{\Gamma}-\overline{\mathrm{M}}$. The green lines represent the dispersion of the classical thin film plasmon modes as given by Eq. (10.1), plotted for the corresponding slab thickness (see the text). The colour bar applies to all plots, with its maximum normalized individually for each case.

results reported in Ref. [YG06] for Ag slabs modeled by the jellium approximation. The low-energy mode analogous to the classical symmetric ω_{-} plasmon appears as a faint feature in comparison with the rest of the peaks present in $\mathrm{Im}[g(\mathbf{q}_{\parallel},\omega)]$. On the contrary, the high-energy mode is the most intense feature in the surface loss function of freestanding Pb(111) films, except for the single monolayer. In the latter case, a slightly upwards dispersing interband peak raises at energies $\omega \simeq 5.5-6$ eV. It exhibits the highest intensity [see Fig. 10.8 (a) and (b)] together with a vanishing linewidth at momentum transfer smaller than 0.1 a.u. This long-living mode stems from transitions between the highest occupied and lowest unoccupied QWSs around the SBZ center (see Fig. 9.2), representing strong QSE. Once more the 2 MLs results represent the crossover with larger thicknesses for which the quantization of the states is not reflected in the same fashion in the calculated surface loss function. Nevertheless, in the evaluated $\mathrm{Im}[g(\mathbf{q}_{\parallel},\omega)]$ corresponding to the 2 MLs thick slab, still two peaks similar to the long-living mode in 1ML are found overlaping with each other. However, their intensity is

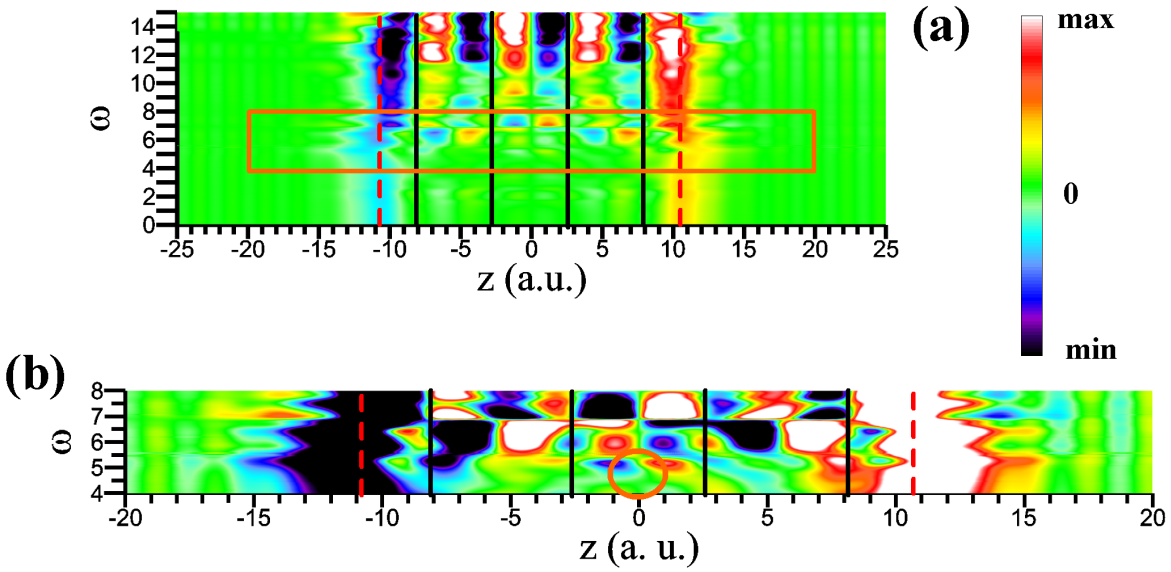

Figure 10.7: Real part of the induced density at q=0.014 a.u. for the 4 MLs Pb(111) film, as a function of the energy transfer ω and the z coordinate. Panel (b) is a zoom in the (ω, z) range delimited by the orange rectangle in panel (b). The orange circle in (b) highlights the fingerprint of the low-energy symmetric mode (see the text). Black solid (red dashed) lines mark the position of the atomic layers (jellium edges). ω in eV.

greatly decreased in comparison with the corresponding feature in the single monolayer case.

In Fig. 10.7 the real part of the two-dimensional Fourier transform of the induced density [see Eq. (3.14)] $\mathrm{Re}[\rho_{ind}(z, \mathbf{q}_{\parallel}, \omega)]$ for the 4 MLs thick slab is shown. The results correspond to a momentum transfer of $q = 0.0114$ a.u. First, note the antisymmetric distribution of the induced density with respect to z=0. Second, for spatial positions inside the film, several changes of the sign of $\mathrm{Re}[\rho_{ind}]$ are found. In panel (b) results for $4 \leqslant \omega \leqslant 8$ eV are zoomed in. Interestingly a sharp change of phase of $\mathrm{Re}[\rho_{ind}]$ can be recognized at $\omega \simeq 7$ eV, signaling about the presence of the dispersionless peak seen in $\mathrm{Im}[g(\mathbf{q}_{\parallel}, \omega)]$ at this energy. This is a general behaviour found at all thicknesses at $\omega \simeq 7$ eV.

Moreover, the fingerprint of the low-energy mode analogous to the classical symmetric ω_- plasmon is found, as marked by the circle in panel (b) of Fig. 10.7. As can be seen, $\omega \sim 5$ eV is the only energy at which there is a noticeable weight of $\mathrm{Re}[\rho_{ind}(z, \mathbf{q}_{\parallel}, \omega)]$ at the center of the slab, $z = 0$. This notable distortion in the general antisymmetric distribution of the real part of the two-dimensional Fourier transform of the induced density signals about the presence of the symmetric plasmon mode. This faint but appreciable ω_-−like fingerprint has been found at all thicknesses in which the symmetric mode could be resolved.

10.4.2 Thickness dependence

In order to relate the results for different thicknesses, several cuts of $\mathrm{Im}[g(\mathbf{q}_\parallel, \omega)]$ are plotted in Fig. 10.8 comparing the surface loss function of Pb(111) films of distinct thicknesses for the same momentum transfer values of $\mathbf{q}_\parallel$ along the $\overline{\Gamma} - \overline{\mathrm{M}}$ high-symmetry direction.

In panel (a) of Fig. 10.8 the black curve at $\omega \gtrsim 11$ eV shows the manifold of interband peaks which replaces a single high-energy antisymmetric mode for the Pb monolayer, as discussed in Section 10.4.1. An additional important feature in the surface loss function results for the 1 ML slab is the long-living interband peak found at small momentum transfer, seen at $\omega = 5.5$ eV in panels (a) and (b) of Fig. 10.8.

For the 3, 5 and 8 MLs thick films the surface plasmon is already present at q=0.1256 a.u., as seen in panel (c) of Fig. 10.8. Note that it presents a remarkably smaller intensity than the high-energy asymmetric mode. On the other hand, the low-energy symmetric mode can not be seen in the scale of Fig. 10.8, as it is a faint feature (see also Fig. 10.6).

10.4.3 Surface plasmon

In Fig. 10.8 the vertical dashed line marks the classical surface plasmon energy $\omega_s = \omega_p/\sqrt{2} = \sqrt{1.5 r_s^{-3}}$, which for the averaged valence electron density of bulk lead $r_s^{\mathrm{Pb}} = 2.298$ gives the value $\omega_s^{\mathrm{Pb}} = 9.57$ eV. Also, the results of the experimental electron energy-loss measurements of 10.6±0.2 eV [JP60] are represented by the thin shaded area. As can be seen, the classical expression gives a too low value of the surface plasmon energy by about 1 eV.

On the other hand, in the optical limit ($q \to 0$) the surface response function can be calculated from the bulk dielectric function as [Lie87, Lie97]

$$g(q \to 0, \omega) = \frac{\varepsilon^{\mathrm{bulk}}(q \to 0, \omega) - 1}{\varepsilon^{\mathrm{bulk}}(q \to 0, \omega) + 1}, \tag{10.3}$$

and thus the surface loss function is

$$\mathrm{Im}[g(\mathrm{q} \to 0, \omega)] \propto -\mathrm{Im}\left[\frac{1}{\varepsilon^{\mathrm{bulk}}(\mathrm{q} \to 0, \omega) + 1}\right]. \tag{10.4}$$

In Fig. 10.8 the orange (grey) thick solid curve represents $\mathrm{Im}[g(\mathrm{q} \to 0, \omega)]$ calculated using Eq. (10.4) and including the $5d$ electrons in the core (valence). The energy of this peak at HWHM is of 10.85 (9.3) eV with the semicore electrons excluded from (included in) the valence configuration. When using the bulk dielectric function obtained without including the $5d$ electrons, the value retrieved is close to the experimental one of 10.6±0.2 eV. However, the agreement is worsen upon taking the semicore electrons into account in the evaluation of $\varepsilon^{bulk}(q \to 0, \omega)$. Note that the surface loss function

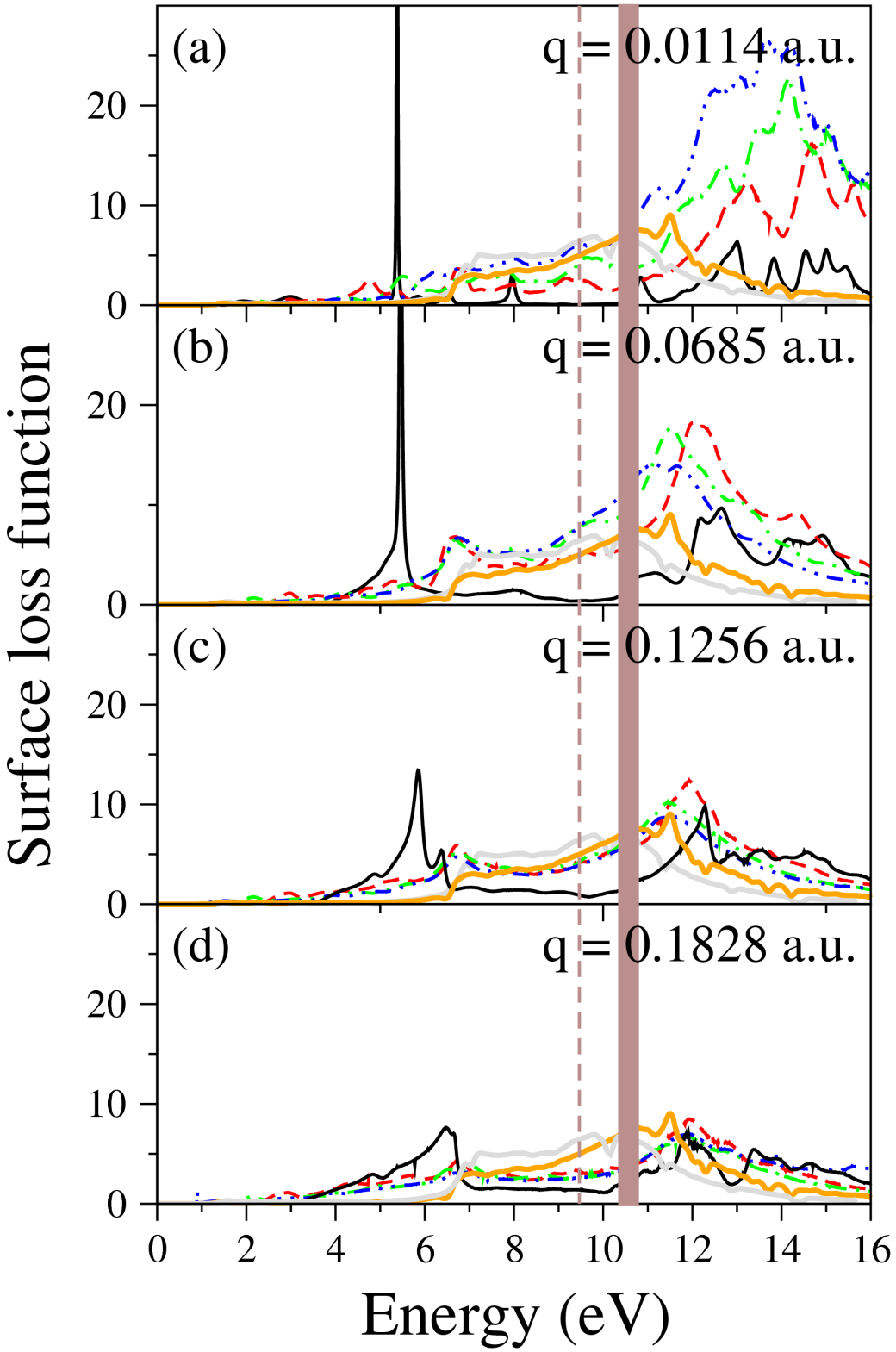

Figure 10.8: Surface loss function for different values of $\mathbf{q}_{\parallel}$ along $\overline{\Gamma}-\overline{\mathrm{M}}$ and different film thicknesses. Black solid, red dashed, green dashed-dotted and blue dashed-dotted-dotted curves represent results for 1, 3, 5, and 8 MLs thick Pb(111) films, respectively. The thick orange (grey) solid curve stands for the results deduced from bulk calculations without (with) inclusion of the $5d$ electrons. The vertical dashed line marks the classical Pb surface plasmon energy of 9.57 eV, while the shaded energy interval corresponds to the electron energy loss experimental value of 10.6±0.2 eV [JP60].

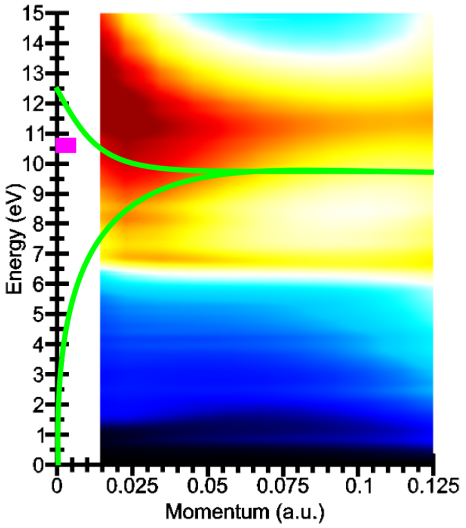

Figure 10.9: Scalar-relativistic surface loss function of the 15 MLs thick Pb(111) film, $\mathbf{q}_{\parallel}$ along $\overline{\Gamma} - \overline{\mathrm{M}}$. The green lines stand for the dispersion of the classical thin film modes as given by Eq. (10.1). The pink square represents the experimental data of Ref. [JP60] of $\omega_s^{\mathrm{exp}} = 10.6 \pm 0.2$ eV.

obtained from a bulk calculation (without the semicore) through Eq. (10.4) is in qualitative agreeement with the slab surface plasmon for thicknesses greater than 2 MLs at momentum transfer values where the modes $\omega_{\pm}$ are uncoupled, see panel (c) in Fig. 10.8.

Surprisingly, $\mathrm{Im}[g(q \to 0, \omega)]$ calculated from the knowledge of $\varepsilon^{bulk}(q \to 0, \omega)$ shows a faint peak at 7 eV, mimicking the dispersionless feature which plays the role of the short wavelength limit of symmetric mode ω_{-} in the the thinnest films (see Section 10.4.1). This signals about the bulk-like character of the aforementioned dispersionless interband mode.

From Figs. 10.6 and 10.9, it seems the surface plasmon disperses roughly linearly with the momentum transfer. In Fig. 10.10 the calculated dispersion $\omega_s = \omega_s(q)$, with $\mathbf{q}_{\parallel}$ along $\overline{\Gamma} - \overline{\mathrm{M}}$, is shown for the 7 ML thick Pb(111) film. Thicker films did not present any remarkable difference in the surface plasmon dispersion. The values of ω_s were evaluated at the position of the HWHM. As can be seen, the surface plasmon presents a fairly linear dispersion as a function of the momentum transfer for $q \gtrsim 0.1$ a.u.

The straight line in Fig. 10.10 is the result of fitting $\omega(q) = A + B \cdot q$ for $q > 0.1$ a.u. The obtained values of the fitting parameters are $A = 10.58$ eV and $B = 7.35$ eV·a.u. It is interesting to compare this findings with a simple model giving a similar behaviour of $\omega_s = \omega_s(q)$.

In a semiinfinite jellium surface, using the so-called on-step hydrodynamic approach [MPMSVCME07, Lun83], the following expression for the dispersion of the surface plasmon is found at long wavelengths:

$$\omega_s(q) = \frac{\omega_p}{\sqrt{2}} + \frac{\beta q}{2}, \tag{10.5}$$

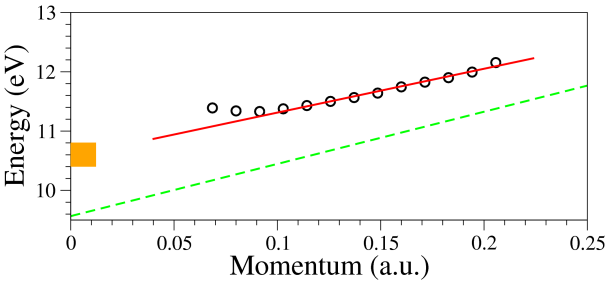

Figure 10.10: Surface plasmon dispersion for the 7 MLs thick Pb(111) film as a function of $\mathbf{q}_{\parallel}$ (along $\overline{\Gamma}-\overline{\mathrm{M}}$). The circles represent the calculated values of the HWHM position at each q. The red solid line is a linear fit of the computational results, while the green dashed one stands for the surface plasmon dispersion in a hydrodynamic approach of the jellium semiinfinite surface (see the text). The shaded orange square marks the experimental interval of $\omega_s^{\mathrm{exp}} = 10.6 \pm 0.2$ eV [JP60].

where $\omega_p/\sqrt{2} = \sqrt{1.5 r_s^{-3}}$ and $\beta = \sqrt{3/5}(v_F/2)$ [MPMSVCME07, Lun83], being $v_F = (9\pi/4)^{1/3} r_s^{-1}$ the Fermi velocity of a free-electron gas of average valence electron density parameter r_s. Using r_s^{Pb} one gets $\omega_p^{\mathrm{Pb}}/\sqrt{2} = 9.57$ eV and $\beta^{\mathrm{Pb}}/2 = 8.801$ eV·a.u. This dispersion is plotted in Fig. 10.10 as a green dashed line, while the orange square shows the energy interval for the experimentally determined value of $\omega_s^{\mathrm{exp}} = 10.6 \pm 0.2$ eV [JP60]. The dispersion derived from the hydrodynamic approach fails in reproducing a correct value for the optical surface plasmon energy (as pointed above). However, the difference in the obtained slope of the two lines in Fig. 10.10 makes the model dispersion Eq. (10.5) move closer to the first-principles result as q increases. Note that strictly speaking, Eq. (10.5) is valid for $q \ll 2\omega_p/\beta$ [MPMSVCME07, Lun83]. In the case of lead, this gives the condition $q \ll 1.087$ a.u.

Finally, note it is difficult to deduce a value of $\omega_s(q \to 0)$ from the present calculations, as the surface plasmon disperses with the momentum transfer in contrast to the classical picture described by Eq. (10.1). In addition, the well-known negative dispersion of the surface plasmon as a function of $\mathbf{q}_{\parallel}$ in the long wavelength limit is not retrieved in the present work, as even for the thickest film studied (15 MLs) the low- and high- energy modes are splitted for the smallest values of $\mathbf{q}_{\parallel}$ used.

10.5 SOC effects

In Chapter 9 it was shown that SOC affects remarkably the electronic structure of a 1 ML Pb(111) slab close to E_F, while mostly leaving unchanged the energy bands of thicker Pb(111) films. In order to check the SOC effects on the surface loss function of the Pb(111) thin films, $\mathrm{Im}[g(\mathbf{q}_{\parallel}, \omega)]$ for the 1 and 2 MLs thick slabs has been calculated with full SOC inclusion. The results are shown in Fig. 10.11 together with the scalar-relativistic counterparts.

As readily seen in Fig. 10.11, in both cases the low-energy thin film plasmon mode disappears upon inclusion of the SOC. This is not a surprising finding for the single monolayer case, as it acquires a semimetallic character when the spin-orbit interaction is switched on (see Fig. 9.2). However, the 2 MLs thick film results also show no signature of the low-energy mode when SOC is included. This is an unexpected result,

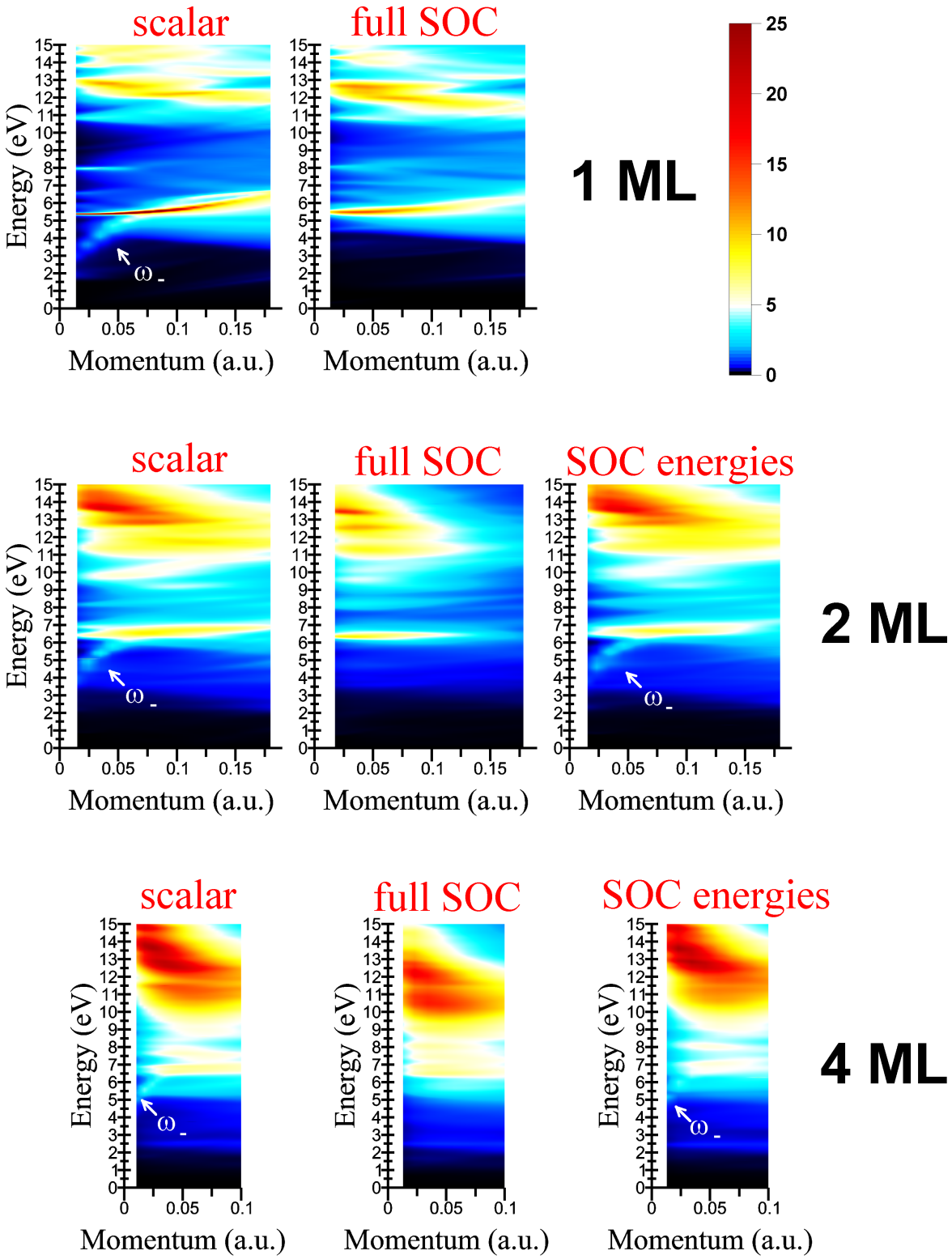

Figure 10.11: Surface loss function of 1, 2 and 4 MLs thick Pb(111) films obtained at the scalar-relativistic level ("scalar"), with full inclusion of the SOC ("full SOC") and using the scalar-relativistic wave functions together with the SOC-included energy bands ("SOC energies") in the calculations. The low-energy symmetric mode ω_- is highlighted when present.

as the band structrure of the 2 MLs thick film calculated with inclusion of SOC is qualitatively unaffected in comparison with its scalar-relativistic counterpart. In order to get further insight into this issue, $\mathrm{Im}[g(\mathbf{q}_\parallel, \omega)]$ for the 2 MLs slab was evaluated using the scalar-relativistic wave functions together with the SOC-included energy bands, and the results are shown in the leftmost panel of Fig. 10.11. As readily seen, the surface loss function obtained is almost unchanged with respect to the purely scalar-relativistic calculation. Thus, the low-energy mode is retrieved as long as the scalar-relativistic states are used in the evaluation of the susceptibility. This is a remarkable and unexpected SOC effect. Work is in progress to gain further insight into this SOC-induced disappearance of the low-energy symmetric mode.

In general, apart of removing the low-energy mode, SOC leaves the surface loss function qualitatively unchanged, as seen in Fig. 10.11. However, the intensity of $\mathrm{Im}[g(\mathbf{q}_\parallel, \omega)]$ is greatly decreased for the 2 MLs slab. Comparing the results obtained using the scalar-relativistic wave functions together with the SOC-included energy bands, it is concluded that the lowering of intensity of the surface loss function upon full SOC inclusion is a consequence of the incorporation of the two-component spinors, while the SOC-induced energy splittings have a negligible effect on the calculated $\mathrm{Im}[g(\mathbf{q}_\parallel, \omega)]$. Also, the long-living interband peak present in the scalar-relativistic surface loss function of the single monolayer is strongly smeared by the SOC, while its dispersion remains unaffected. This, again, is interpreted as a consequence of the coupling between two-component spinor wave functions, as the QWS energies around $\overline{\Gamma}$ are unchanged by the SOC in the single monolayer band structure (see Fig. 9.2).

10.6 Summary

In the work reported in the present Chapter we have shown that the three-dimensional estimation of the interacting susceptibility as given by Eqs. (3.28)-(3.29) draws an incorrect picture for the surface loss function of thin films in the long wavelength limit. The correct results are retrieved when the integrations in the Dyson-like equation Eq. (3.15) are restricted to a finite z range.

For 1 and 2 MLs thick films strong QSE have been found. The high-energy mode is completely absent in the single monolayer. This is a direct consequence of the quantization of the electronic states, leading instead to the appearance of discrete interband transitions for the high-energy range at small momentum transfer q [see Fig. 10.8 (a)].

Incorporation of the the full 3D *ab initio* band structure also shows a new feature. It does not disperse with the momentum transfer for films thicker than 2 MLs, presenting an energy of $\omega \sim 7$ eV. In practice, this new mode plays the role of the classical surface plasmon as the long-q limit of the low-energy thin film mode, as ω_- disappears upon coupling to the dispersionless peak. To the best of our knowledge, this is the first work predicting the existence of this new mode as the short wavelength limit of the low-

energy mode, replacing the role of the classical surface plasmon of energy $\omega_s = \omega_p/\sqrt{2}$. Indeed, in Ref. [JP60] a value of 7.2±0.1 eV was reported as the average energy of a feature below the surface plasmon energy in EELS measurements. We identify this feature as the dispersionless mode found in the present *ab initio* study. Surprisingly, the optical surface loss function evaluated from bulk calculations [see Eq. (10.4)] also shows a faint peak at ~ 7 eV.

Also, the surface loss function calculated from Eq. (10.4) without including the semicore electrons (see Section 7.2) is in agreeement with the first-principle results [see Fig. 10.8 (c) and (d)]. As regards the surface plasmon dispersion, a linear dependence with q has been found in the present work. Once its dispersion is fitted to a linear function of the momentum transfer, extrapolation of the fitting to $q \to 0$ gives a value of 10.58 eV, close to the experimental $\omega_s^{\rm exp} = 10.6 \pm 0.2$ eV [JP60].

Unexpectedly, SOC is found to remove the low-energy symmetric mode through the passage from scalar-relativistic states to two-component spinors as wave functions.

New electron energy loss spectroscopy measurements on Pb(111) thin films are highly desirable to check the present predictions and gain further insight in the dynamics of collective excitations of nanostructured systems and the consequences of the quantization of the electronic states. New experimental work could help solving the question about the theoretically predicted disappearance of the low-energy mode once SOC is taken into account.

Chapter 11

Summary and general conclusions

Here we schematically summarize the theoretical frameworks used and the physical properties studied in the present work. Then a brief outline of the most important results obtained in this thesis is presented, followed by a summary of the comparison with available experimental results. Finally, we give an outlook of the possible future steps to be undertaken.

I The present work has been based on the theoretical frameworks listed here:

(i) We have modeled the lattice potential felt by the valence electrons using norm-conserving pseudopotentials (NCP), which also serve as the theoretical method for the inclusion of the spin-orbit coupling (SOC) in the Hamiltonian.

(ii) The density-functional theory (DFT) together with the Local Density Approximation (LDA) have been used to obtain the electronic ground state properties of both bulk Pb and Pb(111) thin films.

(iii) Linear-response theory has been applied to evaluate the density-density response function, particularly the plasma losses, of bulk Pb and Pb nanosized films. The computational scheme was extended to allow calculations of the susceptibility incorporating two-component spinors form for representing the electron wave functions.

(iv) Many-body perturbation theory has been applied through the GW approximation to obtain and analyze the inelastic decay rates of excited electrons and holes in bulk Pb.

(v) For slab calculations, a supercell scheme has been used together with a corrected approach to evaluate the interacting susceptibility, allowing the study of the surface loss function of nanosized Pb films.

(vi) Throughout this thesis, simple models of the electron dynamics have been used to gain insight into the properties of electronic single-particle and collective excitations. Particularly, the free-electron gas (FEG) has served as

a reference for most of the properties studied in the present work.

II We have performed a first-principles study of the following properties of the electronic structure, and the dynamics of electronic single-particle and collective excitations of Pb in two different solid forms:

(i) In bulk lead we have performed the study of

- SOC effects on the electronic ground state,
- influence of different physical factors [SOC, local-field effects (LFE) and inclusion of xc effects] on energy-loss function on the low-energy transfer range,
- acoustic plasmons, analyzing their anisotropic character,
- the importance of the inclusion of the Pb $5d$ semicore electons on the study of the bulk plasmon dynamics,
- and the inelastic electron-electron $(e-e)$ contribution to the lifetime of excited quasiparticles.

(ii) In Pb(111) 1 - 15 monolayers (ML) thick films we carried out calculations on

- quantum-size effects (QSE) on the density of states (DOS), effective masses m^* and work function,
- SOC effects in the electronic ground state and surface loss function of the films,
- and the thickness dependence of the main plasmon modes.

III Based on the studies outlined above, we have obtained a general picture of the dynamical electronic excitations in Pb bulk and thin films and the effects of the different physical ingredients. Particular emphasis has been placed on ths study of SOC effects. The following are the main conclusions drawn by the present thesis:

(i) SOC effects.

- Spin-orbit interaction affects the band structure of bulk Pb and Pb(111) films in a notably distinct way. While producing large energy spliitings on bulk, it slightly affects the electronic structure of Pb(111) freestanding slabs except for the single ML case which becomes semimetallic upon SOC inclusion. This is understood in terms of the bulk electronic structure along $\Gamma-$L.

- Two manifestations of SOC effects on the energy-loss function of bulk lead have been found. In the low-energy transfer range, SOC improves the agreement with optical measurements. In the high-energy transfer range, it strongly affects the bulk plasmon dynamics mainly through the SOC-induced energy splitting between the $5d_{5/2}$ and $5d_{3/2}$ semicore levels.
- SOC also lowers the group velocity of the bulk acoustic plasmons found in the calculations.
- SOC affects the effective screening at low quasiparticle energies. Moreover, it reduces the decay rate of excited electrons around the Brillouin zone (BZ) center by as much as 60%.
- The incorporation of the two-component spinors on the evaluation of the susceptibility causes the disappearance of the low-energy symmetric mode on Pb(111) films.

(ii) Acoustic plasmons in bulk Pb.

- The existence of acoustic plasmon modes in bulk Pb has been predicted.
- The number and group velocity of these acoustic modes depends on the direction of the momentum transfer and on the inclusion of SOC.
- The possibility of experimental check of the existence of these acoustic modes by electron energy-loss measurements seems feasible as these modes keep their character up to $\omega \simeq 2$ eV.
- The acoustic plasmon along Γ-K in the second BZ is suggested as the most suitable for its experimental detection.

(iii) High-energy transfer dielectric response of bulk Pb.

- The inclusion of the $5d$ semicore electrons completely changes the high-energy transfer dielectric properties of bulk Pb. In particular, it lowers the bulk plasmon energy in the long wavelength limit by roughly 2.5 eV and it also shortens the momentum transfer range in which the bulk plasmon can exist.
- LFE greatly affect the energy-loss function of bulk Pb once the semicore electrons are explicitly included. This reflects the highly localized character of the $5d$ electrons in Pb.
- In general, we found that the high-energy transfer dielectric response of bulk Pb is shaped by the interplay between the transitions stemming from the semicore $5d$ electrons, the SOC effects and LFE.

(iv) Inelastic $e-e$ contribution to the decay rate of excited quasiparticles in Pb.

- Strong localization effects are found on the inelastic electron-electron contribution to the decay rate of excited electrons with energies 5.5 eV $\leqslant \epsilon \leqslant 8$ eV, where $\Gamma_{n\mathbf{k}}$ for d states is roughly 2 times larger than for p states.

- For the p electrons the damping rates $\Gamma(\epsilon)$ averaged over the BZ present a quadratic dependence on energy ϵ, whereas for p holes the quasi-linear dependence of $\Gamma(\epsilon)$ for energies ϵ below -2.5 eV reflects a non-free-electron-like nature of the electronic states at the bottom of the lowest p band.
- The calculated lifetime ratio $\tau_e(\epsilon)/\tau_h(\epsilon)$ reveals that band structure effects are important in electron-electron inelastic scattering processes for quasiparticles with binding energies less than 2 eV.
- By comparing the obtained results with experimental measurements of the lifetime of quantum-well states (QWS) in thin Pb films, we conclude that low-energy quasiparticles dynamics in the latter systems can be well represented by that in bulk Pb, even for a single Pb ML. This is understood in terms of the screening length in lead.
- As a preliminary result, at the scalar-relativistic level, *xc* effects have been found to noticeably increase the inelastic damping rates with respect to the RPA calculations. This holds for all the states analyzed, independently of their energy or orbital character.

(v) Fresstanding Pb(111) thin films: QSE and dielectric response.

- QSE have been found in the DOS, effective masses m^* and work function of the thin lead films.
- Plasmon modes analogous to the ones deduced from classical electrodynamics are found. The faint low-energy symmetric thin film plasmon mode can be resolved for slabs with a thickness $\leqslant$5 MLs. The high-energy antisymmetric one is the most intense feature in the surface loss function for all the studied thickenesses.
- Remarkable QSE are found in the surface loss function of the single Pb(111) monolayer, the 2MLs thick slab representing the crossover with the thickness regime in which QSE are absent. This is shown to be related to the thickness of the slab in units of the Pb Fermi wavelength.
- A dispersionless mode at energy $\omega \simeq 7$ eV has been found in film calculations. This peak appears as also as a faint feature in the optical surface loss function deduce from bulk calculation, signaling the bulk-like character of this mode.

IV Summary of comparisons with experimental and other theoretical works.

(i) The calculated band structure of bulk Pb with SOC included is in good agreement with previous experimental [JP90] and theoretical [JVTJ$^+$08] studies.

(ii) The calculated binding energies of the SOC-splitted semicore $5d_{5/2}$ and $5d_{3/2}$ levels are lower than the ones reported in photoionization measurements

[IPAA12] by ~ 2.4 eV, while they are in excellent agreement with a previous theoretical study [JVTJ$^+$08].

(iii) Good agreement with available optical experimental data [GMPM71] on the bulk Pb dielectric function is interpreted as an evidence of remarkable SOC effects, also in agreement with other theoretical works [SMWRLdB09, GAD10].

(iv) Comparison with reflectance measurements [MAWG73] shows good agreement with the calculated bulk plasmon energy ω_p, while no agreement has been found with the ω_p obtained in electron energy-loss measurements as reported in Ref. [JP60]. However, on the latter experimental work a broad feature centered at 23.3 eV was found, which is in fairly good agreement with a peak obtained at a close energy in our calculations.

(v) Good agreement of the calculated inelastic decay rates with the time-resolved two photon photoemission (TR-2PPE) experimental data of Ref. [MRD$^+$10] is found.

(vi) Present lifetime calculations for bulk Pb are in good agreement with inelastic damping rates of quantum well states of metallic thin films measured recently [HBP$^+$09, SKRZ$^+$10], presenting thereby evidence that quasiparticle dynamics can be considered as being bulk-like even in very thin Pb films.

(vii) QSE on the calculated DOS and work functions are in good agreement with a large bibliography of both theoretical and experimental studies, see Ref. [JLZX07] for a review on this issue.

(viii) As the 15 MLs thick Pb(111) film still presents in its calculated surface loss function the effects of the finite thickness, no unambiguous comparison with experimental values of the Pb surface plasmon energy was allowed.

(iv) Our first-principles results predict the existence of a mostly dispersionless new mode as the short wavelength limit of the low-energy mode are in good agreement with a mode found at 7.2±0.1 eV in EELS measurements reported in Ref. [JP60]. This mode presents a negligible dispersion up to $q = 0.25$ a.u. We trace back the origin of this mode to the bulk.

V Outlook of possible future work.

(i) Inclusion of the image potential tail as the correct asymptotic form of the Hartree potential in the vacuum. This could lead to changes in the surface loss function, as the $1/z$ decay of the potential would give to the electron states close to vacuum level a larger weight outside the slab surfaces [Lie97].

(ii) Inclusion of the substrate in the slab calculations in a realistic fashion. A starting strategy could consist in performing *ab initio* calculations of the

band structure of Pb(111) films on a silicon substrate. Once the effective masses of the QWSs are obtained, one could use this data to perform model calculations analogous to the ones reported in Ref. [ZZMS$^+$09] for the Pb/Cu(111) system, using a one-dimensional pseudopotential for modeling the substrate and the jellium model for the Pb overlayers.

(iii) Perform slab calculations of first-principles $e-e$ decay rates of film electronic states.

Appendices

Appendix A

Acronyms

2D	Two-dimensional
3D	Three-dimensional
ALDA	Adiabatic LDA
AP	Acoustic plasmon
ARPES	Angle-resolved photoemission spectroscopy
ASP	Acoustic surface plasmon
a.u.	Atomic units
BZ	Brillouin zone
CPA	Coherent potential approximation
CPU	Central processing unit
DFT	Density functional theory
DOS	Density of states
EELS	Electron-energy loss spectroscopy
FEG	Free-electron gas
fcc	Face-centered cubic
FER	Field emission resonance
FWHM	Full-width at half-maximum
GW	G: Green's function and W: Screened Coulomb interaction (from the German word *Wechselwirkung*)

HK	Hohenberg-Kohn
HSC	Hamann-Schlüter-Chiang
HWHM	Half-width at half-maximum
IBZ	Irreducible Brillouin zone
IPES	Inverse photoemission spectroscopy
ISBZ	Irreducible surface Brillouin zone
KKR	Korringa-Kohn-Rostoker
KS	Kohn-Sham
LDA	Local density approximation
LDF	Lindhard dielectric function
LFE	Local-field effects
ML	Monolayer
NCP	Norm-conserving pseudopotential
OPW	Orthogonalized plane wave
QF	Quinn-Ferrell
QSE	Quantum-size effect
QWS	Quantum-well state
RPA	Random phase approximation
SBZ	Surface Brillouin zone
SOC	Spin-orbit coupling
STM	Scanning tunneling microscope
STS	Scanning tunneling spectroscopy
TDDFT	Time-dependent DFT
TDLDA	Time-dependent LDA
TM	Troullier-Martins
TR-2PPE	Time-resolved two-photon photoemission
xc	Exchange-correlation

Appendix B

SOC matrix element derivation

Here we derive the SOC matrix elements Eqs. (2.36)-(2.38) for a plane wave basis. Then the proof of the property given by Eq. (2.42) is shown.

B.1 SOC matrix elements

In this Section the matrix element of the operator [Eq. (2.31)]

$$\widehat{V}^{SOC} = \sum_l V_l^{SOC}(r)\mathbf{L}\cdot\boldsymbol{\sigma}\mathrm{P_l} \tag{B.1}$$

is derived below using plane waves $\{|\mathbf{k}+\mathbf{G}\rangle\}$ as the basis. $\mathrm{P_l}$ stands for the projector on the angular momentum channel l.

First, the total operator is the sum of operators (B.1) for all the atoms in the crystal. Each atom is positioned in a unit cell whose origin is placed at $\mathbf{R}_\mu$ and with the position vector $\boldsymbol{\tau}_i$ inner to the unit cell. Thus the atomic coordinates are given by $\mathbf{r}_{\mu,i} = \mathbf{R}_\mu + \boldsymbol{\tau}_i$. Then,

$$\begin{aligned} V^{SOC}(\mathbf{G},\mathbf{G'}) &= \sum_{\mu,i}\langle \mathbf{k}+\mathbf{G}|\widehat{V}^{SOC}(\mathbf{r}-\mathbf{R}_\mu-\boldsymbol{\tau}_i,\mathbf{r'}-\mathbf{R}_\mu-\boldsymbol{\tau}_i)|\mathbf{k}+\mathbf{G'}\rangle = \\ &= \frac{1}{\Omega}\sum_{\mu,i}\int_\Omega\int_\Omega e^{-i(\mathbf{k}+\mathbf{G})\cdot\mathbf{r}}\widehat{V}^{SOC}(\mathbf{r}-\mathbf{R}_\mu-\boldsymbol{\tau}_i,\mathbf{r'}-\mathbf{R}_\mu-\boldsymbol{\tau}_i)e^{i(\mathbf{k}+\mathbf{G'})\cdot\mathbf{r'}}d\mathbf{r}d\mathbf{r'}, \end{aligned} \tag{B.2}$$

where Ω stands for the total volume of the system. Now, the change of variable $\mathbf{r} \to \mathbf{r} + \mathbf{R}_\mu + \boldsymbol{\tau}_i$ and the analogous of $\mathbf{r'}$ are applied. Then using the definition of reciprocal lattice vectors

$$\sum_\mu e^{\pm i(\mathbf{G}-\mathbf{G'})\cdot\mathbf{R}_\mu} = N_{cells}, \tag{B.3}$$

being N_{cells} the total number of unit cells in the crystal, the following expression is obtained

$$V^{SOC}(\mathbf{G},\mathbf{G'}) = \frac{1}{\Omega_{cell}} \sum_i \int_\Omega \int_\Omega e^{-i(\mathbf{k}+\mathbf{G})\cdot\mathbf{r}} \widehat{V}^{SOC}(\mathbf{r},\mathbf{r'}) e^{i(\mathbf{k}+\mathbf{G'})\cdot\mathbf{r'}} e^{-i(\mathbf{G}-\mathbf{G'})\cdot\boldsymbol{\tau}_i} d\mathbf{r} d\mathbf{r'}, \quad \text{(B.4)}$$

where $\Omega_{cell} = \Omega/N_{cells}$ is the volume of the unit cell. For the next step the structure factor defined as

$$S(\mathbf{G}) = \frac{1}{\Omega_{cell}} \sum_i e^{-i\mathbf{G}\cdot\boldsymbol{\tau}_i}, \quad \text{(B.5)}$$

is introduced in Eq. (B.4) together with the expression (2.31) for the SOC potential operator, leading to the equation

$$V^{SOC}_{\sigma,\sigma'}(\mathbf{G},\mathbf{G'}) = S(\mathbf{G}-\mathbf{G'})\times \\ \times \int_\Omega \int_\Omega e^{-i(\mathbf{k}+\mathbf{G})\cdot\mathbf{r}} \sum_{l,m} V_l^{SOC}(r) \mathbf{L}\cdot\boldsymbol{\sigma} Y_{l,m}(\theta,\varphi) Y^*_{l,m}(\theta',\varphi') e^{i(\mathbf{k}+\mathbf{G'})\cdot\mathbf{r'}} r^2 dr d\Omega d\Omega'. \quad \text{(B.6)}$$

Here $Y_{l.m}(\theta,\varphi)$ are spherical harmonics and Ω is the solid angle, not to be confused with the volume of the system usually denoted by the same greek letter (as above).

As explained in Section 2.6.1, the operator product $\mathbf{L}\cdot\boldsymbol{\sigma}$ transforms the SOC matrix element in a 2×2 matrix in the electron spin 1/2 subspace. As a result, three different matrix elements are retrieved, whose derivation is followed in parallel. Consequently, Eq. (B.6) is unfold in three [see Eq. (2.32)],

$$V^{SOC}_{\uparrow\uparrow}(\mathbf{G},\mathbf{G'}) = \frac{S(\mathbf{G}-\mathbf{G'})}{2}\times \\ \times \int_\Omega \int_\Omega e^{-i(\mathbf{k}+\mathbf{G})\cdot\mathbf{r}} \sum_{l,m} V_l^{SOC}(r) m Y_{l,m}(\theta,\varphi) Y^*_{l,m}(\theta',\varphi') e^{i(\mathbf{k}+\mathbf{G'})\cdot\mathbf{r'}} r^2 dr d\Omega d\Omega', \quad \text{(B.7)}$$

$$V^{SOC}_{\uparrow\downarrow}(\mathbf{G},\mathbf{G'}) = \frac{S(\mathbf{G}-\mathbf{G'})}{2}\times \\ \times \int_\Omega \int_\Omega e^{-i(\mathbf{k}+\mathbf{G})\cdot\mathbf{r}} \sum_{l,m} V_l^{SOC}(r) C_-(l,m) Y_{l,m}(\theta,\varphi) Y^*_{l,m}(\theta',\varphi') e^{i(\mathbf{k}+\mathbf{G'})\cdot\mathbf{r'}} r^2 dr d\Omega d\Omega', \quad \text{(B.8)}$$

$$V^{SOC}_{\downarrow\uparrow}(\mathbf{G},\mathbf{G'}) = \frac{S(\mathbf{G}-\mathbf{G'})}{2}\times \\ \times \int_\Omega \int_\Omega e^{-i(\mathbf{k}+\mathbf{G})\cdot\mathbf{r}} \sum_{l,m} V_l^{SOC}(r) C_+(l,m) Y_{l,m}(\theta,\varphi) Y^*_{l,m}(\theta',\varphi') e^{i(\mathbf{k}+\mathbf{G'})\cdot\mathbf{r'}} r^2 dr d\Omega d\Omega', \quad \text{(B.9)}$$

where $C_{\pm}(l,m) = \sqrt{l(l+1) - m(m \pm 1)}$ are Clebsch-Gordan coefficients [JS94] and the action of the angular momentum operators $\hat{L}_z$, $\hat{L}_-$ and $\hat{L}_+$ on the spherical harmonics (here we explicitly include $\hbar$),

$$\begin{aligned} \hat{L}_z Y_{l.m}(\theta,\varphi) &= \hbar m Y_{l.m}(\theta,\varphi), \\ \hat{L}_- Y_{l.m}(\theta,\varphi) &= \hbar C_-(l,m) Y_{l.m}(\theta,\varphi), \\ \hat{L}_+ Y_{l.m}(\theta,\varphi) &= \hbar C_+(l,m) Y_{l.m}(\theta,\varphi), \end{aligned} \tag{B.10}$$

has been used.

At this point the expansion of the exponential function in terms of spherical harmonics is introduced,

$$e^{i\mathbf{k}\cdot\mathbf{r}} = 4\pi \sum_{l,m} i^l j_l(kr) Y^*_{l,m}(\hat{k}) Y_{l,m}(\hat{r}) \tag{B.11}$$

where $\mathbf{k} = |\mathbf{k}|\hat{k}$ and $\mathbf{r} = |\mathbf{r}|\hat{r}$, and the orthogonality of the spherical harmonics $\langle Y_{l,m}(\theta,\varphi)|Y_{l',m'}(\theta,\varphi)\rangle = \delta_{ll'}\delta_{mm'}$ is applied to retrieve the final form of the SOC matrix elements,

$$\widehat{V}^{SOC}_{\uparrow\uparrow}(\mathbf{G},\mathbf{G'}) = S'(\mathbf{G},\mathbf{G'}) \sum_{l,m} m Y^*_{l,m}(\widehat{K}_{G'}) Y_{l,m}(\widehat{K}_G) A_l(K_G, K_{G'}), \tag{B.12}$$

$$\widehat{V}^{SOC}_{\uparrow\downarrow}(\mathbf{G},\mathbf{G'}) = S'(\mathbf{G},\mathbf{G'}) \sum_{l,m} C_-(l,m) Y^*_{l,m}(\widehat{K}_{G'}) Y_{l,m-1}(\widehat{K}_G) A_l(K_G, K_{G'}), \tag{B.13}$$

$$\widehat{V}^{SOC}_{\downarrow\uparrow}(\mathbf{G},\mathbf{G'}) = S'(\mathbf{G},\mathbf{G'}) \sum_{l,m} C_+(l,m) Y^*_{l,m}(\widehat{K}_{G'}) Y_{l,m+1}(\widehat{K}_G) A_l(K_G, K_{G'}), \tag{B.14}$$

which coincides with Eqs. (2.36)-(2.38). Here $K_G \equiv \mathbf{k}+\mathbf{G}$, and $S'(\mathbf{G}-\mathbf{G'}) = 2\pi^2 S(\mathbf{G}-\mathbf{G'})$ as in Section 2.6.1. $A_l(K_G, K_{G'})$ is given by Eq. (2.39)

B.2 Proof of Eq. (2.42)

Here I prove the antihermicity of $\langle e^{i(\mathbf{k}+\mathbf{G'})\mathbf{r}}\chi_{\sigma'}|\hat{V}^{SOC}|e^{i(\mathbf{k}+\mathbf{G})\mathbf{r}}\chi_{\sigma}\rangle$ regarding the spin *for a centrosymmetric system*. The presence of a centre of inversion in a crystal results in the following symmetry: $\mathrm{F}(\pm\mathbf{k} \pm \mathbf{G}) = \mathrm{F}(\mathbf{k}+\mathbf{G})$ for any function $\mathrm{F}(\mathbf{k})$. Then it is

straightforward to prove Eq. (2.42) as follows,

$$
\begin{aligned}
&-\langle e^{i(\mathbf{k}+\mathbf{G}')\mathbf{r}}\chi_{\sigma=\uparrow}|H^{SO}_{\uparrow\downarrow}|e^{i(\mathbf{k}+\mathbf{G})\mathbf{r}}\chi_{\sigma'=\downarrow}\rangle^* = \\
&= -[S'(\mathbf{G}-\mathbf{G}')\sum_l\sum_{m=-l+1}^{+l}\sqrt{l(l+1)-m(m-1)}Y^*_{l,m}(\widehat{K}_{G'})Y_{l,m+1}(\widehat{K}_G)A_l(K_G,K_{G'})]^* = \\
&= -S'(\mathbf{G}-\mathbf{G}')\sum_l\sum_{m=-l+1}^{+l}\sqrt{l(l+1)-m(m-1)}Y_{l,m}(\widehat{K}_{G'})Y^*_{l,m+1}(\widehat{K}_G)A_l(K_G,K_{G'}) = \\
&= S'(\mathbf{G}-\mathbf{G}')\sum_l\sum_{m=-l+1}^{+l}\sqrt{l(l+1)-m(m-1)}Y^*_{l,-m}(\widehat{K}_{G'})Y_{l,-m-1}(\widehat{K}_G)A_l(K_G,K_{G'}) = \\
&= S'(\mathbf{G}-\mathbf{G}')\sum_l\sum_{m=-l}^{+l-1}\sqrt{l(l+1)-m(m+1)}Y^*_{l,m}(\widehat{K}_{G'})Y_{l,m-1}(\widehat{K}_G)A_l(K_G,K_{G'}) = \\
&= \langle e^{i(\mathbf{k}+\mathbf{G}')\mathbf{r}}\chi_{\sigma=\downarrow}|H^{SO}_{\downarrow\uparrow}|e^{i(\mathbf{k}+\mathbf{G})\mathbf{r}}\chi_{\sigma'=\uparrow}\rangle,
\end{aligned}
$$

where the property $Y^*_{l,m} = (-1)^m Y_{l,-m}$ of the spherical harmonics has been used.

The structure factor $S'(\mathbf{G}-\mathbf{G}')$ is supposed to be real and actually it is in systems which present a centre of inversion. If it is not the case, the structure factor is in general a complex quantity, but one could still make use of Eq. (2.42) by only changing the structure factor by its complex conjugated value: $S'(\mathbf{G}-\mathbf{G}') \Rightarrow S'(\mathbf{G}-\mathbf{G}')^*$.

Appendix C

Variational principle and its application to SOC inclusion in electronic structure calculations

What follows is a brief review of the general variational method and its particular use in the inclusion of the SOC in electronic structure calculations.

C.1 General formulation of the variational method

Let suppose that the system under study is described by the following eigenvalue equation:

$$H^0\psi_n = \epsilon_n\psi_n, \tag{C.1}$$

and that the eigenstates of the system are orthonormal: $\langle\psi_n|\psi_m\rangle = \delta_{nm}$. Expanding them on the basis $\{\phi_i\}$, which is supposed to be complete and infinite,

$$\psi_n = \sum_{i=1}^{\infty} c_{n_i}\phi_i. \tag{C.2}$$

Obviously, in practice the upper limit of the sum in (C.2) will be a finite integer.

Now, a linear combination of eigenstates of (C.1) can be built as:

$$\Psi = \sum_{n=N_1}^{N_2} \xi_n\psi_n = \sum_{n=N_1}^{N_2} \xi_n \sum_{i=1}^{\infty} c_{n_i}\phi_i. \tag{C.3}$$

Concerning the value of N_1 and N_2, see the discussion following Eq. (C.8).

Now the obtention of the eigenvalues and eigenstates of a different system described by the Hamiltonian $\hat{H} = \hat{H}^0 + \hat{H}^1$ is sought. Let define the functional $L = L[\Psi]$ as

$$L[\Psi] = \langle\Psi|\hat{H}^0 + \hat{H}^1|\Psi\rangle - E\langle\Psi|\Psi\rangle. \tag{C.4}$$

The basis functions $\{\phi_i\}$ and their linear combinations $\{\psi_n\}$ as solutions of Eq. (C.1) are known and fixed, so L is only a function of the expansion coefficients in Eq. (C.3), ξ_n. Putting (C.3) in Eq. (C.4) and using Eq. (C.1) together with the orthonormality of $\{\psi_n\}$ we get:

$$L[\xi_n, \xi_m] = \sum_{n,m} \xi_n \xi_m^* \epsilon_n \delta_{n,m} + \sum_{n,m} \xi_n \xi_m^* \langle \psi_m | \hat{H}^1 | \psi_n \rangle - E \sum_{n,m} \xi_n \xi_m^* \delta_{n,m}, \tag{C.5}$$

where the coefficients ξ_n are complex in general.

The next step is to apply the variational method to L,

$$\frac{\partial L}{\partial \xi_n} = 0, \tag{C.6}$$

which leads to

$$\frac{\partial L}{\partial \xi_m^*} = \sum_n \xi_n \epsilon_n \delta_{n,m} + \sum_n \xi_n \langle \psi_m | H^1 | \psi_n \rangle - \sum_n E \xi_n \delta_{n,m} = 0. \tag{C.7}$$

In order to get a non-trivial solution, $\xi_n \neq 0$, of Eq. (C.7) we must solve

$$det|(\epsilon_n - E)\delta_{n,m} - \langle \psi_m | \hat{H}^1 | \psi_n \rangle| = 0. \tag{C.8}$$

Solving Eq. (C.8) the coefficients ξ_n and the new eigenvalues are collected, being the latter the variational estimate of the energy levels of the Hamiltonian $\hat{H}^0 + \hat{H}^1$.

A few words about the values that m and n take in Eq. (C.7) must be said. From Eq. (C.7) one sees clearly that there is a *mixing* introduced by $\langle \psi_m | \hat{H}^1 | \psi_n \rangle$ between different eigenstates of the original Hamiltonian $\hat{H}^0$. In the spirit of perturbation theory, taking $\hat{H}^1$ as the perturbation, m and n could be only those labels corresponding to the original eigenstates which present a non-negligible value of $\langle \psi_m | \hat{H}^1 | \psi_n \rangle$ and thus a noticeable mixing between them once the perturbation is switched on. Then, we have the freedom of choosing which energy levels are going to be perturbed. This freedom can be used to analyzed the way the perturbation $\hat{H}^1$ mixes the different unperturbed eigenfunctions.

The approximation of the eigenstates of the $\hat{H}^0 + \hat{H}^1$ Hamiltonian which results from the present procedure is

$$\Psi_j = \sum_n \xi_n^j \psi_n, \tag{C.9}$$

with $\{\xi_n^j\}$ corresponding to the variationally estimated eigenvalue ε_j of $\hat{H}^0 + \hat{H}^1$.

C.2 Applying the method to the inclusion of the SOC in plane wave basis calculations

In this Section the methodology described above is applied to the inclusion of the SOC, $\hat{H}^1 \equiv \hat{V}^{SOC}$, in electronic structure calculations using two-component spinorial plane

waves as basis functions,

$$\left\{e^{i(\mathbf{k}+\mathbf{G})\mathbf{r}}\chi_\sigma\right\}, \tag{C.10}$$

where spin wave functions χ_σ are given by Eq. (3.15), and in our case $\mathbf{G}$ are reciprocal lattice vectors. Thus the eigenstates of our $\hat{H}^0$ Hamiltonian -some scalar-relativistic Hamiltonian- are expanded in the basis Eq. (C.10),

$$\psi_{n,\mathbf{k},\sigma} = (\sum_{\mathbf{G}} c_{n,\mathbf{k}}(\mathbf{G})e^{i(\mathbf{k}+\mathbf{G})\mathbf{r}})\chi_\sigma \equiv \psi_{n,\mathbf{k}}(\mathbf{r})\chi_\sigma. \tag{C.11}$$

Their linear combination gives the spinor

$$\begin{aligned}\Psi_{\mathbf{k}} = \sum_{n=N_1}^{N_2}\sum_{\sigma=\uparrow,\downarrow}\xi_{n,\mathbf{k},\sigma}\psi_{n,\mathbf{k},\sigma} = \sum_{n=N_1}^{N_2}\sum_{\sigma=\uparrow,\downarrow}\xi_{n,\mathbf{k},\sigma}(\sum_{\mathbf{G}} c_{n,\mathbf{k}}(\mathbf{G})e^{i(\mathbf{k}+\mathbf{G})\mathbf{r}})\chi_\sigma = \\ = \sum_{n=N_1}^{N_2}\sum_{\sigma=\uparrow,\downarrow}\xi_{n,\mathbf{k},\sigma}\chi_\sigma(\sum_{\mathbf{G}} c_{n,\mathbf{k}}(\mathbf{G})e^{i(\mathbf{k}+\mathbf{G})\mathbf{r}}) = \sum_{n=N_1}^{N_2}\sum_{\sigma=\uparrow,\downarrow}\xi_{n,\mathbf{k},\sigma}\chi_\sigma\psi_{n,\mathbf{k}}(\mathbf{r}).\end{aligned} \tag{C.12}$$

Introducing it in Eq. (C.4), one is left with the functional:

$$\begin{aligned}L[\xi_{n,\mathbf{k},\sigma},\xi_{n',\mathbf{k},\sigma'}] = \sum_{n,n'}\sum_{\sigma,\sigma'}\xi_{n,\mathbf{k},\sigma}\xi^*_{n',\mathbf{k},\sigma'}\epsilon_{n,\mathbf{k},\sigma}\delta_{n,n'}\delta_{\sigma,\sigma'} \ + \\ + \sum_{n,n'}\sum_{\sigma,\sigma'}\xi_{n,\mathbf{k},\sigma}\xi^*_{n',\mathbf{k},\sigma'}\langle\psi_{n',\mathbf{k},\sigma'}|\hat{V}^{SOC}|\psi_{n,\mathbf{k},\sigma}\rangle - E_{\mathbf{k}}\sum_{n,n'}\sum_{\sigma,\sigma'}\xi_{n,\mathbf{k},\sigma}\xi^*_{n',\mathbf{k},\sigma'}\delta_{n,n'}\delta_{\sigma,\sigma'}.\end{aligned} \tag{C.13}$$

Appplying now the variational procedure,

$$\begin{aligned}\frac{\partial L}{\partial\xi^*_{n',\mathbf{k},\sigma'}} = \sum_{n,\sigma}\xi_{n,\mathbf{k},\sigma}\epsilon_{n,\mathbf{k},\sigma}\delta_{n,n'}\delta_{\sigma,\sigma'} \ + \\ + \sum_{n,\sigma}\xi_{n,\mathbf{k},\sigma}\langle\psi_{n',\mathbf{k},\sigma'}|\hat{V}^{SOC}|\psi_{n,\mathbf{k},\sigma}\rangle - \sum_{n,\sigma}E_{\mathbf{k}}\xi_{n,\mathbf{k},\sigma}\delta_{n,n'}\delta_{\sigma,\sigma'} = 0,\end{aligned} \tag{C.14}$$

and taking $\xi_{n,\mathbf{k},\sigma}$ out as a common factor, one is left with the following system of linear equations:

$$\sum_{n,\sigma}\xi_{n,\mathbf{k},\sigma}[\epsilon_{n,\mathbf{k},\sigma}\delta_{n,n'}\delta_{\sigma,\sigma'} + \langle\psi_{n',\mathbf{k},\sigma'}|\hat{V}^{SOC}|\psi_{n,\mathbf{k},\sigma}\rangle - E_{\mathbf{k}}\delta_{n,n'}\delta_{\sigma,\sigma'}] = 0, \tag{C.15}$$

from where it follows that

$$det|(\epsilon_{n,\mathbf{k},\sigma} - E_{\mathbf{k}})\delta_{n,n'}\delta_{\sigma,\sigma'} - \langle\psi_{n',\mathbf{k},\sigma'}|\hat{V}^{SOC}|\psi_{n,\mathbf{k},\sigma}\rangle| = 0. \tag{C.16}$$

Solving Eq. (C.16) the variational estimate of the energy levels and of the coefficients $\xi^j_{n,\mathbf{k},\sigma}$ in the expansion

$$\Psi_j = \sum_{n,\sigma}\xi^j_{n,\mathbf{k},\sigma}\psi_{n,\sigma} \tag{C.17}$$

of the variational estimate of the eigenfunctions of $\hat{H}^0+\hat{V}^{SOC}$ are obtained. It is worth recalling that the coefficients $\xi^j_{n,\mathbf{k},\sigma}$ are complex in general.

Finally, note that the matrix element $\langle\psi_{n',\mathbf{k},\sigma'}|\hat{V}^{SOC}|\psi_{n,\mathbf{k},\sigma}\rangle$ in the formalism adopted in the present work (see Appendix B) is unfolded in three, which exhibit the following form,

$$\langle\psi_{n',\mathbf{k}\uparrow}|\hat{V}^{SOC}_{\uparrow\uparrow}|\psi_{n,\mathbf{k},\uparrow}\rangle = \sum_{\mathbf{G},\mathbf{G}'} c_{n,\mathbf{k}}(\mathbf{G})c^*_{n',\mathbf{k}}(\mathbf{G'})S'(\mathbf{G}-\mathbf{G}')\times \\ \times\sum_{l,m} mY^*_{l,m}(\widehat{K}_{G'})Y_{l,m}(\widehat{K}_G)A_l(K_G,K_{G'}) \quad \text{(C.18)}$$

$$\langle\psi_{n',\mathbf{k},\uparrow}|\hat{V}^{SO}_{\uparrow\downarrow}|\psi_{n,\mathbf{k},\downarrow}\rangle = \sum_{\mathbf{G},\mathbf{G}'} c_{n,\mathbf{k}}(\mathbf{G})c^*_{n',\mathbf{k}}(\mathbf{G'})S'(\mathbf{G}-\mathbf{G}')\times \\ \times\sum_{l,m} C_-(l,m)Y^*_{l,m}(\widehat{K}_{G'})Y_{l,m-1}(\widehat{K}_G)A_l(K_G,K_{G'}) \quad \text{(C.19)}$$

$$\langle\psi_{n',\mathbf{k}\downarrow}|\hat{V}^{SO}_{\downarrow\uparrow}|\psi_{n,\mathbf{k},\uparrow}\rangle = \sum_{\mathbf{G},\mathbf{G}'} c_{n,\mathbf{k}}(\mathbf{G})c^*_{n',\mathbf{k}}(\mathbf{G'})S'(\mathbf{G}-\mathbf{G}')\times \\ \times\sum_{l,m} C_+(l,m)Y^*_{l,m}(\widehat{K}_{G'})Y_{l,m+1}(\widehat{K}_G)A_l(K_G,K_{G'}) \quad \text{(C.20)}$$

where $S'(\mathbf{G}-\mathbf{G}')=2\pi^2 S(\mathbf{G}-\mathbf{G}')$, being $S(\mathbf{G}-\mathbf{G}')$ the structure factor. $C_\pm(l,m)=\sqrt{l(l+1)-m(m\pm1)}$ are Clebsch-Gordan coefficients [JS94] and $A_l(K_G,K_{G'})$ is given by Eq. (2.39).

Note in the depicted application of the variational method to the inclusion of the SOC we suppose that $\hat{H}^0$ has a implicit up-down spin structure. As a consequence the eigenstates of $\hat{H}^0$ are chosen as purely spin-up or spin-down, with exactly the same spatial part of the wave function for the modes corresponding to the same scalar-relativistic electron states. This way we introduce *at hand* the electron 1/2 spin expanding the Hilbert space of the truly scalar-relativistic Hamitonian, a procedure needed to include the SOC in the electronic structure calculations following the variational recipe. Strictly, there is no spin in the scalar-relativistic system, as no spin-dependent terms appear in the Hamiltonian $\hat{H}^0$, see Eq. (2.20).

Appendix D

Numerical representation of the energy conservation in the dynamical structure factor

In order to evaluate Eq. (3.19) in practice one needs to replace $\delta(\varepsilon_{n,\mathbf{k}} - \varepsilon_{n',\mathbf{k+q}} + \omega)$, the Dirac delta which ensures energy conservation, with some function of finite width.

Probably the most usual choice is a Gaussian (see i.e. [AG94]),

$$\delta(x) \rightarrow \frac{1}{\sigma\sqrt{\pi}} e^{-x^2/\sigma^2}, \tag{D.1}$$

where σ controls the width of the Gaussian. Using a Gaussian to model the Dirac delta $\delta(\varepsilon_{n,\mathbf{k}} - \varepsilon_{n',\mathbf{k+q}} + \omega)$ presents a drawback. When ω is smaller than the Gaussian width, in practice this applies for the first values of ω in the numerical grid $\{\omega_i\}$, some spectral weight is lost. In other words, there is a small leackage of the calculated dynamical structure factor to the range of negative energy tranfer $\omega < 0$ (see Fig. D.1). We want to avoid this, as it represents (via the fluctuation-dissipation theorem) a violation of the sum rule any susceptibility must fulfill [GV05].

To solve this problem, a slightly different function is used to model the delta function, namely the following function

$$\delta(x) \rightarrow \mathrm{C}\ x e^{-x^2/\sigma^2}. \tag{D.2}$$

The normalization factor C is obtained from the condition

$$\int_0^\infty \mathrm{C}\ x e^{-x^2/\sigma^2} dx = 1. \tag{D.3}$$

More precisely, in our case we carry the substitution

$$\delta(\omega) \rightarrow \mathrm{C}\ \omega e^{-(\Delta+\omega)^2/\sigma^2}, \tag{D.4}$$

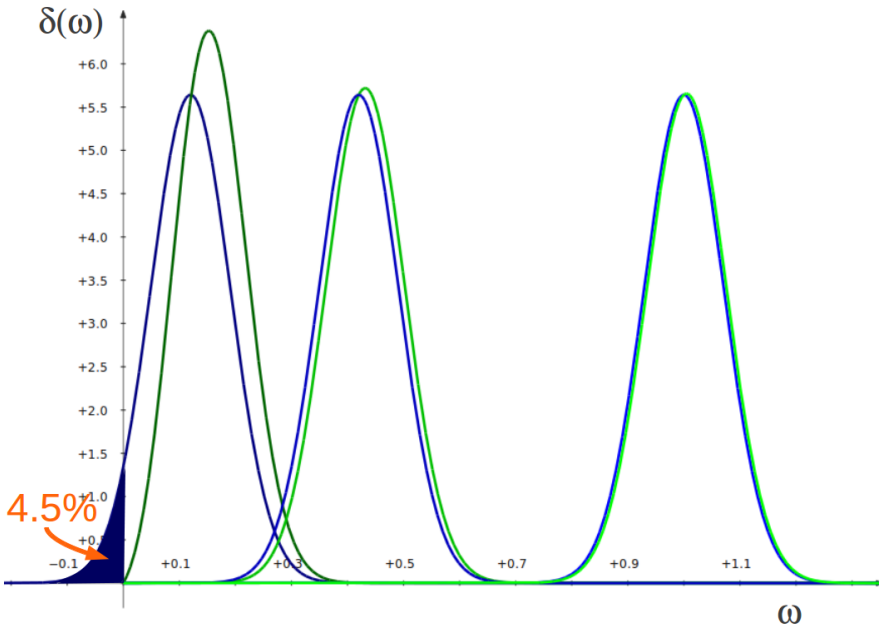

Figure D.1: Comparison of a Gaussian Eq. (D.1) with the modified function Eq. (D.4) for three different values of $\Delta = 0.12, 0.42, 1.00$, from left to right. Blue (green) curves correspond to the different Gaussians (modified functions). The shaded area represents the weight loss for a Gaussian when $\Delta \ll 1$, which for the depicted example is of $\sim 4.5\%$. All curves are drawn for a fixed $\sigma = 0.1$.

defining $\Delta \equiv (\varepsilon_{n,\mathbf{k}} - \varepsilon_{n',\mathbf{k}+\mathbf{q}})$. Then applying Eq. (D.3) we obtain

$$\mathrm{C} = \frac{2}{\sigma^2 e^{-\frac{|\Delta|^2}{\sigma^2}} + \sqrt{\pi}\sigma|\Delta|\left[1 + erf\left(\frac{|\Delta|}{\sigma}\right)\right]}, \tag{D.5}$$

where

$$erf(x) = \frac{2}{\sqrt{\pi}} \int_0^x e^{-t^2} dt, \tag{D.6}$$

is the so-called *error function* [AS64]. In Fig. D.1

One could still argue that a Gaussian, Eq. (D.1), can be used by only being careful in choosing a σ small enough with respect to the $\{\omega_i\}$ grid step $\Delta\omega_i$ in order to avoid the leacking of spectral weight. The point is that σ has to be high enough to ensure some overlap between the Dirac delta-like peaks centered at contiguous ω_i of the energy momentum mesh. This is needed to avoid spurious oscillations in the dynamical structure factor and consequently in the imaginary part of the susceptibility [see Eq. 3.23]. The presence of such oscillations would represent a numerical noise which would be reflected by the Kramers-Kronig relations [see Eq. (3.5) Section 3.2.1)] in the real part of the density-density response and dielectric functions. As it is stated in Section 3.2.1, peaks in the loss function correspond classically to the condition

$\mathrm{Re}[\varepsilon(\mathbf{q},\omega)] = 0$. Thus, strong numerical noise in $\mathrm{Re}[\varepsilon(\mathbf{q},\omega)]$ would introduce not only spurious oscillations in the energy-loss functions, but also spurious peaks.

The succession of peaks drawn in Fig. D.1 where the Dirac delta is modeled both by a Gaussian (blue curves) and by our modified function Eq. (D.4) (green curves) shows that our choice for replacing the Dirac delta avoids the leackage of spectral weight while slightly distorting its shape compared to a Gaussian only for values of $\Delta \ll 1$. As can be seen from the Figure, the dispersion of a peak remains unchanged, except for a small blueshift when $\omega \to 0$.

Appendix E

Lindhard dielectric function

The so-called Lindhard dielectric function corresponds to the quantum-mechanically derived longitudinal dielectric function of the electron gas. In three-dimensions it presents the form (throughout this Appendix we explicitly write down $\hbar$)

$$\varepsilon(\mathbf{q},\omega) = 1 + \frac{8\pi e^2}{q^2\Omega}\sum_{\mathbf{k}} \frac{f(\mathbf{k}) - f(\mathbf{k}+\mathbf{q})}{E(\mathbf{k}+\mathbf{q}) - E(\mathbf{k}) - \hbar\omega - i\eta} \tag{E.1}$$

Replacing $\mathbf{k}+\mathbf{q} \rightarrow$ **k'** in the term containing $f(\mathbf{k}+\mathbf{q})$ and relabelling it $\mathbf{k}$, we obtain

$$\varepsilon(\mathbf{q},\omega) = 1 + \frac{8\pi e^2}{q^2\Omega}\sum_{\mathbf{k}} \left[\frac{f(\mathbf{k})}{E(\mathbf{k}+\mathbf{q}) - E(\mathbf{k}) - \hbar\omega - i\eta} + \right.$$
$$\left. + \frac{f(\mathbf{k})}{E(\mathbf{k}+\mathbf{q}) - E(\mathbf{k}) + \hbar\omega + i\eta} \right], \tag{E.2}$$

where $q = |\mathbf{q}|$. The factor $8\pi e^2/q^2\Omega$ results of multiplying the Fourier transform of the Coulomb interaction $V(q) = 4\pi q^{-2}$ by a factor 2 which accounts for the spin degeneracy, finally dividing by the volume of the system, Ω. $\eta = 0^+$ is a positive infinitesimal.

In order to derive an analytical expression, the zero-temperature limit is assumed, in which the Fermi-Dirac distributions $f(\mathbf{k})$ becomes a Heaviside step function $\theta(\mathbf{k}-\mathbf{k}_F)$. Then, recalling that in the free electron gas $E(\mathbf{k}) = \hbar^2k^2/2m$ ($k = |\mathbf{k}|$) one gets

$$\varepsilon(\mathbf{q},\omega) = 1 + \frac{2me^2}{\pi\hbar^2}\frac{k_F}{q^2} + \frac{me^2}{\pi\hbar^2}\frac{1}{q^3}\left[k_F^2 - \left(\frac{q}{2} - \frac{\widetilde{\omega}}{2q}\right)^2\right] \ln\frac{2qk_F + q^2 - \widetilde{\omega}}{-2qk_F + q^2 - \widetilde{\omega}} +$$
$$+ \frac{me^2}{\pi\hbar^2}\frac{1}{q^3}\left[k_F^2 - \left(\frac{q}{2} + \frac{\widetilde{\omega}}{2q}\right)^2\right] \ln\frac{2qk_F + q^2 + \widetilde{\omega}}{-2qk_F + q^2 + \widetilde{\omega}}, \tag{E.3}$$

where we have defined $\widetilde{\omega} \equiv (2m/\hbar)(\omega + i\eta/\hbar)$. To separate the real and imaginary parts, the limit $\eta \rightarrow 0$, or equivalently Im $\widetilde{\omega} \rightarrow 0$ is taken. The logarithmic function

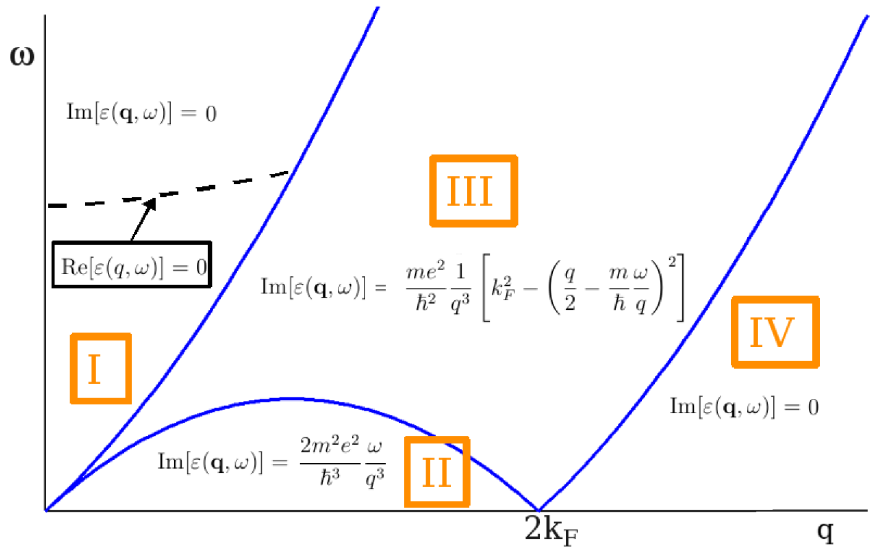

Figure E.1: Sketch of the different regions (labelled by capital roman numbers) in the (q,ω) surface of the imaginary part of the Lindhard $\varepsilon(\mathbf{q},\omega)$. The dashed line represents the dispersion of the plasmon as the dispersion of the locus of (q,ω) points at which the real part of the Lindhard dielectric function vanishes (see text).

of complex argument is defined with the cut from $-\infty$ to 0, then $\ln z = \ln|z| + i\arg z$ with $-\pi < \arg z < \pi$. The real part of Eq. (E.3) becomes

$$\mathrm{Re}[\varepsilon(\mathbf{q},\omega)] = 1+\frac{2me^2}{\pi\hbar^2}\frac{k_F}{q^2}+\frac{me^2}{\pi\hbar^2}\frac{1}{q^3}\left[k_F^2-\left(\frac{q}{2}-\frac{m}{\hbar}\frac{\omega}{q}\right)^2\right]\ln\left|\frac{2qk_F+q^2-(2m/\hbar)\omega}{-2qk_F+q^2-(2m/\hbar)\omega}\right|+$$
$$+\frac{me^2}{\pi\hbar^2}\frac{1}{q^3}\left[k_F^2-\left(\frac{q}{2}+\frac{m}{\hbar}\frac{\omega}{q}\right)^2\right]\ln\left|\frac{2qk_F+q^2+(2m/\hbar)\omega}{-2qk_F+q^2+(2m/\hbar)\omega}\right|. \quad \text{(E.4)}$$

The imaginary part of the Lindhard dielectric function is not analytic. It can be summarized as follows,

$$\mathrm{Im}[\varepsilon(\mathbf{q},\omega)] = \begin{cases} \dfrac{2m^2e^2}{\hbar^3}\dfrac{\omega}{q^3} & \text{if } q < 2k_F \text{ and } 0 \leqslant (2m/\hbar)\omega \leqslant 2qk_F - q^2 \\ \dfrac{me^2}{\hbar^2}\dfrac{1}{q^3}\left[k_F^2-\left(\dfrac{q}{2}-\dfrac{m}{\hbar}\dfrac{\omega}{q}\right)^2\right] & \text{if } 2qk_F - q^2 \leqslant (2m/\hbar)\omega \leqslant 2qk_F + q^2 \\ 0 & \text{in other cases.} \end{cases} \quad \text{(E.5)}$$

The structure of $\mathrm{Im}[\varepsilon(\mathbf{q},\omega)]$ is better assimilated by plotting the three parabolas $(2m/\hbar)\omega = 2qk_F + q^2$, $(2m/\hbar)\omega = 2qk_F - q^2$ and $(2m/\hbar)\omega = -2qk_F + q^2$. This is done in Fig. E.1.

In regions I and IV electron-hole pairs of momentum q can not be generated, as $\mathrm{Im}[\varepsilon]$ vanishes. Notice this has important consequences. In Fig. E.1 the dashed line

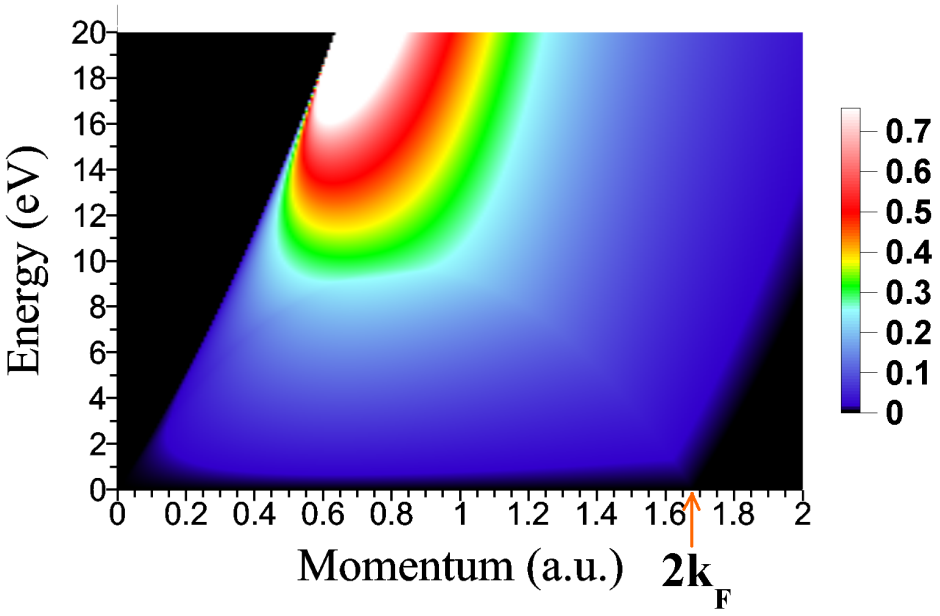

Figure E.2: Lindhard energy-loss function in arbitrary units, evaluated at the bulk lead density given by $r_s^{\mathrm{Pb}} = 2.298$ or equivalently $k_F^{\mathrm{Pb}} = 0.835$ Bohr^{-1}. All three boundaries plotted in Fig. E.1 can be seen reflected here. ω in eV, q in Bohr^{-1}.

represents the plasmon dispersion [an approximation of it is given by Eq. (3.34)], which takes place for a certain range of q momenta in region I, that is, outside the electron-hole continuum. Consequently the plasmon is undamped because its decay on electron-hole pairs is impossible in that range of (q, ω). Thus it presents a vanishing linewidth, or equivalently an infinite lifetime.

It can be easily shown that in the static limit $\omega \to 0$ the Lindhard dielectric function presents a singularity at $q = 2k_F$. This singular behaviour is responsible for several interesting phenomena. Specific examples are the Friedel oscillations [Fri58] and in one-dimensional systems the Peierls instability [EP55], related to the appearance of charge density waves.

From Eqs. (E.4) and (E.5) the energy-loss function can be built as

$$\mathrm{Im}[\varepsilon^{-1}(\mathbf{q}, \omega)] = \frac{-\mathrm{Im}[\varepsilon(\mathbf{q}, \omega)]}{\mathrm{Re}[\varepsilon(\mathbf{q}, \omega)]^2 + \mathrm{Im}[\varepsilon(\mathbf{q}, \omega)]^2}. \tag{E.6}$$

Because of the non-analyticity of the imaginary part of the Lindhard dielectric function, Eq. (E.6) must be evaluated separately for each of the regions defined in Fig. E.1. Notice that from Eq. (E.6) one deduces that the energy-loss function vanishes for regions I and II.

In Fig. E.2 the energy-loss function built using Eqs. (E.4) - (E.6) for the lead bulk valence electronic density is plotted. This density corresponds to $r_s^{\mathrm{Pb}} = 2.298$ [see Eq. (2.15)], which gives a (free-electron-like) Fermi momentum of $k_F^{\mathrm{Pb}} = 0.835$ Bohr^{-1}.

Notice the dissapearance of the plasmon (see the dashed line in Fig. E.1). Using the simple expression $\omega_p = \sqrt{3r_s^{-3}}$ and $r_s^{\mathrm{Pb}} = 2.298$ we deduce the value $\omega_p^{\mathrm{Pb}} \simeq 13.5$ eV. The plasmon is missing in Fig. E.2 as a consequence of its presence outside the electron-hole continuum, as it is mentioned above. Thus we are not able of catching the plasmon because it is undamped, becoming a Dirac delta which can not be reproduced. Actually, the small region of maximum intensity in the energy-loss function in Fig. E.2 corresponds to the entrance of the plasmon in the electron-hole continuum, instantly acquiring a finite width and showing up as the most prominent feature in the energy-loss spectra.

Appendix F

Derivation of the Quinn-Ferrell formula

As the starting point, let us consider the damping rate of electrons within the RPA [MPPZK$^+$04],

$$\Gamma(\omega) = \frac{2}{(2\pi)^3} \int v(q) \mathrm{Im}[-\varepsilon^{-1}(q,\omega)] d\mathbf{q}, \tag{F.1}$$

where $\mathrm{Im}[-\varepsilon^{-1}(q,\omega)]$ is the energy-loss function (see Section 3.3.1), $v(q) = 4\pi/q^2$ is the Fourier transfrom of the bare Coulomb potential and the momentum transfer is subject to the condition $0 < \omega < E_i - E_F$.

As we are interested in electrons with energies close to E_F, the frequency entering $\mathrm{Im}[\varepsilon^{-1}(q,\omega)]$ is always small. This allows us to use the low energy transfer limit of the imaginary part of the Lindhard dielectric function (see Appendix E),

$$\mathrm{Im}[\varepsilon(q,\omega \to 0)] \simeq \frac{2\omega}{q^3}. \tag{F.2}$$

Then it follows that

$$\mathrm{Im}[-\varepsilon^{-1}(q,\omega \to 0)] = \frac{\mathrm{Im}[\varepsilon(q,\omega \to 0)]}{|\varepsilon(q,0)|^2} \simeq \frac{2\omega}{q^3} [\varepsilon(q,0)]^{-2}, \tag{F.3}$$

as $\varepsilon(q,\omega = 0)$ is real.

Introducing Eq. (F.3) in Eq. (F.1) and in the limit $|E_i/E_F| \simeq 1$ we obtain the following equation:

$$\Gamma(E_i) = \frac{2}{\pi} \int_0^{2k_F} \frac{dq}{q^4} [\varepsilon(q,0)]^{-2} \frac{(E_i - E_F)^2}{k_i}, \tag{F.4}$$

where k_F and k_i represent the Fermi and initial momentum, respectively.

In the high-density limit ($k_F \to \infty$) a simple and appropiate choice for the static dielectric function is the Thomas-Fermi model [GPP00],

$$\varepsilon_{TF}(q) \simeq 1 + \frac{q_{TF}^2}{q^2}, \tag{F.5}$$

where $q_{TF} = \sqrt{4k_F/\pi}$ is the Thomas-Fermi momentum in atomic units. Using $\varepsilon_{TF}(q)$ in Eq. (F.4) and exteding the integration to infinity (allowed by the high-density limit), we obtain the expression:

$$\Gamma(E_i) = \frac{(\pi/k_F)^{3/2}}{16} \frac{(E_i - E_F)^2}{k_i} \tag{F.6}$$

Applying again the approximation $|E_i/E_F| \simeq 1$, we replace $k_i \to k_F$ and retrieve the QF formula

$$\Gamma_{QF}(E_i) = C(r_s)(E_i - E_F)^2 \tag{F.7}$$

The constant $C(r_s)$ is calculated using the expression of the Fermi momentum as a function of the density parameter, $k_F = (9\pi/4)^{1/3} r_s^{-1}$, finally obtaining the expression

$$\tau_{QF}(E_i) = \frac{0.3997}{r_s^{5/2}(E_i - E_F)^2}, \tag{F.8}$$

where $\tau_{QF}(E_i)$ is in femtoseconds when $(E_i - E_F)$ in electronvolts.

List of Figures

List of Tables

Bibliography

[AB08] F. Aryasetiawan and S. Biermann. *Phys. Rev. Lett.*, 100:116402, 2008.

[ABB+99] E. Anderson, Z. Bai, C. Bischof, S. Blackford, J. Demmel, J. Dongarra, J. Du Croz, A. Greenbaum, S. Hammarling, A. McKenney, and D. Sorensen. *LAPACK Users' Guide*. Society for Industrial and Applied Mathematics, Philadelphia, PA, 1999.

[ACSDRME00] M. A. Cazalilla, J. S. Dolado, A. Rubio, and P. M. Echenique. *Phys. Rev. B*, 61:8033, 2000.

[AG94] F. Aryasetiawan and O. Gunnarsson. *Phys. Rev. B*, 49:16214, 1994.

[AG98] F. Aryasetiawan and O. Gunnarsson. *Rep. Prog. Phys.*, 61:237, 1998.

[AK94] F. Aryasetiawan and K. Karlsson. *Phys. Rev. Lett.*, 73:1679, 1994.

[ANPZVC07] I. A. Nechaev, V. P. Zhukov, and E. V. Chulkov. *Phys. Solid State*, 49:1811, 2007.

[ANVC06] I. A. Nechaev and E. V. Chulkov. *Phys. Rev. B*, 73:165112, 2006.

[ANVC09] I. A. Nechaev and E. V. Chulkov. *Phys. of the Solid State*, 51:1772, 2009.

[ANVC10] I. A. Nechaev and E. V. Chulkov. *Eur. Phys. J. B*, 77:31, 2010.

[ANVCME07] I. A. Nechaev, E. V. Chulkov, and P. M. Echenique. *Phys. Rev. B*, 76:245125, 2007.

[ANYSMS+08] I. A. Nechaev, I. Yu. Sklyadneva, V. M. Silkin, P. M. Echenique, and E. V. Chulkov. *Phys. Rev. B*, 78:085113, 2008.

[AOZ07] A. Ayuela, E. Ogando, and N. Zabala. *Phys. Rev. B*, 75:153403, 2007.

[AQGE93] A. A. Quong and A. G. Eguiluz. *Phys. Rev. Lett.*, 70:3955, 1993.

[Ary01] F. Aryasetiawan. *Strong Coulomb Correlations in Electronic Structure Calculations,* edited by V. I. Anisimov. Gordon and Beach, Singapore, 2001.

[AS64] M. Abramowitz and I.A. Stegun. *Handbook of Mathematical Functions.* Dover, New York, fifth edition, 1964.

[ATO] ATOM, a program for DFT calculations in atoms and pseudopotential generation, distributed as part of the SIESTA software package. See http://www.icmab.cat/leem/siesta.

[BAYCT00] K. Budde, E. Abram, V. Yeh, and M. C. Tringides. *Phys. Rev. B*, 61:10602(R), 2000.

[BB10] M. Becker and R. Berndt. *Phys. Rev. B*, 81:205438, 2010.

[BBRHS82] G. B. Bachelet, D. R. Hamann, and M. Schlüter. *Phys. Rev. B*, 26:4199, 1982.

[BCAW51] H. B. Callen and T. A. Welton. *Phys. Rev.*, 83:34, 1951.

[BHP+09] C. Brun, I-P. Hong, F. Pattley, I. Y. Sklyadneva, R. Heid, P. M. Echenique, K. P. Bohnen, E. V. Chulkov, and W.-D. Schneider. *Phys. Rev. Lett.*, 102:207002, 2009.

[BRS61] J. Bardeen and J. R. Schrieffer. in *Progress in Low Temperature Physics,* edited by C. J. Groter. Interscience Publishers, Inc., New York, 1961.

[BRZ+09] J. Braun, P. Ruggerone, G. Zhang, J. P. Toennies, and G. Benedek. *Phys. Rev. B*, 79:205423, 2009.

[BSPD+10] A. B. Schmidt, M. Pickel, M. Donath, P. Buczek, A. Ernst, V. P. Zhukov, M. Echenique. P., L. M. Sandratskii, E. V. Chulkov, and M. Weinelt. *Phys. Rev. Lett.*, 105:197401, 2010.

[BVCMEMS08] A. Balassis, E. V. Chulkov, P. M. Echenique, and V. M. Silkin. *Phys. Rev. B*, 78:224502, 2008.

[BVR06] F. Bruneval, N. Vast, and L. Reining. *Phys. Rev. B*, 74:045102, 2006.

[Caz12] M. Cazzaniga. *Phys. Rev. B*, 86:035120, 2012.

[Chi00] T.-C. Chiang. *Surf. Sci. Rep.*, 39:181, 2000.

[CLPR73] J. C. Lemonnier, M. Prial, and S. Robin. *Phys. Rev. B*, 8:5452, 1973.

[CMPR+99] I. Campillo, J. M. Pitarke, A. Rubio, E. Zarate, and P. M. Echenique. *Phys. Rev. Lett.*, 83:2230, 1999.

[CMSMP+00] I. Campillo, V. M. Silkin, J. M. Pitarke, A. Rubio, and P. M. Echenique. *Phys. Rev. B*, 61:13484, 2000.

[CPK59] J. C. Phillips and L. Kleinman. *Phys. Rev.*, 116:287, 1959.

[CTJH74] W. C. Topp and J. J. Hopfield. *Phys. Rev. B*, 7:1295, 1974.

[CWH+11] M. Cazzaniga, H.-C. Weissker, S. Huotari, T. Pylkkänen, P. Salvestrini, G. Monaco, G. Onida, and L. Reining. *Phys. Rev. B*, 84:075109, 2011.

[CYLLBS+09] M. C. Yang, C. L. Lin, W. B. Su, S. P. Lin, S. M. Lu, H. Y. Lin, C. S. Chang, W. K. Hsu, and T. T. Tsong. *Phys. Rev. Lett.*, 102:196102, 2009.

[DLK70] N. D. Lang and W. Kohn. *Phys. Rev. B*, 1:4555, 1970.

[DM90] G. D. Mahan. *Many-Particle Physics*. Plenum Press, New York, 1990.

[DMSPMS+11] R. Diez Muino, D. Sanchez-Portal, V. M. Silkin, E. V. Chulkov, and P. M. Echenique. *PNAS*, 108:971, 2011.

[DPCECRS94] P. Duffy, D. P. Chong, M. E. Casida, and D. R. Salahub. *Phys. Rev. A*, 50:4707, 1994.

[DPV+07] B. Diaconescu, K. Pohl, L. Vattuone, L. Savio, P. Hofmann, V. M. Silkin, J. M. Pitarke, E. V. Chulkov, P. M. Echenique, D. Farías, and M. Rocca. *Nature*, 448:57, 2007.

[DWWGMRJN98] I. D. White, R. W. Godby, M. M. Rieger, and R. J. Need. *Phys. Rev. Lett.*, 80:4265, 1998.

[EB97] M. Ehrnsperger and H. Bross. *J. Phys.: Condens. Matter*, 9:1225, 1997.

[EKMSUN+10] E. E. Krasovskii, V. M. Silkin, V. U. Nazarov, P. M. Echenique, and E. V. Chulkov. *Phys. Rev. B*, 82:125102, 2010.

[EKS99] E. E. Krasovskii and W. Schattke. *Phys. Rev. B*, 59:15609(R), 1999.

[EP55] R. E. Peierls. *Quantum theory of solids*. Clarendon Press, Oxford, 1955.

[EP89] W. E. Pickett. *Comp. Phys. Rep.*, 9:115, 1989.

[EQCKS06] D. Eom, S. Qin, M.-Y. Chou, and C. K. Shih. *Phys. Rev. Lett.*, 96:027005, 2006.

[Ern07] A. Ernst. *Multiple-scattering theory: new developments and applications.* PhD thesis, Martin-Luther-Universität Halle-Wittenberg, 2007.

[ERPR+10] I. Errea, A. Rodríguez-Prieto, B. Rousseau, V. M. Silkin, and A. Bergara. *Phys. Rev. B*, 81:205105, 2010.

[ESK00] W. Ekardt, W.-D. Schöne, and R. Keyling. *Appl. Phys. A: Mater. Sci. Process.*, 71:529, 2000.

[ETJA12] B. E. Tegner and G. J. Ackland. *Computational Material Science*, 52:2, 2012.

[FD92] J. F. Dobson. *Phys. Rev. B*, 46:10163, 1992.

[Fer28] E. Fermi. *Z. Phys.*, 48:73, 1928.

[Fri58] J. Friedel. *Nuovo Cimento*, 7:287, 1958.

[FS06] C. Friedrich and A. Schindlmayr. *NIC Series*, 31:335, 2006.

[G̈96] A. Görling. *Phys. Rev. A*, 54:3912, 1996.

[GAD10] K. Glantschnig and C. Ambrosch-Draxl. *New J. Phys*, 12:103048, 2010.

[GE83] A. G. Eguiluz. *Phys. Rev. Lett.*, 51:1907, 1983.

[GGMPME04] I. G. Gurtubay, J. M. Pitarke, and P. M. Echenique. *Phys. Rev. B*, 69:245106, 2004.

[GIL76] O. Gunnarsson and B. I. Lundqvist. *Phys. Rev. B*, 13:4274, 1976.

[GL93] A. Görling and M. Levy. *Phys. Rev. B*, 47:13105, 1993.

[GLFLC82] S. G. Louie, S. Froyen, and M. L. Cohen. *Phys. Rev. B*, 26:1738, 1982.

[GMPM71] A. G. Mathewson and H. P. Myers. *Phys. Scr.*, 4:291, 1971.

[GMV90] X. Gonze, J.-P. Michenaud, and J.-P. Vigneron. *Phys. Rev. B*, 41:11827, 1990.

[GPP00] G. Grosso and G. Pastori Parravicini. *Solid State Physics.* Academic Press, San Diego (California), 2000.

[GV05] G. Giuliani and G. Vignale. *Quantum theory of the electron liquid.* Cambridge University Press, Cambridge, 2005.

[GZB+04] Y. Guo, Y.-F. Zhang, X.-Y. Bao, T.-Z. Han, Z. Tang, L.-X. Zhang, W.-G. Zhu, E. G. Wang, Q. Niu, Z. Q. Qiu, J.-F. Jia, Z.-X. Zhao, and Q.-K. Xu. *Science*, 306:1915, 2004.

[HBP+09] I-P. Hong, C. Brun, F. Patthey, I. Yu. Sklyadneva, X. Zubizarreta, R. Heid, V. M. Silkin, P. M. Echenique, K. P. Bohnen, E. V. Chulkov, and W.-D. Schneider. *Phys. Rev. B*, 80:081409(R), 2009.

[HBYSVC10] R. Heid, K.-P. Bohnen, I. Yu. Sklyadneva, and E. V. Chulkov. *Phys. Rev. B*, 81:174527, 2010.

[HDHUK+10] J. H. Dil, B. Hülsen, T. U. Kampen, P. Kratzer, and K. Horn. *J. Phys.: Condens. Matter*, 22:135008, 2010.

[Hed65] L. Hedin. *Phys. Rev.*, 139:A796, 1965.

[HK64] P. Hohenberg and W. Kohn. *Phys. Rev. B*, 136:B864, 1964.

[HR57] R. H. Ritchie. *Phys. Rev.*, 106:874, 1957.

[HT27] L. H. Thomas. *Camb. Philos. Soc.*, 23:542, 1927.

[IPAA12] D. Iablonskyi, M. Patanen, S. Aksela, and H. Aksela. *Phys. Rev. B*, 86:041101(R), 2012.

[IR60] E. I. Rashba. *Sov. Phys. Solid State*, 2:1109, 1960.

[IR93] Y. Ishii and J. Ruvalds. *Phys. Rev. B*, 48:3455, 1993.

[JB70] A. J. Bennett. *Phys. Rev. B*, 1:203, 1970.

[JHB96] M. Jalochowski, M. Hoffmann, and E. Bauer. *Phys. Rev. Lett.*, 76:4227, 1996.

[JHKPTZ89] B. J. Hinch, C. Koziol, J. P. Toennies, and G. Zhang. *Europhys. Lett.*, 10:341, 1989.

[JLZX07] J.-F. Jia, S.-C. Li, Y.-F. Zhang, and Qi-K. Xue. *JPSJ*, 76:082001, 2007.

[JMDP76] H. J. Monkhorst and J. D. Pack. *Phys. Rev. B*, 13:5188, 1976.

[JP60] C. J. Powell. *Proc. Phys. Soc.*, 76:593, 1960.

[JP90] G. Jézéquel and I. Pollini. *Phys. Rev. B*, 41:1327, 1990.

[JQAF58] J. J. Quinn and R. A. Ferrell. *Phys. Rev.*, 112:812, 1958.

[JS94] J. J. Sakurai. *Modern quantum mechanics*. Addison-Wesley, Reading, Massachusetts, 1994.

[JSZ02] M. Jałochowski, M. Strożak, and R. Zdyb. *Phys. Rev. B*, 66:205417, 2002.

[JSZ04] M. Jałochowski, M. Strożak, and R. Zdyb. *J. Phys.: Cond. Mat.*, 16:S4345, 2004.

[JVTJ+08] M. J. Verstraete, M. Torrent, F. Jollet, G. Zérah, and X. Gonze. *Phys. Rev. B*, 78:045119, 2008.

[JWHWYZ06] Y. Jia, B. Wu, H. H. Weitering, and Z. Y. Zhang. *Phys. Rev. B*, 74:035433, 2006.

[KEPTSGE02] W. Ku, W. E. Pickett, R. T. Scalettar, and A G. Eguiluz. *Phys. Rev. Lett.*, 88:057001, 2002.

[Kir08] P. S. Kirchmann. *Ultrafast Electron Dynamics in Low-Dimensional Materials*. PhD thesis, Freie Universität Berlin, 2008.

[KJS65] W. Kohn and L. J. Sham. *Phys. Rev. B*, 140:A1133, 1965.

[KMB82] L. Kleinman and D. M. Bylander. *Phys. Rev. Lett.*, 48:1425, 1982.

[KQY+10] J. Kim, S. Qin, W. Yao, Q. Niu, M. Y. Chou, and C.-K. Shih. *PNAS*, 107:12761, 2010.

[KSE00] R. Keyling, W.-D. Schöne, and W. Ekardt. *Phys. Rev. B*, 61:1670, 2000.

[KUGK85] E. K. U. Gross and W. Kohn. *Phys. Rev. Lett.*, 55:2850, 1985.

[Kuz98] H. Kuzmany. *Solid-State Spectroscopy. An introduction*. Springer, Berlin Heidelberg, 1998.

[LA62] S. L. Adler. *Phys. Rev.*, 126:413, 1962.

[Lax01] M. Lax. *Symmetry Pinciples in Solid State and Molecular Physics*. Dover, Mineola, New York, 2001.

[LFDW71] A. L. Fetter and J D. Walecka. *Quantum Theory of Many-Particle Systems*. McGraw-Hill, Boston, 1971.

[LHPAD04] F. Ladstädter, U. Hohenester, P. Puschnig, and C. Ambrosch-Draxl. *Phys. Rev. B*, 70:235125, 2004.

[Lie87] A. Liebsch. *Phys. Scr.*, 35:354, 1987.

[Lie97] A. Liebsch. *Electronic excitations at metal surfaces*. Plenum, New York, 1997.

[LJSPMV05] V. Lucarini, J. J. Saarinen, K.-E. Peiponen, and E. M. Vartiainen. *Kramers-Kronig Relations in Optical Materials Research*. Springer, Berlin Heidelberg, 2005.

[LSFD94] W. L. Schaich and J. F. Dobson. *Phys. Rev. B*, 49:14700, 1994.

[Lun83] S. Lundqvist. *Theory of the Inhomogeneous Electron Gas*. Plenum, New York, 1983.

[MAWG73] A. M. Ashton and G. W. Green. *J. Phys. F: Metal Phys.*, 3:179, 1973.

[MCJA80] D. M. Ceperley and B. J. Alder. *Phys. Rev. Lett.*, 45:1196, 1980.

[MDSRO02] A. Marini, R. Del Sole, A. Rubio, and G. Onida. *Phys. Rev. B*, 66:161104, 2002.

[Mea88] D. Mearns. *Phys. Rev. B*, 38:5906, 1988.

[MEBP78] P. M. Echenique and J. B. Pendry. *J. Phys. C*, 11:2065, 1978.

[MEMPVCR00] P. M. Echenique, J. M. Pitarke, E. V. Chulkov, and A. Rubio. *Chem. Phys.*, 251:1, 2000.

[Mes99] A. Messiah. *Quantum mechanics*. Dover, New York, 1999.

[MLBSLL+10] S. M. Lu, W. B. Su, C. L. Lin, W. Y. Chan, H. L. Hsiao, C. S. Chang, and T. T. Tson. *J. Appl. Phys.*, 108:083707, 2010.

[MM04] R. M. Martin. *Electronic structure: basic theory and practical methods*. Cambridge University Press, Cambridge, 2004.

[MORTHW06] M. M. Ozer, J. R. Thompson, and H. H. Weitering. *Nat. Phys.*, 2:173, 2006.

[MPMSVCME07] J. M. Pitarke, V. M. Silkin, E. V. Chulkov, and P. M. Echenique. *Rep. Prog. Phys.*, 70:1, 2007.

[MPPZK+04] J. M. Pitarke, V. P. Zhukov, R. Keyling, E. V. Chulkov, and P. M. Echenique. *ChemPhysChem*, 5:1284, 2004.

[MPUNMS+04] J. M. Pitarke, V. U. Nazarov, V. M. Silkin, E. V. Chulkov, E. Zaremba, and P. M. Echenique. *Phys. Rev. B*, 70:205403, 2004.

[MRD+10] S. Mathias, A. Ruffing, F. Deicke, M. Wiesenmayer, M. Aeschlimann, and M. Bauer. *Phys. Rev. B*, 81:155429, 2010.

[MSBMEVC09] V. M. Silkin, A. Balassis, P. M. Echenique, and E. V. Chulkov. *Phys. Rev. B*, 80:054521, 2009.

[MSGLMP+04] V. M. Silkin, A. García-Lekue, J. M. Pitarke, E. V. Chulkov, E. Zaremba, and P. M. Echenique. *Europhys. Lett.*, 66:260, 2004.

[MSMPVC+08] V. M. Silkin, J. M. Pitarke, E. V. Chulkov, B. Diaconescu, K. Pohl, L. Vattuone, L. Savio, Ph. Hofmann, D. Farías, M. Rocca, and P. M. Echenique. *Phys. Status Solidi A*, 205:1307, 2008.

[MSMPVCME05] V. M. Silkin, J. M. Pitarke, E. V. Chulkov, and P. M. Echenique. *Phys. Rev. B*, 72:115435, 2005.

[MSND+11] V. M. Silkin, T. Nagao, V. Despoja, J. P. Echeverry, S. V. Eremeev, E. V. Chulkov, and P. M. Echenique. *Phys. Rev. B*, 84:165416, 2011.

[MSPCMKVC09] V. M. Silkin, I. P. Chernov, Yu. M. Koroteev, and E. V. Chulkov. *Phys. Rev. B*, 80:245114, 2009.

[MSVCME03] V. M. Silkin, E. V. Chulkov, and P. M. Echenique. *Phys. Rev. B*, 68:205106, 2003.

[MSVCME04] V. M. Silkin, E. V. Chulkov, and P. M. Echenique. *Phys. Rev. Lett.*, 93:176801, 2004.

[MSZG+09] V. M. Silkin, J. Zhao, F. Guinea, E. V. Chulkov, P. M. Echenique, and H. Petek. *Phys. Rev. B*, 80:121408, 2009.

[MWYC02] C. M. Wei and M. Y. Chou. *Phys. Rev. B*, 66:233408, 2002.

[Nag10] T. Nagao. in *Dynamics at Solid State Surfaces and Interfaces,* Vol. I, U. Bovensiepen, H. Petek, M. Wolf (eds.). Wiley VCH, Weinheim, 2010.

[NFAMS12] M. N. Faraggi, A. Arnau, and V. M. Silkin. *Phys. Rev. B*, 86:035115, 2012.

[NHHH01] T. Nagao, T. Hildebrandt, M. Henzler, and S. Hasegawa. *Phys. Rev. Lett.*, 86:5747, 2001.

[NJPZ85] B. N. J. Persson and E. Zaremba. *Phys. Rev. B*, 31:1863, 1985.

[Noz62] P. Nozières. *Theory of Interacting Fermi Liquids.* Benjamin, New York, 1962.

[OJG89] R. O. Jones and O. Gunnarsson. *Rev. Mod. Phys.*, 61:689, 1989.

[OLVdPM02] R. Otero, A. L. Vazquez de Parga, and R. Miranda. *Phys. Rev. B*, 66:115401, 2002.

[ORR02] G. Onida, L. Reining, and A. Rubio. *Rev. Mod. Phys.*, 74:601, 2002.

[PC12] A. Politano and G. Chiarello. *Influence of Electron Quantum Confinement on the Electronic Response of Metal/Metal Interfaces*, volume 2010 of *Reviews in Plasmonics*. Springer New York, 2012.

[PDV+10] K. Pohl, B. Diaconescu, G. Vercelli, L. Vattuone, V. M. Silkin, E. V. Chulkov, P. M. Echenique, and M. Rocca. *Europhys. Lett.*, 90:57006, 2010.

[PEVCMEMS12] J. P. Echeverry, E. V. Chulkov, P. M. Echenique, and V. M. Silkin. *Phys. Rev. B*, 85:205135, 2012.

[Pin56] D. Pines. *Can. J. Phys.*, 34:1379, 1956.

[PKFJ06] A. Pucci, F. Kost, G. Fahsold, and M. Jalochowski. *Phys. Rev. B*, 74:125428, 2006.

[PN58] D. Pines and P. Nozières. *Phys. Rev.*, 109:1062, 1958.

[PN66] D. Pines and P. Nozières. *The Theory of Quantum Liquids*. Benjamin, New York, 1966.

[PPBE96] J. P. Perdew, K. Burke, and M. Ernzerhof. *Phys. Rev. Lett.*, 77:3865, 1996.

[PPL85] J. P. Perdew and M. Levy. *Phys. Rev. B*, 31:6264, 1985.

[PPZ81] J. P. Perdew and A. Zunger. *Phys. Rev. B*, 23:5048, 1981.

[PZAVC+01] V. P. Zhukov, F. Aryasetiawan, E. V. Chulkov, I. G. de Gurtubay, and P. M. Echenique. *Phys. Rev. B*, 64:195122, 2001.

[PZAVCME02] V. P. Zhukov, F. Aryasetiawan, E. V. Chulkov, and P. M. Echenique. *Phys. Rev. B*, 65:115116, 2002.

[PZMSVCME01] V. P. Zhulkov, V. M. Silkin, E. V. Chulkov, and P. M. Echenique. *Phys. Rev. B*, 64:180507, 2001.

[PZVC09] V. P. Zhukov and E. V. Chulkov. *Phys. Usp.*, 52:105, 2009.

[PZVCME04] V. P. Zhukov, E. V. Chulkov, and P. M. Echenique. *Phys. Rev. Lett.*, 93:096401, 2004.

[PZVCME05] V. P. Zhukov, E. V. Chulkov, and P. M. Echenique. *Phys. Rev. B*, 72:155109, 2005.

[QKNS09] S. Qin, J. Kim, Q. Niu, and C-K. Shih. *Science*, 324:1314, 2009.

[RBSKE02] M. R. Bacelar, W.-D. Schöne, R. Keyling, and W. Ekardt. *Phys. Rev. B*, 66:153101, 2002.

[RHSC79] D. R. Hamann, M. Schlüter, and C. Chiang. *Phys. Rev. Lett.*, 43:1494, 1979.

[RKUG84] E. Runge and E. K. U. Gross. *Phys. Rev. Lett.*, 52:997, 1984.

[RLdB05] P. Romaniello and P. L. de Boeij. *J. Chem. Phys.*, 122:164303, 2005.

[RPAMG85] D. R. Penn, S. Appel, and S. M. Girvin. *Phys. Rev. B*, 32:7753, 1985.

[SBW+02] O. Schmidt, M. Bauer, C. Wiemann, R. Porath, M. Scharte, O. Andreyev, G. Schönhense, and M. Aeschlimann. *Appl. Phys. B.*, 74:223, 2002.

[Sch03] W.-D. Schöne. *Int. J. Mod. Phys. B*, 17:5655, 2003.

[Sch07] W.-D. Schöne. *Prog. Surf. Sci.*, 82:161, 2007.

[SKB08] P. S. Kirchmann and U. Bovensiepen. *Phys. Rev. B*, 78:035437, 2008.

[SKBE99] W.-D. Schöne, R. Keyling, M. Bandić, and W. Ekardt. *Phys. Rev. B*, 60:8616, 1999.

[SKRZ+10] P. S. Kirchmann, L. Rettig, X. Zubizarreta, V. M. Silkin, E. V. Chulkov, and U. Bovensiepen. *Nat. Phys.*, 6:782, 2010.

[SKWHD+07] P. S. Kirchmann, M. Wolf, J. H. Dil, K. Horn, and U. Bovensiepen. *Phys. Rev. B*, 76:075406, 2007.

[SLS82] C. Schwartz and W. L. Schaich. *Phys. Rev. B*, 26:7008, 1982.

[SMOHD11] B. Slomski, F. Meier, J. Osterwalder, and J. H. Dil. *Phys. Rev. B*, 83:035409, 2011.

[SMWRLdB09] W. S. M. Werner, P. Romaniello, and P. L. de Boeij. *J. Phys. Chem. Ref. Data*, 38:1013, 2009.

[Tin71] M. Tinkam. *Group Theory and Quantum Mechanics*. McGraw-Hill, New York, 1971.

[TLM91] N. Troullier and J. L. Martins. *Phys. Rev. B*, 43:1993, 1991.

[TWPL+91] K.-D. Tsuei, E. W. Plummer, A. Liebsch, E. Pehlke, K. Kempa, and P. Bakshi. *Surf. Sci.*, 247:302, 1991.

[VCGBPG+06] E. V. Chulkov, A. G. Borisov, J. P. Gauyacq, D. Sánchez-Portal, V. M. Silkin, V. P. Zhukov, and P. M. Echenique. *Chem. Rev.*, 106:4160, 2006.

[VCMSME97] E. V. Chulkov, V. M. Silkin, and P. M. Echenique. *Surf. Sci.*, 391:L1217, 1997.

[VCMSME99] E. V. Chulkov, V. M. Silkin, and P. M. Echenique. *Surf. Sci.*, 437:330, 1999.

[VCSK+12] E. V. Chulkov, I. Sklyadneva, M. Kira, S. W. Koch, J. M. Pitarke, L. M. Sandratskii, P. Buczek, K. Ishioka, J. Schäfer, and M Weinelt. in *Dynamics at Solid State Surfaces and Interfaces,* Vol. I, U. Bovensiepen, H. Petek, M. Wolf (eds.). Wiley VCH, Weinheim, 2012.

[VEANMK+12] S. V. Eremeev, I. A. Nechaev, Yu. M. Koroteev, P. M. Echenique, and E. V. Chulkov. *Phys. Rev. Lett.*, 108:246802, 2012.

[vFDS04] I. Žutić, J. Fabian, and S. Das Sarma. *Rev. Mod. Phys.*, 76:323, 2004.

[WADM76] N. W. Ashcroft and N. D. Mermin. *Solid State Physics.* Thomson Learning, Southbank, Victoria, 1976.

[Win03] R. Winkler. *Spin-orbit coupling effects in two-dimensional electron and hole systems.* Springer, Berlin, 2003.

[Wis63] N. Wiser. *Phys. Rev.*, 129:62, 1963.

[WSH+06] H.-C. Weissker, J. Serrano, S. Huotari, F. Bruneval, F. Sottile, G. Monaco, M. Krisch, V. Olevano, and L. Reining. *Phys. Rev. Lett.*, 97:237602, 2006.

[WSH+10] H.-C. Weissker, J. Serrano, S. Huotari, E. Luppi, M. Cazzaniga, F. Bruneval, F. Sottile, G. Monaco, V. Olevano, and L. Reining. *Phys. Rev. B*, 81:085104, 2010.

[YBBZW+00] V. Yeh, L. Berbil-Bautista, C. Z. Wang, K. M. Ho, and M. C. Tringides. *Phys. Rev. Lett.*, 85:5158, 2000.

[YG06] Z. Yuan and S. Gao. *Phys. Rev. B*, 73:155411, 2006.

[YG09] Z. Yuan and S. Gao. *Computer Physics Communications*, 180:466, 2009.

[YMR+10] Z. Yi, Y. Ma, M. Rohlfing, V. M. Silkin, and E. V. Chulkov. *Phys. Rev. B*, 81:125125, 2010.

[YPJ08] F. Yndurain and M. P. Jigato. *Phys. Rev. Lett.*, 100:205501, 2008.

[YSBVC+11] I. Yu. Sklyadneva, G. Benedek, E. V. Chulkov, P. M. Echenique, R. Heid, K.-P. Bohnen, and J. P. Toennies. *Phys. Rev. Lett.*, 107:095502, 2011.

[ZAME99] E. Zarate, P. Appel, and P. M. Echenique. *Phys. Rev. B*, 60:2326, 1999.

[ZCL+10] T. Zhang, P. Cheng, W.-J. Li, Y.-J. Sun, G. Wang, X.-G. Zhu, K. He, L. Wang, X. Ma, and X. Chen. *Nat Phys.*, 6:104, 2010.

[ZHLK10] M. Z. Hasan and C. L. Kane. *Rev. Mod. Phys.*, 82:3045, 2010.

[ZS80] A. Zangwill and P. Soven. *Phys. Rev. Lett.*, 45:204, 1980.

[ZZGBVC11a] A. Zugarramurdi, N. Zabala, A. G. Borisov, and E. V. Chulkov. *Phys. Rev. Lett.*, 106:249601, 2011.

[ZZGBVC11b] A. Zugarramurdi, N. Zabala, A. G. Borisov, and E. V. Chulkov. *Phys. Rev. B*, 84:115422, 2011.

[ZZMS+09] A. Zugarramurdi, N. Zabala, V. M. Silkin, A. G. Borisov, and E. V. Chulkov. *Phys. Rev. B*, 80:115425, 2009.

[ZZMS+12] A. Zugarramurdi, N. Zabala, V. M. Silkin, E. V. Chulkov, and A. G. Borisov. *Phys. Rev. B*, 86:075434, 2012.

List of Publications

The articles published (or in process of preparation) during the period of this thesis are listed below:

1. I-Po Hong, Christophe Brun, Franois Patthey, I. Yu. Sklyadneva, X. Zubizarreta, R. Heid, V. M. Silkin, P. M. Echenique, K. P. Bohnen, E. V. Chulkov, and Wolf-Dieter Schneider,
   Decay mechanisms of excited electrons in quantum-well states of ultrathin Pb islands grown on Si(111): Scanning tunneling spectroscopy and theory,
   Phys. Rev. B **80**, 081409(R) (2009).

2. E. V. Chulkov, A. Zugarramurdi, S. S. Tsirkin, X. Zubizarreta, I. A. Nechaev, I. Yu. Sklyadneva and S. V. Eremeev,
   Electronic structure and excitations on clean and nanostructured metal surfaces,
   The European Physical Journal B **75**, 37-47 (2010).

3. P. S. Kirchmann, L. Rettig, X. Zubizarreta, V. M. Silkin, E. V. Chulkov and U. Bovensiepen,
   Quasiparticle lifetimes in metallic quantum-well nanostructures,
   Nat. Phys. **6**, 782 (2010).

4. X. Zubizarreta, V. M. Silkin, and E. V. Chulkov,
   First-principles quasiparticle damping rates in bulk lead,
   Phys. Rev. B **84**, 115144 (2011).

5. X. Zubizarreta, E. V. Chulkov and V. M. Silkin,
   Quantum effects on the loss function of Pb(111) thin films: an ab initio study,
   (To be submitted).

6. X. Zubizarreta, V. M. Silkin, and E. V. Chulkov,
   Ab initio study of low-energy electronic collective excitations in bulk Pb: anisotropy and acoustic modes,
   (To be submitted).